

**DEMONSTRATION OF ELECTRON BERNSTEIN WAVE
HEATING IN A REVERSED FIELD PINCH**

By

Andrew H. Seltzman

A dissertation submitted in partial fulfillment of
the requirements for the degree of

Doctor of Philosophy

(Physics)

At the

UNIVERSITY OF WISCONSIN-MADISON

2017

Date of final oral examination: 8/11/2017

The dissertation is approved by the following members of the Final Oral Committee:

Cary Brett Forest,	Professor, Physics
Jay Anderson,	Senior Scientist, Physics
John Sarff,	Professor, Physics
David Anderson,	Professor, Electrical and Computer Engineering
Jan Egedal,	Associate Professor, Physics

Abstract

DEMONSTRATION OF ELECTRON BERNSTEIN WAVE HEATING IN A REVERSED FIELD PINCH

Andrew H. Seltzman

Under the supervision of Professor Cary B. Forest, Dr. Jay K. Anderson

At the University of Wisconsin-Madison

The Electron Bernstein wave (EBW) presents an alternative to conventional electron cyclotron resonance heating and current drive in overdense plasmas, where the electromagnetic waves are inaccessible. The EBW is a short wavelength electrostatic wave excited by mode conversion of externally launched electromagnetic (O- or X-) modes. In this experiment, an edge launched X mode tunnels through a narrow evanescent region before conversion to the Bernstein mode, with efficiency maximized near 100% for optimal edge density gradient scale length. No previous observations of RF heating have been observed in the reversed-field pinch (RFP).

The RFP presents a set of unique challenges to RF heating. The confining magnetic field is generated almost entirely from current within the plasma, resulting in a dynamic equilibrium with $|B|$ maximized on the magnetic axis (no high field side exists) and a broad spectrum of current-driven instabilities. Consequent strong edge density fluctuations can diminish coupling to the EBW using OXB conversion, and the multiple internal resonant modes lead to a stochastic

magnetic field over much of the plasma minor radius. A close-fitting conducting shell is required for stabilization of ideal external modes; in the case of the Madison Symmetric Torus (MST), a thick shell which also serves as a single turn toroidal field coil, provides vertical field through induced image currents, and stabilizes the slower growing resistive wall mode. Other RFP devices have a thin conducting shell with active saddle coil sets for controlling the resistive mode. The relatively weak magnetic field of the configuration leads to very overdense plasma ($\omega_p/\omega_c > 5$) but also, when combined with inductive current profile control to reduce tearing fluctuations, allows for generation of high beta plasmas (10-25%).

Previous studies of EBW physics in the RFP show efficient coupling, both through reciprocity in a blackbody emission measurement and through optimization of a waveguide grill launching structure, provided the edge density gradient is suitable. Ray tracing studies predict accessibility of EBW heating and current drive over the outer half of the minor radius.

This thesis presents the first observation of RF heating of a RFP plasma using the EBW. The X-mode is launched from the low field side at 5.5 GHz with up to 150kW source power in 3ms long pulses; mode conversion occurs efficiently in the antenna near field ($K_0 L_n \sim 1$); no dedicated limiter surrounding the antenna was used to steepen the edge density gradient. Good coupling due to the naturally steep edge density gradient in the RFP resulted in net/F power ratios of 60-70% at second harmonic. The wave propagates radially inward through a magnetic field that is either stochastic or has broken flux surfaces, before depositing its power on a substantially Doppler-shifted cyclotron resonance. The radial EBW deposition profile is measured through thick-target bremsstrahlung with insertable probes near the plasma periphery on the $n=2$ harmonic ($\omega = n\omega_{ce} - k||v||$), also allowing a novel measurement of particle transport

in the edge ($r/a > 0.9$) of the RFP. Emission from a fixed limiter shows evidence of EBW absorption on harmonics from $n=1-7$ in the normal operating range of MST ($I_p = 50-500\text{kA}$).

Deposition location was controllable with $|B|$ and matched analytical models and equilibrium reconstruction. In the thick-shelled MST RFP, the radial accessibility of EBW is limited to $r/a > 0.8$ ($\sim 10\text{cm}$) by magnetic field error induced by the porthole necessary for the antenna; accessibility in a thin-shelled device with actively controlled saddle coils is likely to be $r/a > 0.5$ in agreement with ray tracing studies. Confinement timescales of fast electrons were too short to depend on collisional effects; RFP transport causes the observed loss of fast electron population. Radial diffusion rates were probed with EBW heated electrons. Enhanced confinement plasmas reduced perpendicular diffusion and allowed EBW heating in plasmas with beta of 15-20%.

Acknowledgements

I would like to thank my advisers, Jay Anderson, and Cary Forest for numerous discussions about RF heating and plasma theory, as well as John Goetz for his expertise in interpreting results from the RF system, Karsten McCollum, Brett Chapman, and Don Holly for operating and setting up the BtPPS, Abdulgader Almagri and Ami DuBois for assistance with probe and x-ray diagnostic setup, Mark Thomas for his work on the pillbox window design, and Paul Nonn for his insight into problem that occur with the RF and HV system. In addition, the construction of the EBW experiment would not have been possible without mechanical help from Robert Ganch, and Bill Zimmerman. The physics instrument shop machinists were a critical part of getting the EBW experiment running. The construction of the EBW experiment often required complex, precision machining of numerous components, occasionally out materials that were difficult to machine. Without the machinists, the EBW experiment would not have been possible.

Life in grad school would have not been the same without the many friends and colleagues I have made over the years in Madison. You all have made grad school and life in Madison an enjoyable and educational experience.

Lastly, I would like to thank my parents for inspiring an interest in science at an early age, as well as their continued support of my scientific pursuits.

Table of Contents

<i>Abstract</i>	<i>i</i>
<i>Acknowledgements</i>	<i>iv</i>
<i>Table of Contents</i>	<i>v</i>
<i>List of Figures</i>	<i>x</i>
<i>List of Tables</i>	<i>xxiii</i>
<i>Nomenclature</i>	<i>xxiv</i>
<i>Important Notes</i>	<i>xxvi</i>
<i>Introduction</i>	<i>1</i>
0.1 Overview	1
0.2 Research Contributions	3
0.3 Overview of Chapters	4
<i>Chapter 1 Motivation for EBW Heating</i>	<i>6</i>
1.1 Electromagnetic Accessibility in the RFP and the EBW	7

1.1.1	Cold plasma dispersion and edge propagation.....	7
1.1.2	Hot plasma dispersion relation and EBW propagation	11
1.1.3	Mode conversion to the Bernstein wave	12
1.1.4	Parametric decay instability during mode conversion	14
1.1.5	EBW absorption on the Doppler shifted cyclotron harmonic	16
1.1.6	Previous EBW Research	17
1.2	Motivation for EBW Heating and Current Drive in MST	23
1.2.1	Magnetic geometry of the RFP	23
1.2.2	Difficulty of RF heating the RFP	28
1.3	Summary	31
 <i>Chapter 2 Modeling of EBW heating in the RFP.....</i>		 <i>32</i>
2.1	Modeling of EBW Mode Conversion.....	34
2.1.1	Edge density and magnetic field profiles	34
2.1.2	Porthole field error contribution.....	37
2.2	Modeling of Heated Electrons in MST.....	41
	Heated electron collisions with background electrons and ions	41
2.2.1	Heated electron collisions with background neutrals.....	45
2.2.2	Perpendicular diffusion of heated electrons	48
2.2.3	Heated electron trapping in banana orbits.....	49
2.2.4	Toroidal drifts in MST	50
2.3	Genray simulations and wave propagation	55

2.4	Summary	57
<i>Chapter 3</i>	<i>Hardware</i>	58
3.1	RF Power Generation and Transmission	60
3.1.1	Klystron and support equipment	60
3.1.2	Antenna	61
3.2	RF Diagnostics and Control System	66
3.2.1	RF system overview	66
3.2.2	High speed isolation amplifier	68
3.2.1	Phase detection	71
3.2.1	High speed diode detector	74
3.2.2	Voltage variable attenuator	78
3.2.3	Klystron Power Feedback and Control	83
3.2.4	Antenna Arc Detection.....	87
3.2.1	Optical Arc Detection.....	91
3.2.2	Klystron Arc Detection	94
3.3	High Voltage Pulsed Power Supply.....	98
3.4	X-ray Diagnostics	103
3.4.1	X-ray emission from heated electrons.....	103
3.4.2	X-ray absorption and filtering	109
3.4.1	HXR detection system.....	110
3.4.1	Target probe system	112

3.4.2	Lower Hybrid Antenna Limiter.....	113
3.5	Summary.....	116
<i>Chapter 4 EBW Heating Results in MST.....</i>		<i>118</i>
4.1	Coupling and Mode Conversion at the UH Layer	120
4.1.1	Measurement of mode conversion to the EBW	120
4.1.1	Coupling efficiency to the EBW	122
4.1.2	Heating non-linearity with RF power.....	123
4.2	EBW Heating and Accessibility in the RFP	126
4.2.1	Radial deposition control of the EBW and accessibility limits....	126
4.2.2	Toroidal falloff of drifting electrons and effects of field pitch	135
4.2.3	High harmonic EBW heating	137
4.2.1	EBW heating in PPCD plasmas	138
4.3	Heated electron confinement time	141
4.4	Reconstruction of electron energy distribution function	146
4.4.1	Electron energy distribution function reconstruction.....	146
4.5	Summary.....	151
<i>Chapter 5 Conclusions and Recommendations.....</i>		<i>153</i>
5.1	Summary of Research.....	155
5.2	Conclusions.....	163
5.3	Future Work.....	164

<i>Bibliography</i>	166
<i>Appendix A</i>	176
1.1.1 Direct Measurement of EBW Mode Conversion	177
1.1.2 Observation EBE and EBW Heating and Current Drive in a Stellarator	179
1.1.3 Observation EBW Heating and Current Drive in a Tokamak.....	184
1.1.4 Observation EBW Heating and Current Drive in a Spherical Tokamak	189
1.1.5 EBW Simulations and Observation of Emission and Coupling in the RFP	196

List of Figures

- Figure 0.1.** Magnetic field geometry of the RFP showing axisymmetric $|B|$ and field reversal at the wall. Figure courtesy of MST group.2
- Figure 0.2.** Location of resonant and cutoff surfaces from MSTfit reconstruction in a 306kA plasma. Locations of fundamental through 5th harmonic EC resonances are shown. Electromagnetic cutoffs at 5.5GHz are shown to exist at the edge for X and O modes. See Chapter 1 for definitions of resonances and cutoffs.2
- Figure 1.1.** Index of refraction calculated for the x-mode wave, an illustrative curve for EBW, cutoff, and resonance locations are plotted in (a). Plasma frequencies are plotted in (b) for 5.5GHz x-mode edge launch in a 210kA plasma.10
- Figure 1.2.** Coupling between the slow X-mode electromagnetic wave, and the Bernstein wave occur at the UH layer.11
- Figure 1.3.** Maximum conversion efficiency vs density scale length with and without porthole field error at constant I_p14
- Figure 1.4.** Parametric excitation of multiples of the lower hybrid frequency (left) in a cylindrical plasma experiment. Figure courtesy of [13]. Parametric excitation of the lower hybrid frequency during EBW heating on MAST (right). Figure courtesy of [12].15
- Figure 1.5.** Contours of the EBW-heated electron distribution(circles) with trapped vs passing boundary marked in black lines for 2MW of RF heating.17
- Figure 1.6.** Toroidal(red), poloidal(blue), and magnitude(yellow) of magnetic fields in MST for a 395kA standard plasma.23
- Figure 1.7.** Toroidal electric field driven by transformer action (red), current drive $E_{||}$ (blue), and current profile (g) in MST.24
- Figure 1.8.** Safety factor in a typical standard MST plasma with rational surfaces marked. Note that y axis scale is expanded.25

- Figure 1.9.** Poincare surfaces of magnetic field before(left) and after(right) PPCD predicting significant reduction in stochastic magnetic field. Figure courtesy of [39].26
- Figure 1.10.** $J(r)$ control used to flatten lambda profile(left) and subsequent reduction in magnetic tearing modes(right). Figure courtesy of MST group.....27
- Figure 1.11.** EBW absorption location is plotted in blue for corrections for dopler shift and porthole field error, and in green corrected for dopler shift in the absence of a porthole.....29
- Figure 2.1.** Magnetic fields in the RFP demonstrating reversal of the toroidal field(green) at the edge, dominance of the poloidal field(blue) near the wall, and radial rependance of $|B|$ (red).....35
- Figure 2.2.** Magnetic field contours(left) and field lines(right) for 5cm porthole.38
- Figure 2.3.** ECR frequencies in the edge for first harmonic (red) and second harmonic (blue). Solid lines represent edge field without porthole field error, dashed lines include the field error contribution for a 5cm (left) and 12cm (right) porthole. The 5.5GHz launch frequency is denoted by the horizontal red line.38
- Figure 2.4.** Edge electron temperature estimated by MSTfit(blue) and a linear fit (red) are plotted for a 250kA plasma.43
- Figure 2.5.** Edge electron density(left) measured with a triple tip langmuir probe in a 200kA, $f=-0.18$, $n_e=1.2e19m^{-3}$ plasma. Figure courtesy of [56]. Plasma conditions for EBW target plasmas are typically half the line average density of this plot. Measured probe values are scaled linearly when used in EBW modeling to approximate typical target plasma conditions.....43
- Figure 2.6.** Electron on electron scattering times for heated electrons between 2 keV and 50 keV in a plasma of $n_e=2e17 m^{-3}$45
- Figure 2.7.** DEGAS2 simulations of neutral density(left) and temperature(right) in a 250kA and 350kA standard plasma indicate that density at 4cm from wall is $n_0(250kA)=6.8e16 [m^{-3}]$ and $n_0(350kA)=1.2e17 [m^{-3}]$46
- Figure 2.8.** Extrapolation(lines) of total interaction cross section for energies up to 50keV based on measured data(marked points) from [60].47

- Figure 2.9.** Collision times for 10-50keV electrons with neutral hydrogen are calculated to be in the 200-400 μ s range using plasma conditions modeled in DEGAS2 4cm from the wall.48
- Figure 2.10.** Mirror ratio and velocity ratio for trapped particles in a 250kA plasma, 3.5cm marked with vertical red line.50
- Figure 2.11.** Poloidal cross section of MST with magnetic field contours (black), possible EBW trajectory @138° Toroidal (red), and a possible banana orbit of heated electrons (green). Banana orbit has no radial width.....50
- Figure 2.12.** Banana orbit of heated electrons (green), limiter @150° Toroidal (blue solid line), and target probe P1 @300° Toroidal (black line) are observed by HXR detectors D6 and Q12, respectively.....51
- Figure 2.13.** Toroidal drift velocity for trapped electrons due to ∇B (blue solid), curvature drift for pitch angle scattered electrons with E in the parallel v direction(dashed blue).53
- Figure 2.14.** Toroidal transit time for one cycle around MST for an orbit at a radius of R+a for a 20keV trapped electron.54
- Figure 2.15.** Parallel refractive index(left) and doppler shift(right) plotted vs absorption position for the n=2 harmonic.56
- Figure 3.1.** Klystron tube being lowered into magnet (left). Klystron in magnet assembly with cooling oil bath attached (right).61
- Figure 3.2.** Cylindrical waveguide antenna. Leftmost component is a differentially pumped seal allowing the molybdenum antenna (center left) to slide and rotate without admitting gas to MST. Rectangular to cylindrical transition (rightmost) connects cylindrical pillbox window (center right) to the waveguide leading to the klystron tube.62
- Figure 3.3.** Differentially pumped sliding seal for cylindrical molybdenum antenna. Seal components (left) shows arrangement of o-rings and plastic spacers that stack within the stainless case. Assembled seal (right), shows pumping port located between the two o-rings. Plastic spacers provide ground loop isolation by insulating antenna from the shell of MST.63
- Figure 3.4.** Antenna mounting position on MST with differentially pumped seal.64

Figure 3.5. Klystron connects to antenna through an isolator assembly (circulator with waveguide load) to absorb reflected power and a directional coupler for forward and reflected power monitoring.	65
Figure 3.6. Block diagram of RF system.	67
Figure 3.7. High speed isolation amplifier schematic.....	69
Figure 3.8. High speed isolation amplifier boards are shown on the left, boards mounted within an RF shielded enclosure are shown on the right...	69
Figure 3.9. Frequency response (top) and phase shift (bottom) between input and output signals of the high speed isolation amplifier.....	70
Figure 3.10. Pulse response of isolation amplifier indicating 24ns delay time between input (green) and output (blue) pulses, and 19ns rise time (left). Phase shift for a 10MHz sin wave is -75 degrees (right)	71
Figure 3.11. Simplified block diagram of phase detection system.	72
Figure 3.12. Schematic of IF amplifier.	72
Figure 3.13. Phase detector amplifier board (left) with one of the two channels populated. Assembled 4 channel phase detector (right).....	73
Figure 3.14. High speed diode power detector amplifier schematic.....	75
Figure 3.15. High speed diode power detector amplifier board (left), and 4 channel power detector module (right).	75
Figure 3.16. Test of pulse detection with fast diode power detector and isolation amplifier. Control signal (green) switches a fast RF pin diode switch. Voltage waveforms are monitored from an un-amplified diode detector (purple), the fast diode detection system with amplifier board (blue), and output of the isolation amplifier. The fast power detector amplifier board contributes 19ns delay to the monitoring system while the fast isolation amplifier contributes 23ns delay.	76
Figure 3.17. Power detector calibration curves and fitted equations.	78
Figure 3.18. VVA typical attenuation vs voltage. Figure courtesy of Mini-Circuits.	79
Figure 3.19. Sweep of voltage (green) vs RF power detected on the output (pink) is shown on the left. The resulting RF level data is plotted vs voltage	

- for the range of interest (right) indicating best control sensitivity occurs between 0.4-0.8V input.....80
- Figure 3.20.** Frequency response compensation system for VVA. Circuit provides the inverse frequency response of the VVA, extending the system bandwidth to 2MHz.....81
- Figure 3.21.** VVA frequency response with (blue) and without (black) input compensation provided by the driver board. Inverse of the gain of the compensation system (red) shows close match to the gain of the uncompensated attenuator. Phase between input and output is plotted for the compensated system.81
- Figure 3.22.** Voltage output of compensator circuit (blue) in response to a step in input voltage (green) is shown on the left. RF output power from VVA shown with (blue) and without (grey) use of the compensation system are plotted on the right in response to a step in input voltage (green).82
- Figure 3.23.** VVA driver board(left) and assembled VVA system (right).83
- Figure 3.24.** Schematic of PID-X1k control board, figure courtesy of manufacturer (www.zapstudio.com)85
- Figure 3.25.** Bench test setup of the AGC system for verifying noise reduction and power control performance.....86
- Figure 3.26.** Modulation voltage (dark blue) to a second VVA in series with the output of an RF generator is switched at 1MHz producing a simulated 1MHz noise signal on the RF power signal (light blue). Without AGC control, power modulation is highly evident in the output (left), with AGC control a significant reduction in power noise is observed (center). Using the AGC system to track an external 20kHz power reference signal (green) allows control of output power level in the the presence of external noise. Modulation signal to the VVA in the AGC loop is shown in pink.....86
- Figure 3.27.** RF pulses without and with AGC operation. Klystron voltage (blue) and current (yellow) are identical between plots. Without the AGC system enabled (left), klystron power (green) shows distinct droop, ripple, and noise with a constant input power (pink). With the AGC enabled (right), klystron output power is stabilized at a constant level, and power noise is reduced. Note that the inverse of the droop, ripple and noise now appears in the input power to the tube (pink).87

- Figure 3.28.** Metalization of a quartz window within the pillbox assembly. Sputtering is concentrated along the electric field component within the pillbox (left). Significant metalization (right) due to numerous sustained arcs degrades window transmission.88
- Figure 3.29.** An arc occurs within the EBW antenna at ~20.2ms into the discharge. Reflected power drops from ~50% of forward power before the arc to under ~10% after the arc(top), simultaneously RF power in the plasma measured by an receiving antenna near the heating antenna drops to zero(middle), and fluctuations in forward to reflected phase, shown greatly smoothed, significantly reduce in amplitude. The antenna arc is sustained over the remaining duration of the heating pulse.89
- Figure 3.30.** New arc detector system in shielded box for noise immunity(left). System contains two arc detection systems, one for the antenna and one for the klystron. Old arc detection system (right) mounted in a 19" rack case suffered from noise pickup issues and often generated false trigger events.91
- Figure 3.31.** Fiber optic cable connecting PMT to pillbox window connects to a coupler that screws into the wall of the air side of the pillbox (left). The coupler compresses an o-ring between the pillbox and a quartz window, maintaining the integrity of the pressure seal when filling the waveguide with SF6. The coupler is shown screwed into the pillbox window in the right.92
- Figure 3.32.** Optical arc detector schematic.....93
- Figure 3.33.** Optical arc detection test. An LED provides photons to a photomultiplier tube through an attenuator when voltage is applied (pink) simulating light emission from an arc. Photons are counted by the photomultiplier tube (yellow) triggering a charge pump that increases voltage on a capacitor(blue). When capacitor voltage exceeds a preset ~2V level, a comparator triggers a pulse generator to inhibit RF output.94
- Figure 3.34.** Operation of the klystron arc detector and crowbar sparkgap during a klystron arc. Shown in the top plot, klystron voltage(black) and current(blue) are crowbarred as the sparkgap fires. The lack of a sharp increase in klystron current indicates that the crowbar circuit successfully triggered before the arc reached the cathode. Measured klystron drive power shown in the second panel, marks the periods of commanded RF output; a brief pulse is likely due to noise pickup during sparkgap operation. A significant drop in forward power,

- shown in black in the third panel, indicates the formation of an arc in a resonant cavity of the klystron. Triggering of the arc detection circuit is shown in the fourth panel, and marked with a dashed green line in all other panels in the figure.....96
- Figure 3.35.** High voltage pulsed power supply.98
- Figure 3.36.** Resonant transformer without parallel capacitor attached is shown on the left. Voltage boost ratio as a function of frequency is compared to simulated performance on the right.....99
- Figure 3.37.** H-bridges (left) drive each of three resonant transformers (right) connected in a Y configuration100
- Figure 3.38.** Schematic of voltage doubling rectifier, RL output snubber, and spark gap crowbar.100
- Figure 3.39.** Stabilized voltage output (light blue) using feedback control to H-bridge tune switching frequency (pink) towards resonance as capacitor bank voltage (dark blue) droops during the shot is shown plotted on the left. Generation of ~120kHz 6th harmonic ripple on the output voltage (blue) is shown in the FFT (red) on the right. ...101
- Figure 3.40.** Bremstrahlung spectrum from evaluation of Kramer's formula for electrons of mono-energetic(left) and dual gaussian(right) energy distributions colliding with a molybdenum target. Change in slope is noted at 10keV, however bremsstrahlung distribution remains monotonically decreasing with energy.....105
- Figure 3.41.** EEDF reconstruction from a bremsstrahlung spectrum produced by analytic EEDF functions showing exact reconstruction of EEDF(left), and reconstruction of non-analytic EEDF functions showing artifacts in the reconstructed EEDF (right).....108
- Figure 3.42.** X-ray transmission for 150um beryllium x-ray window without air gap (blue, solid), with air gap (black, dashed), and for 150um beryllium window + 200um aluminum filter without air gap (blue, dashed) and with air gap (red, dashed).....110
- Figure 3.43.** An HXR detector (left) showing the CdZnTe crystal. The radial array on MST consisting of multiple HXR detectors mounted on MST (middle). A poloidal cross section of MST (right) indicating potential locations of HXR detectors observing an insertable target probe (Probe1) and the LHCD antenna limiter (Limiter).....111

- Figure 3.44.** Gaussian pulse output from HXR detector for an Am241 gamma ray at 59.54keV.112
- Figure 3.45.** Target probe tip including a 25mm diameter, 25mm length molybdenum cylinder and boron nitride shield surrounding adjustable length copper rod.113
- Figure 3.46.** Lower hybrid antenna assembly including boron nitride limiter(white) and molybdenum interdigital straps(horizontal bars in center). Picture courtesy of John Goetz.114
- Figure 4.1.** Insertable RF probe head showing two crossed dipole antennas and two crossed magnetic loops (left). Diagram of insertable probe positioned in front of 3.6GHz antenna (right).121
- Figure 4.2.** Insertable RF probe data for electric field perpendicular to propagation, E_{ϕ} , and parallel to propagation, E_r , shows a shift in wave polarization from perpendicular to parallel to the propagation direction as the X-mode wave crosses the UH layer, located ~1.5cm from the wall. Measured field components go to zero past the UH layer as the EBW wavelength is too small to be detected by the probe.121
- Figure 4.3.** Net launched RF power vs forward power for plasma currents between 1st and 11th harmonic. Net launched power is highest for first harmonic absorption and decreases up to the 5th harmonic, then increases slightly up to the 11th harmonic. Significantly better coupling occurs for XB launch(blue) than for OXB launch(red). Harmonic jumps marked with red lines.123
- Figure 4.4.** HXR flux from LHCD antenna per kW net launched power for third harmonic heating in standard plasmas at increasing power levels. 124
- Figure 4.5.** HXR flux from LHCD antenna for third harmonic heating in standard plasmas vs power level at various plasma currents.125
- Figure 4.6.** Grouping of emission data points normalized linearly by Flux/kW(left) and non-linearly by Flux/kW²(right). The non-linear normalization produces significantly closer grouping of data by modeling the non-linear dependence on HXR flux on net RF power. 125
- Figure 4.7.** Poloidal cross section and 3D view of MST with magnetic field (black contours), possible EBW trajectory @138° Toroidal (red dots), banana orbit of heated electrons (green), and limiter @150° Toroidal (blue solid line) and target probe P1 @300° Toroidal (black line) observed by HXR detectors D6 and Q12, respectively.127

- Figure 4.8.** Radial profile of fast electron population from 0-10cm for select plasma currents measured with a target probe (\blacktriangledown) and limiter (X), toroidally displaced 162 degrees and 15 degrees, respectively, from EBW antenna. Midplane limiters (red box) fix the LCFS at 1.27 cm from the wall. Probe positions outside the LCFS measure negligible fast electron population.128
- Figure 4.9.** Radial profile of fast electron population from 0-10cm for all plasma currents measured with a target probe (\blacktriangledown) and limiter (X), toroidally displaced 162 degrees and 15 degrees, respectively, from EBW antenna. Midplane limiters (red box) fix the LCFS at 1.27 cm from the wall. Probe positions outside the LCFS measure negligible fast electron population.129
- Figure 4.10.** Reconstructed deposition location with correction for shadowing for the outboard limiter (green) and without correction (red), showing inaccurate location for the three highest I_p points. These I_p values correspond to high emission from the LHCD limiter.131
- Figure 4.11.** (a) HXR emission from limiter (blue) has distinct transitions between absorption outside (low) and inside (high) the LCFS. Peak emission from a target probe 4 cm from the wall occurs at lower I_p than peak from limiter due to increasing deposition depth. (b) Doppler shifted resonance location with porthole field error (blue) for harmonics ($n=1-4$) matches measured first moment ($n=2$) of deposition (green) and transitions to absorption outside LCFS. UH layer plotted in red.....133
- Figure 4.12.** HXR flux measured on LHCD antenna for normal and reversed B_t direction. Reversing B_t flips field line pitch but does not effect currents corresponding to high limiter emission.136
- Figure 4.13.** Toroidal decay of heated electron population at 2.5cm and 4cm from the wall represented by decreasing HXR production rate from an inserted target probe. An exponential fit of averaged data is plotted in black.137
- Figure 4.14.** HXR emission from limiter (blue) has distinct transitions between absorption outside(low) and inside(high) the LCFS. Accessibility windows in I_p , where the EBW is damped within the LCFS, are marked in red for $n=1-7$ harmonics. Harmonics $n=8-11$ are damped outside the LCFS.138
- Figure 4.15.** Time evolution of a typical PPCD discharge. Although plasma is nearly constant during the RF heating pulse, the inductive current

- drive continuously reduces the reversal parameter F , resulting in a steady increase in edge magnetic field.139
- Figure 4.16.** HXR spectrum during a PPCD plasma showing termination of 2nd harmonic EBW enhancement at ~15ms (left) while $|B(a)|$ increases. Emission from the LHCD antenna plotted vs $|B(a)|$ shows absorption at magnetic fields consistent with standard plasmas on the right. .140
- Figure 4.17.** Ensemble of HXR counts recorded on inboard target probe and LHCD antenna over an RF pulse train(left), and summation of counts aligned in time(right).142
- Figure 4.18.** EBW induced x-ray measurements using a target probe inserted 3 cm from the wall 162° toroidally away from the EBW heating location in a 175 kA plasma. HXR rise time from probe (a) and limiter (c) is shown following the start of the pulse (note different timescale). HXR fall time from probe (b) and limiter (d) following rf pulse end. Time axis is with respect to pulse start. (e) HXR spectrum from target probe is shown averaged over pulse period.144
- Figure 4.19.** Time constant of electron population decay rate in a 240kA plasma for standard(blue) and PPCD(red) plasmas showing increased electron confinement during reduced stochasticity periods.145
- Figure 4.20.** Comparison of HXR spectrum emitted from the LHCD antenna(left) and outboard limiter(right) during a 248kA PPCD plasma. 14keV and 22keV are marked by vertical red lines, K-shell lines are marked by blue lines.148
- Figure 4.21.** HXR energy spectrum(top) and electron energy reconstruction(bottom) from target probe in a 235kA plasma measuring EBW heated electrons inside the LCFS at 315T.149
- Figure 5.1.** (Left) X mode electromagnetic waves do not propagate past the periphery in the RFP due to cutoffs within a few cm of the wall, shown in blue and red. Mode conversion to the EBW, shown in red, at the UH layer, shown in green, allows accessibility to RF heating within the electromagnetic cutoff layers.155
- Figure 5.2.** Equilibrium reconstruction of an $I_p=265$ kA shot achieving $\beta=18.5\%$ during PPCD operation.158
- Figure 5.3.** (Left) (a) HXR emission from limiter (blue) has distinct transitions between absorption outside (low) and inside (high) the LCFS. Peak emission from a target probe 4 cm from the wall occurs at lower I_p than peak from limiter due to increasing deposition depth. (b)

- Doppler shifted resonance location with porthole field error (blue) for harmonics (n=1-4) matches measured first moment of n=2 deposition (green) and transitions to absorption outside LCFS. UH layer plotted in red.....159
- Figure 5.4.** Porthole field error reduces local magnetic field near the wall resulting in introduction of higher harmonic resonances near the edge, shown in blue. Radial accessibility is reduced by the transition to edge absorption at a higher I_p than would occur in the absence of a porthole, shown in green.161
- Figure 5.5.** Genray plot of first harmonic EBW deposition in a 260kA standard plasma (left) and 225kA PPCD plasma (right). Approximate location of the $r/a=0.5$ flux surface is marked in blue.....162
- Figure A.1.** Refractive index of plasma as a function of ω_p^2 / ω_c^2 showing mode conversion from fast and slow X-mode to EBW at the UH resonance. Figure courtesy of [100].177
- Figure A.2.** Interferometer output of radially scanned antenna observing mode conversion between fast x-mode and EBW waves as density increases(a, left plot), and comparison of measured k_{\perp} to theoretical value for the EBW. Figure courtesy of [100].178
- Figure A.3.** ECE and SXR emission from plasma correlated with non-resonant OXB heating (between markers). Figure courtesy of [101].180
- Figure A.4.** EBW ray tracing for OXB launch between 58GHz and 68GHz from the edge of W7AS (left). Shaded volume indicates emitting portion of plasma that will be measured on the EBE diagnostic. Measurements of EBE emission channels shown compared to T_e from SXR during a ramp up of density (right). EBE chord signal turns on as O-mode cutoff is reached for the given frequency, opening the BXO window. Figure courtesy of [102].181
- Figure A.5.** Co and counter EBW current drive in a current free plasma, measured as a function of loop voltage (left). Freely evolving EBW driven current in a stellarator plasma (right). Figure courtesy of [103].182
- Figure A.6.** Increase in electric field amplitude of E_y electric field and phase jump as EC wave crosses the UHR (left). Amplitude and phase of EBW heated thermal and fast electrons showing majority of power

- deposition occurs on the Doppler shifter fast electron tail inside the LCFS (right). Figure courtesy of [104].184
- Figure A.7.** Ray trajectory of launched X-mode wave passing through the first harmonic resonance, mode converting to the EBW at the UHR and being absorbed near the core (left). Power deposition profile of X-mode and EBW waves showing EBW absorption nearer to the core than the x-mode deposition (right). Figure courtesy of [105].185
- Figure A.8.** EBW heating of the plasma is correlated with a decrease in loop voltages as well as increase in H-alpha, SXR, HXR and ECE emission (left). SXR tomography of plasma demonstrating EBW heating location is shown with an overlay of ray paths (right). Figure courtesy of [106].187
- Figure A.9.** EBW ray tracing simulation for heating scenario in Compass-D showing X-mode launch through ECR layer at perpendicular angle, mode conversion at UHR and subsequent EBW absorption (left). Plasma parameters during EBW experiment showing locations of Thomson scattering measurements (right). Figure courtesy of [107].188
- Figure A.10.** Thomson scattering measurements of central electron temperature profiles and measurement of central electron temperature vs. toroidal launch angle showing peak heating efficiency occurs at 0 degrees (left). Current drive vs. toroidal launch angle estimated from V_{loop} and T_e measurements showing a peak at 0 degrees (right). Figure courtesy of [107].189
- Figure A.11.** Density profiles with (triangles) and without (diamonds) installation of the local limiter showing steepening of the edge density gradient (left). Measured emission with (diamonds) and without (triangles) installation of a local limiter for L_n optimization showing an order of magnitude increase in measured signal (right). Figure courtesy of [108].191
- Figure A.12.** Cross section of TST-2 showing locations of R and L cutoffs, and launcher (left). Measured SXR emission during RF shot (right). Figure courtesy of [109].193
- Figure A.13.** Simulation of reduction in V_{α} / ω strongly effecting intensity of EBW ray (left). Comparison of measured EBW transmission efficiency and T_e at the UHR layer with (red) and without (black) Li wall conditioning (right). Figure courtesy of [110].195

- Figure A.14.** Measurement of EBW driven current ramp up to 20kA in LATE.
Figure courtesy of [111].196
- Figure A.15.** Edge density in standard (O) and PPCD (square) plasmas,
characteristic frequencies, and dispersion relation (left). Evolution of
 I_p , N_e , N_e at 3.5cm, position of UHR (Xuh), and density scale
length during a PPCD shot for 3.6GHz. Figure courtesy of [112]. 199
- Figure A.16.** Reflection coefficient vs. density scale length from a single
waveguide (triangles) compared to theoretical values (blue squares)
(left). Reflection coefficient vs. density scale length from a phased
array at optimum launch angle (triangles) compared to theoretical
values (red circles) (right). Figure courtesy of [112].200
- Figure A.17.** Measurement of reflection coefficient vs phase for 3.6GHz X-mode
launch into a 190kA PPCD plasma. Launch with a BN cover at 1W
(square), 50kW (+) and without a BN cover 1W (triangle), and
standard plasma at 1W (o). Figure courtesy of [112].201
- Figure A.18.** Measurement of X and O mode EBE over 4-8GHz(left).
Temperature measurement mapped to minor radius and compared to
Thomson data(right). Figure courtesy of [113].202
- Figure A.19.** Genray trajectories of EBW at 3 poloidal launch angles(left). Value
of N_{\perp} and N_{\parallel} as the ray approaches the absorption
location(center). Magnitude of driven current density(right). Figure
courtesy of [114].204

List of Tables

Table 1-1: Overview of EBW Heating Parameters in Previous Devices.....	19
Table 3-1: X-ray K edges and characteristic X-ray lines in keV	105
Table 3-2: Characteristic X-ray line widths in eV	106

Nomenclature

CPDR	Cold Plasma Dispersion Relation
EB	Electron Bernstein
EBE	Electron Bernstein Emission
EBW	Electron Bernstein Wave
EC	Electron Cyclotron
F	Reversal parameter
FELD	Fast Electron Loss Diagnostic
HXR	Hard X-Ray
IGBT	Insulated Gate Bipolar Transistor
L	Left [electron cyclotron cutoff]
LCFS	Last Closed Flux Surface
LH	Lower Hybrid [resonance or frequency]
LHCD	Lower Hybrid Current Drive
MST	Madison Symmetric Torus
P	Plasma [frequency]
PFN	Pulse Forming Network
PPCD	Pulsed Poloidal Current Drive

q	Safety factor
RFP	Reversed Field Pinch
R	Right [electron cyclotron cutoff]
SMPS	Switch Mode Power Supply
ST	Spherical Tokamak
SXR	Soft X-Ray
UH	Upper Hybrid [resonance or frequency]

Important Notes

- Depending on reference or person the term “first harmonic” with reference to RF absorption/emission may be interpreted as either $n=1$ or $n=2$ for $\omega_{rf} = n\omega_{ce}$. In this thesis, “first harmonic” is taken to be synonymous with fundamental ($n=1$) harmonic.
- Significant effort was invested in the development of a switching power supply to drive the klystron tube. This thesis focuses on the physics of electron Bernstein wave heating in the reversed-field pinch and only briefly outlines the power supply. For a detailed documentation of the hardware, please refer to my master’s thesis: “Design of a resonant soft switching power supply for stabilized dc impulse delivery” Thesis, University of Wisconsin, 2012

Introduction

0.1 Overview

The Electron Bernstein wave (EBW) [1], [2] presents an alternative to access the electron cyclotron resonance for heating and current drive in overdense ($\omega_{pe} > \omega_{ce}$) plasmas where the conventional electromagnetic waves are cut off at the periphery. The EBW is a short wavelength electrostatic wave excited by mode conversion of externally launched electromagnetic (O- or X-) modes. The reversed-field pinch (RFP) presents a unique set of challenges to RF heating. The confining magnetic field is generated almost entirely from current within the plasma, resulting in a large Ohmic heat input and a dynamic equilibrium with $|B|$ maximized on the magnetic axis, as shown in **Figure 0.1** (no high field side exists); $B(r)$ profiles are proportional to plasma current. In Madison Symmetric Torus (MST) [3] a thick shell, which also serves as a single turn toroidal field coil, provides vertical field through induced image currents, and stabilizes the slower growing resistive wall mode.

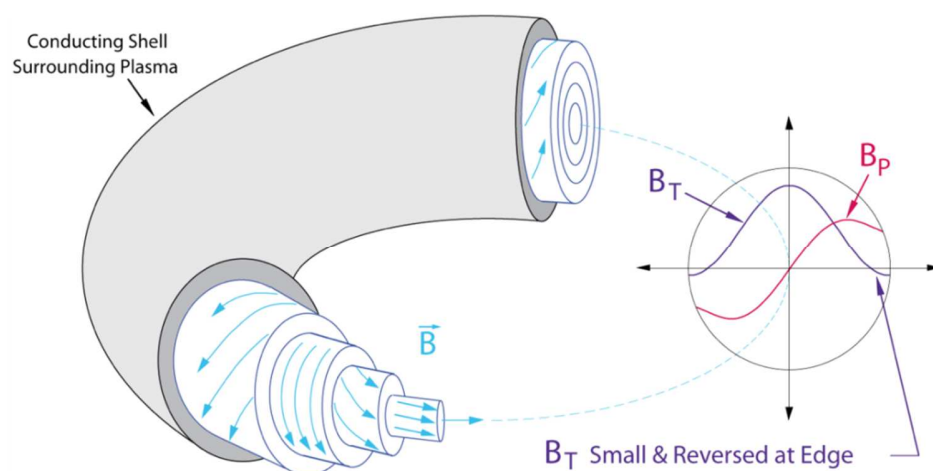


Figure 0.1. Magnetic field geometry of the RFP showing axisymmetric $|B|$ and field reversal at the wall. Figure courtesy of MST group.

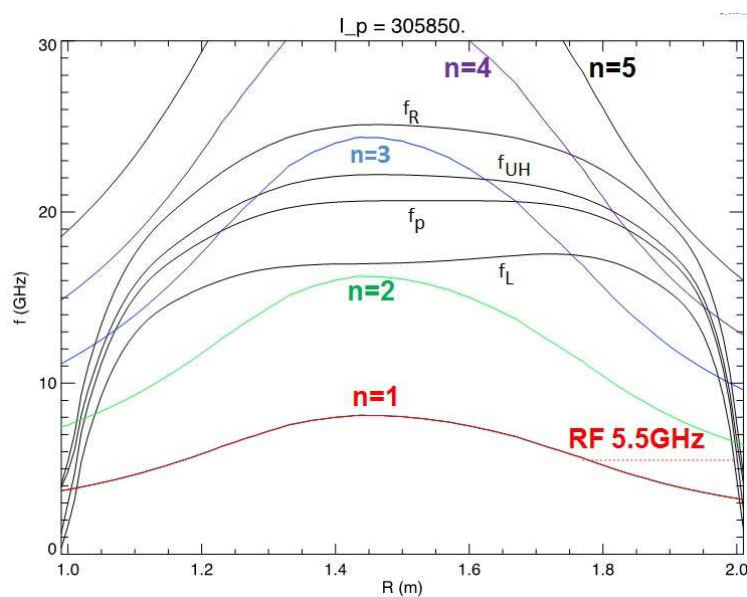


Figure 0.2. Location of resonant and cutoff surfaces from MSTfit reconstruction in a 306kA plasma. Locations of fundamental through 5th harmonic EC resonances are shown. Electromagnetic cutoffs at 5.5GHz are shown to exist at the edge for X and O modes. See Chapter 1 for definitions of resonances and cutoffs.

The EC wave cutoff surrounding the plasma in an RFP prevents X and O mode accessibility in the RFP as shown in **Figure 0.2**. Mode conversion of X/O waves into EBW allows deeper radial accessibility into the plasma edge. As a fast X-mode electromagnetic wave propagates into higher density it first reaches the right(R) cutoff. The wave then evanescently decays between the R and upper hybrid (UH) layers. The wave then can exist as a slow x-mode wave between the UH and left (L) cutoff layer. In contrast to electromagnetic waves that have a high density cutoff, the EBW has a low density cutoff at the UH resonance. The simultaneous existence of the slow X and EBW in the same location allows energy to be transferred from the x-mode to excite the EBW.

The efficiency of coupling to the EBW is strongly controlled by the edge density scale length, which sets the distance between the L,R, and UH layers. In the RFP, the steep ($L_n \sim 0.5\text{-}2$ cm) edge density gradient allows efficient coupling to the EBWs in the low GHz range by providing a narrow evanescent decay region between the R and UH layers. The EBW may then propagate inward to higher densities until it is absorbed on a Doppler shifted EC resonance harmonic. The EBW is strongly damped on all EC harmonics. The driven current is controlled by the sign of the $N_{||}$ spectrum at location it is absorbed. In general, a below midplane launch in MST will result in negative current drive, while an above midplane launch will result in positive current drive [4].

0.2 Research Contributions

EBW heating has been previously demonstrated in tokamaks, stellarators, and the spherical tokamak, however it has not been previously demonstrated in the RFP. Localized RF heating of

electrons may be an important diagnostic or control tool in the RFP, however the overdense plasma prevents accessibility of X and O mode RF heating. Launching of the EBW may be used to overcome these limitations and allow edge localized heating. This thesis presents the first demonstration of RF heating in the RFP, confirmed by localized RF heating inside the L cutoff layer and ability to control deposition location by adjusting $|B|$. Heated electron locations are confirmed from HXR measurements of bremsstrahlung from insertable target probes. EBW heating is demonstrated on fundamental and higher harmonics. The radial accessibility in a thick walled RFP is estimated to be $r/a \sim 0.8$.

0.3 Overview of Chapters

Chapter 1 consists of an overview of previous EBW heating and current drive research in stellarators, tokamaks, spherical tokamaks, and cylindrical plasma devices. In addition, research on electron Bernstein emission (EBE) as well as X and O mode launch and coupling in the RFP is reviewed.

Chapter 2 discusses modeling of X mode wave launch and mode conversion to the EBW. Consideration of edge field, density, and magnetic field profile in MST are analyzed and modeled. Modeling of porthole field error in a thick walled RFP is presented. Mode conversion, propagation and absorption of the EBW in the RFP is shown to allow accessibility past the electromagnetic cutoffs in an overdense plasma.

Chapter 3 discusses the design and construction of the EBW heating experiment on MST consisting of several distinct sections. First an overview of RF heating hardware is presented, including a klystron tube, pulsed power supply, waveguide components, and launcher antenna assembly. Second, associated RF control and diagnostic hardware for the EBW experiment is

presented, including an active RF power stabilization and control system, IF demodulation for forward to reflected phase comparison, and arc detection. Finally, x-ray diagnostics used in the experiment are presented.

Chapter 4 discusses the results from the EBW experiment. Heated electrons in the plasma were confirmed by x-ray bremsstrahlung from a distribution of insertable probes and limiters. Measurement of radial electron profiles at a toroidally displaced location allow mapping of EBW deposition depth at locations matching theoretical predictions. Porthole field error was found to limit radial accessibility by introducing a jump to higher harmonic absorption near the wall at higher plasma currents than would occur in the absence of field error. Measurements of falloff time from passing and trapped electrons imply heating in a magnetic field that is either stochastic or has broken flux surfaces.

Chapter 5 discusses the interpretation of the results and potential applications of EBW in the RFP. MST serves as a testbed to study EBW physics in a stochastic magnetic field or on broken flux surfaces, possibly similar to environments that will be encountered when resonant magnetic perturbations are applied to the edge of a tokamak for ELM control, or during the handoff between helicity injection and RF current drive startup in a spherical tokamak. In addition EBW is likely to be needed in high density stellarators, and may be used in the RFP to probe field stochasticity and local beta limits.

Chapter 1 Motivation for EBW Heating

This chapter presents an overview of relevant research in EBW emission, heating, and current drive in toroidal and cylindrical devices. Cold and Hot plasma treatments of wave cutoffs and resonances are presented to illustrate the lack of RF accessibility in the RFP. The first section presents an overview of published work in EBW physics. EBW experiments and results from tokamaks, stellarators, and spherical tokamaks are compared and reviewed.

The second section focuses on the potential uses of EBW current drive in the RFP to stabilize magnetic tearing modes. The mismatch in current drive and current profile in the RFP is presented along with the physics behind mode growth and eventual stochastic magnetic field lines leading to reduced particle and temperature confinement. The use of EBW for sustained off axis non-inductive current drive is presented as a method to align current drive and current profile leading to enhanced confinement.

1.1 Electromagnetic Accessibility in the RFP and the EBW

Many fusion research devices rely on X and O mode wave heating for electron cyclotron heating and current drive, profile control, and stabilization of tearing modes. The RFP presents a case where both X and O waves are cut off at the periphery of the plasma due to overdense ($\omega_{pe} > \omega_{ce}$) conditions. Such conditions typically exist in RFPs, spherical tokamaks, and next generation stellarators currently in development. Use of a hot plasma electrostatic wave, the Electron Bernstein Wave (EBW) allows heating on the cyclotron resonance in locations of the plasma that would be inaccessible to electromagnetic wave heating. Conversion of the X wave to the EBW is possible with high efficiency in the RFP allowing heating within the electromagnetic cutoffs.

1.1.1 Cold plasma dispersion and edge propagation

Wave propagation from the launcher antenna to the edge of the plasma to the mode conversion region is well approximated by the cold plasma dispersion relation (CPDR) [5], [6]; the CPDR is non-dissipative. The CPDR is useful in determining wave cutoff locations, or regions in the plasma where the index of refraction becomes negative causing the wave to exponentially decay. These cutoffs occur for electromagnetic X-mode waves at densities between the upper hybrid (UH) and right (R) frequencies, and above the left (L) frequency, , controlled by plasma density and magnetic field, and defined below. These characteristic frequencies form layers resembling nested circles in the poloidal cross section of MST as both density and $|B|$ are roughly functions of minor radius. For a 5.5GHz launch the R, L and UH cutoff layers occur within the first few cm of the edge. Although cutoffs are modeled, finite

plasma conductivity, collisional damping and losses are not included in this model. Cyclotron damping does not appear in the CPDR and requires use of the hot plasma dispersion relation.

The CPDR can be written as:

$$\tan^2(\theta) = \frac{-P(n^2 - L)(n^2 - R)}{(Sn^2 - RL)(n^2 - P)} \quad (1.1)$$

Where terms S, D, R, L, and P are given below

$$P = 1 - \frac{\omega_e^2}{\omega^2} \quad (1.2)$$

$$S = 1 - \frac{\omega_{pe}^2}{\omega^2 - \omega_{ce}^2} \quad (1.3)$$

$$D = -\frac{\omega_{ce}}{\omega} \frac{\omega_{pe}^2}{\omega^2 - \omega_{ce}^2} \quad (1.4)$$

$$R = 1 - \frac{\omega_{pe}^2}{\omega(\omega + \omega_{ce})} \quad (1.5)$$

$$L = 1 - \frac{\omega_{pe}^2}{\omega(\omega - \omega_{ce})} \quad (1.6)$$

For a radial launch from the plasma edge, propagation is perpendicular to the local magnetic field, $\vec{k} \perp \vec{B}_0$ leading to $\theta=90^\circ$ and $\tan^2(\theta) = \infty$. The solutions to this equation indicate that

$$(Sn^2 - RL)(n^2 - P) = 0 \quad (1.7)$$

The two solutions to this equation correspond to the X-mode and O-mode launch conditions.

While both waves propagate across magnetic field lines, the O mode wave has electric field polarization parallel to the magnetic field, while the X mode wave has electric field polarization perpendicular to the magnetic field. The X-mode wave exists in two variants, the fast x wave and

the slow x-wave. The fast x-wave, known as “fast” due to the high phase velocity, exists in regions of the plasma where the wave frequency is greater than the R frequency. The slow x-wave, known as “slow” due to the low phase velocity, exists in regions of the plasma where the wave frequency is between the L and UH frequencies. This thesis will focus on the X mode wave launch. In a cold plasma the refractive index of the x-mode wave is given by

$$n^2 = \left(\frac{ck_{\perp}}{\omega} \right)^2 = - \frac{[\omega_p^2 - \omega(\omega + \omega_c)][\omega_p^2 - \omega(\omega - \omega_c)]}{\omega^2(\omega_p^2 + \omega_c^2 - \omega^2)} \quad (1.8)$$

$$n^2 = \frac{RL}{S} \quad (1.9)$$

As the launched fast X-mode wave travels inward from the edge it first encounters the R cutoff(1.12) and begins to evanescently decay. For sufficiently steep edge density gradient, efficient tunneling between the R(1.12) and UH(1.13) layers is possible. Mode conversion to the EBW occurs at the UH layer with slow X wave existence between the UH and L(1.14) cutoff layers. A plot of edge frequencies in a typical MST plasma is shown in **(Figure 1.1)** and in the plasma edge.

$$\omega_p = \left[\frac{n_e e^2}{m_e \epsilon_0} \right]^{1/2} \quad (1.10)$$

$$\omega_c = \frac{eB}{m_e} \quad (1.11)$$

$$\omega_R = \frac{1}{2} \left[\omega_c + (\omega_c^2 + 4\omega_p^2)^{1/2} \right] \quad (1.12)$$

$$\omega_{UH} = (\omega_c^2 + \omega_p^2)^{1/2} \quad (1.13)$$

$$\omega_L = \frac{1}{2} \left[-\omega_c + (\omega_c^2 + 4\omega_p^2)^{1/2} \right] \quad (1.14)$$

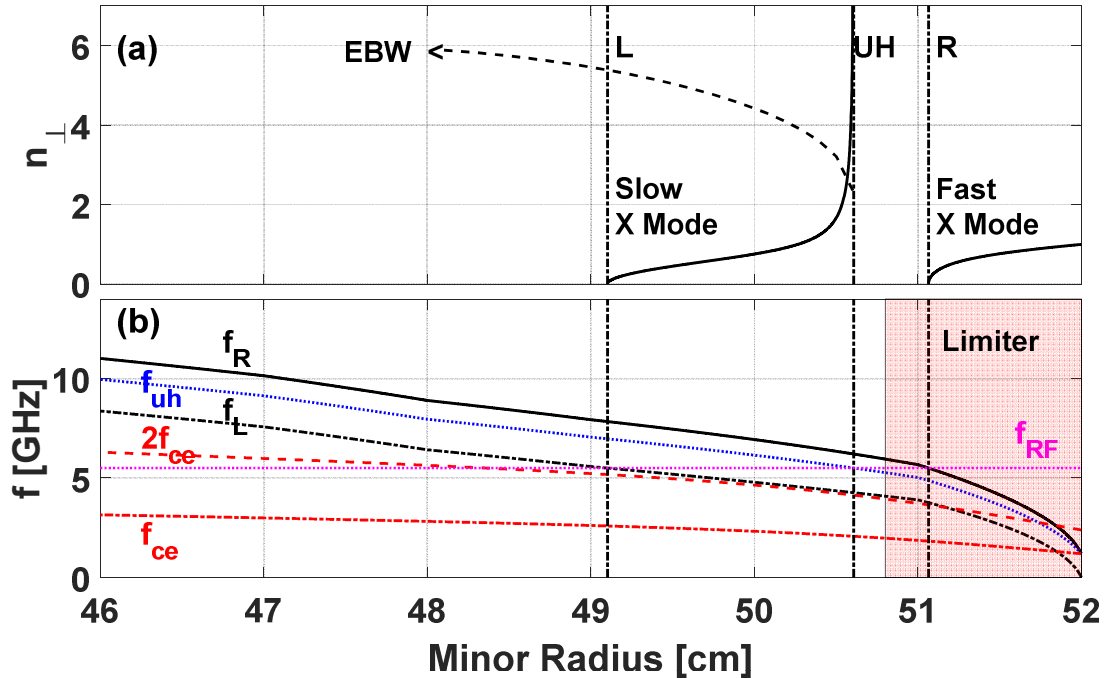


Figure 1.1. Index of refraction calculated for the x-mode wave, an illustrative curve for EBW, cutoff, and resonance locations are plotted in (a). Plasma frequencies are plotted in (b) for 5.5GHz x-mode edge launch in a 210kA plasma.

Overlap of dispersion relations for slow X and EBW exist at similar wavelengths on the UH layer allowing coupling of power between X and Bernstein waves to occur. The EBW is a hot plasma electrostatic wave with electric field polarization parallel to propagation direction that is carried by the synchronization of electron gyro-orbits, as shown in **Figure 1.2**. The EBW does not have a high density limit like X and O waves allowing heating in an overdense plasma in locations where electromagnetic waves are cut off. The EBW is cutoff for frequencies lower than the UH frequency requiring excitation be mode conversion from an electromagnetic X or O wave launched from the plasma edge. The EBW is presented in greater depth in following sections.

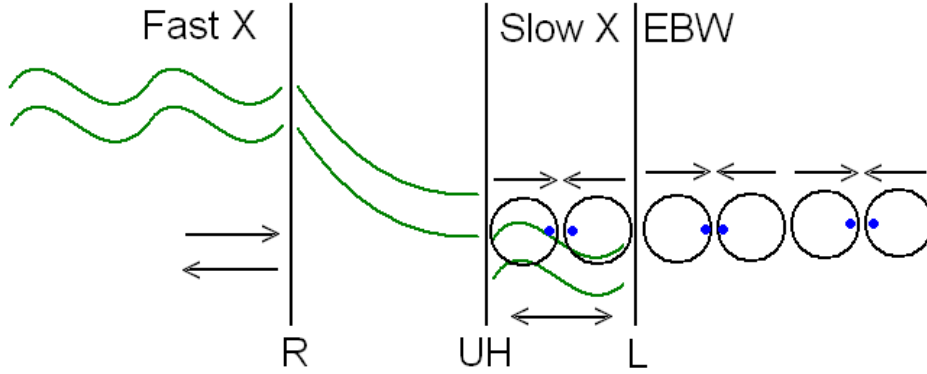


Figure 1.2. Coupling between the slow X-mode electromagnetic wave, and the Bernstein wave occur at the UH layer.

1.1.2 Hot plasma dispersion relation and EBW propagation

Bernstein wave propagation is governed by the hot plasma dispersion relation that takes into account the finite size of the electron gyro-orbits. In a hot plasma, finite Larmor radius effects allow an electron Bernstein mode to exist in an over dense plasma, at frequencies greater than the upper hybrid resonance.

The hot plasma dielectric relation [6] with propagation perpendicular to B, n_{\parallel} finite and $T_{\parallel}=T$ and a small k_{\parallel} is given by (1.15), where ω is the wave frequency, ω_p is the plasma frequency, ω_{ce} is the cyclotron frequency, V_{th} is the thermal velocity, Z is defined in (1.16), and I is a Bessel function containing μ (1.17).

$$k_{\perp}^2 + k_{\perp}^2 + \sum_s \frac{2\omega_{p,s}^2}{V_{th,s}^2} e^{-\mu_s} \sum_{n=-\infty}^{\infty} \left[1 + \frac{\omega}{k_{\parallel} V_{th,s}} Z(\zeta_s) \right] I_n(\mu_s) = 0 \quad (1.15)$$

$$Z'_0(\zeta_n) = \frac{k_{\parallel}^2 \omega^2}{(\omega - i\nu - n\omega_{ce})^2} \quad (1.16)$$

$$\mu = \frac{k_{\perp}^2 v_{th}^2}{2\omega_{ce}^2} = \frac{k_{\perp}^2 kT}{m\omega_{ce}^2} \quad (1.17)$$

For E parallel to B, $n^2 > |e_{ij}|$, propagation perpendicular to the magnetic field, and neglecting ion contributions, the dispersion relation becomes (1.18). It is evident from the equation that resonances occur when the wave frequency is at harmonics of the cyclotron frequency.

$$\epsilon_{xx} = 0 = 1 - \frac{\omega_{pe}^2}{\omega_{ce}^2} \frac{2 \sum_{n=1}^{\infty} e^{-\mu} I_n(\mu_e) \frac{n^2}{\omega^2 - n^2}}{\mu_e} \quad (1.18)$$

1.1.3 Mode conversion to the Bernstein wave

Optimization of EBW coupling has previously been examined on a 3.6GHz experiment [7], [8] using a phased array antenna in MST. Optimum launch angle for the X mode wave was found to be perpendicular to the magnetic field. A launched X wave propagates inward, evanescently decaying between the R and UH layer. Near the UH layer the electric field Eigen mode is given by (1.19) and the index of refraction is given by (1.20)

$$\tilde{E} = \begin{pmatrix} \frac{iD}{S} \tilde{E}_0 \hat{r} & \tilde{E}_0 \hat{\theta} & 0 \hat{\phi} \end{pmatrix} \quad (1.19)$$

$$n^2 = \frac{RL}{S} \quad (1.20)$$

As the wave approached the UH layer $\omega \rightarrow \omega_{UH} = \sqrt{\omega_{ce}^2 + \omega_{pe}^2}$ and $s \rightarrow 0$ causing the index of refraction to approach infinity and the radial component of the electric field component of the wave to become large with $\vec{E} \parallel \vec{k}$ assisting with efficient coupling to the EBW. Connection between the slow X branch and EBW branch occurs at the UH layer causing mode conversion to the EBW which then can propagate past the L cutoff into denser plasma.

Launched power that is not lost to the parametric decay instability (PDI) or the evanescent decay between the R and UH layers can be mode converted to the EBW at a finite mode conversion efficiency depending on launch angle and frequency as well as plasma magnetic field, and density scale length for OXB [9] and XB [10],[11] launch. At optimum launch angle of the X wave to the magnetic field, in this case radially inward, the maximum achievable mode conversion efficiency is given by C_{max} (1.21) with η as the Budden parameter given in (1.22), θ as the phase of $\Gamma(-i\eta/2)$, and ϕ as the phase between the slow X wave to and from the UHR.

$$C_{XB} = \underbrace{4e^{-\pi\eta} (1 - e^{-\pi\eta})}_{C_{max}} \sin^2 \left(\theta + \frac{\phi}{2} \right) \quad (1.21)$$

$$\eta = \frac{\omega_{ce} L_n}{c} \left[\frac{\alpha}{\sqrt{\alpha^2 + 2(L_n / L_B)}} \right] \left[\frac{\sqrt{1 + \alpha^2} - 1}{\alpha^2 + (L_n / L_B) \sqrt{1 + \alpha^2}} \right]^{1/2} \quad (1.22)$$

In MST the magnetic scale length \gg the density scale length, $L_B \gg L_n$, allowing the Budden parameter in the mode conversion region to be simplified to (1.23), and evaluated at the UH layer location.

$$\eta \approx \frac{\omega_{ce} L_n}{c \alpha} \left[\sqrt{1 + \alpha^2} - 1 \right]^{1/2} \quad (1.23)$$

$$\alpha = \omega_{pe} / \omega_{ce} \quad (1.24)$$

For an edge density of $2e17/m^{-3}$ and constant plasma currents of 250kA and 350kA, maximum mode conversion efficiency is plotted vs. density scale length in (**Figure 1.3**). Field error corrections, discussed in a later section, are applied to the magnetic field at the mode conversion location (UH layer).

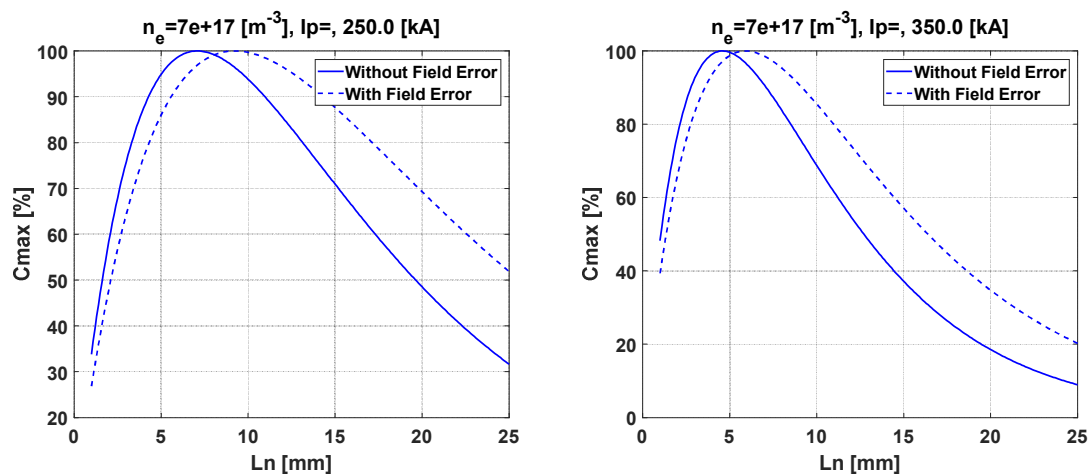


Figure 1.3. Maximum conversion efficiency vs density scale length with and without porthole field error at constant I_p .

1.1.4 Parametric decay instability during mode conversion

At the UHR it is possible to excite the parametric decay instability (PDI), if a sufficient power density is launched. The PDI is caused by the electric field from one oscillating wave exciting a wave of another frequency that it can couple to. In practice a small amount of damping, either collisional or collision less will prevent excitation of the PDI unless there is sufficient power in the launched wave driving the oscillation. This is observed when the PDI occurs above a certain power threshold. When the parametric instability occurs, a fraction of the injected RF power excites an additional wave at the lower hybrid (LH frequency(1.25) or

multiples thereof shown in **(Figure 1.4)**. In MST the LH frequency is on the order of 40MHz at the UH layer for a 250kA plasma with $n_e=7E17m^{-3}$.

$$\omega_{LH}^2 = \omega_{ce} \omega_{ci} \left(\frac{\omega_{pe}^2 + \omega_{ce} \omega_{ci}}{\omega_{pe}^2 + \omega_{ce}^2} \right) \quad (1.25)$$

Parametric decay has been observed during EBW experiments on MAST [12] at 80kW of heating power at 60GHz and a power density of $\sim 1kW/cm^2$, and in cylindrical magnetized plasma experiments at 2-4GHz at 200W of power injected by a 3cm diameter antenna [13]; by comparison for 80kW launched power in MST through a 5cm porthole the power density is $\sim 4kW/cm^2$ allowing the possibility of PDI excitation during EBW mode conversion. Observation of the PDI is a sign of mode conversion to the Bernstein wave [14]; there is no substantial power loss to the PDI during EBW mode conversion. Due to the lack of sufficiently narrow notch filters to measure any PDI within 40MHz of the RF heating power, no attempt was made to measure this effect.

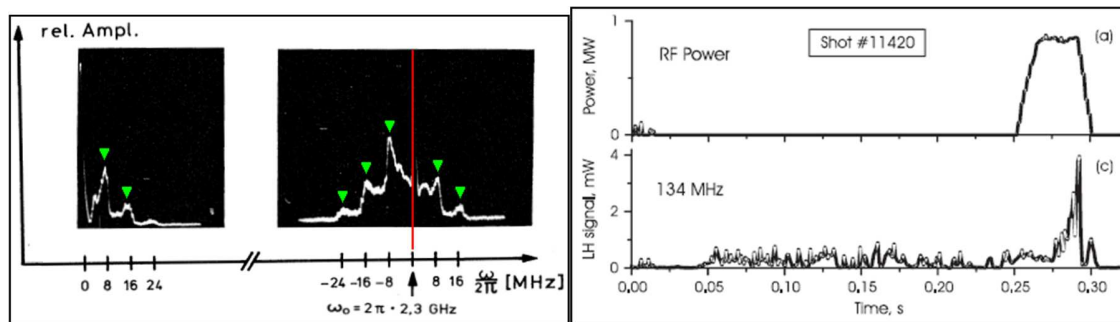


Figure 1.4. Parametric excitation of multiples of the lower hybrid frequency (left) in a cylindrical plasma experiment. Figure courtesy of [13]. Parametric excitation of the lower hybrid frequency during EBW heating on MAST (right). Figure courtesy of [12].

1.1.5 EBW absorption on the Doppler shifted cyclotron harmonic

The hot plasma dispersion relation has resonances near multiples of the cyclotron resonance, offset by a Doppler shift. The EBW is optically thick on all harmonics [15] allowing efficient absorption at low magnetic fields. The absorption of EBWs in a hot plasma on the Doppler shifted cyclotron resonance (1.26) heats a fraction of the fast electron tail of the Maxwellian distribution of electrons.

$$\omega_{rf} = n\omega_{ce} - \frac{k_{\parallel}v_{\parallel}}{\gamma} \quad (1.26)$$

$$\gamma = \frac{1}{\sqrt{1 - \frac{v^2}{c^2}}} \quad (1.27)$$

The bump on tail has asymmetry in the distribution of heated electrons that allows current drive controlled on launch position. Launch of the EBW above or below the mid-plane will preferentially drive a net current in the plasma, either positive or negative, depending on the sign of k_{\parallel} .

EBW heating and current drive can be calculated by CQL3D [16], [17], a bounce averaged Fokker-Plank code utilizing the collisional quasi-linear diffusion. CQL3D simulates the effects of RF absorption on the resulting electron distribution. In MST, CQL3D predicts a current drive efficiency of approximately $\sim 150\text{A/kW}$ [18], [19] for zero diffusion. An example output showing resonantly heated electron distributions compared to the passing / trapped boundary is shown in **(Figure 1.5)**. The distortion in electron distribution is noted to the right of center where the contours distort rightward indicating heating of electrons in the positive v_{\parallel} direction.

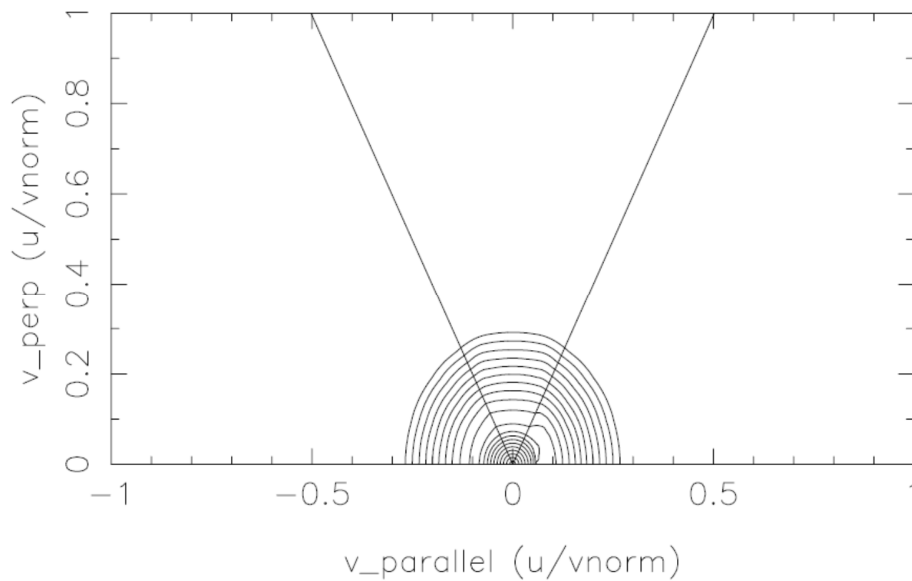


Figure 1.5. Contours of the EBW-heated electron distribution(circles) with trapped vs passing boundary marked in black lines for 2MW of RF heating.

1.1.6 Previous EBW Research

A number of previous fusion experiments have utilized the EBW for heating, current drive, and diagnostic purposes. Laboratory scale EBW experiments involving both X and O mode launches have involved direct measurement of EBW mode conversion, EBW heating and current drive of a plasma, and EBW emission from a plasma. Direct measurement of EBW mode conversion using scanned RF probes are possible for lower frequency ($\sim 1\text{-}3\text{GHz}$) when the EBW has a sufficiently long wavelength to couple to an insertable antenna. EBW heating experiments conducted in toroidal fusion devices heat plasma in a localized area and measure temperature increase via SXR or HXR diagnostics. EBW current drive experiments measure RF driven current by measurement of loop voltage or counter current drive required to null current in a

stellarator. EBW emission experiments for purposes of radiometry of overdense ($\omega_{pe} > \omega_{ce}$) plasmas allow measurement of plasma temperature from inside the x-mode cutoff layer; reciprocity implies EBW accessibility where emission is detected.

EBW heating has been used on stellarators, tokamaks, and spherical tokamaks in overdense plasma conditions. Edge mode conversion allows accessibility of the overdense region for heating, current drive, and EBE based radiometry measurements. A tabulation of relevant device parameters has been compiled in (Table 1-1). **A detailed overview of each experiment listed below is presented in (Appendix A).**

Table 1-1: Overview of EBW Heating Parameters in Previous Devices

Author	Date	Machine	Type	Mode Conv	Freq [GHz]	P _{RF} [kW]	B [T]	ne scale [mm]	CD Eff [A/kW]	Novel Contribution
Seltzman	2017	MST	RFP	XB,OXB	5.5	130	0.1			EBWH in an RFP
Uchida	2010	LATE	ST		5	190	0.096		105	Current drive in ST
Diem	2009	NSTX	ST	OXB	12	--	0.4			EBE/Li wall conditioning
Podoba	2007	WEGA	Stell.	OXB	2.45	26	0.05	100		EBW conversion in stellarator
Cengher	2006	MST	RFP	XB,OXB	3.6	0.01	0.1	12.5		EBW coupling in RFP
Shiraiwa	2006	TST-2	ST	XB	8.2	200	0.3	5		EBWH in ST
Laqua	2003	W7AS	Stell.	OXB	70	400	2.15	10	3	EBWCD in stellarator
Jones	2003	CDXU	ST	XB	4	--	0.21	6.6		EBE in a ST
Shevchenko	2002	CompassD	Toka	XB	60	600	2		167	EBWCD in a tokamak
Chattopadhyay	2001	MST	RFP	XB	3-8	--	0.1	14		EBE in the RFP
Maekawa	2001	WT-3	Toka	XB	48	100	1.75			EBWH in a tokamak
Laqua	1998	W7AS	Stell.	OXB	58-72	--	2.1	10		EBE in a stellarator
Laqua	1997	W7AS	Stell.	OXB	70	220	2	10		EBWH in a stellarator
Luce	1992	DIII-D	Toka	XB	60	1000	2.14			Inadvertent mode conv
Sugai	1981	N/A	Linear	XB	0.75-3	2	0.05	40		EBW mode conversion

Direct measurement of EBW mode conversion with insertable probes connected to heterodyne detectors has been observed by Sugai [20] in a cylindrical device and Podoba, in WEGA [21]; both are low field (~50mT) devices with RF excitation at 2-3GHz. Sugai used a triple dipole antenna, while Podoba used a dipole/magnetic loop probe. Phase and amplitude measurements of wave electric field components indicated the expected shift from perpendicular to parallel to the wave vector at the UH surface. Sugai measured the wavelength of the EBW after mode conversion, finding a match with expected values.

EBE diagnostics have been implemented on MST [22], W7AS [23], CDXU [24] and NSTX [25] allowing absolute radiometry measurements from inside the cutoff layer using

conversion to either X or O mode. Comparison of radiation temperature from optically thick EBW emission matched a calibrated temperature diagnostic, either SXR or Thomson scattering.

In W7AS, EBE radiometry with OXB mode conversion used an obliquely mounted antenna receiving 58-72GHz. Radiometry T_e measurements were comparable to SXR T_e measurements.

In CDXU, XB conversion measured T_e comparable to Thomson T_e measurements. An adjustable local limiter used to steepen the edge density gradient improved conversion efficiency to 100% compared to 10% conversion efficiency for an antenna mounted outside the machine aimed through a window.

In NSTX, a radiometry system using OXB mode conversion was operated at 18-36GHz. Collisional edge damping reduced coupling efficiency to the EBW when $\nu_{ei}/\omega > 10^{-4}$. No local limiter around the antenna was used. Lithium wall conditioning improved conversion efficiency from 10% to 60% by depleting edge electron density. The resulting inward shift in the UH location increased electron temperature at mode conversion from 5eV to 20eV and steepened edge density gradient.

EBE radiometry in MST [26] operating in the 3-8GHz range measured T_e profiles with an absolutely calibrated radiometer. A quad ridged antenna without a local limiter was used as a receiver. Comparison to Thomson measurements indicated 75% mode conversion efficiency, with X-mode polarization dominating.

EBWs heated and drove current in the W7AS [27], [28] and WEGA [29] stellarators. In W7AS, OXB mode conversion was used for heating and current drive with 220kW at 70GHz. Non-resonant heating used an EBW bouncing between inboard and outboard UH layers

gradually heating the plasma. Obliquely launched OXB conversion of 400kW at 70GHz drove current in a neutral beam sustained plasma by resonant absorption at efficiencies of 3A/kW (1.2kA). The WEGA experiment measured EBW heating with OXB conversion with a 2.45GHz, 26kW source resulting in a measurable increase in electron temperature inside the LCFS. Mode conversion to the EBW was directly measured with an insertable probe.

EBW heating and current drive on WT-3 [30] and Compass-D [31] tokamaks used an X-mode wave, passing through an optically thin ECR layer, mode converted to the EBW at the UHR located at the low field side, and reflected back for core absorption. In WT3, EBW heating was observed with XB conversion of a 48GHz, 150kW source. The launch scenario of the WT3 experiment is unique with an O-wave launched from the top of the machine reflecting off of an OX mode converter plate on the inboard side with XB conversion at the UH layer resulting in centrally localized EBW heating observed with SXR tomography. In Compass-D, a high field side launch of an X-mode wave with a 60GHz, 600kW source drove current at an efficiency of 167A/kW (100kA drive). EBW heating was observed in DIII-D [32], [33] using a 60GHz, 1MW X-mode wave converted into the Bernstein wave by reflecting off of the UH layer.

EBW experiments in Spherical tokamaks have demonstrated heating in TST-2 [34] and current drive in LATE [35]. In TST-2, a low field side launch of 8.2GHz at 200kW was converted to the EBW by XB conversion. Edge density gradient steepening with a local limiter surrounding the antenna improved mode conversion efficiency to 80%. Core heating was measured with a 20 chord SXR detector. Collisional damping in the edge was not found to be an issue for a single pass of the wave. In LATE, EBW was used for non-inductive current ramp up

with a 5GHz, 190kW source. Currents of 20kA were driven yielding a current drive efficiency of 105A/kW.

In the previous EBW experiments, several trends can be observed. Experiments utilizing probes to measure direct conversion to the EBW used low current, low field devices and 2-3GHz sources allowing a long enough wavelength of both the EBW and launched wave to be measured through heterodyne phase detection. Both experiments were conducted in devices where a low density, low or zero current plasma was possible, allowing the use of physically small probes (~3mm antenna tips) that would not survive in a fusion test environment. Heating and current drive experiments in stellarators utilized outboard side oblique launch with OXB mode conversion, while tokamaks favored high field side XB launch through an optically thin EC resonance, converted to EBW at the low field side UHR and reflected back to the core for absorption. Spherical tokamaks used XB mode conversion from a low field side launch. Heating location in most experiments was measured by SXR tomography and bulk temperature rise was measured with Thomson scattering. In most XB mode conversion cases, for EBE/heating/current drive, a local limiter optimized edge density gradient, increasing mode conversion efficiency.

1.2 Motivation for EBW Heating and Current Drive in MST

1.2.1 Magnetic geometry of the RFP

The RFP is a toroidal fusion device characterized by an overdense, high beta plasma with self-organizing magnetic fields. The edge magnetic field is mainly poloidal with a small toroidal component that reverses near the edge (**Figure 1.6**). The magnitude of the field approximately doubles from the edge to the core.

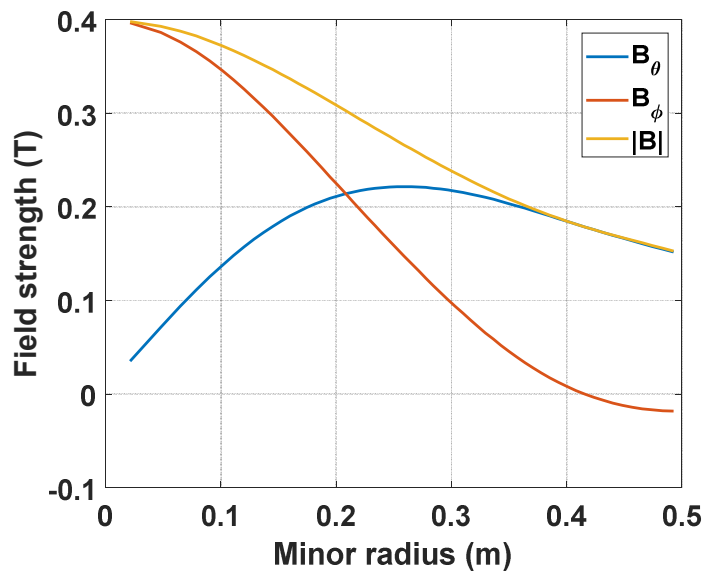


Figure 1.6. Toroidal(red), poloidal(blue), and magnitude(yellow) of magnetic fields in MST for a 395kA standard plasma.

Current in the plasma is sustained inductively by a loop voltage of $\sim 20V$ in the toroidal direction. Magnetic field reversal near the edge produces a mismatch in inductive current drive and current profile as plotted in (**Figure 1.7**).

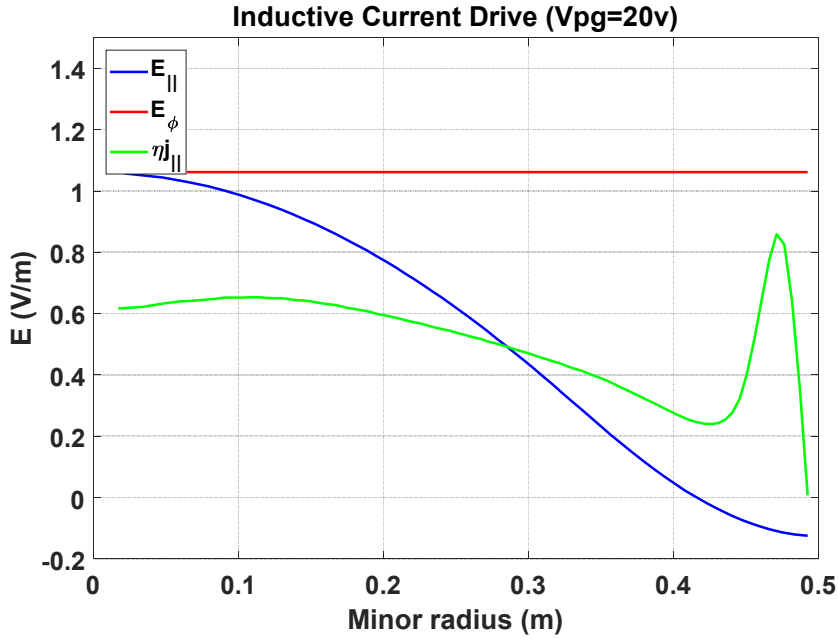


Figure 1.7. Toroidal electric field driven by transformer action (red), current drive E_{\parallel} (blue), and current profile (g) in MST.

E_{ϕ} drives a peaked lambda profile, where lambda is defined in(1.28). The lowest energy configuration of current and magnetic field distributions in the plasma is represented by a flat lambda profile [36]. The gradient in lambda represents the amount of MHD energy available to drive growing magnetic modes.

$$\lambda = \frac{\vec{J} \cdot \vec{B}}{B^2} \quad (1.28)$$

These modes are resonant on flux surfaces with rational numbers of safety factor (1.29) with $m=1$ modes being the least stable. Rational safety factor locations become spaced closer together near the reversal surface as plotted in (**Figure 1.8**).

$$q(r) = \frac{m}{n} = \frac{rB_T}{RB_p} = \frac{rB_\phi(r)}{RB_\theta(r)} \quad (1.29)$$

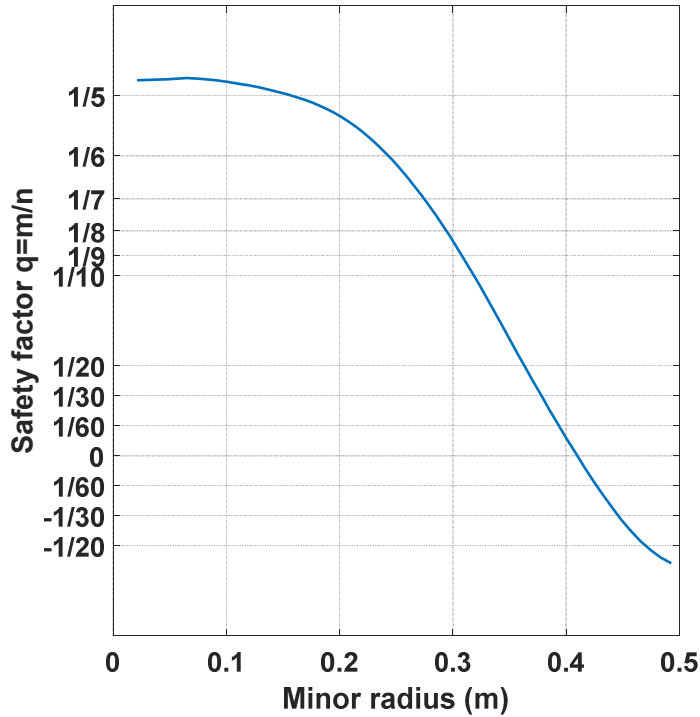


Figure 1.8. Safety factor in a typical standard MST plasma with rational surfaces marked.

Note that y axis scale is expanded.

The magnetic fluctuations grow non-linearly during a saw tooth crash [37], introducing a radial perturbation that generates magnetic islands. Growing magnetic fluctuation amplitude increases island width until overlap causes field lines to become stochastic leading to decreased particle and energy confinement. Simultaneously parallel current is driven near the edge, flattening the lambda profile and stabilizing the fluctuations.

A method of inductive poloidal current drive, called pulsed poloidal current drive (PPCD) [38], aligns current drive with current profile resulting in a reduction in stochasticity [39], as plotted in **Figure 1.9** for simulations based on MHD modeling, improved plasma confinement and increased temperature. Due to the inductive nature of PPCD, it cannot be sustained indefinitely.

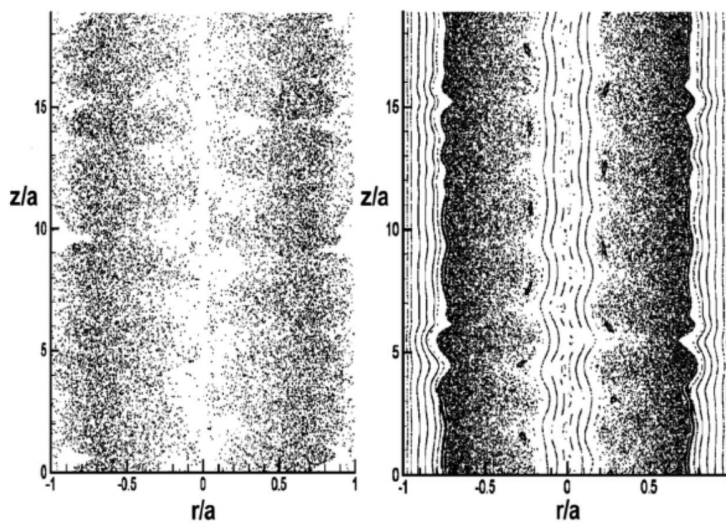


Figure 1.9. Poincare surfaces of magnetic field before(left) and after(right) PPCD predicting significant reduction in stochastic magnetic field. Figure courtesy of [39].

One proposed non-inductive method is the use of RF current drive in the plasma edge (**Figure 1.10**) to align the current drive in the RFP to the current profile. Two potential candidates for RF current drive in the RFP have been identified: lower hybrid current drive [40], [41], and EBW current drive [42]. Absorption of the EBW on the Doppler shifted cyclotron resonance generates a suprathermal electron tail. Current drive through selective heating on one side of electron distribution function can be optimized through two possible methods, the Fisch-

Boozer [43] mechanism for co-current drive and the Ohkawa [44] mechanism for counter-current drive.

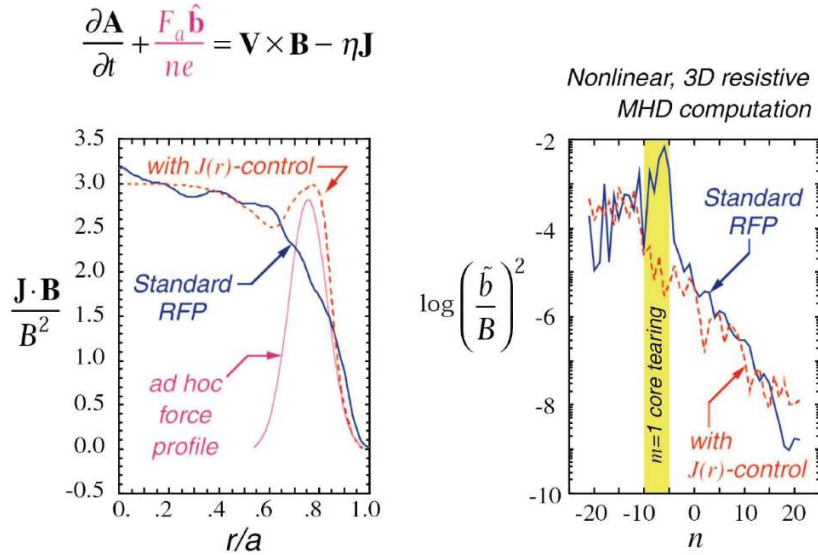


Figure 1.10. $J(r)$ control used to flatten lambda profile(left) and subsequent reduction in magnetic tearing modes(right). Figure courtesy of MST group.

In the Fisch-Boozer mechanism, ECCD or EBW heating is used to transfer perpendicular energy to resonant electrons creating an asymmetric resistivity because the more energetic electrons are less collisional. The asymmetry in resistivity generates a net electron flow in the same direction as the resonant electron's parallel velocity. It has been experimentally observed that Fisch-Boozer current drive efficiency decreases when absorption takes place in a magnetic geometry where a large number of the resonant electrons may become trapped in banana orbits, such as near the edge of a tokamak. In addition to trapping electrons due to the immediate addition of angular momentum, the loss of efficiency is further effected by the pitch angle scattering of passing heated electrons into trapped banana orbits. For bounce periods much less

than the scattering time, symmetrically de-trapped electrons will produce an effective net counter-current drive.

The Ohkawa mechanism utilizes the effects from the trapped electron fraction to generate current and is significantly more efficient than the Fisch-Boozer mechanism at locations where the magnetic geometry allows a significant trapped electron fraction [45], such as near the edge of a tokamak. The Ohkawa method heats electrons on one side of the velocity distribution in a location where they are then pitch angle scattered into trapped banana orbits, then symmetrically de-trapped in velocity space, generating net current drive.

Distributions of parallel and perpendicular energy transfer are governed by the quasi-linear diffusion operator and must be simulated in Fokker-Plank codes, such as CQL3D; both trapped and un-trapped electron populations are heated by the EBW. Simulations of EBW propagation with the ray tracing code Genray estimate Doppler shift and parallel index of refraction in MST, however accurate ray tracing in the edge is not possible due to the presence of porthole field error. Analytical models are used to predict deposition location as a function of edge field.

1.2.2 Difficulty of RF heating the RFP

MST presents a number of similarities and differences to the previous experiments. The high beta and magnetic geometry in the RFP presents a dominant poloidal field in the edge, with $|B|$ proportional to I_p . The edge field increases by approximately a factor of 2 at the core. Spacing between cyclotron harmonics becomes small for high harmonic launch, limiting radial accessibility as absorption shifts from one harmonic to the next higher harmonic at the wall as

shown in **Figure 1.11**; greatest heating depth is obtained for fundamental harmonic launch. In this figure, EBW is excited from the edge, near a depth of 1cm and propagates inward until it hits a line on the graph. EBW heating experiments are performed at 5.5GHz with direct probe measurements at 3.6GHz.

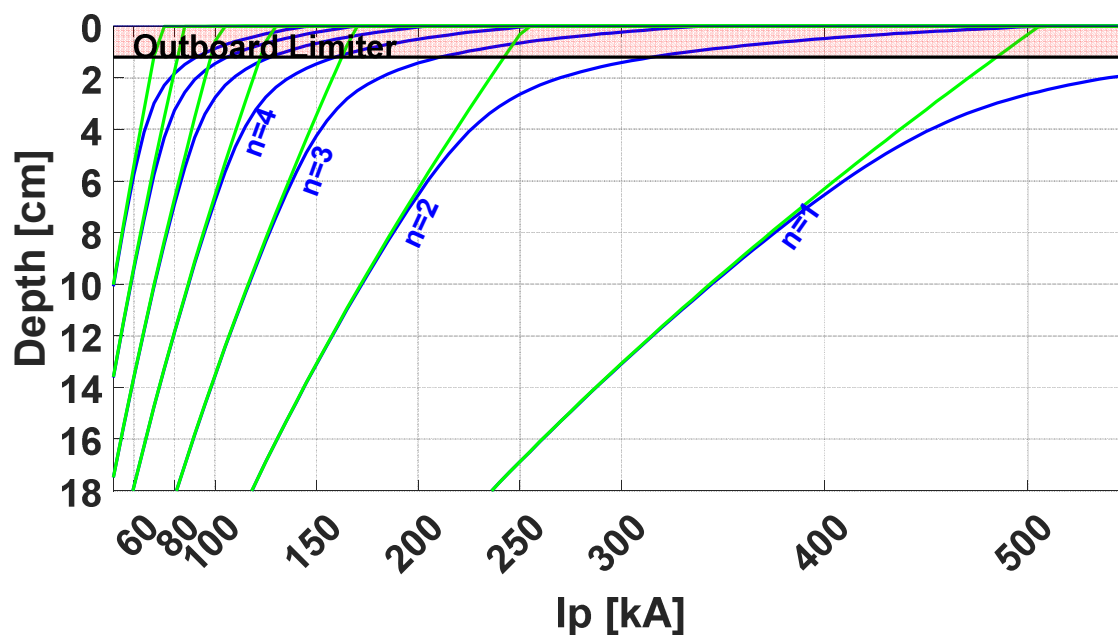


Figure 1.11. EBW absorption location is plotted in blue for corrections for doppler shift and porthole field error, and in green corrected for doppler shift in the absence of a porthole.

Porthole availability mandates a radial launch for single waveguide antennas, requiring an XB conversion scenario for optimal coupling. Large wall currents in MST yield a porthole field error reducing $|B|$ by a factor of 2 at the edge [46]. Error field extends ~ 1 porthole diameter radially inward. Field lines at the edge bend into the porthole, directing plasma into the antenna aperture, creating a challenging launch environment. Previous coupling experiments at 3.6GHz [47] demonstrated steepening the edge density gradient with PPCD or the use of a BN cover on

the antenna aperture improved coupling. Use of 5.5GHz allows a smaller antenna and porthole with reduced field error. Use of a BN limiter with smaller portholes is challenging due to confined space.

Direct current drive measurement in the RFP may not be possible due to low predicted current drive efficiency in the RFP ($\sim 150\text{A/kW}$) [18] in comparison to the high values of inductively driven current ($\sim 2\text{MW Ohmic}$, 200-500kA). Measurement of heating locations with SXR PIN diode arrays was not possible due to their low sensitivity and RF pickup. Single photon counting CdZnTe detector arrays observing target emission from heated electrons colliding with insertable probes and limiters allowed deposition profile measurement. Thomson scattering is limited to core locations and is not able to resolve bulk heating of the plasma by the EBW due to the edge localized deposition and significant Ohmic heating power.

Deposition depth of the EBW was measured by calculating the first moment of the radial heated electron profile using target bremsstrahlung from insertable probes and limiters. Deposition depth was controllable with plasma current and matched the Doppler shifted resonance location corrected for porthole field error for the $n=2$ harmonic. Direct probing of plasmas where the EBW is absorbed on the fundamental ($n=1$) harmonic were not possible due to higher plasma currents that prohibited the use of insertable probes. Based on modeling, $n=1$ heating will achieve heating at $r/a \sim 0.8$. Heated electron loss rates were found to be much faster than collisional time scales, with falloff rates in fast electron population in the 10s of μs as measured with target probes. The high falloff rate in electron population in standard plasmas indicates that the high rate of RFP transport [48] dominates background plasma and neutral scattering of heated electrons.

1.3 Summary

EBW heating and current drive has been previously observed in tokamaks, stellarators, and spherical tokamaks. The first observation of RF heating in the RFP using the electron Bernstein wave has been demonstrated on MST. The RFP suffers from a misalignment of current drive and current profile leading to growing magnetic modes that cause magnetic field lines to become stochastic resulting in poor energy confinement. Inductive methods such as PPCD can align current drive with current profile, but cannot be sustained. RF heating and current drive has been proposed as a method to provide sustained off axis current drive in the RFP, however the overdense nature of the plasma in MST prevents use of electromagnetic X and O waves that are cutoff within the first few cm of the edge.

EBW does not suffer from density limitations and has the require accessibility to heat and drive current in the plasma edge. Theoretical modeling and EBE observations on the RFP have implied that edge localized EBW heating and current drive in the RFP is possible.

Chapter 2 Modeling of EBW heating in the RFP

This chapter presents modeling of EBW launch, propagation and absorption. The first section focuses on a mathematical description of x-mode wave launch and mode conversion to the Bernstein wave. The mode conversion mechanism between X/O waves and EBW as well as the propagation and absorption of the Bernstein wave on the Doppler shifted resonance is described. The second section focuses on numerical modeling and computer simulations of EBW propagation and absorption. Genray is used to determine predicted ray paths as well as calculate the difference in absorption position from the CPDR due to the Doppler shifted resonance. Predictions of RF accessibility are presented to predict the maximum depth that EBW may be used to drive edge currents in an RFP.

EBW heating in the RFP involves a challenging launch scenario including porthole field error, cutoffs and mode conversion in the antenna near field, and propagation of the Bernstein wave in a magnetic field that is either stochastic or has broken flux surfaces. In MST, overdense ($\omega_{pe} > \omega_{ce}$) plasma cuts off X and O mode electromagnetic waves in the first few cm of the plasma edge. The naturally steep edge density gradient in MST, compared to a tokamak, allows efficient mode conversion without a dedicated antenna limiter. The EBW is strongly damped for all harmonics leading to edge absorption of the first Doppler shifted cyclotron resonance the wave

encounters. Porthole field error weakens edge field by a factor of 2 at the wall reducing accessibility by introducing higher harmonic resonances in the edge.

2.1 Modeling of EBW Mode Conversion

2.1.1 Edge density and magnetic field profiles

Modeling of mode conversion efficiency requires knowledge of density and magnetic field profiles in the edge. The efficiency of EBW mode conversion depends on the frequency, plasma density, magnetic field and their scale lengths. Edge density scale length is given by

$$L_n = \left[n_e \left(\frac{\partial n_e}{\partial x} \right)^{-1} \right]_{UHR} \quad (2.1)$$

Edge density profile can be modeled with(2.2), with n_0 being a measured or estimated density at distance x_0 from the wall, x being the distance from the wall and L_0 being a density scale length.

$$n = n_0 \exp\left[(x - x_0) / L_0\right] \quad (2.2)$$

The magnetic geometry of the RFP, plotted in **Figure 2.1**, consists of a toroidal field profile peaked on the magnetic axis that decreases towards the wall, eventually crossing through zero and attaining a small amount of reversal at the edge. The poloidal field is large near the wall and zero on the magnetic axis.

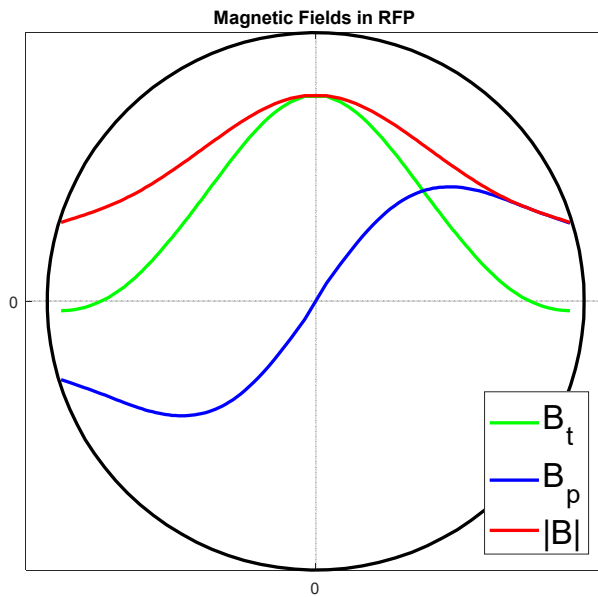


Figure 2.1. Magnetic fields in the RFP demonstrating reversal of the toroidal field (green) at the edge, dominance of the poloidal field (blue) near the wall, and radial dependence of $|B|$ (red).

Two variables, F and θ , are used to describe the relations between the toroidal field at the wall, $B_t(a)$, the poloidal field at the wall, $B_p(a)$, and the average toroidal field over the plasma volume $\langle B_t \rangle$. F , known as the reversal parameter (2.3), indicates how deeply the toroidal field reverses, while θ , known as the pinch parameter (2.4), indicates the relative strength of the poloidal field with respect to the toroidal field.

$$F = \frac{B_t(a)}{\langle B_t \rangle} \quad (2.3)$$

$$\theta = \frac{B_p(a)}{\langle B_t \rangle} \quad (2.4)$$

In RFP plasmas $B_t(a) \ll B_p(a)$ thus $|B(a)|$ is largely unaffected when switching between $F \sim -0.2$ (reversed) and $F=0$ (non-reversed) plasmas, as is occasionally done in operation. The data collected in thesis uses $F \sim -0.2$ plasmas. The total edge magnetic field (2.5) can be found knowing F (2.3), θ (2.4), and the average toroidal field. Since $F^2 \ll \theta^2$, the dominant edge field contribution is from the poloidal field, and toroidal field can be ignored, allowing modeling of the edge field profile with ampere's law.

$$|\vec{B}(a)| = \sqrt{B_p^2 + B_t^2} = \langle B_t \rangle \sqrt{\theta^2 + F^2} \quad (2.5)$$

In MST the relation between I_p and $|B(a)|$ from equilibrium reconstruction, regression fit of $|B(a)|$ vs. I_p , and amperes law (2.6) are within 0.6% error.

$$B_\theta(a) = \frac{\mu_0}{2\pi a} \times I_p \approx 3.846 [kG / kA] \times I_p \quad (2.6)$$

In the absence of porthole field error, the poloidal component of the edge magnetic field can be modeled by(2.7), where ‘‘a’’ is the minor radius and x is the distance from the wall. It should be noted that this formula is not valid for large radial displacements ($r/a < 0.8$) into the plasma, where $|B(r)|$ diverges from $B_p(r)$.

$$B_\theta = \frac{\mu_0 I_p}{2\pi(a-x)} \hat{\theta} \quad (2.7)$$

Modeling of edge fields near the wall start with ampere's law, and add effects due to porthole field error, discussed in the next section. This local magnetic field is used to determine the expected location of EBW absorption by adding Doppler shift to the computed radial cyclotron frequency profile.

2.1.2 Porthole field error contribution

The presence of a porthole in the current carrying shell of MST disrupts the wall currents, contributing a perturbation to the magnetic field near the wall. Results include a reduction of local magnetic field and a “bulging” of the field lines radially outward into the porthole. Since the EBW is strongly damped on all harmonics, the launched wave will be absorbed on the next higher harmonic at the wall, reducing radial accessibility. These effects can be mitigated by the use of error correction coils (not implemented on this experiment), or the reduction of the porthole diameter, which reduces the spatial extent of the field error.

Porthole field error has been examined in RFPs in [49], [50] and can be modeled analytically [51] by assuming a porthole located on a conducting plane. The scale length of the equilibrium field is assumed to be much larger than the porthole, the port radius is much smaller than the minor radius of MST, and the port has no effect on the global plasma current. The perturbation to the edge magnetic field around the porthole is plotted in a cross section of MST, shown in **(Figure 2.2)**. Effects of the porthole error field contribution are evident in the right plot; field lines and vectors are drawn outward into the porthole. The magnitude of the field error calculated with [51], and corresponding ECR frequencies on the porthole axis is plotted in **(Figure 2.3)** for a 350kA plasma for 5cm (left) and 12cm (right) portholes. The magnitude of the field error on the porthole axis is unaffected by the hole size, field magnitude is reduced by a factor of 2 flush with the wall. The spatial extent of the field error is proportional to the diameter of the porthole; larger portholes introduce field error farther into the plasma, with the error extending approximately ~ 1 diameter into the plasma.

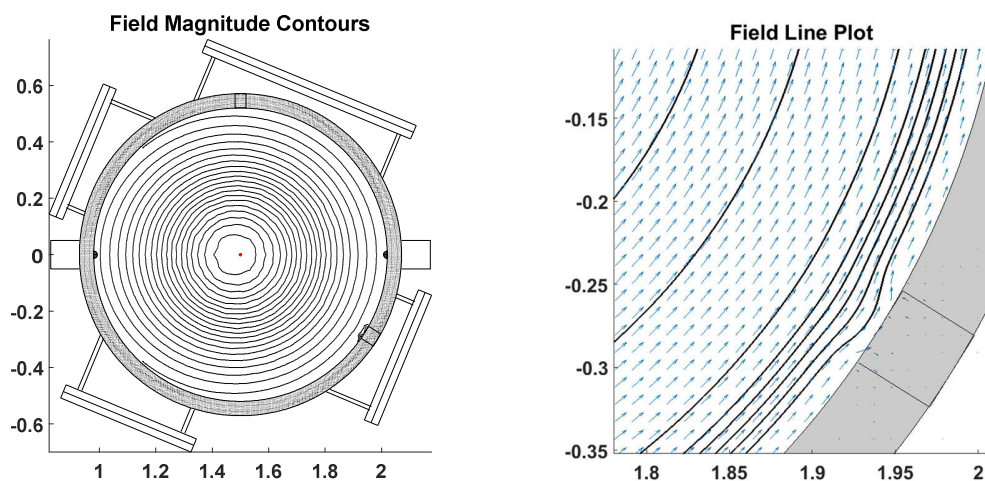


Figure 2.2. Magnetic field contours(left) and field lines(right) for 5cm porthole.

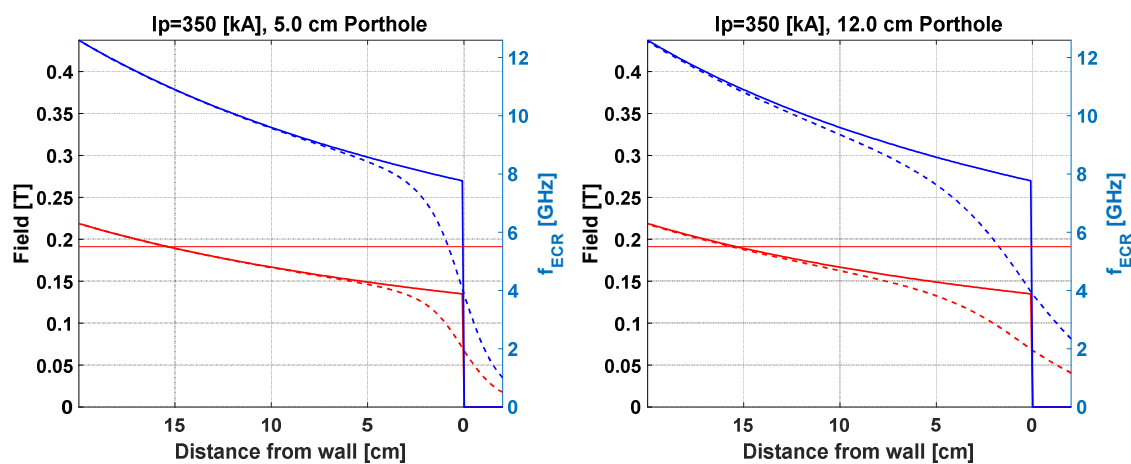


Figure 2.3. ECR frequencies in the edge for first harmonic (red) and second harmonic (blue). Solid lines represent edge field without porthole field error, dashed lines include the field error contribution for a 5cm (left) and 12cm (right) porthole. The 5.5GHz launch frequency is denoted by the horizontal red line.

Of important note in **Figure 2.3** is the introduction of edge absorption of a higher harmonic. Note that no correction for Doppler shift is provided in these plots, the actual resonance would

occur closer to the wall when the Doppler correction is applied. In this example, first harmonic absorption (red), and second harmonic absorption (blue) are shown for a 350kA plasma. In the absence of porthole field error, magnetic field goes to zero at the wall, indicated by the solid vertical lines at 0 depth. An EBW launch at this plasma current would propagate inward until absorption at 15cm on the first harmonic. In the presence of a porthole, magnetic field begins to fall off farther from the wall and is non zero within the porthole. As a result the second harmonic resonance, shown in dashed blue appears near the edge, damping the EBW at the wall. To compensate for this effect, plasma current must be increased to move the second harmonic resonance at the wall to above the launch frequency, however in doing so, the first harmonic line also moves upward intersecting the resonance closer to the wall. Thus the maximum radial accessibility is limited by the presence of the porthole error field.

For first harmonic this poses an additional problem of the second harmonic resonance entering the waveguide antenna causing localized EC absorption in the antenna and arcing; the efficiency of ECH vs. harmonic is given by [52]. The optical depth [53], [54] for normal incidence for X/O-mode fundamental and second harmonic absorption show good absorption causing arcing problems in the antenna. This does not pose an issue for second and higher EBW harmonic heating as the third and higher EC resonances are very weakly damped and do not cause arcing problems in the antenna. This effect was observed to be especially pronounced in a 12cm porthole launch where the spatial distributions of the field error are large. The 5.5 GHz system could not achieve first harmonic heating with a launch from the 12cm porthole due to arcing problems in the antenna. Subsequent construction of a 5cm porthole mount antenna, with a correspondingly smaller field error, successfully heated on the first harmonic.

2.2 Modeling of Heated Electrons in MST

Heated electron collisions with background electrons and ions

Measurements presented later will show EBW heated electron dynamics, where the observed time scales are used to infer underlying physics. An important comparison is to the expected classical time scales. Estimates of the local T_e , n_e , and neutral density from previous probe measurements and simulations are used to compute the classical collision times and drift rates. These calculations are used later in the thesis.

Heated electrons traveling through the plasma will scatter off of electrons, ions, and neutrals in the background plasma. The lifetime of energized electrons and their density and energy spectrum at a given toroidal angle will be determined by their scattering rates. The scattering and energy equalization times are presented below. The density and temperature 3.5cm from the edge of MST is $n_e \sim 2 \times 10^{17} \text{ m}^{-3}$ and $T_e \sim 20 \text{ eV}$, while the incident EBW heated electrons are on the order 10-60 keV.

In MST the density is measured with a CO2 interferometer that measures phase shift of a 10.6um laser passing through the core of the plasma. Measured density is a line averaged value, related to core density, n_0 , by (2.8) assuming a $(1-r^2/a^2)$ profile shape. Averaging leads to a 2/3 scale factor between the line averaged and core values.

$$\bar{n} = \frac{1}{2a} \int_{-a}^a n_0 \left(1 - \left(\frac{r}{a} \right)^2 \right) dr = \frac{1}{2a} n_0 \left(r - \frac{r^3}{3a^2} \right)_{-a}^a = \frac{2}{3} n_0 \quad (2.8)$$

In MST electron temperature data can be directly measured with the Thomson scattering system, or optionally with Langmuir probes in the edge. In the absence of Thomson data, the temperature profile can be estimated using the Hokin / Biewer scaling law [55]. A central temperature value ((2.9)) is assumed based on plasma current and core density, where core density is assumed to be 1.25 times the line averaged density measured by the CO2 laser interferometer.

$$T_{e,0} [eV] \approx 200 \left(\frac{I_p [kA]}{200} \right)^{1.09} \left(\frac{n_0 [cm^{-3}]}{1e13} \right)^{-0.34} \quad (2.9)$$

This core temperature value is used to scale Thomson measurements to the match the peak value, and an estimated profile is generated.

The edge electron temperature for the last 7 cm is modeled with a linear fit for (**Figure 2.4**) for temperature data from a 250kA plasma.

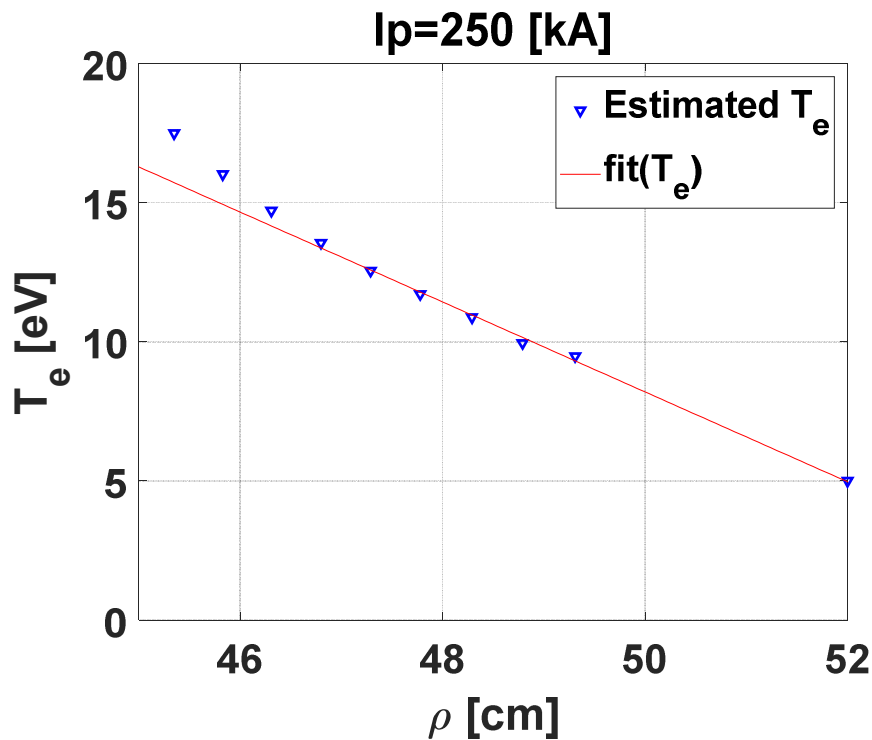


Figure 2.4. Edge electron temperature estimated by MSTfit(blue) and a linear fit (red) are plotted for a 250kA plasma.

The fitted electron temperature in the edge is modeled in (2.10), where x is the distance from the wall, assuming a 3.34 eV edge temperature.

$$T_{eV,edge} = 3.21x + 3.34[\text{eV}] \quad (2.10)$$

Langmuir probe measurements may also be used to determine edge electron temperature. In experiments conducted by Miller [56], a triple tip Langmuir probe was scanned radially into a 200kA plasma discharge. Resulting electron temperature and density profiles were measured within the first 11cm of the edge (**Figure 2.5**).

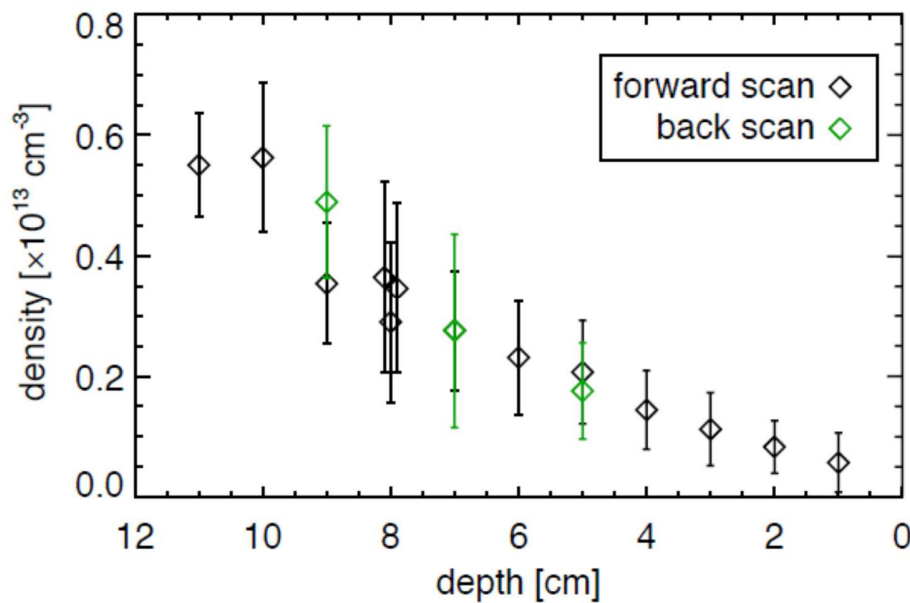


Figure 2.5. Edge electron density(left) measured with a triple tip langmuir probe in a 200kA, $f=0.18$, $n_e=1.2e19\text{m}^{-3}$ plasma. Figure courtesy of [56]. Plasma conditions for EBW target plasmas

are typically half the line average density of this plot. Measured probe values are scaled linearly when used in EBW modeling to approximate typical target plasma conditions.

The 90 degree scattering times [57], [58] are (2.11), (2.12) where m_e is electron mass, T is plasma temperature, n_e is density, Z is ion atomic number, and $\text{Ln}(\Lambda)$ is the coulomb logarithm, calculated from(2.14). Computed electron scattering times assuming 20eV background plasma, $n_e=2e17 \text{ m}^{-3}$ density, and $T_e = E_{incident}$ is plotted in **(Figure 2.6)**.

$$\tau_{90}^{ee} = \frac{6\pi\epsilon_0^2 \sqrt{3} \sqrt{m_e} (kT)^{3/2}}{n e^4 \ln(\Lambda)} \quad (2.11)$$

$$\tau_{90}^{ei} = \frac{6\pi\epsilon_0^2 \sqrt{3} \sqrt{m_e} (kT)^{3/2}}{n_i (Ze)^2 e_i^2 \ln(\Lambda)} \quad (2.12)$$

The coulomb logarithm is calculated to be $\text{Ln}(\Lambda) \sim 14$ using the above approximations for typical background plasma temperatures in MST.

$$\lambda_D = \sqrt{\frac{\epsilon_0 k T_p}{4\pi n e^2}} \quad (2.13)$$

$$\ln(\Lambda) = \ln\left(n_e \frac{4\pi}{3} \lambda_D^3\right) = n_e \left(12\pi \left[\frac{(\epsilon_0 k T)^3}{n_2 e_2^4 e_1^2}\right]^{1/2}\right) \quad (2.14)$$

The fast electron collision times on background electrons ranges from 100ms to ~1s over the range of measured energies. As will be mentioned in later sections, this time scale is significantly greater than other processes affecting electron confinement in the RFP.

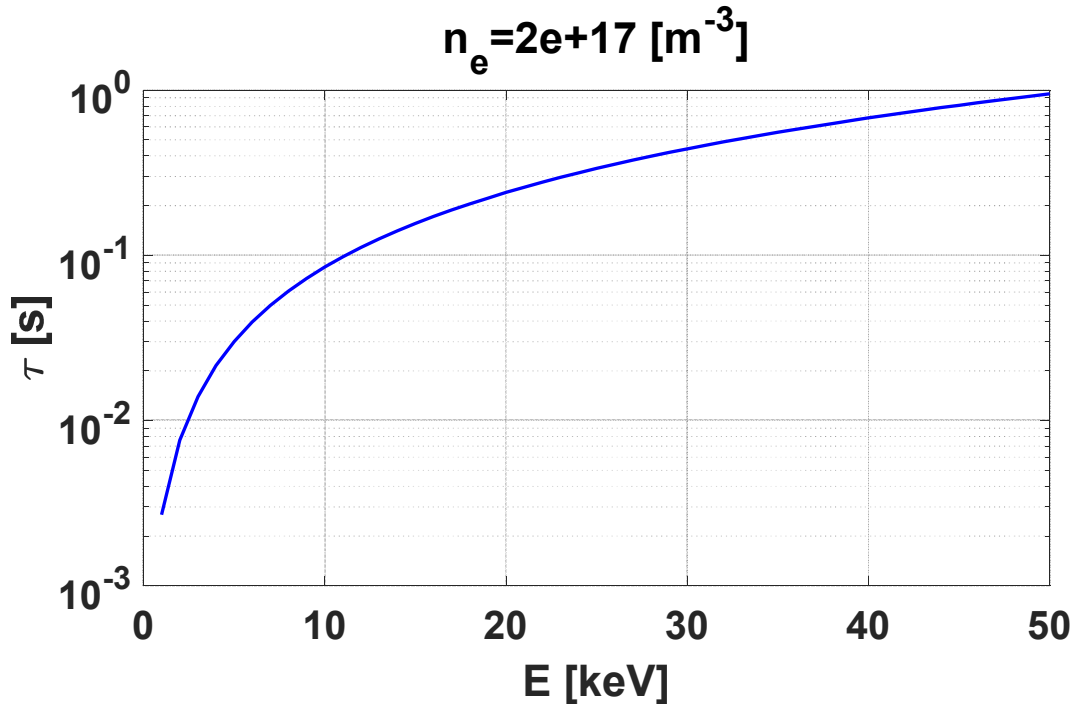


Figure 2.6. Electron on electron scattering times for heated electrons between 2 keV and 50 keV in a plasma of $n_e = 2e17 \text{ m}^{-3}$.

2.2.1 Heated electron collisions with background neutrals

Scattering times of electrons on neutrals is calculated with (2.15) [59], where n_0 is the neutral density, σ_s is the scattering cross section, m_α is the electron mass, and T_α is the electron temperature. Neutral density 4cm from the wall ($n_0 = 7E16 \text{ m}^{-3}$) is calculated with DEGAS2 for 250kA and 350kA plasmas, shown plotted in (Figure 2.7).

$$\tau_\alpha = \frac{1}{n_0 \sigma_s^{\alpha|0} v_\alpha} = \frac{1}{n_0 \sigma_s^{\alpha|0}} \sqrt{\frac{m_\alpha}{kT_\alpha}} \quad (2.15)$$

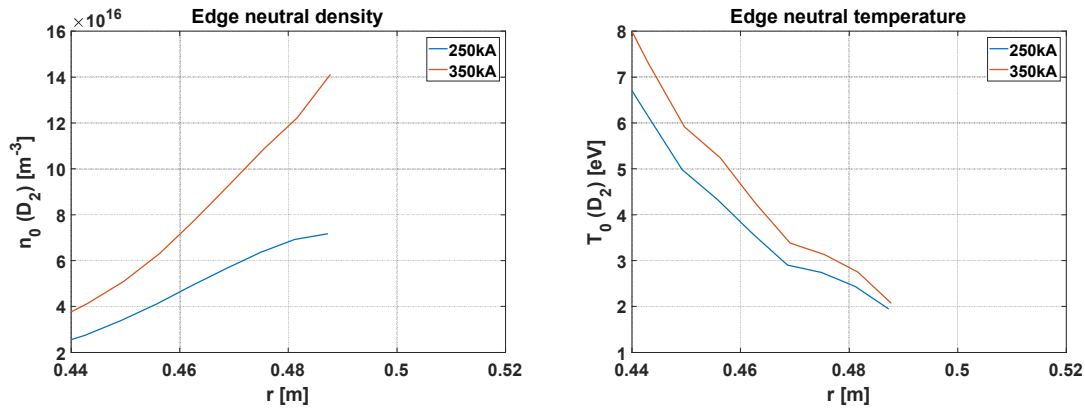


Figure 2.7. DEGAS2 simulations of neutral density(left) and temperature(right) in a 250kA and 350kA standard plasma indicate that density at 4cm from wall is $n_0(250kA)=6.8e16$ [m⁻³] and $n_0(350kA)=1.2e17$ [m⁻³].

The cross section of electrons colliding with molecular hydrogen [60], [61] is the sum of the individual cross sections for elastic scattering, ionization, and Lyman band photon emission, the dominant interaction processes. The cross sections are tabulated for electron energies between 1eV to 1keV, requiring extrapolation to energies typical of EBW heated electrons. Above 10eV, the cross section decreases exponentially with energy allowing extrapolation to the 10keV to 50keV range, plotted in (**Figure 2.8**). At 20keV, the estimated total cross section is $\sigma_s^{e20keV|H_2^0} \sim 1E-17$ [cm²], with neutral ionization being the dominant contribution to the cross section.

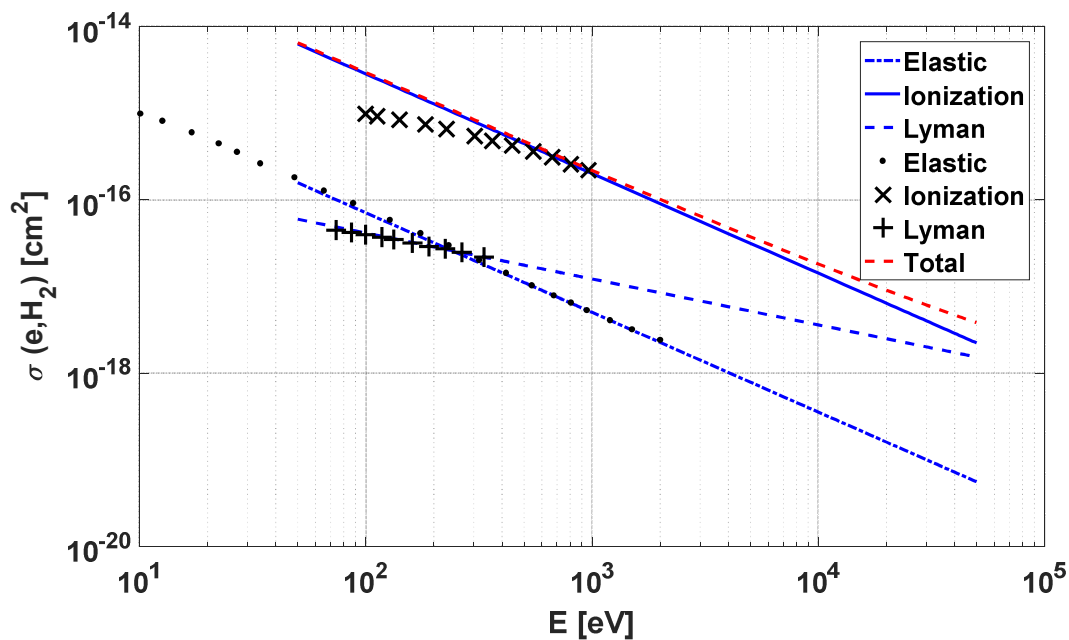


Figure 2.8. Extrapolation(lines) of total interaction cross section for energies up to 50keV based on measured data(marked points) from [60].

Scattering times of electrons on the background neutrals are plotted in (**Figure 2.9**). Scattering times of heated electrons on neutrals are 200-400 μs at 4cm depth over the 10-50keV energy range. Collisional timescales of electrons on neutrals are much longer than timescales of other plasma processes presented in later sections.

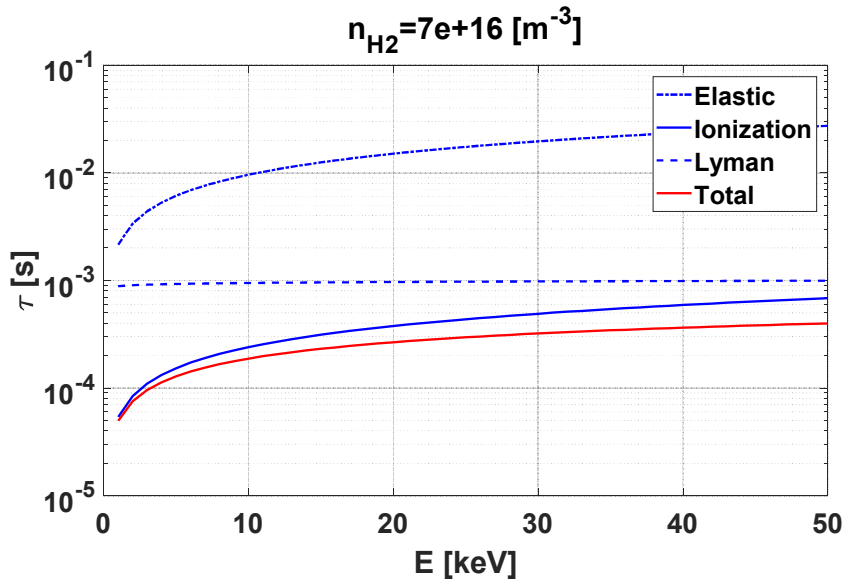


Figure 2.9. Collision times for 10-50keV electrons with neutral hydrogen are calculated to be in the 200-400 μ s range using plasma conditions modeled in DEGAS2 4cm from the wall.

2.2.2 Perpendicular diffusion of heated electrons

High electron diffusion rates [62], [63] in the RFP are expected to be a dominant contribution to EBW heated electron population loss. The radial diffusion rate is proportional to the parallel velocity and the magnetic stochasticity in a broken magnetic field [64], as given in (2.16).

$$D_{\perp} = v_{\parallel} D_m \quad (2.16)$$

Perpendicular diffusion for thermal electrons is found to be 30m²/s for standard plasmas and 3m²/s for PPCD plasmas [65] near the edge. The perpendicular diffusion coefficient for EBW heated electrons (2.17) in a standard plasma is estimated by scaling the thermal electron diffusion coefficient with the parallel velocity of EBW heated electrons ($\sim 7.5Te$) given by the Doppler shifted resonance condition.

$$D_{\perp,EBW} \approx \sqrt{\frac{v_{\parallel,EBW}}{v_{\parallel,thermal}}} D_{\perp,thermal} \approx 82 [m^2 s^{-1}] \quad (2.17)$$

Diffusion time in a standard plasma calculated with (2.18), where Δr is a characteristic distance of a 4cm probe insertion depth, yields a 19 μ s time scale. Diffusion timescales are much faster than collisional timescales in the RFP and are expected to be the dominant electron loss mechanism.

$$\tau = \Delta t = \frac{(\Delta r)^2}{D_{\perp}} \quad (2.18)$$

2.2.3 Heated electron trapping in banana orbits

Trapped and passing electrons both play an important role in the heated distribution since a large EBW k_{\parallel} upshift [4] and absence of a high toroidal field side trap only a modest fraction. In MST a small mirror ratio exists due to toroidicity, as plotted in **(Figure 2.10)**. Radial B profiles are proportional to plasma current, thus mirror ratio is invariant in I_p . Typical bounce times of 200ns are expected for EBW heated electrons near the edge. In MST banana orbits are in the poloidal direction with no radial width, as plotted in **Figure 2.11** and drift in the toroidal direction, as will be shown in the following section.

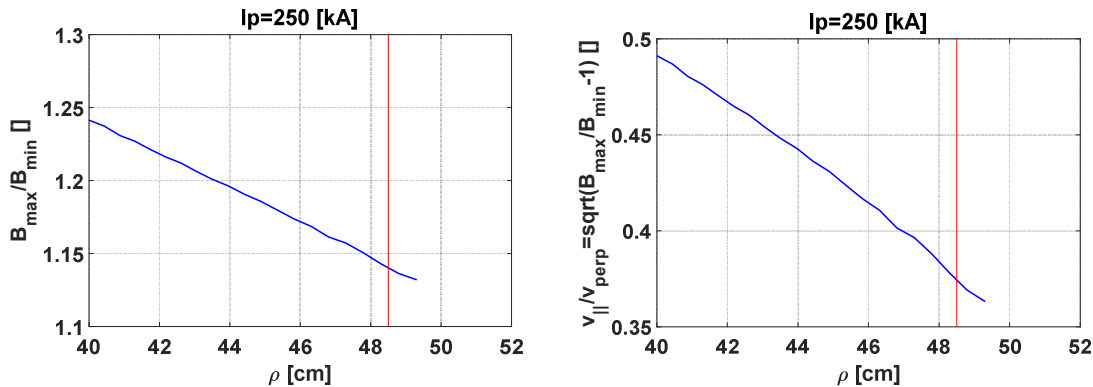


Figure 2.10. Mirror ratio and velocity ratio for trapped particles in a 250kA plasma, 3.5cm marked with vertical red line.

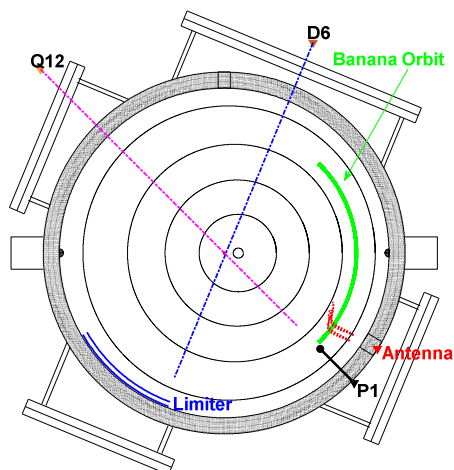


Figure 2.11. Poloidal cross section of MST with magnetic field contours (black), possible EBW trajectory @138° Toroidal (red), and a possible banana orbit of heated electrons (green). Banana orbit has no radial width.

2.2.4 Toroidal drifts in MST

Due to the magnetic geometry in the RFP, trapped electrons drift toroidally at a speed proportional to their perpendicular energy and I_p ; near the edge drift speed does not depend on minor radius. An insertable target probe, labeled P1 in **Figure 2.12**, serves as a key diagnostic by detecting trapped electrons that have drifted 150 degrees toroidally from the heating location.

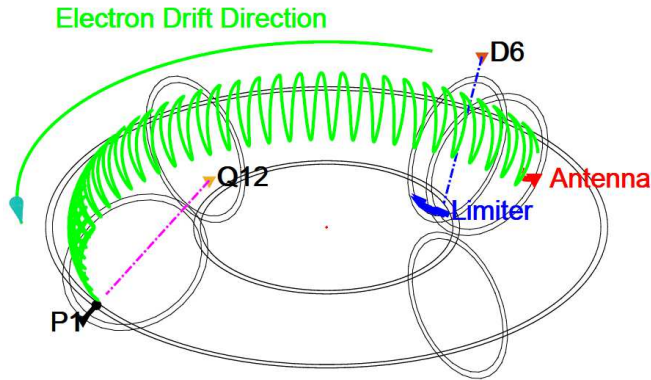


Figure 2.12. Banana orbit of heated electrons (green), limiter @150° Toroidal (blue solid line), and target probe P1 @300° Toroidal (black line) are observed by HXR detectors D6 and Q12, respectively.

Trapped electrons measured by the target probe are critical in determining heated electron radial profiles, and thus deposition depth. Since trapped electrons are transported toroidally by drifting, the effective parallel velocity along field lines is less than passing electrons, reducing loss due to perpendicular diffusion. Trapped electrons drift around MST in the positive toroidal direction for standard plasma current direction due to the grad B and curvature drifts(2.19). As the ∇B drift is due to perpendicular energy and curvature drift is due to the parallel energy of the bouncing electron, both are considered. Drift velocity is invariant with radius near the edge as the terms in the magnetic field gradient term in (2.20) cancel out factors of minor radius in (2.19)

$$v_B = \left(\underbrace{\frac{m_e v_{\perp}^2}{2q|B|}}_{\nabla B} + \underbrace{\frac{m_e v_{\parallel}^2}{q|B|}}_{curv} \right) \frac{\vec{B} \times \nabla |B|}{|B|^2} = - \left(\underbrace{\frac{kE_{\perp}}{e|B|}}_{\nabla B} + \underbrace{\frac{2kE_{\parallel}}{e|B|}}_{curv} \right) \frac{\vec{B} \times \nabla |B|}{|B|^2} \quad (2.19)$$

$$\nabla|B| = \frac{\partial}{\partial r} \left[\frac{\mu_0 I_p}{2\pi r} \right] = -\frac{\mu_0 I_p}{2\pi r^2} \hat{r} = -|B| \frac{1}{r} \hat{r} \quad (2.20)$$

In the limit where $B_t \ll B_p$, the ∇B drift is given by (2.21), a function of only I_p and E_\perp .

$$v_{\nabla B} = \frac{kE_\perp}{e|B|} \frac{1}{r} \text{sgn}(B_\theta) \hat{\phi} = \frac{2\pi kE_\perp}{e\mu_0 |I_p|} \text{sgn}(B_\theta) \hat{\phi} \quad (2.21)$$

The combined ∇B and curvature drift is given by (2.22)

$$v_B = -\frac{k(E_\perp + 2E_\parallel)}{e|B|} \frac{\vec{B} \times \nabla|B|}{|B|^2} = -\frac{2\pi k(E_\perp + 2E_\parallel)}{e\mu_0 |I_p|} \text{sgn}(B_\theta) \hat{\phi} \quad (2.22)$$

For an electron of total energy E , the average drift velocity will be between the ∇B and curvature drift speed. The drift velocities plotted in **(Figure 2.13)** indicate that trapped 20keV electrons drift toroidally at $\sim 4E5\text{m/s}$. The toroidal transit time (2.23) required for heated electrons to make one complete circuit around MST is plotted in **(Figure 2.14)**.

$$\tau_{T,transit} = \frac{L_{tor,path}}{v_{drift}} \sim \frac{2\pi(R_0 + \langle \rho \rangle_{orbit})}{v_{drift}} \quad (2.23)$$

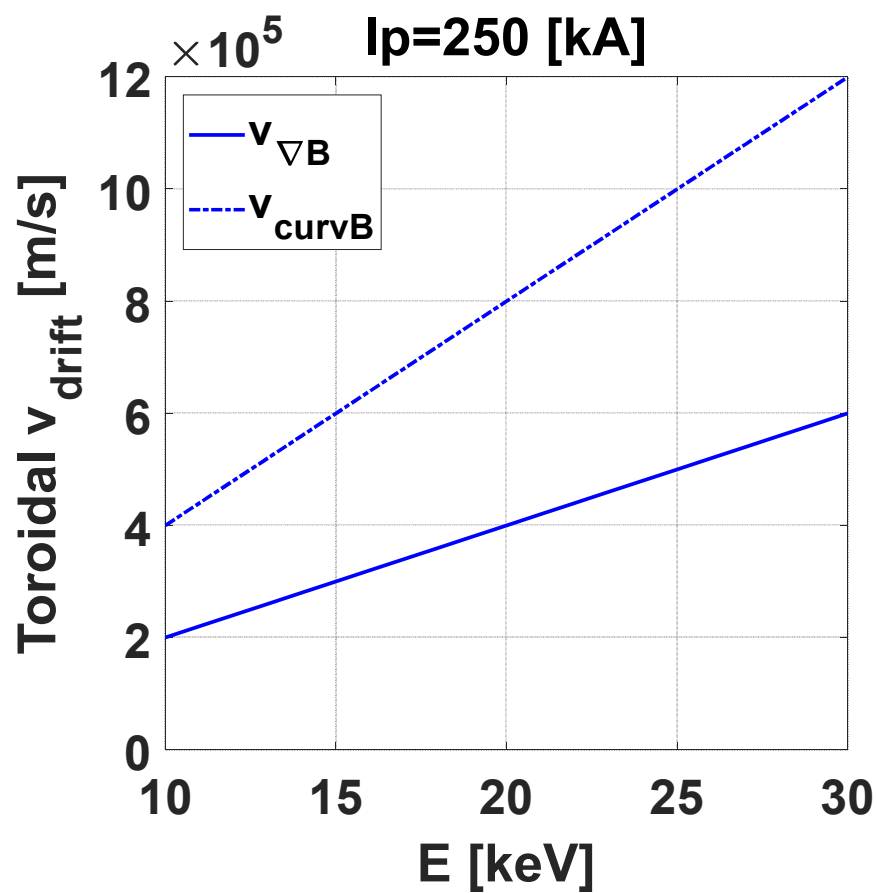


Figure 2.13. Toroidal drift velocity for trapped electrons due to ∇B (blue solid), curvature drift for pitch angle scattered electrons with E in the parallel v direction (dashed blue).

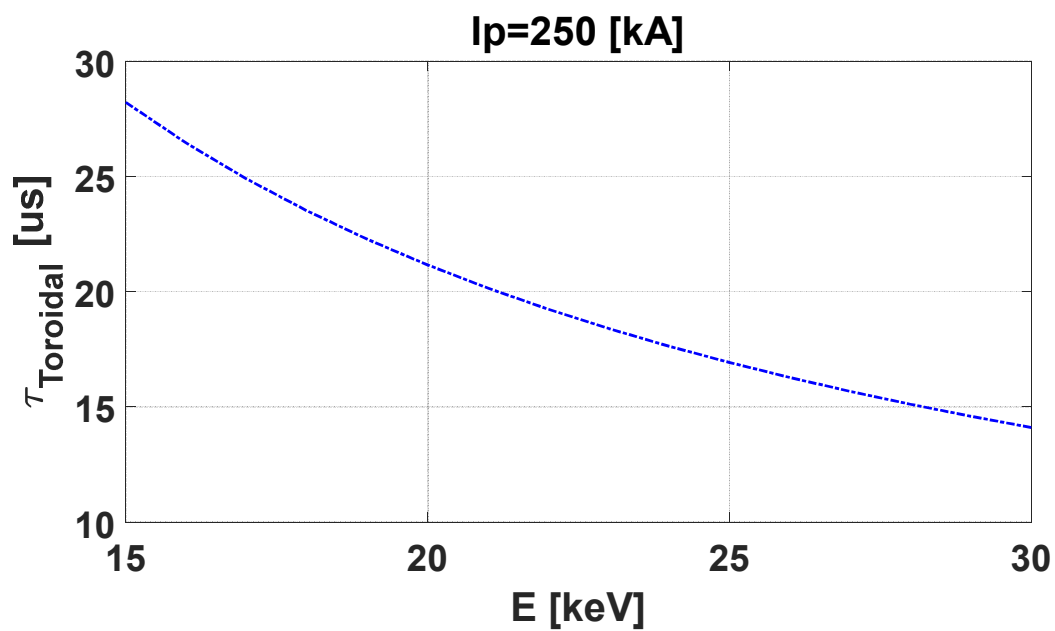


Figure 2.14. Toroidal transit time for one cycle around MST for an orbit at a radius of $R+a$ for a 20keV trapped electron.

2.3 Genray simulations and wave propagation

Genray [66] is a ray tracing program that numerically solves for the EBW trajectory in the plasma based on the index of refraction at each given point along the ray. The ray is launched at the UHR surface after mode conversion. Initial conditions given to Genray specify the launch point at 98% of the minor radius, the X wave is assumed to travel radially inward from the wall to the point of mode conversion.

Propagation and dispersion of the EBW depends on magnetic field and electron temperature [67]. A Doppler shift is added to the cyclotron resonance condition to correct for electron velocity in the plasma. The Doppler shift, ω_{dop} (2.24) goes to zero at the wall as a result of decreasing electron temperature, while the increasing Doppler shift at increasing depth. Launch position above or below the mid-plane controls N_{\parallel} shift direction resulting in the EBW trajectory bending towards the weaker magnetic field, with the parallel refractive index decreasing along the ray (becoming more negative) until it is absorbed at the Doppler shifted resonance.

$$\omega_{\text{rf}} = n\omega_{\text{ce}} - \frac{k_{\parallel}v_{\parallel}}{\gamma} = n\omega_{\text{ce}} - \omega_{\text{doppler}} \quad (2.24)$$

Our primary use of Genray is to compute the Doppler shift at the expected location of EBW damping as effects of porthole field error prevent calculation of the correct deposition location. Within the presence of the field error the magnetic model given to Genray would be incorrect when simulating deposition within a porthole diameter from the edge, while outside the field error the transition to the next higher harmonic would be calculated to occur at an incorrect plasma current. EBW damping calculated with the cold plasma dispersion location corrected for porthole field error and Doppler shift are used to accurately model heating locations.

The magnitude of the Doppler shift is computed as follows. The parallel refractive index is calculated by Genray ignoring field error as plotted in (**Figure 2.15**). The local magnetic field is used to calculate the cyclotron frequency. The difference in cyclotron frequency and launched RF frequency is then used to find the Doppler shift as a function of minor radius for each harmonic using(2.24). The field error correction and Doppler shift are now applied to the magnetic field profile to determine the location of the launched RF resonance.

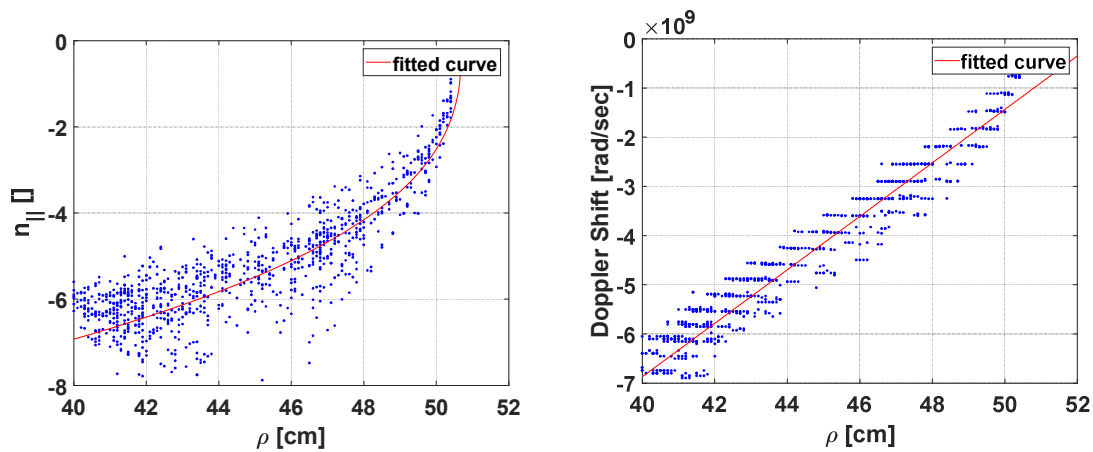


Figure 2.15. Parallel refractive index(left) and doppler shift(right) plotted vs absorption position for the n=2 harmonic.

Modeling with GENRAY provides profiles of Doppler shift as a function of local electron temperature. Computed Doppler shift information is applied to models of edge magnetic field to provide corrections in absorption position allowing accurate modeling of heating locations in the presence of porthole field error.

2.4 Summary

This chapter presented modeling of EBW launch, propagation, absorption and subsequent transport of the heated electrons. Observed effects in the EBW experiment can be explained accurately with classical models.

The first section presented a description of x-mode launch and conversion to the EBW. Edge density and magnetic field profiles were used to model the location of the R, L, and UH locations. Port hole field error modeling demonstrated the reduced radial accessibility of the EBW. Conversion efficiency to the EBW depends on density gradient scale length. Losses due to parametric decay were addressed. The hot plasma dispersion relation controlling EBW absorption on a Doppler shifted cyclotron resonance leads to efficient EBW absorption on fundamental and higher resonances.

Section two presented modeling of drifts and transport of the EBW heated electrons including collisions with plasma electrons, ions, and neutrals. Toroidal drift rates were modeled by classical formulas to estimate trapped toroidal drift speed as a function of electron energy. The effects of heated electrons colliding with limiters and probes were used to model possible bremsstrahlung spectrums based on various energy distributions.

Section three presented Genray modeling and its limitations. Porthole field error prevents accurate calculation of ray trajectories and absorption positions in Genray; n_{\parallel} spectrum and Doppler shift can be accurately calculated allowing Doppler shift estimations to be added to an analytical model of absorption position.

Chapter 3 Hardware

This chapter presents an overview of the hardware and experimental design of the 5.5GHz EBW experiment. A diverse variety of RF and diagnostic equipment was constructed in the commissioning of the EBW experiment. Several hardware revisions optimized the heating system for consistent and reliable operation. Hardware developed for the experiment can be classified as either RF heating hardware, RF control systems, and x-ray diagnostic systems. RF heating hardware includes the klystron tube, cylindrical molybdenum antenna, and waveguide hardware.

A variety of RF control systems were implemented to provide an RF pulse at a stable power level through feedback control from the measured forward power from the klystron tube. Previous implementations of RF power and phase detectors had unacceptable noise pickup during operation. A complete redesign of the RF diagnostics with substantial design effort in noise shielding resulted in significant reduction in noise pickup and the ability to accurately control RF power.

X-ray diagnostics were constructed to measure electrons heated by the EBW. A spatial distribution of probes and limiters observed by single photon counting hard x-ray (HXR) detectors measured electron energy and radial profiles required to determine the absorption depth of the EBW. Careful selection in filters and detector layout was instrumental in allowing

measurement of electrons in PPCD plasmas where background emission must be separated from RF heating effects.

3.1 RF Power Generation and Transmission

3.1.1 Klystron and support equipment

A klystron and support equipment generates several hundreds of kW of RF power for launch into MST through a waveguide antenna. The klystron requires a number of RF control and protection systems to ensure stable and safe operation without damage to the antenna or klystron itself. In addition a high voltage pulsed power supply capable of up to 100kV at 50A (run at ~78kV, 30A) was constructed to power the klystron. A high voltage transmission system including high voltage pulse snubbers, crowbar spark gaps, and an actively cooled oil bath for the klystron were also constructed. Significant effort went into the design and construction of the pulsed power system to drive the klystron tube.

RF power for the EBW experiment was generated by a surplus radar klystron tube (USN-8406A/VKC-7762B), shown in **Figure 3.1**, designed for 1MW peak, 18 μ s wide pulses at 5.5GHz with a 428pps pulse rate. The tube is designed to operate at 75-85kV with 35A of beam current and 5-20W input power. When operated at a reduced output power on the order of 100-300kW, the tube will operate at pulse lengths of 3-4ms without arcing. The klystron was installed in a cart containing the required solenoid magnet for beam focusing and an oil bath for insulating and cooling the cathode. The oil circulated through a liquid-liquid heat exchanger removing heat from the filament that boiled the insulating oil in previous designs. Water was circulated through the tube body, collector, and magnet for cooling. A filament transformer provided ~5Vac power to the tube filament using a high voltage x-ray cable as the secondary winding.



Figure 3.1. Klystron tube being lowered into magnet (left). Klystron in magnet assembly with cooling oil bath attached (right).

3.1.2 Antenna

RF power is launched into the plasma from a cylindrical molybdenum antenna, shown in **Figure 3.2**, designed to insert flush to the inner wall without a limiter. The molybdenum is resistant to plasma bombardment and the low secondary electron emission coefficient further decreases the probability of arcing. The antenna launches the TE₁₁ mode that couples to the x-mode in a plasma. Power handling of the antenna in the presence of plasma was found to be ~150kW, limited by signs of arcing in the antenna and RF window. A tapered transition adapts the cylindrical cross section of the antenna to the rectangular cross section of the transmission

waveguide. Between the antenna and the transition, a pillbox window acts as a vacuum break, separating the high vacuum environment of MST from the pressurized waveguide.



Figure 3.2. Cylindrical waveguide antenna. Leftmost component is a differentially pumped seal allowing the molybdenum antenna (center left) to slide and rotate without admitting gas to MST. Rectangular to cylindrical transition (rightmost) connects cylindrical pillbox window (center right) to the waveguide leading to the klystron tube.

The second part of the vacuum break is formed by a differentially pumped sliding seal, shown in **Figure 3.3**. The differentially pumped seal allows the antenna to slide in and out of the antenna porthole and rotate to change launch polarization without admitting gas to MST. The sliding seal also isolates the antenna ground from the MST shell with a set of insulating plastic bushings that hold the sealing o-rings. The differentially pumped seal connects to a gate valve on the shell of MST, allowing isolation of the antenna port when the antenna is removed for servicing.



Figure 3.3. Differentially pumped sliding seal for cylindrical molybdenum antenna. Seal components (left) shows arrangement of o-rings and plastic spacers that stack within the stainless case. Assembled seal (right), shows pumping port located between the two o-rings. Plastic spacers provide ground loop isolation by insulating antenna from the shell of MST.

The antenna is connected to the klystron through a series of flexible and rigid waveguide segments as well as a circulator (that acts as an isolator) and directional coupler shown in **Figure 3.4** and **Figure 3.5**. Use of flexible segments greatly improved ease of system assembly and did not limit power handling or cause arcing within the waveguide. Launch polarization is controlled by installing the waveguide twist segment shown in **Figure 3.4**, for an x-mode launch, or use of a straight segment for o-mode launch. The red strap shown in **Figure 3.4** supports the antenna, preventing off axis loads that may cause leaks in the differentially pumped seal. A plastic bushing is installed on the antenna when inserted or retracted to maintain proper depth.

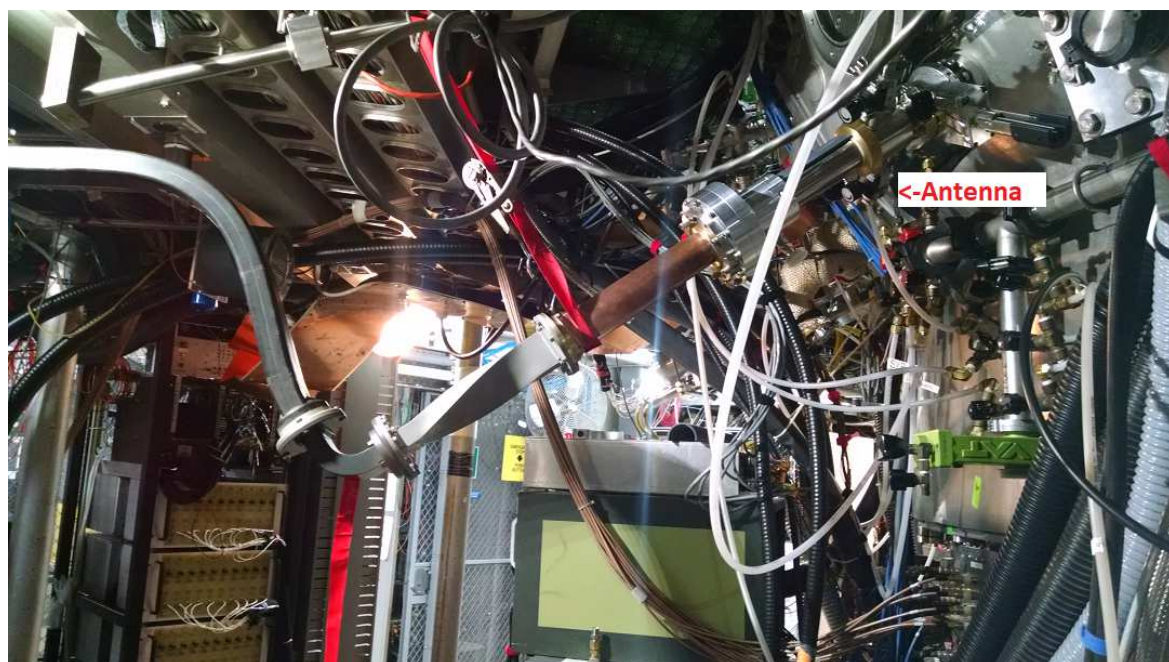


Figure 3.4. Antenna mounting position on MST with differentially pumped seal.

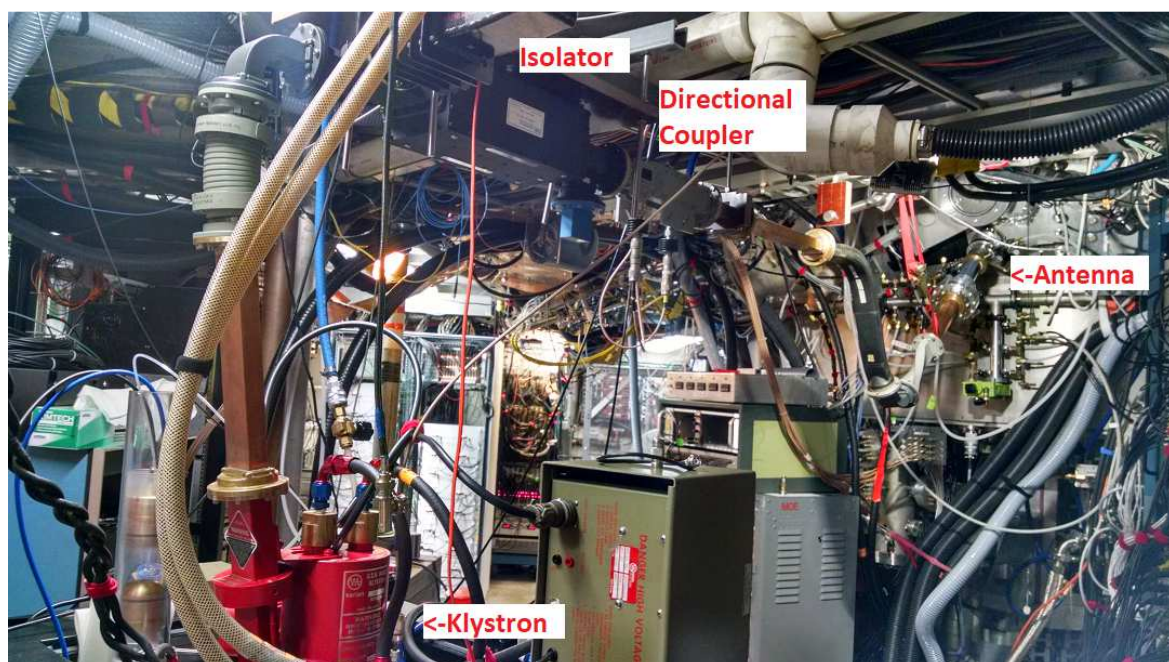


Figure 3.5. Klystron connects to antenna through an isolator assembly (circulator with waveguide load) to absorb reflected power and a directional coupler for forward and reflected power monitoring.

3.2 RF Diagnostics and Control System

3.2.1 RF system overview

The EBW RF heating system consists of several interconnected RF power and control systems. The heating system is built around a 5.5GHz radar klystron conditioned to operate at pulse lengths longer than its original design, although at a lower power. The klystron is driven by a traveling wave tube (TWT) amplifier connected to an RF signal generator tuned to 5.5GHz. Windowing of RF pulses is controlled by an HP11720A fast PIN diode switch, providing 10ns rise and fall times, located between the RF generator and TWT. The TWT boosts the signal level power from the RF generator from signal level (10s of mW), to the 10-20W required to drive the tube. The klystron further boosts the RF power up to several hundred kW, though for reliability, the system is typically operated at ~80-150kW. A 25dB circulator (CML engineering), functioning as an isolator, absorbs reflected power from the plasma that could damage the tube or interfere with operation, and a bidirectional coupler located between the antenna and isolator measures forward and reflected power from the plasma. Signals from the directional coupler are split into a fast RF diode power detector and an intermediate frequency (IF) demodulator to monitor relative phase between forward and reflected power. Power is launched into the plasma from a cylindrical molybdenum antenna, and antenna arcing is monitored with optical methods and measurement of forward and reflected power.

Earlier versions of the RF system did not include an active power feedback control system resulting in an unstable power output from the klystron tube. The current hardware version, shown in **Figure 3.6**, uses a high speed diode detector to monitor power output from the klystron

tube, and a high speed proportional-integral-derivative (PID) control system to stabilize output power at a preset level. This control loop acts as an automatic gain control (ACG) for the klystron, stabilizing output power and reducing power noise. Due to operation in a pulsed magnetic field environment, ground loop isolation is required to prevent noise pickup between the experimental hardware, located in the safety gated section of the machine area, and the control systems, located in the control room. A high speed isolator breaks the ground loop, while providing high bandwidth transmission of analog monitoring and control signals.

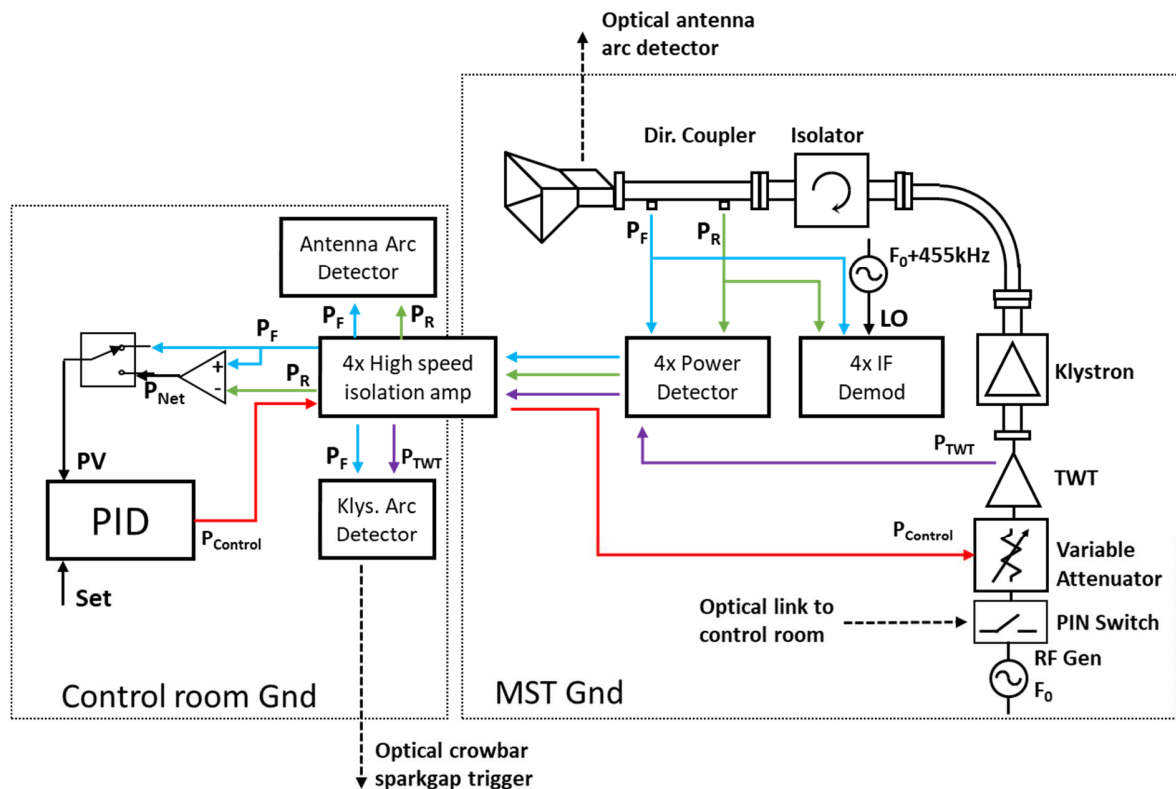


Figure 3.6. Block diagram of RF system.

3.2.2 High speed isolation amplifier

Due to the pulsed magnetic fields in the MST machine area, a voltage potential will be induced around a ground loop. Isolation of signal and ground lines to and from the control room will prevent noise pickup from induced potentials of loops. Lower cost isolation amplifiers based on Analog Devices AD210 isolators achieve 20kHz bandwidth, while isolators based on AD215 isolators achieve 100kHz bandwidth. Isolation amplifiers with these bandwidth limitations would not be able to provide sufficient response to reduce high frequency fluctuations in klystron power, typically at and above 120kHz due to the 6th harmonic of switching frequency, or higher at higher frequencies due to voltage noise. In addition, lower bandwidth isolation amplifiers have slower rise time and longer delay between input and output pulses, preventing fast response to klystron and antenna arc detection when monitoring rapid changes in forward/reflected/TWT power measurements.

A high speed isolation amplifier based on the Cheele CIM1100 was designed to provide ground loop isolation with a ~3.3kV voltage standoff. The amplifier has 120MHz bandwidth, 900v/ μ s slew rate, 1.1kohm input impedance, and 150ohm output impedance. The amplifier will pass a voltage of +-1.2V without clipping. Power is supplied to each side of the isolation amplifier by isolated dc-dc converters. Due to the high bandwidth and fast pulse response required, the amplifier circuit requires impedance matching to a 50ohm coaxial cable to prevent ringing, achieved with the use of buffer amplifiers, as shown in **Figure 3.7**. The buffer amplifiers also provide sufficient output current to drive the output cable, and provide overvoltage transient protection to the input.

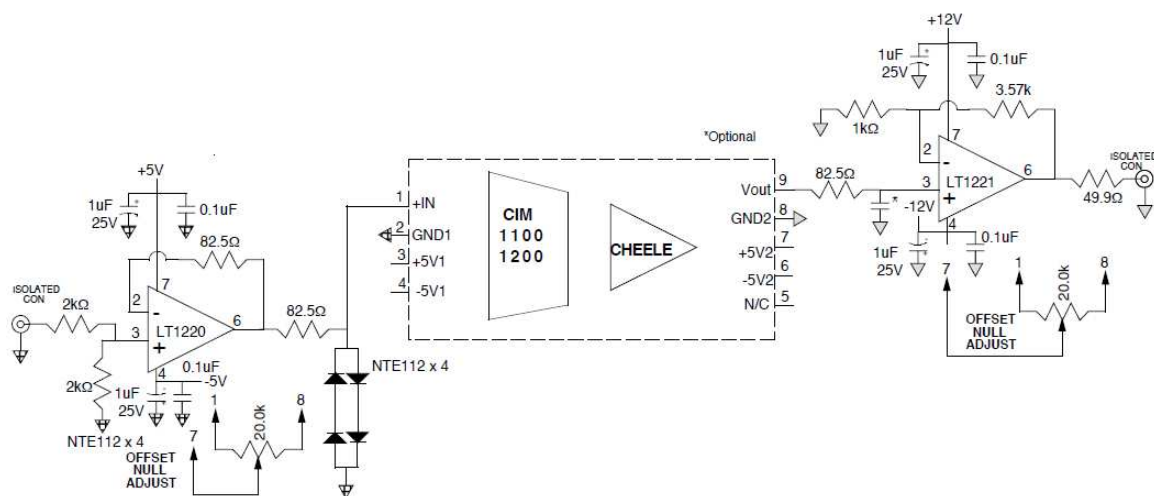


Figure 3.7. High speed isolation amplifier schematic.



Figure 3.8. High speed isolation amplifier boards are shown on the left, boards mounted within an RF shielded enclosure are shown on the right.

Isolation amplifiers were assembled on circuit board cards, shown in **Figure 3.8**, and packaged in an RF shielded box for noise immunity. Testing of the isolation amplifier design indicated low signal distortion up to $\sim 10\text{MHz}$, with relatively flat gain up to 20MHz , shown in **Figure 3.9**. The large signal response at 20MHz shows the onset slew rate limiting in the output signal. Due to the lack of a gain margin at the phase inversion frequency of the isolation

amplifier, external bandwidth limiting of the PID control system is required to maintain system stability. Testing of pulse response characteristics, shown in **Figure 3.10**, indicated a $\sim 24\text{ns}$ delay time between input and output pulses, with minimal Gibbs overshoot. Integration of the isolation amplifier into the RF control system significantly improved the frequency response characteristics of the system allowing klystron power noise reduction and power level stabilization, as will be shown in later sections.

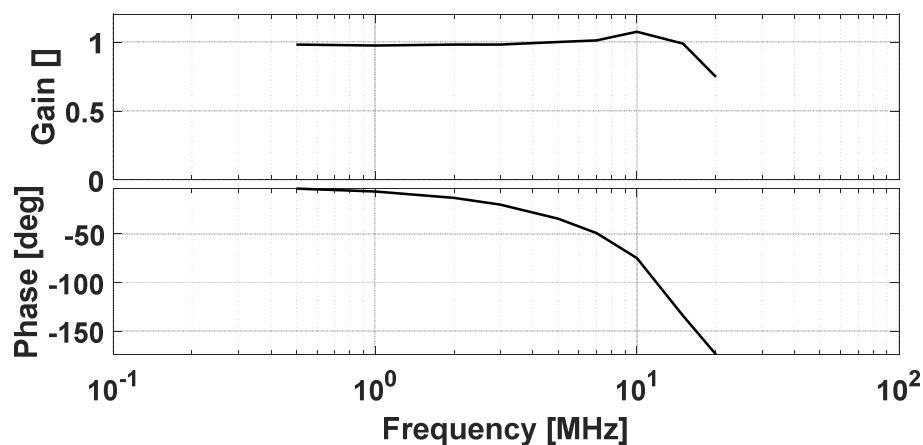


Figure 3.9. Frequency response (top) and phase shift (bottom) between input and output signals of the high speed isolation amplifier.

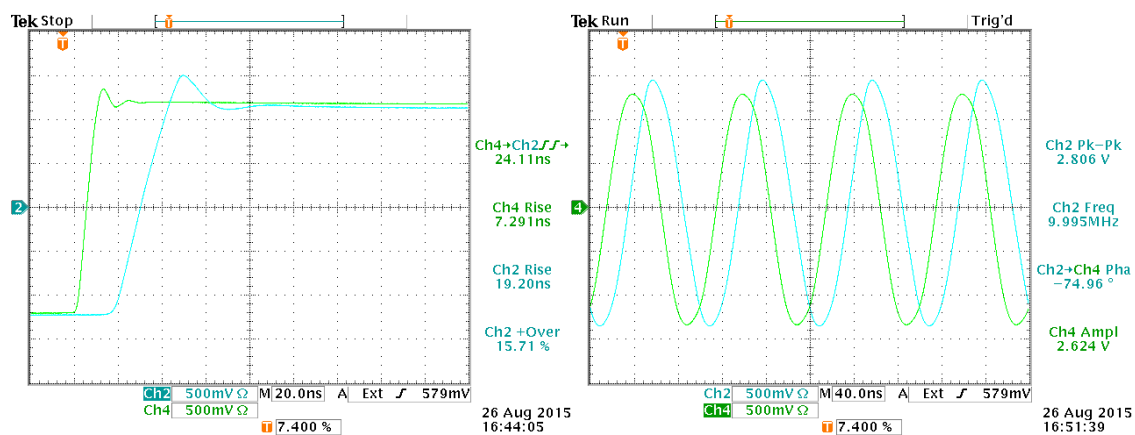


Figure 3.10. Pulse response of isolation amplifier indicating 24ns delay time between input (green) and output (blue) pulses, and 19ns rise time (left). Phase shift for a 10MHz sin wave is -75 degrees (right)

3.2.1 Phase detection

Measurement of the phase difference between forward and reflected power from the antenna provides an effective distance measurement to the first reflecting surface in the plasma. Previous phase detection systems suffered from poor sensitivity due to the lack of an output amplifier, and noise pickup due to poor shielding.

The phase detector, shown in **Figure 3.11**, and **Figure 3.13** is connected to a local oscillator (LO) that is phase locked to the RF generator driving the klystron tube. The LO operates at 455kHz above the klystron frequency. The LO signal passes through a ground loop isolator and is amplified by an RF bay LNA-4560 low noise amplifier (LNA). The LNA output is split into 4 equal signals driving independent IF detection channels. IF detection channels are connected to the forward and reverse arms of the directional coupler to sample power to and reflected from the plasma. The input of each IF channel passes through a ground loop isolator and an 800MHz high pass filter for additional noise reduction. The IF frequency is generated by mixing the LO and RF signals with a MITEQ DMX0418L double balanced mixer. The output of the mixer is connected to a high bandwidth amplifier [68], shown in **Figure 3.12**, based on an analog devices AD826 operational amplifier (OP amp). The input to the amplifier board is isolated by a mini-circuits TT25 IF transformer, while the output is isolated by a T1-6 IF transformer. The resulting IF signal is digitized by the MST data acquisition system and digitally demodulated.

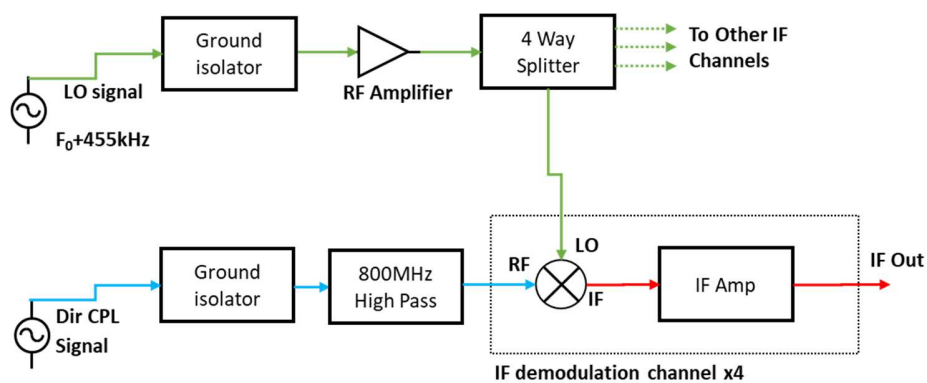


Figure 3.11. Simplified block diagram of phase detection system.

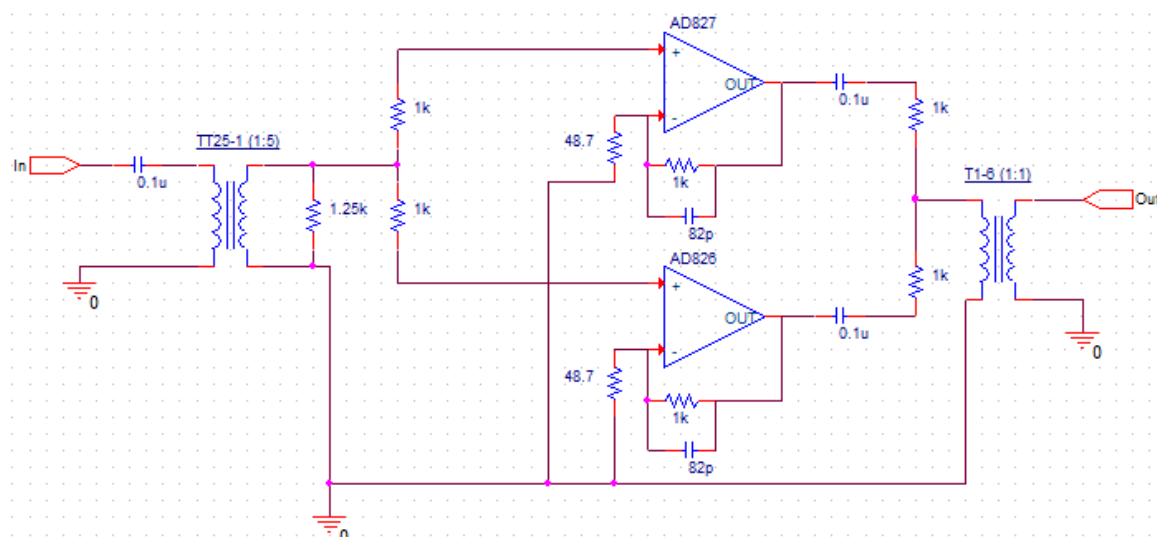


Figure 3.12. Schematic of IF amplifier.



Figure 3.13. Phase detector amplifier board (left) with one of the two channels populated. Assembled 4 channel phase detector (right).

Phase information is recovered from the IF signals through digital synchronous demodulation (DSD) [69], where the phase of a carrier wave is determined from the phase of the IF output. In a DSD system, IF signals are directly digitized and processed in software, rather than using analog hardware to recover a phase signal. A filter function, (3.1), windows the Fourier components from a FFT of the IF signal by convolution to a $\pm 50\text{kHz}$ window around the LO frequency. The filtered FFT is then inverted with an inverse Fourier transform (IFFT) and multiplied with its complex conjugate to provide a complex phase (3.2). The complex phase is converted to a real phase angle (3.3), providing a relative phase for each IF channel. Since the LO and RF signals are phase locked, the difference in phase angles between the forward and reverse arms of the directional coupler provide the phase between the signals at the RF frequency.

$$Filter(f) = \theta(F_{carrier+IF-50kHz} - f) - \theta(F_{carrier+IF+50kHz} - f) \quad (3.1)$$

$$Phase_C = IFFT\left(FFT(IF_{sig}) \cdot Filter(f)\right) \cdot IFFT\left(FFT(IF_{ref}) \cdot Filter(f)\right)^* \quad (3.2)$$

$$Phase_{angle} = \arctan\left(\frac{imag(Phase_c)}{real(Phase_c)}\right) \quad (3.3)$$

The phase diagnostic provides information on the relative location, and fluctuation frequency of distance to locations of power reflection in the plasma. While this may be used for analysis of edge density fluctuations, the most useful aspect of the phase diagnostic is to indicate arcing in the antenna or pillbox window by observing a reduction in phase fluctuation frequency, discussed below in a later section.

3.2.1 High speed diode detector

Active feedback control to stabilize RF power and reduce power noise requires high bandwidth measurements of klystron power. In addition, fast response to power changes reduces the time delay between initiation and detection of an antenna or klystron arc, thereby reducing the amount of power dissipated into the antenna, and reducing sputtering onto the pillbox window. A high speed diode detector based on an HP33330b diode was designed to provide high bandwidth power measurement. Each diode has a ground loop isolator and is connected to an independent high speed amplifier powered by an isolated dc-dc converter. Amplifier channels are based on an analog devices AD828 OP amp calibrated to provide 1V output to a 50ohm load per 10mW input on the detector diode. A 100ohm resistor is placed in parallel with the detector diode to improve bandwidth, as show in **Figure 3.14**. The diode detector system has several HP33330b diodes mounted within a shielded RF enclosure, as shown in **Figure 3.15**.

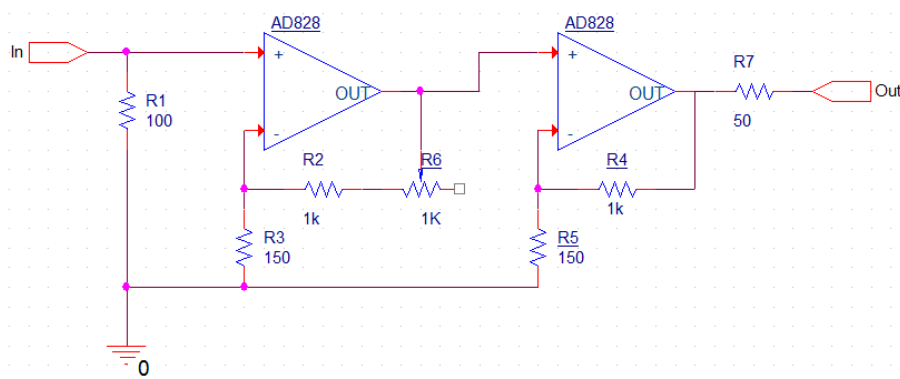


Figure 3.14. High speed diode power detector amplifier schematic.



Figure 3.15. High speed diode power detector amplifier board (left), and 4 channel power detector module (right).

Pulse measurements of a 10mW RF signal with 10 μ s rise time, shown in **Figure 3.16**, show a ~19ns delay between voltage waveforms on the diode and the output of the amplifier board. Including delay from the isolation amplifier, the total delay from an arc based power fluctuation to detection at the control/monitoring system is ~42ns, indicating the system achieves the rapid

pulse response time required to minimize energy dissipated in antenna arcs, and high bandwidth required for noise reduction.

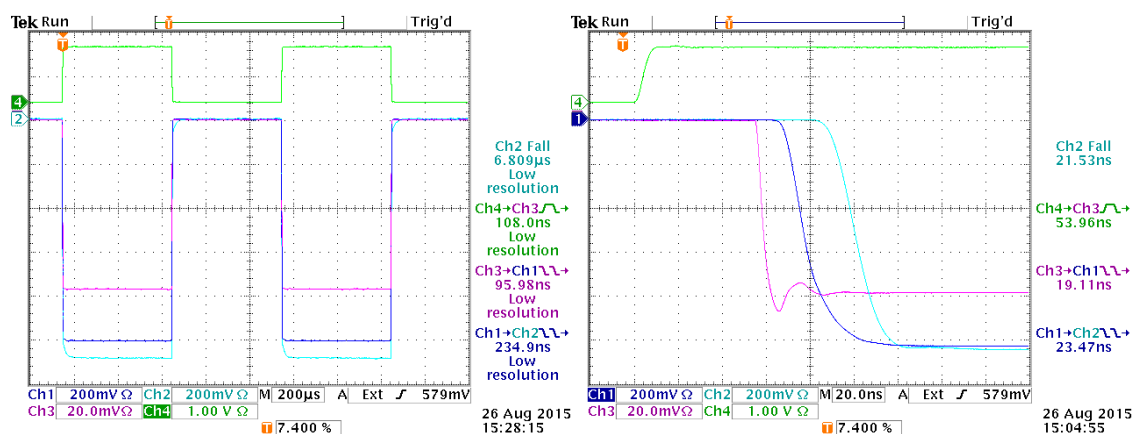


Figure 3.16. Test of pulse detection with fast diode power detector and isolation amplifier. Control signal (green) switches a fast RF pin diode switch. Voltage waveforms are monitored from an un-amplified diode detector (purple), the fast diode detection system with amplifier board (blue), and output of the isolation amplifier. The fast power detector amplifier board contributes 19ns delay to the monitoring system while the fast isolation amplifier contributes 23ns delay.

RF diodes provide a non-linear voltage response to RF power at high signal levels. Previous versions of power detectors operated the diodes in their linear region by placing ~70-90dB of attenuation before the diode detector, and significant amplification after the detector to raise the voltage to levels that can be digitized at acceptable resolution. While this method provides a power signal that is proportional to voltage, the high amplification required introduces significant noise to the measurement and cross-coupling between adjacent amplifier channels.

Subsequent analog noise filtering will further reduce measurement bandwidth but will not solve cross coupling, particularly evident in pickup of the IF frequency on the power channels.

The HP33330b diode used in the fast power detector has a 200mW maximum continuous power rating, allowing for substantial input power without damage. To simplify calibration of the detector system, a full scale power of 10mW was chosen to allow direct connection to the calibrated RF signal generator. Operation in non-linear mode greatly reduces noise pickup but requires calibration to determine power from measured voltage. A power sweep of the diode detector, shown in **Figure 3.17**, provides calibration of detector power by fitting a polynomial to the measured curve. Typical R^2 values for 3 and 5 term polynomials ranged from 0.9998-0.9999, indicating an excellent fit. Post processing of detector voltage signals in software is required to provide power measurements. The power feedback control system is able to directly accept an analog output from the diode power detection system since the non-linearity is minor and well behaved, allowing for stable control.

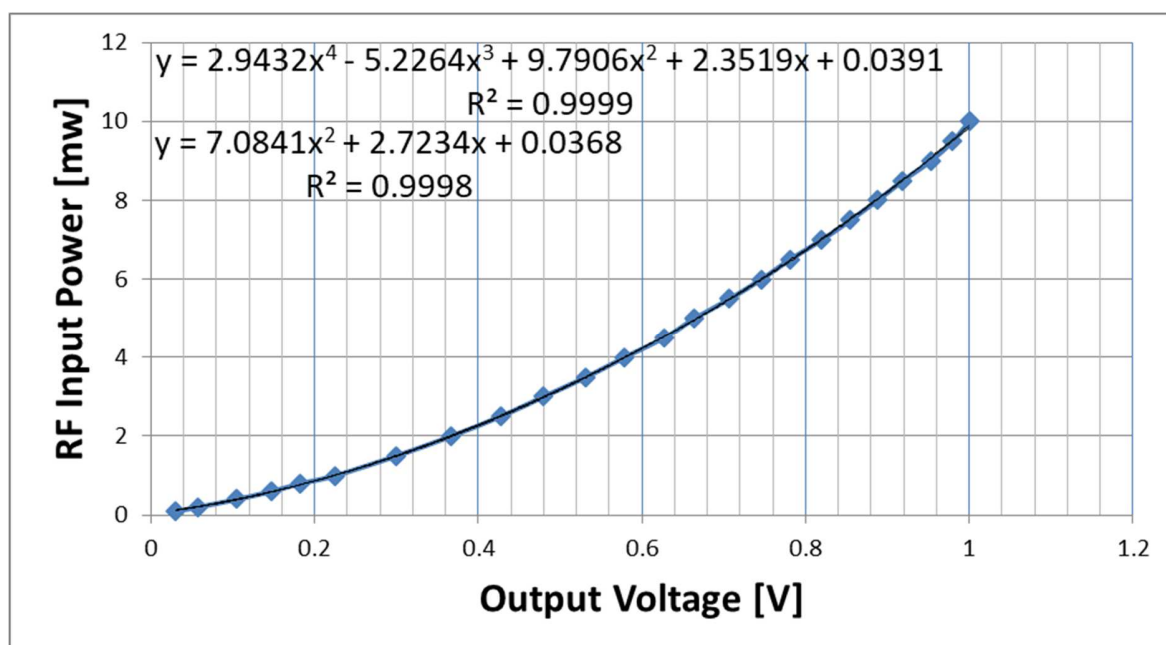


Figure 3.17. Power detector calibration curves and fitted equations.

3.2.2 Voltage variable attenuator

High speed control of klystron power is accomplished by inserting a voltage variable attenuator (VVA) between the RF signal generator and the TWT. The RF signal generator's automatic level control (ALC) cannot be controlled externally, and an internal high pass filter on the AM control input blocks DC level signals, inhibiting direct level feedback from inputs on the generator. Although the high voltage power supply driving the klystron tube compensates for voltage droop during the RF pulse, space charge depletion at the cathode causes power droop during the pulse and voltage ripple injects power noise on the tube output. A VVA allows for high speed control of an RF signal by attenuating power based on a voltage input. Unlike a mixer, a VVA has almost full scale dynamic range without signal distortion, allowing almost complete cutoff of RF power.

A Mini-Circuits HVA-73+ VVA was chosen as the attenuator in the power control system due to its ability to operate in the 5.5-7GHz range and provide up to 2dB to ~30dB attenuation with a control voltage under ~6V. A plot of typical attenuation as a function of voltage is presented in **Figure 3.18**, showing an inflection at ~1.2V. Operation of the attenuator with the feedback control system is preferable where attenuation is most linear, for voltages between 0.4-1.2V, however the steady state input voltage to the attenuator must be limited below 1.2V by a diode voltage clamp in parallel with the output to prevent the control system from jumping into a positive feedback region if the command voltage "jumps" over the peak of the attenuation curve.

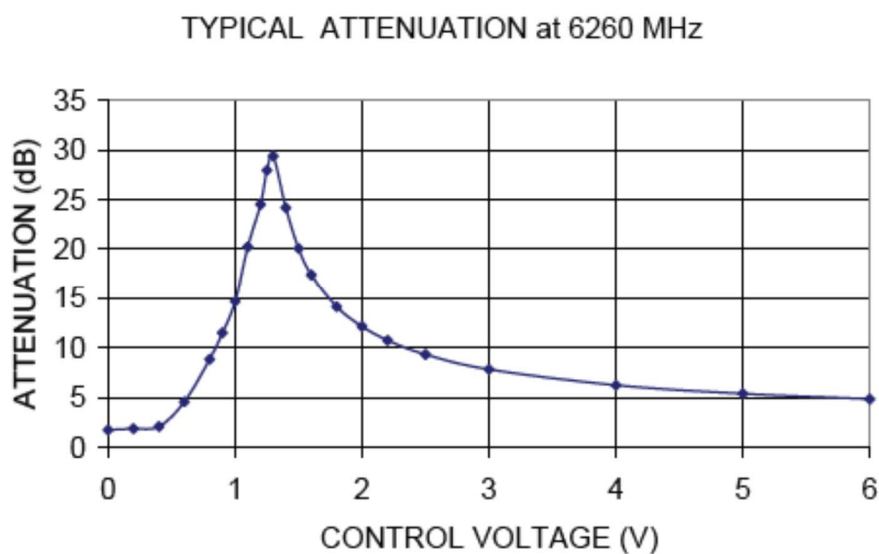


Figure 3.18. VVA typical attenuation vs voltage. Figure courtesy of Mini-Circuits.

Testing of the VVA modules provided a more accurate measurement of voltage levels corresponding to best control sensitivity. A voltage sweep on the input, shown in **Figure 3.19**, is plotted vs RF power detected on the output of the module. The highest control sensitivity occurs in the linear region between 0.4-0.8V input. In practice, the RF generator should be set to provide a power level that centers the voltage input to the VVA in the middle of the linear region so that the AGC loop achieves the maximum dynamic range of controllable power.

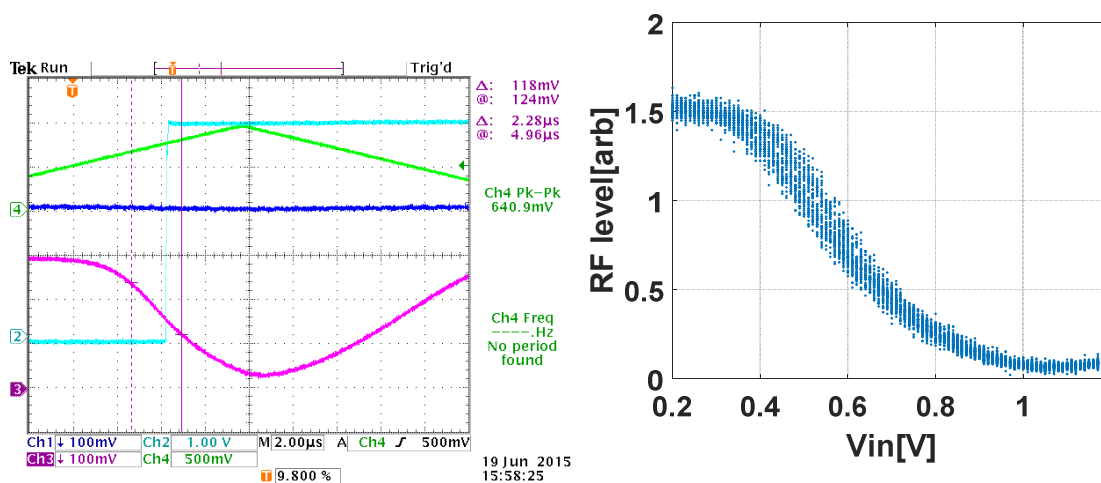


Figure 3.19. Sweep of voltage (green) vs RF power detected on the output (pink) is shown on the left. The resulting RF level data is plotted vs voltage for the range of interest (right) indicating best control sensitivity occurs between 0.4-0.8V input.

Testing of the frequency response of the voltage variable attenuator indicate a sharp roll off in gain starting at 100kHz, and a system bandwidth of ~300kHz. An input response compensation system, shown in **Figure 3.20**, is based on an analog devices AD826 OP amp tuned to provide a frequency response inverse to that of the VVA. Using the compensation circuit to drive the VVA extends the system bandwidth to 2MHz, as shown in **Figure 3.21**.

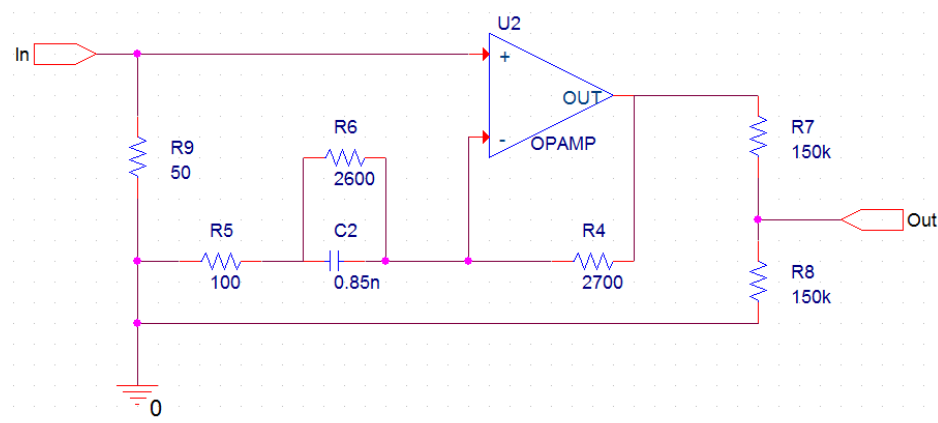


Figure 3.20. Frequency response compensation system for VVA. Circuit provides the inverse frequency response of the VVA, extending the system bandwidth to 2MHz.

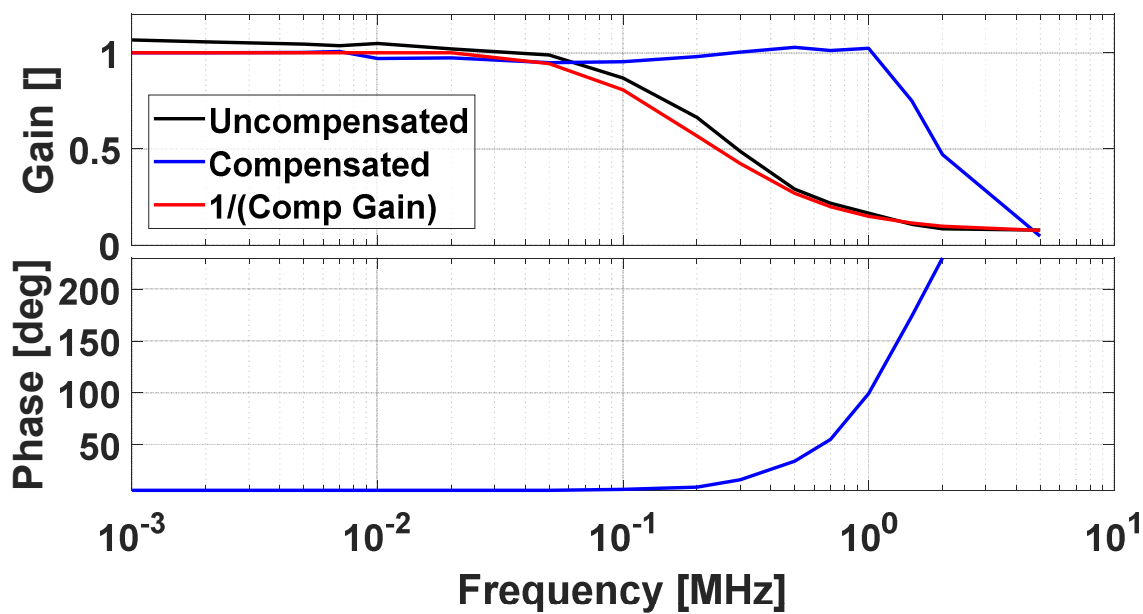


Figure 3.21. VVA frequency response with (blue) and without (black) input compensation provided by the driver board. Inverse of the gain of the compensation system (red) shows close match to the gain of the uncompensated attenuator. Phase between input and output is plotted for the compensated system.

Use of the compensation system shows a distinct improvement in the step response characteristics of the VVA, shown in **Figure 3.22**. Without the compensation system, the VVA responds with a slow exponential climb in power over several μs . Addition of the compensation system significantly improves the step response of the VVA, achieving a rise time on the order of 100ns.

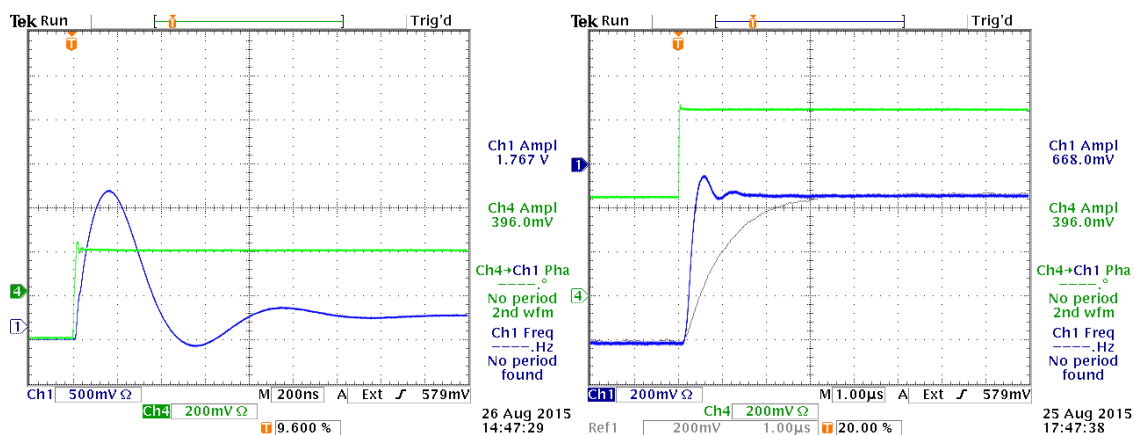


Figure 3.22. Voltage output of compensator circuit (blue) in response to a step in input voltage (green) is shown on the left. RF output power from VVA shown with (blue) and without (grey) use of the compensation system are plotted on the right in response to a step in input voltage (green).

The VVA system was packaged in an RF shielded box for noise immunity, as shown in **Figure 3.23**. The VVA modules were mounted within Mini Circuits TB-511+ test fixtures to convert the surface mount interface of the modules to SMA connectors. Two VVAs were mounted within the same box to allow testing of the AGC system with injection of simulated noise signals, as described in later sections.



Figure 3.23. VVA driver board(left) and assembled VVA system (right).

3.2.3 Klystron Power Feedback and Control

Gain of the klystron tube is strongly dependent on the energy and current of the electron beam in the tube. Droop and ripple of the input voltage waveform will create analogous droop and ripple on the output power of the tube. In addition, high frequency noise from switching harmonics will also generate power noise on the klystron output. Due to the use of a radar klystron designed for $\sim 18\mu\text{s}$ pulses at a 3-4ms pulse length, space charge depletion above the cathode, and potentially thermionic cooling of the cathode surface will reduce electron beam current even if input voltage is held constant. Increasing tube voltage during the pulse can partially compensate for this effect, however, significant increases in input voltage will cause tube arcing. A closed feedback loop monitoring forward power will form an automatic gain control (AGC) to stabilize RF power. A system with sufficiently high bandwidth will also reduce power noise. Additionally, use of an AGC system allows the EBW heating system to operate in a consistent and reliable manner, with predictable control of RF power level with negligible tuning by the operator during the run day. In practice, the power control system allowed almost automatic operation of the RF system with adjustments required only when intentionally changing power levels.

The AGC loop consists of a proportional-integral-derivative (PID) controller comparing forward power to a preset input level. Forward power is converted to an analog voltage by the high speed diode detector connected to the directional coupler and sent to the PID controller by the high speed isolator. The output of the PID controller returns through the high speed isolator

and drives the voltage variable attenuator (VVA) located between the RF signal generator and the TWT amplifier connected to the klystron input, closing the control loop. Windowing of the RF pulse is performed by a fast PIN diode RF switch located between the RF signal generator and the VVA, as a result the integrator in the control system winds up and brings the tube to full power for ~10 μ s during startup before the system stabilizes. This effect is not harmful to the tube or antenna, but is visible on both RF and x-ray diagnostics as a brief peak in power and x-ray production. Future designs of this system are recommended to include an anti-windup system to zero the integrator during periods where the RF power is turned off.

The PID system consists of a modified PID-X1 control board from ZAP Studio, as shown in **Figure 3.24**. The PID control system is driven by two inputs, a process variable (PV), in this case forward RF power, and a set point (SP), in this case the set RF power. A differential amplifier, U1A, generates an internal error signal, $VE=SP-PV$ that drives three separate amplifiers contributing proportional, integral, and derivative gain to the system. The proportional amplifier, U1B, generates an output proportional to the error voltage and is effective at canceling out high frequency noise as well as some of the power offset, however proportional feedback alone will produce a steady state offset. The integral gain amplifier, U2A, provides continuous accumulation of error voltage to force steady state error to zero. The derivative amplifier, U2B, provides additional damping by providing voltage feedback in opposition to any change in the error signal. The output of the three amplifiers feeds a summing amplifier, U3A that produces the output voltage VO to control the voltage variable attenuator. Resistor and capacitor values on the stock board, shown in the schematic, were modified and tuned for optimal performance. In

addition, the output was modified with a diode rectifier to pass only a positive output voltage within the operating limits of the VVA.

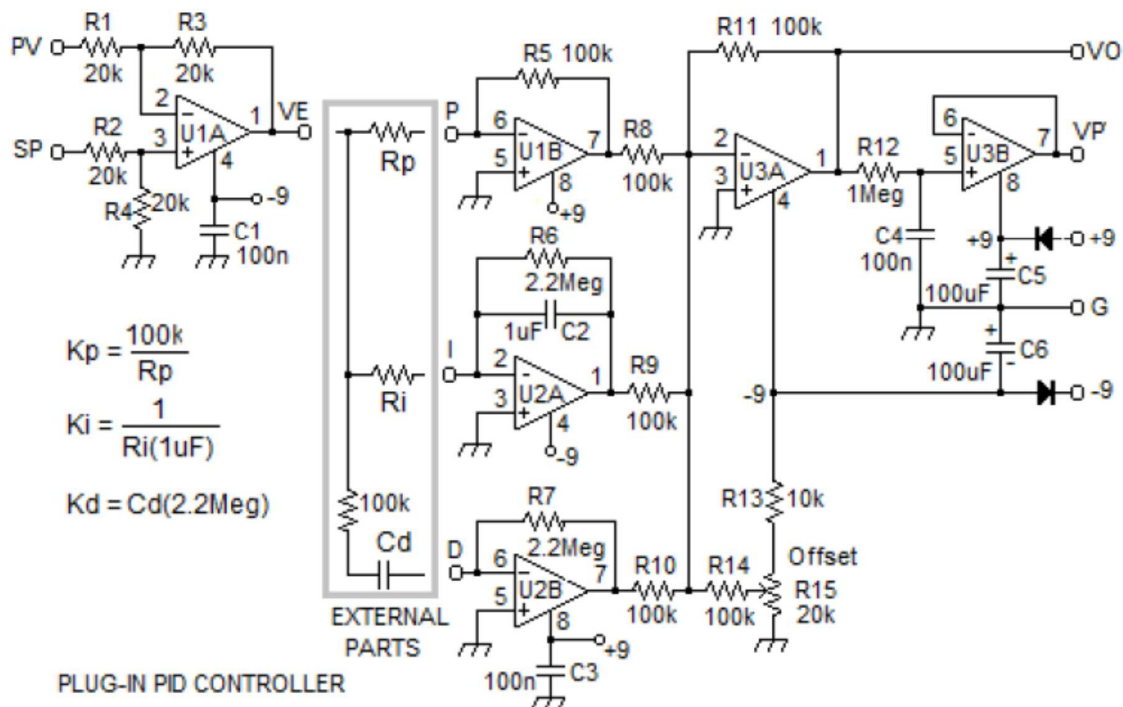


Figure 3.24. Schematic of PID-X1k control board, figure courtesy of manufacturer (www.zapstudio.com)

Bench testing of the AGC system used a simulated noise signal to verify system performance, as shown in **Figure 3.25**. A VVA injecting a 1MHz noise signal superimposed on a constant power output from a RF signal generator is placed in series with the AGC VVA before the high speed diode power detector which is connected to the PID controller through the high speed isolation amplifier. The second VVA injects a simulated noise signal which the ACG corrects by adjusting the VVA included in the AGC loop to null out the simulated noise signal,

as shown in **Figure 3.26**. Subsequent installation of the AGC system into the RF heating system produced similar results when controlling the klystron tube, shown in **Figure 3.27**, resulting in a significant improvement in power stability and power noise reduction.

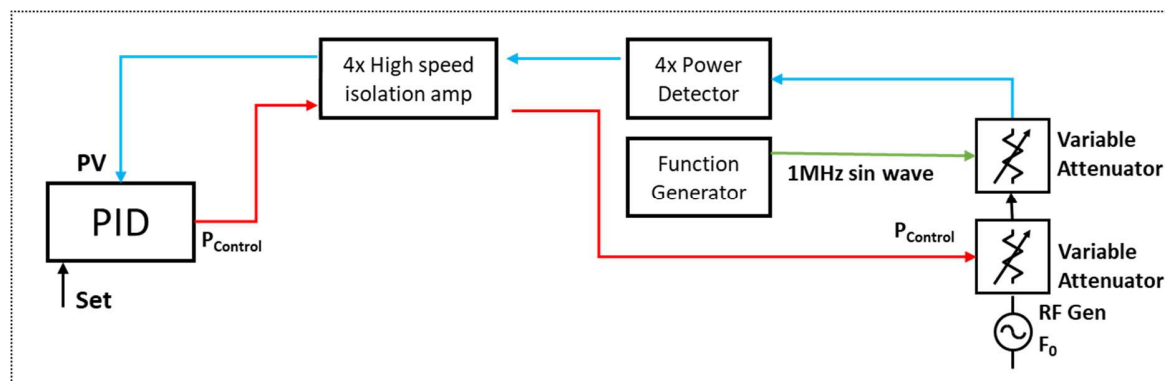


Figure 3.25. Bench test setup of the AGC system for verifying noise reduction and power control performance.

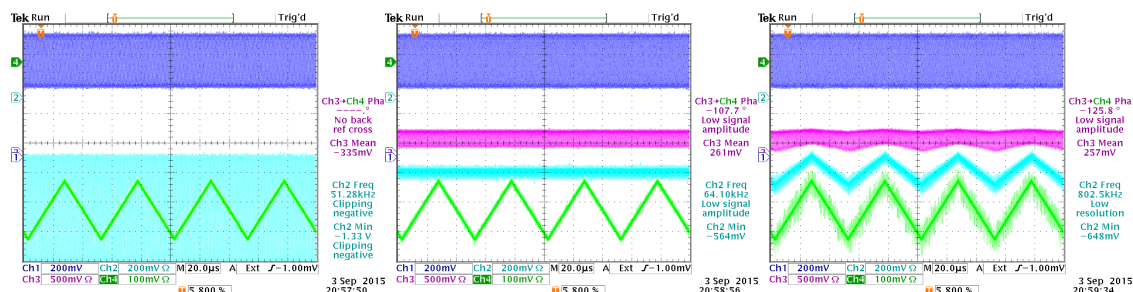


Figure 3.26. Modulation voltage (dark blue) to a second VVA in series with the output of an RF generator is switched at 1MHz producing a simulated 1MHz noise signal on the RF power signal (light blue). Without AGC control, power modulation is highly evident in the output (left), with AGC control a significant reduction in power noise is observed (center). Using the AGC system to track an external 20kHz power reference signal (green) allows control of output power level in

the the presence of external noise. Modulation signal to the VVA in the AGC loop is shown in pink.

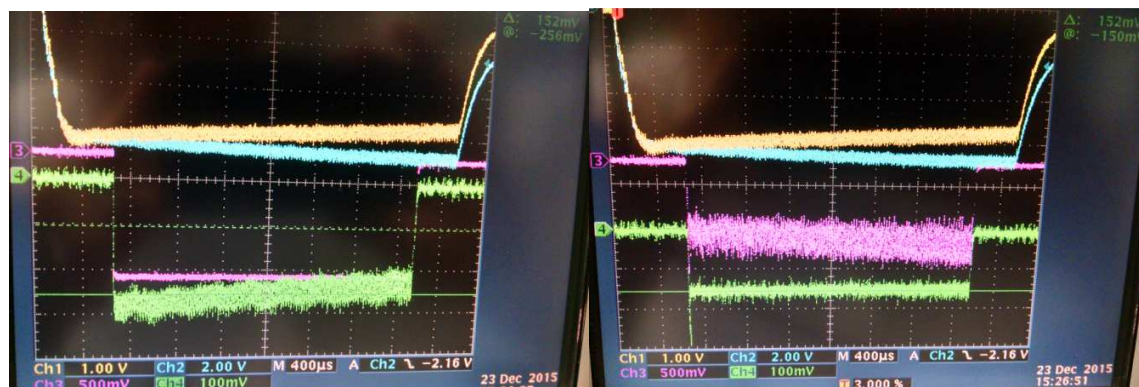


Figure 3.27. RF pulses without and with AGC operation. Klystron voltage (blue) and current (yellow) are identical between plots. Without the AGC system enabled (left), klystron power (green) shows distinct droop, ripple, and noise with a constant input power (pink). With the AGC enabled (right), klystron output power is stabilized at a constant level, and power noise is reduced. Note that the inverse of the droop, ripple and noise now appears in the input power to the tube (pink).

3.2.4 Antenna Arc Detection

Arcing may occur within the antenna or pillbox window when operating near the maximum power handling threshold. A high potential of arcing occurs when operating in large (~150mm) diameter portholes with a first harmonic launch as porthole field error introduces the second harmonic x-mode resonance within the antenna aperture. After arc initiation, a plasma discharge will form within the antenna, and will be sustained by the RF power flow. The arc may

propagate backwards into the pillbox window assembly, where sputtering of the metal walls onto the window, as shown in **Figure 3.28**, will increase reflection and degrade power handling of the window leading to more frequent window arcs on subsequent shots. Sputtering on windows was found to be worse on antenna designs where a boron nitride limiter cap was placed over the antenna aperture, than on antennas where the aperture was open to the plasma.



Figure 3.28. Metalization of a quartz window within the pillbox assembly. Sputtering is concentrated along the electric field component within the pillbox (left). Significant metalization (right) due to numerous sustained arcs degrades window transmission.

Sputtering on quartz windows may be cleaned with hydrochloric or phosphoric acid. Success of the cleaning attempt depends on the extent of the sputtering, and the type of metal sputtered onto the window. Antennas with both stainless steel and aluminum pillboxes were tested resulting in sputtering of both types on metal onto the quartz window. Resulting cleaning attempts achieved significantly more success in cleaning sputtered aluminum off of the window than cleaning of sputtered stainless steel. Windows cleaned from sputtered aluminum were successfully returned to service, while windows with stainless sputtering were un-recoverable by

acid based cleaning methods. Abrasive polishing of stainless sputtered windows with cerium oxide Baum may successfully clean the deposition, but this method was not attempted.

A sustained arc can be detected by three distinct methods, a decrease in measured reflected power as forward power is absorbed within the antenna or pillbox, a decrease in phase fluctuations between forward and reflected power, and optical emission of plasma generated within the pillbox. The first two signs, shown in **Figure 3.29**, occur simultaneously for arcs in both the antenna aperture and pillbox, while optical emission from the pillbox window will only occur if the arc initiates within or propagated back into the pillbox. The absorption of power within the antenna during an arc is additionally confirmed by the simultaneous termination of detection of RF heated fast electrons in the plasma, and emitted RF within MST as measured with a probe antenna.

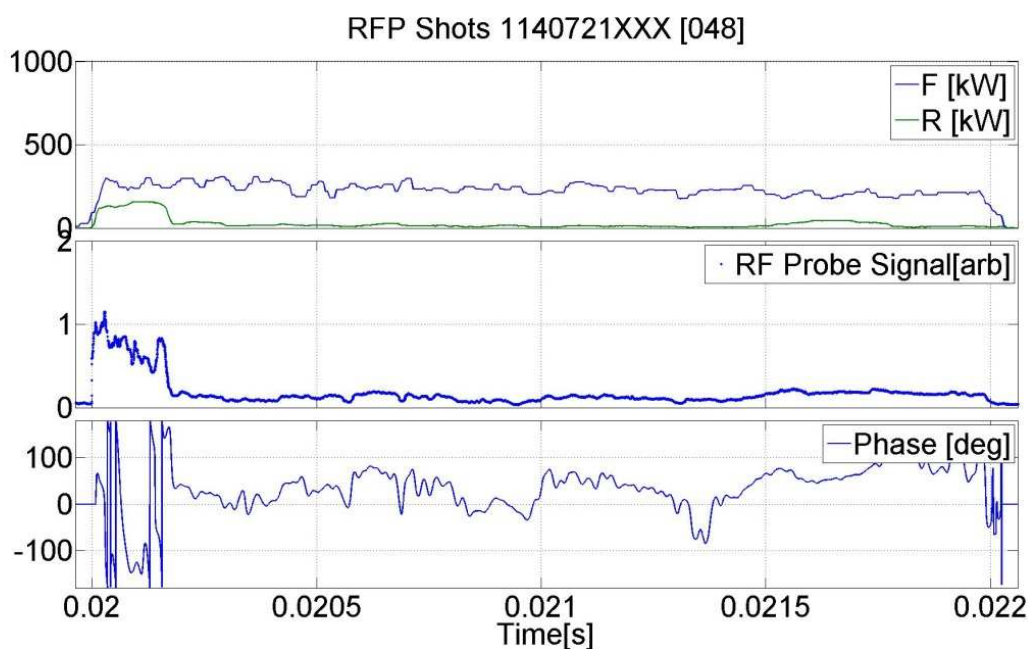


Figure 3.29. An arc occurs within the EBW antenna at ~20.2ms into the discharge. Reflected power drops from ~50% of forward power before the arc to under ~10% after the arc(top),

simultaneously RF power in the plasma measured by a receiving antenna near the heating antenna drops to zero (middle), and fluctuations in forward to reflected phase, shown greatly smoothed, significantly reduce in amplitude. The antenna arc is sustained over the remaining duration of the heating pulse.

Experimentally, the simplest method of implementing arc detection hardware is comparison between forward and reflected power measured from the antenna. A high speed comparator monitors the ratio between reflected and forward power and triggers a variable pulse width generator when the ratio falls below a set threshold. The pulse generator is set to shut down RF power to the antenna for a sufficient time for the arc to dissipate before resuming RF injection. An additional threshold circuit inhibits triggering of the pulse generator when forward power is below a set limit to prevent spurious triggering when forward power is low, or the RF system is turned off. The arc detector receives forward and reverse power measurements from the high speed diode detection system through the high speed isolator. Use of high speed detectors and isolators significantly reduced the delay between arc formation and triggering of the arc detector circuit, thereby reducing any damage caused by power dissipation in the antenna.

The arc detector circuit is mounted in an RF shielded box, as shown in **Figure 3.30**, allowing greater immunity to noise in the MST operating environment. The compact design allowed two such circuits to fit within the same enclosure, providing arc detection for both the klystron and the antenna. The arc detector was located within the MST control room, improving ease of tuning without opening the machine area and interrupting the shot cycle.

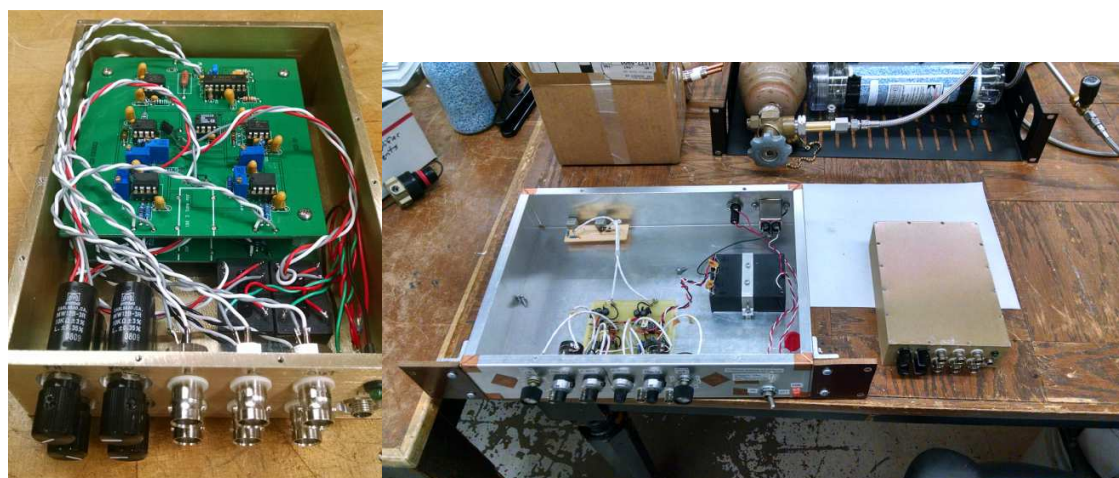


Figure 3.30. New arc detector system in shielded box for noise immunity(left). System contains two arc detection systems, one for the antenna and one for the klystron. Old arc detection system (right) mounted in a 19” rack case suffered from noise pickup issues and often generated false trigger events.

3.2.1 Optical Arc Detection

An antenna arc that propagates into the pillbox assembly is particularly damaging, as sputtered metal coats the quartz window. Optical techniques are used to monitor light generated by arcs within the pillbox assembly while rejecting scattered light from the plasma. A fiber optic cable connects to the air side of the pillbox window, shown in **Figure 3.31**, and couples arc generated light to a Hamamatsu H7828 photon counting head, containing an integrated power supply, photomultiplier tube (PMT), amplifier, comparater, and pulse shaper. The PMT head provides a consistant 30ns wide, 3.5V pulse, each time a photon is detected, greatly simplifying the optical front end of the detector. The fiber optic cable is aimed at the center of the quartz window at a grazing angle, such that the acceptance angle of the fiber preferentially accepts light

generated within the pillbox, while scattered photons generated by the plasma are statistically less likely to be coupled into the fiber. Optical attenuators are added to the PMT until any remaining light detection from the plasma is minimized, while still allowing light from arcs to be detected.



Figure 3.31. Fiber optic cable connecting PMT to pillbox window connects to a coupler that screws into the wall of the air side of the pillbox (left). The coupler compresses an o-ring between the pillbox and a quartz window, maintaining the integrity of the pressure seal when filling the waveguide with SF₆. The coupler is shown screwed into the pillbox window in the right.

Pulses generated by the PMT head are processed by an arc detector board, shown in **Figure 3.32**, that determines if an arc is occurring and generates a variable width blanking pulse to window off RF power. Pulses on pin 6 of an LM331N frequency to voltage converter trigger a charge pump that adds a fixed amount of charge to a capacitor on pin 1, adding a fixed increment of voltage. A resistor in parallel with the capacitor provides a negative exponential voltage

decay. An LM311 comparator generates a trigger signal to a pulse generator when capacitor voltage exceeds a fixed threshold.

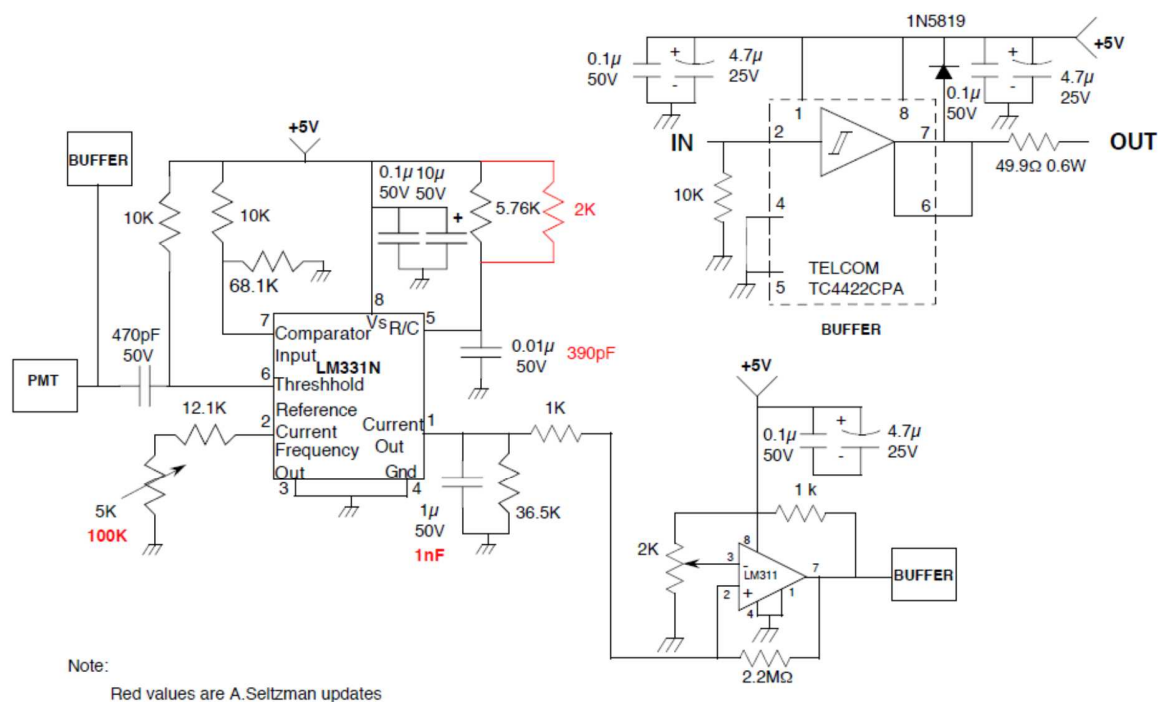


Figure 3.32. Optical arc detector schematic.

Testing of the arc detector circuit indicates response to an LED light source within $\sim 50\mu\text{s}$, as shown in **Figure 3.33**. In practice, the PMT system was installed to allow optical monitoring of pillbox window arcs, but not directly coupled to provide an RF blanking pulse. The system observed light generation due to arcs within the window when other signs of arcing, including low reflected power and reduction in phase fluctuation was present.

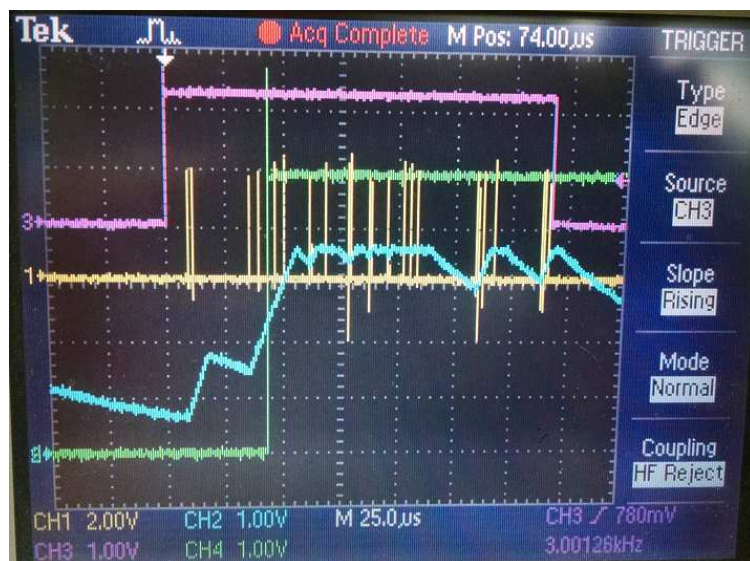


Figure 3.33. Optical arc detection test. An LED provides photons to a photomultiplier tube through an attenuator when voltage is applied (pink) simulating light emission from an arc. Photons are counted by the photomultiplier tube (yellow) triggering a charge pump that increases voltage on a capacitor (blue). When capacitor voltage exceeds a preset $\sim 2\text{V}$ level, a comparator triggers a pulse generator to inhibit RF output.

3.2.2 Klystron Arc Detection

At high output power arcing may occur within the klystron tube itself. Arcs typically occur within resonant cavity structure and propagate backwards toward the cathode where a high current arc will develop between the cathode and grounded tube body as the arc will dissipate the stored energy of the power supply filter capacitors. Repeated arcing will result in damage to the emissive surface of the thermionic cathode, resulting in lower output power as beam current decreases and reduced power stability. In the event of cathode damage, the emissive barium oxide coating may be replenished by running the tube filament at a higher than rated current to

diffuse new barium oxide to the surface of the cathode, however this method will reduce tube life, and should only be used if cathode damage has already occurred, as evident by current reduction at rated voltage or significant deviation from the tube's rated beam current vs filament voltage curve.

Cathode damage may be prevented by crowbaring the tube voltage before an arc that forms within the resonant cavities reaches the cathode. Due to interruption of the electron beam and/or generation of a dissipative plasma within the resonant cavity, tube gain will sharply decrease as the arc forms. A klystron arc detector system detects this change in gain by comparing the ratio of input and output power of the tube. Operation of the arc detector and crowbar spark gap is shown in **Figure 3.34**. Functionally, this circuit operates equivalently to the antenna arc detector, however the output is connected to the trigger circuit of a crowbar spark gap in parallel with the tube cathode.

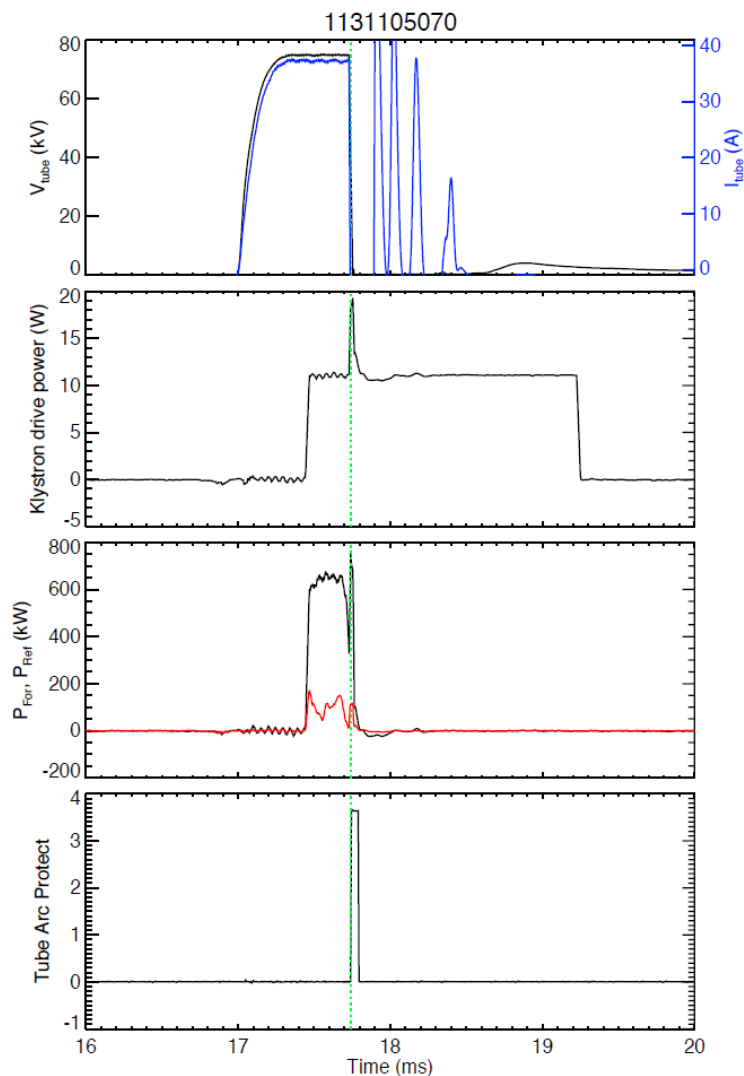


Figure 3.34. Operation of the klystron arc detector and crowbar sparkgap during a klystron arc. Shown in the top plot, klystron voltage(black) and current(blue) are crowbarred as the sparkgap fires. The lack of a sharp increase in klystron current indicates that the crowbar circuit successfully triggered before the arc reached the cathode. Measured klystron drive power shown in the second panel, marks the periods of commanded RF output; a brief pulse is likely due to

noise pickup during sparkgap operation. A significant drop in forward power, shown in black in the third panel, indicates the formation of an arc in a resonant cavity of the klystron. Triggering of the arc detection circuit is shown in the fourth panel, and marked with a dashed green line in all other panels in the figure.

3.3 High Voltage Pulsed Power Supply

A high voltage switched mode power supply (SMPS), shown in **Figure 3.35**, was designed and constructed to provide power to a klystron tube that requires a stable, low noise power source at approximately 78kV, 30A (varying between tubes) pulsed for 3-4ms. Unlike LC PFNs used on the previous EBW experiment, a SMPS allows greater control over pulse duration while allowing generation of longer duration pulses on the order of 3-4ms with constant output voltage by use of feedback regulation. Further documentation of this power supply may be found in [70].

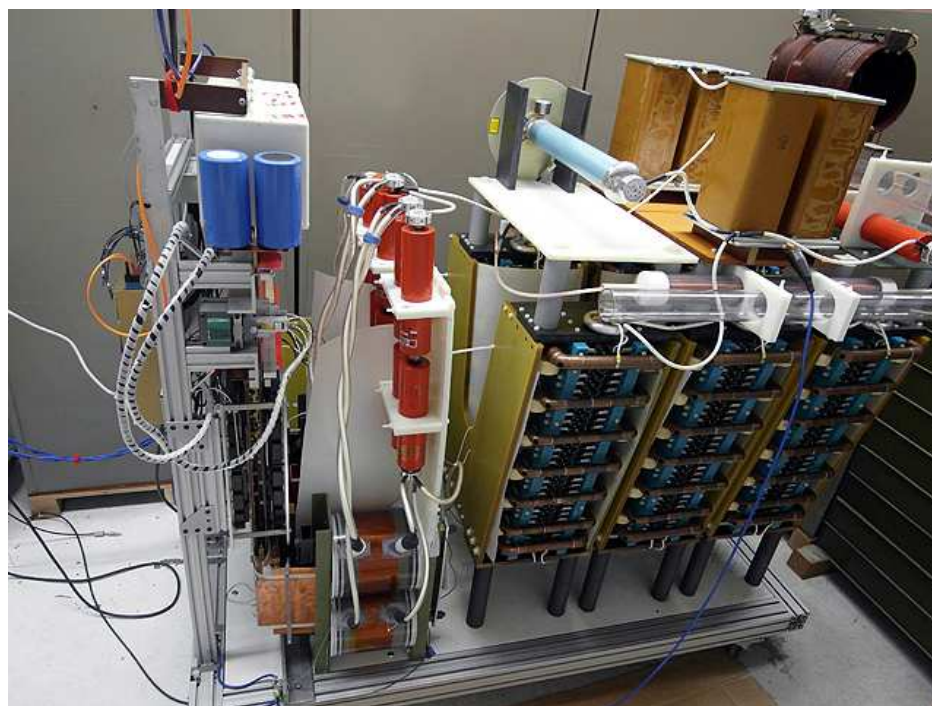


Figure 3.35. High voltage pulsed power supply.

The power supply was based off of a resonant transformer design [71], using a capacitor in parallel with the leakage inductance of a loosely coupled secondary winding to achieve a

voltage boost ratio significantly higher than the turns ratio as shown in **Figure 3.36**. The transformer has a nano-crystalline iron core to allow high power operation without saturation and to reduce core losses due to magnetic hysteresis and eddy currents. The secondary winding has a tuned air gap between the winding and core to provide a large privatized flux that forms a resonant circuit when placed in parallel with a capacitor. When excited by the primary near the resonant frequency, the boost ratio of the transformer significantly exceeds the turns ratio; in this case a transformer with a 13.6:1 turns ratio provides a 120:1 voltage boost.

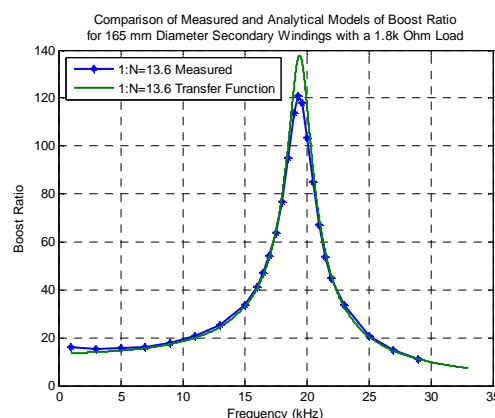


Figure 3.36. Resonant transformer without parallel capacitor attached is shown on the left. Voltage boost ratio as a function of frequency is compared to simulated performance on the right.

The resonant aspect of the transformer gives inherent protection to the klystron by de-Qing the resonator in the event of a klystron arc to limit fault current, reduces transformer size, and provides lower harmonics by providing a sinusoidal output voltage when driven by a square wave on the primary. By operating near the resonance, the current and voltage waveforms on the primary are nearly in phase, allowing the IGBTs to “soft switch”, e.g., turn on and off during

times of low current flow to reduce junction losses. Three transformers were connected in a three phase Y configuration feeding a voltage doubling rectifier, as shown in **Figure 3.37** and **Figure 3.38**. A resonant LC circuit in parallel with the output (not shown) provided further reduction of harmonics due to the rectifier on the DC output.

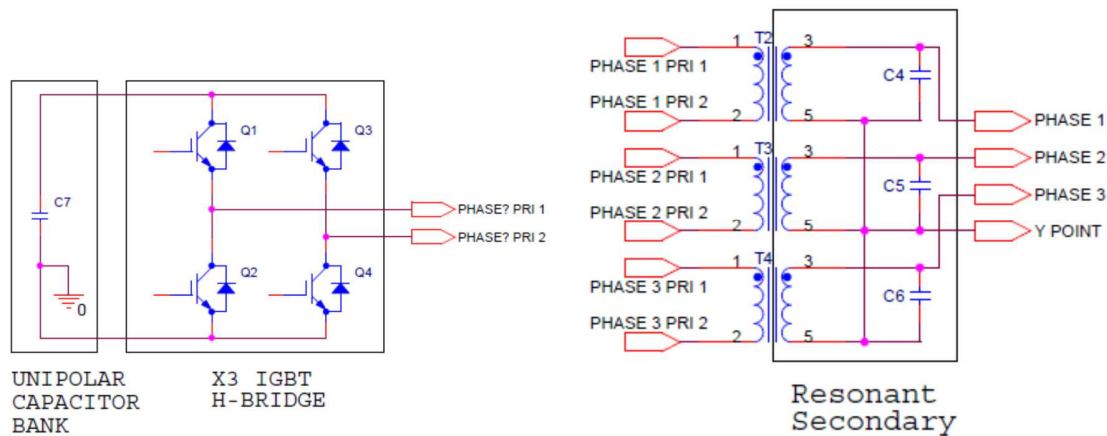


Figure 3.37. H-bridges (left) drive each of three resonant transformers (right) connected in a Y configuration

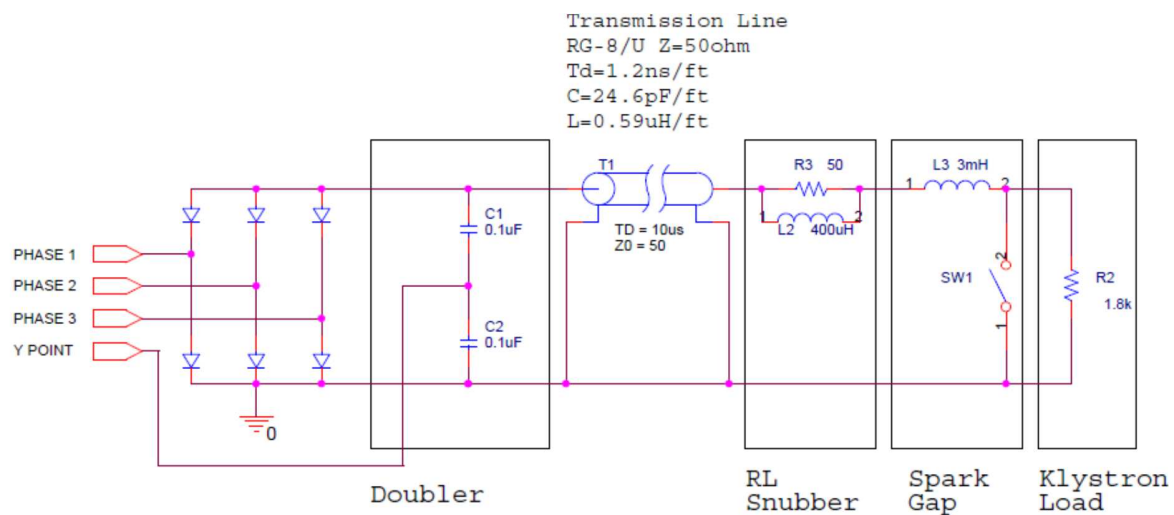


Figure 3.38. Schematic of voltage doubling rectifier, RL output snubber, and spark gap crowbar.

Each transformer was driven by an IGBT based H-bridge controlled by a dsPIC microcontroller and Altera MaxII complex programmable logic device (CPLD) over a fiber optic link. The microcontroller handled waveform generation and feedback control, while the CPLD handled fault monitoring of the IGBT gate drivers, I/O interfacing, and splitting the control signals from the microcontroller to the H-bridges. Due to the resonant nature of the transformer, voltage control was accomplished by frequency modulation of the square wave output from the H-bridges. By tuning towards the resonant frequency of the transformer, voltage boost ratio is increased, while tuning away from the resonant frequency reduced voltage output.

The supply was powered by a 900V electrolytic capacitor bank which drooped in voltage during pulse generation. Use of the frequency modulation control technique developed for this power supply allowed output voltage stabilization by compensating for capacitor bank voltage droop over the output pulse to provide a steady voltage to the klystron load, as shown in **Figure 3.39** left. Remaining ripple shown in **Figure 3.39** right, causes ripple in klystron power that is corrected by the AGC system.

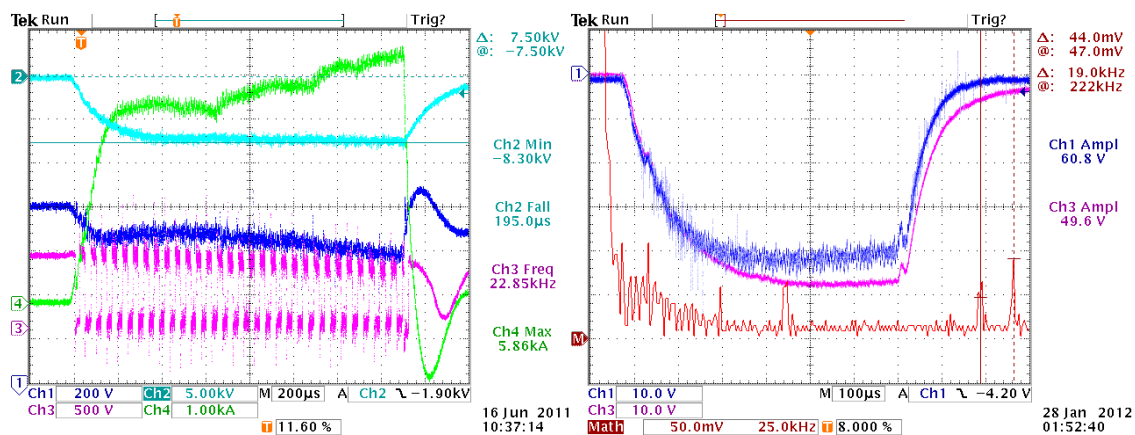


Figure 3.39. Stabilized voltage output (light blue) using feedback control to H-bridge tune switching frequency (pink) towards resonance as capacitor bank voltage (dark blue) droops

during the shot is shown plotted on the left. Generation of $\sim 120\text{kHz}$ 6th harmonic ripple on the output voltage (blue) is shown in the FFT (red) on the right.

3.4 X-ray Diagnostics

3.4.1 X-ray emission from heated electrons

The primary diagnostic used in this experiment measures the intensity, spatial distribution, and spectrum of x-ray bremsstrahlung from EBW heated electrons. When a charged particle is accelerated, it will emit EM radiation. In this case this may occur when a heated electron collides with another electron, ion, impurity, or solid target. The emission rate is determined by the probability that a heated electron interacts by scattering, given by (3.4) where n_b is the bulk density, σ is the interaction cross section, and δ is the distance traveled in a time interval.

$$P = n_b \sigma \delta \quad (3.4)$$

Emission from solid target bremsstrahlung will produce significantly more intensity than free-free emission since emission rate scales with target density. Bremsstrahlung process can be divided into two processes. The first is thin target bremsstrahlung, where electrons are scattered but do not come to rest, typical of a plasma. The second process is thick target bremsstrahlung, where electrons are considered to come to a complete rest. This is typical of emission from accelerated electrons colliding with a solid target such as a probe or limiter. The intensity(3.5) or number flux(3.6) vs. energy relation for thick target interaction is given by Kramer's formula [72], [73], with $K=1.68E-6[\text{keV}^{-1}]$, Z the atomic number of the target, and α a constant.

$$I = KZ (E_e - E_{x\text{-ray}})^\alpha \quad E_{x\text{-ray}} < E_e \quad (3.5)$$

$$N = \frac{KZ}{E_{x\text{-ray}}} (E_e - E_{x\text{-ray}})^\alpha \quad E_{x\text{-ray}} < E_e \quad (3.6)$$

The fraction of total intensity of x-rays produced between E and ΔE [74] is given by(3.7), for target of atomic number Z, with empirically fitted constant G

$$\Delta I = GZ \frac{(E_0 - E)}{E} \Delta E \quad (3.7)$$

Further revisions to the thick target formula [75], [76] indicate improved modeling with (3.8) where $M=0.00599E_0+1.05$ and $B=-0.0322E_0$ where the electron energy is mono-energetic.

$$\Delta I = G \left(Z \frac{E_0 - E}{E} \right)^M e^B \Delta E \quad (3.8)$$

Numerical evaluation of bremsstrahlung spectra for electrons colliding with a molybdenum target are simulated for both mono-energetic and dual Gaussian distributions of impacting electron energies in (**Figure 3.40**). Further examination of bremsstrahlung produced by a non-mono-energetic electron distribution is plotted in (**Figure 3.40**) using two Gaussian distributions of different energy and intensity. This causes an observable change in slope of the bremsstrahlung spectrum at the location of the first Gaussian, however the spectrum remains monotonically decreasing. There is no distribution of non-relativistic electron energies that can produce a thick target bremsstrahlung spectrum with a local maxima in the multi-keV range. Low energy peaks in the $\sim 10\text{eV}$ range due to backscatter effects of low energy electrons are ignored since only energies $>5\text{keV}$ are recorded due to the HXR detector energy limitations.

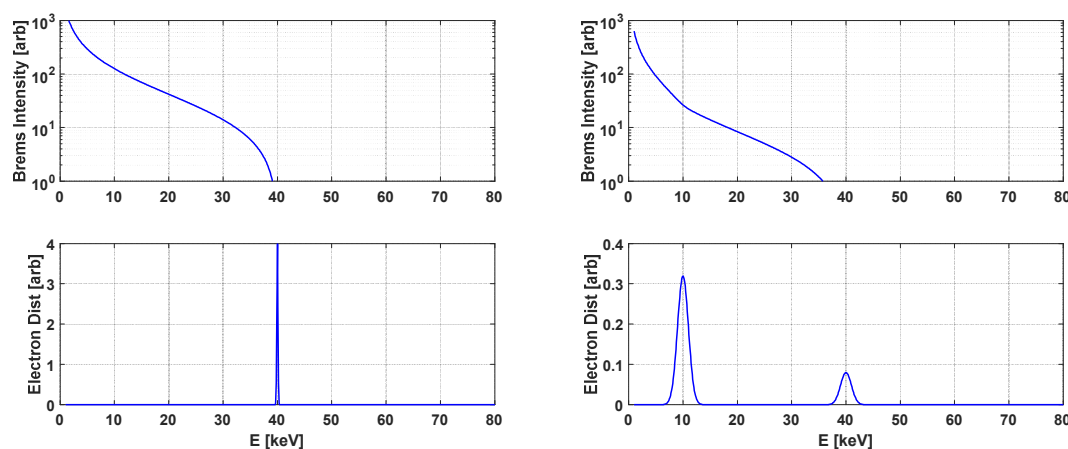


Figure 3.40. Bremsstrahlung spectrum from evaluation of Kramer's formula for electrons of mono-energetic(left) and dual gaussian(right) energy distributions colliding with a molybdenum target. Change in slope is noted at 10keV, however bremsstrahlung distribution remains monotonically decreasing with energy.

Multi-keV characteristic line radiation [77], [78] from K-alpha and K-beta emission from target materials are also of note. Materials of interest are boron and nitrogen used in BN ceramic, carbon used in limiter tiles, Al used in the MST shell, copper and molybdenum used in the LHCD antenna and target probes. Characteristic emission lines that fall into the energy range of the HXR detectors will appear as peaks superimposed over the bremsstrahlung continuum. Relevant emission energies and K edge threshold for line production are listed in (Table 3-1). Copper and molybdenum have K shell emission lines detectable by the HXR array.

Table 3-1: X-ray K edges and characteristic X-ray lines in keV

Z	El	Kedge	Kb2	KB1	KB3	Ka1	Ka2
5	B	0.188				0.183	
6	C	0.282				0.277	

7	N	0.397				0.393	
13	Al	1.562		1.557		1.487	1.486
29	Cu	8.993		8.905	8.903	8.048	8.028
42	Mo	20.002	19.960	19.608	19.590	17.479	17.374

Characteristic line widths [79], [80] listed in (**Table 3-2**) are much narrower than the 2keV energy resolution of the CdZnTe HXR detectors [81].

Table 3-2: Characteristic X-ray line widths in eV

Z	EI	KB2	KB1	KB3	Ka1	Ka2
29	Cu		5.84		2.40	2.98
42	Mo				6.42	6.66

In the absence of x-ray spectral lines, the bremsstrahlung spectrum may be used to determine the EEDF using iterative methods [82], [83]. The total x-ray flux may be calculated by the summation of the contributions of the individual energies of electrons striking a target. In integral form this is given by (3.9), where $I(E)$ is the x-ray flux at energy E , $EEDF(E_0)$ is the electron population at energy E_0 , and $I(E_0, E)$ is the x-ray flux given by Kramer's law at energy E due to monoenergetic electrons of energy E_0 . In summation notation, for finite bin width ΔE , the expression is (3.10) with Kramer's law in the form(3.11), with empirically fitted constant G .

$$I(E) = \int_0^{\infty} I(E_0, E) EEDF(E_0) dE_0 \quad (3.9)$$

$$I(E) = \sum_{\substack{E_0 = E_{\min} \\ \text{step} = \Delta E}}^{E_{\max}} I(E_0, E) EEDF(E_0) \quad (3.10)$$

$$I(E_0, E) = GZ \frac{(E_0 - E)}{E} \Delta E \quad (3.11)$$

A numerical solver may be constructed on this basis of inverting this expression, noting that at any given energy, the bremsstrahlung intensity at that point is only dependent on incident electrons of higher energy. The contribution to the bremsstrahlung spectrum at energy E , for electrons in bin $bin = [E, E - \Delta E]$ is given by (3.12)

$$I(E_0, E) = \lim_{E \rightarrow E_0 - \Delta E} GZ \frac{(E_0 - E)}{E} \Delta E \approx \frac{GZ}{E} (\Delta E)^2 \quad (3.12)$$

The population of electrons in a given bin may approximately be given by (3.13)

$$EEDF(E)_{bin=\Delta E} = \Delta I(E)_{bin=\Delta E} \frac{E}{GZ(\Delta E)^2} \quad (3.13)$$

Where ΔI is the difference between the measured bremsstrahlung spectrum at E and the contributions from the bremsstrahlung spectrum generated by the EEDF with energy $>E$

$$\Delta I(E)_{bin=\Delta E} = I(E)_{measured} - \sum_{\substack{E_0=E \\ step=\Delta E}}^{E_{max}} I(E_0, E) EEDF(E_0) \quad (3.14)$$

Iteratively stepping down from the highest energy and progressively filling the energy bins in the EEDF from high to low will reconstruct the EEDF spectrum generating the measured bremsstrahlung emission. This method of reconstruction works well for bremsstrahlung spectra that are smooth functions, where the generating EEDF is analytic. Non-analytic EEDFs and bremsstrahlung spectrums that are not smooth will generate artifacts on the reconstructed EEDF (**Figure 3.41**).

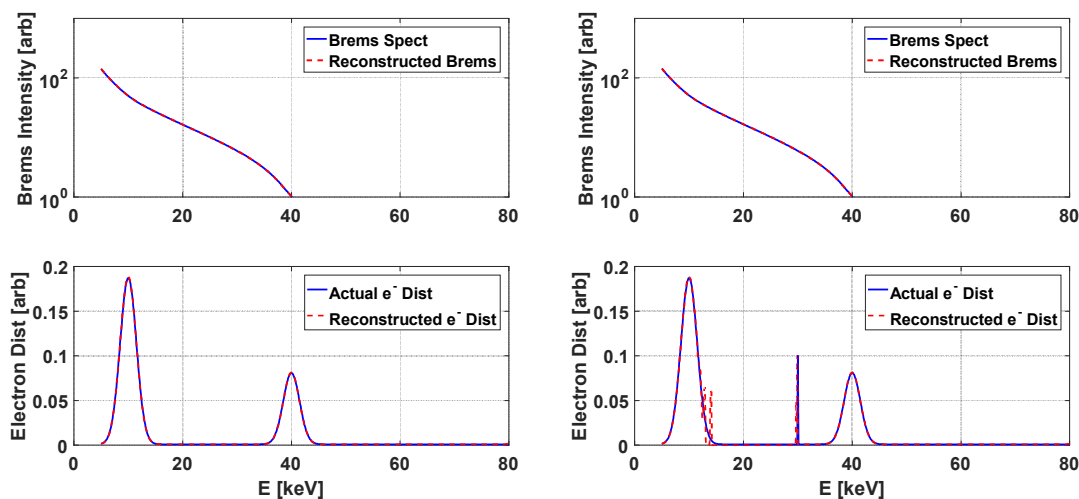


Figure 3.41. EEDF reconstruction from a bremsstrahlung spectrum produced by analytic EEDF functions showing exact reconstruction of EEDF(left), and reconstruction of non-analytic EEDF functions showing artifacts in the reconstructed EEDF (right).

In actual measurements which will be shown in chapter 4, individual x-ray counts are binned by energy into a histogram which is used to reconstruct the measured spectrum. At low energies where quantization of x-ray counts generates a non-monotonic spectrum with local maxima (eg. there will be “bumps” in the measurement due to binning effects), the iterative algorithm will generate a reconstructed bremsstrahlung spectrum that slightly over-estimates the emission on the high energy tail, though the fit is a good match to measured bremsstrahlung spectrum. In practice, applying a smoothing filter to the measured bremsstrahlung spectrum, adding damping to the numerical solver, and placing a single point of high energy electrons above the measured spectrum improve results.

3.4.2 X-ray absorption and filtering

Careful selection of filter thickness on the HXR detectors allows suppression of low energy PPCD background avoiding saturation by sub 10keV energy photons in highly emissive PPCD target plasmas [84] while transmitting higher energy photons in the 10keV-80keV+ range generated by EBW heating. X-rays generated by target bremsstrahlung first pass through the plasma over the diameter of MST, subsequently exiting the machine through a 150 μ m Beryllium vacuum window. The x-rays then pass through a 50mm air gap within a lead collimator assembly before entering the detector. Optional filters of varying thickness and material may be added to the x-ray path. Energy dependent attenuation of emitted HXR must be calculated for accurate HXR spectrum measurements.

Attenuation of HXR in the energy range of interest of the EBW experiment is negligible. The mass density of the deuterium in the plasma is calculated using the atomic mass of deuterium and the line integrated plasma density with(3.15). The mass density is used to calculate the x-ray attenuation [85] over the minor diameter of MST (1.04m) given the x-ray mass attenuation coefficient (μ) of hydrogen [86]. At the minimum 5keV detectable energy on the HXR detectors, the absorption coefficient (3.16) is found to be one part in 1E-9.

$$\rho_D [g / cm^3] = \frac{m_{D,AU} [g / mol] n_e [cm^{-3}]}{N_A [mol^{-1}]} = \frac{2 \times 1E13}{6.02E23} = 3.3E-11 [g / cm^3] \quad (3.15)$$

$$\frac{I}{I_0} = T = 1 - A = e^{-\mu\rho L} = e^{-0.42 \times 3.3e-11 \times 104} \approx 1 \quad (3.16)$$

Attenuation of the 150 μ m beryllium x-ray windows has a noticeable effect at lower energies. X-ray attenuation coefficients for beryllium are found in [87], [88] for energies from 5keV-

30keV, and in [89] for energies over 30keV. The transmission for a 150um beryllium window with and without the addition of a 200um aluminum filter is plotted in (**Figure 3.42**) taking into consideration the absorption of the air gap in the x-ray path. As seen in the plot, the addition of the aluminum filter significantly attenuates x-rays with energies less than 15keV; this filtering method is particularly useful in removing background x-rays generated by an ohmically heated PPCD discharge, from the higher energy x-rays generated by electrons heated by the EBW.

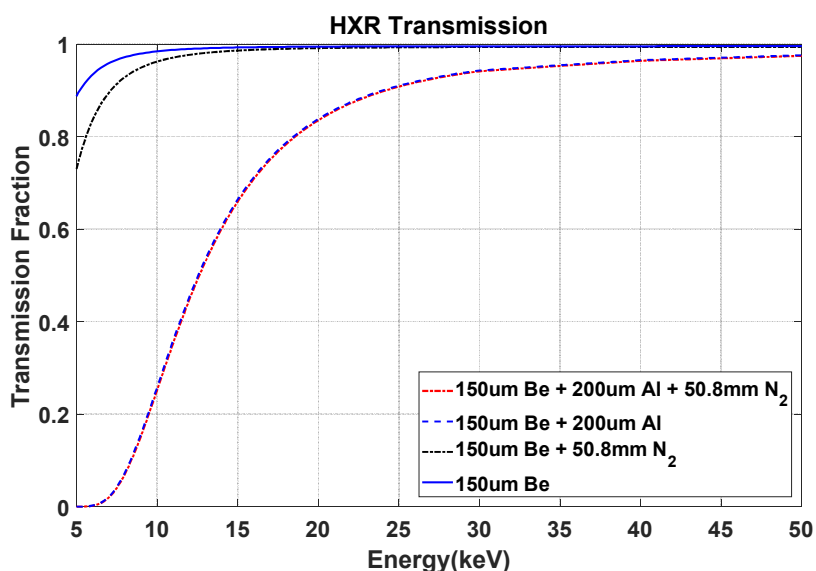


Figure 3.42. X-ray transmission for 150um beryllium x-ray window without air gap (blue, solid), with air gap (black, dashed), and for 150um beryllium window + 200um aluminum filter without air gap (blue, dashed) and with air gap (red, dashed).

3.4.1 HXR detection system

X-ray emission produced by target bremsstrahlung is detected by a set of single photon counting hard x-ray (HXR) detectors, shown in **Figure 3.43**. Detectors are located on the outer shell of MST, and observe x-ray bremsstrahlung from heated electrons colliding with

limiters and probes through beryllium vacuum windows. Each detector module has a cadmium-zinc-telluride crystal that provides a negative exponential voltage pulse proportional in amplitude to the absorbed x-ray photon energy.

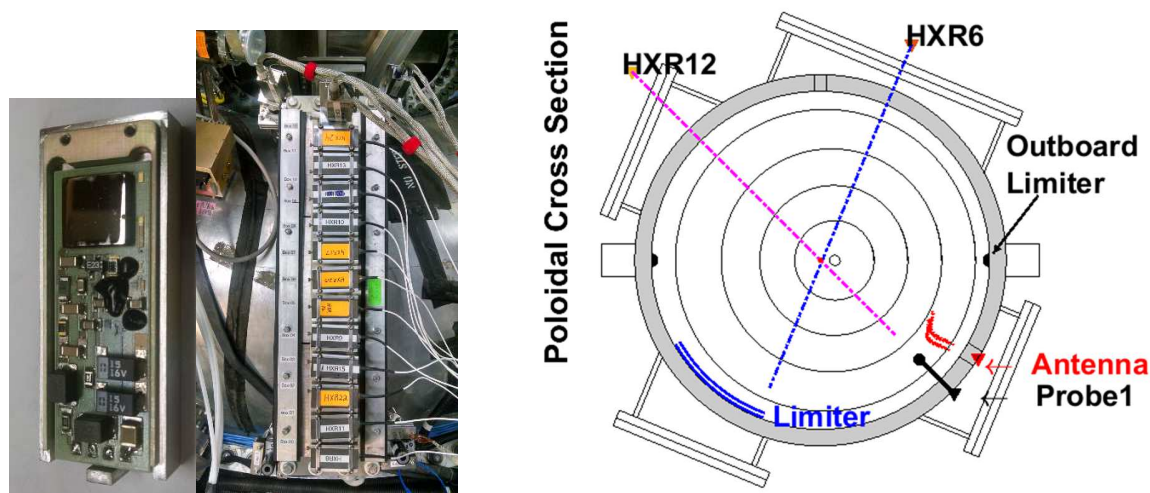


Figure 3.43. An HXR detector (left) showing the CdZnTe crystal. The radial array on MST consisting of multiple HXR detectors mounted on MST (middle). A poloidal cross section of MST (right) indicating potential locations of HXR detectors observing an insertable target probe (Probe1) and the LHCD antenna limiter (Limiter).

A Gaussian shaping amplifier reduces system noise and generates a well-defined peak with a zero dc baseline. The time resolution of the Gaussian pulse is on the order of the amplifier “shaping time”, analogous to the standard deviation of a Gaussian, therefore the full width half max (FWHM) of the Gaussian pulse is 2.4 times the shaping time [90], as given by (3.17).

$$FWHM = 2.4\tau_{shaping} \quad (3.17)$$

A Gaussian pulse from the shaping amplifier output is shown in **Figure 3.44**, with a FWHM of $\sim 1\mu\text{s}$ indicating that the shaping time of the detector is on the order of $\sim 400\text{ns}$. The time

resolution of the detector system is on the order of the shaping time of the Gaussian amplifier indicating that binning of x-ray signals should be on the order of 400ns.

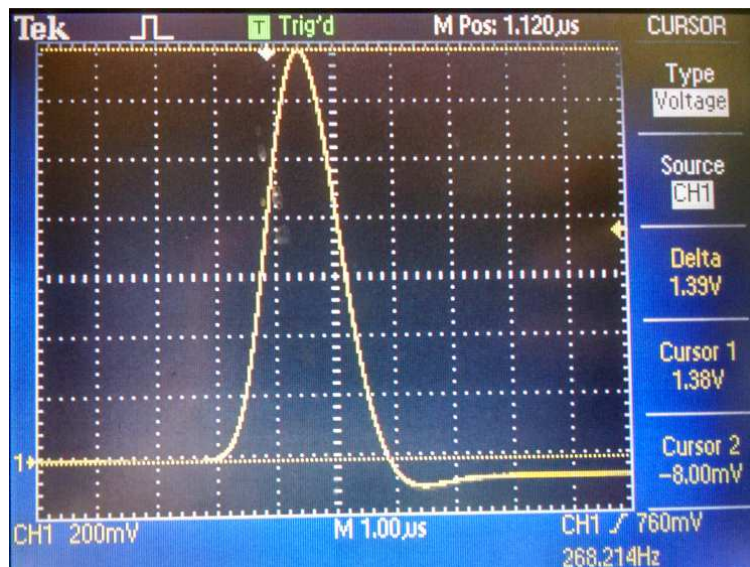


Figure 3.44. Gaussian pulse output from HXR detector for an Am241 gamma ray at 59.54keV.

3.4.1 Target probe system

A target probe is utilized to measure heated electron profiles within the plasma. The target probe consists of a 25.4mm diameter, 25.4mm length molybdenum cylinder on the tip of a boron nitride shielded copper rod. The probe is mounted at various toroidal locations around the machine in direct view of a diametrically opposed HXR detector observing target bremsstrahlung generated when heated electrons strike the molybdenum tip. The probe is scanned radially by adjusting the copper rod through a differentially pumped sliding seal. The target probe is able to operate at up to 12cm insertion depth past the inner wall in 300-400kA plasmas, however due to probe wear and outgassing at these currents, full depth scans are only performed at plasma

currents corresponding to second harmonic heating in the 200-300kA range. The target probe is mounted 162 degrees toroidally away from the EBW antenna on the outboard side. Although the probe is sensitive to both trapped and passing electrons, the higher diffusion rate of passing electrons (see CH4) as they travel to large toroidal displacements preferentially selects trapped electrons for detection by the probe.



Figure 3.45. Target probe tip including a 25mm diameter, 25mm length molybdenum cylinder and boron nitride shield surrounding adjustable length copper rod.

3.4.2 Lower Hybrid Antenna Limiter

HXR emission from EBW heated electrons striking a limiter is used to monitor the fraction of passing electrons generated in the plasma. Although the limiter would also be sensitive to deeply trapped electrons, CQL3D simulations indicate that the majority of EBW heated electrons are in the passing fraction. In close proximity to the heating antenna where the majority of passing electrons are not yet lost due to field stochasticity, the majority of detected emission from the limiter will be due to those passing electrons striking the limiter. The limiter, shown in **Figure 3.46**, was initially installed as part of a previous lower hybrid current drive

(LHCD) experiment, and is located on the inboard side of MST, displaced 12 degrees toroidally from the EBW antenna. The convenient location of the LHCD antenna, and ability to observe the surface with multiple HXR detectors motivated the choice of this particular diagnostic in the EBW experiment.

The sensitivity of diagnostic to edge absorption of the EBW allows accurate measurement of the transition between harmonics as indicated by a sharp increase in HXR emission from the LHCD antenna limiter. Further the larger surface area of the limiter, close proximity to the heating antenna, and greater visibility to multiple detectors provided a sensitive heating diagnostic, particularly at low RF power levels.



Figure 3.46. Lower hybrid antenna assembly including boron nitride limiter(white) and molybdenum interdigital straps(horizontal bars in center). Picture courtesy of John Goetz.

3.5 Summary

An rf system designed for EBW heating of the RFP has been constructed. A diverse set of hardware including a high voltage pulsed power supply, a klystron and RF support systems, a cylindrical launcher antenna, target probes observed by HXR detectors to generate a map of heated electron distributions, and a feedback control system was designed to reduce power noise on the klystron output and provide automatic power leveling in the presence to tube gain variation due to voltage ripple.

Improvements to previously used rf diagnostics were performed. Forward and reflected signals measured with a bidirectional coupler provided both amplitude feedback for power stabilization of the tube output, and phase information to allow measurement of plasma edge location. A high speed PID system (~10MHz bandwidth) controlling a voltage variable attenuator acted as an automatic gain controller for output power, compensating for variations in klystron gain caused by voltage fluctuations. The PID controller also reduced high frequency noise in RF power caused voltage ripple and harmonics from the power supply.

A cylindrical antenna was constructed out of molybdenum to allow direct insertion into the plasma edge without damage from direct exposure to plasma bombardment. The antenna system included a resonant pillbox window as a vacuum break with an optical arc detection system, and a rectangular to circular waveguide transition. The waveguide leading to the klystron RF source was pressurized with Sulphur hexafluoride to prevent arcing while allowing operation at a low fill pressure that would not overstress the pillbox window.

Due to Ohmic heating of the plasma being significantly higher than RF heating, a diagnostic specifically sensitive to the EBW heated electrons was developed to characterize

heated electron distributions by observing target bremsstrahlung from a distribution of insertable probes observed by x-ray detectors. This diagnostic allowed mapping of radial and toroidal spatial distributions of heated electrons, as well as the falloff time of heated electrons inside the LCFS. These results were critical in demonstrating the EBW propagates across and heats in a magnetic field that is either stochastic or has broken flux surfaces, and providing the ability to measure the EBW deposition location was controllable by varying plasma current, as will be shown in chapter 4.

The hardware developed for the EBW experiment was instrumental in providing an experimental platform that operated in a reliable and reproducible manner. Optimization of the power supply and RF hardware provided a stable RF pulse of consistent power and reduced the probability of antenna arcing. Development of the target probe diagnostic was critical in understanding the heated electron distributions in the presence of an ohmically heated background.

Chapter 4 EBW Heating Results in MST

This chapter presents the first observation of RF heating in the RFP using the EBW. In MST, the density and magnetic field place the electromagnetic cutoff within the first few cm of the edge around the entire plasma volume. This characteristic is one of the main obstacles of RF heating and current drive in the RFP. This thesis demonstrates EBW heating by production of RF heated electrons inside the electromagnetic cutoff surface. Deposition location is controlled by I_p and the resulting toroidal and radial distributions of heated electrons are measured. EBW damping occurs in locations in agreement with analytical estimates of the Doppler shifted resonance location.

Measurement of EBW heated electrons in the RFP is a challenging task due to limitations on net launched RF power ($\sim 80\text{kW}$) imposed by the antenna structure, and the large Ohmic heating power ($\sim 2\text{MW}$) in the RFP. EBW heating does not change the bulk plasma temperature a measurable amount. Additionally the intensity of free-free bremsstrahlung emission from EBW heated electrons in the plasma is not distinguishable from background emission. Novel probing techniques utilizing thick target bremsstrahlung from a spatial distribution of insertable probes and limiters were developed to measure the EBW heating location. Both probes and limiters were monitored with single photon counting hard x-ray detectors allowing bremsstrahlung measurements with precise time and energy resolution. A molybdenum tipped target probe was radially scanned from the wall to 10cm insertion depth to map heated electron radial profiles.

Observation of heated electron bremsstrahlung from an inboard limiter shielding a lower hybrid antenna allowed measurement of both edge electrons, and separate measurements of passing and trapped electrons. Integration of both probe and limiter data was used to reconstruct the average deposition position of the EBW which was then compared to analytical models. Heating with an RF pulse train allowed measurement of electron confinement times for both passing and trapped electron fractions confirming EBW propagation and heating in a magnetic field that is either stochastic or has broken flux surfaces. Confinement time measurements at different probe radial positions between 0 and 10cm insertion depth for standard and PPCD plasmas allow an inference of stochastic field reduction during PPCD.

4.1 Coupling and Mode Conversion at the UH Layer

4.1.1 Measurement of mode conversion to the EBW

Direct measurement of the mode conversion process to the EBW in the low GHz range (3.6-5.5GHz) [20],[27], have been reproduced in the RFP. An insertable probe (**Figure 4.1**) mounted on an articulated arm contains dipole and loop antennas capable of detecting electric field components parallel and perpendicular to wave propagation is radially scanned in the antenna near field at signal level power during a 3.6GHz x-mode launch. Measurements indicate that as the X-mode wave crosses the UHR, the electric field component parallel to propagation, $E_{\parallel k}$, increases, while the perpendicular component decreases (**Figure 4.2**) as predicted by the CPDR. As E_r/E_ϕ approached infinity, mode conversion to the EBW occurs. The depth of $E_{\parallel k}$ increase is located at ~ 1.5 cm from the edge, corresponding to the location of the UH layer. The toroidal limiter, extending 1.2cm past the wall, produces a steep edge density gradient at this location. At increasing depth, the EBW wavelength is too small to detect with the probe resulting in zero measured signal. This measurement provides additional verification of the expected behavior of the launched X-mode wave electric field polarizations as it crosses the UH layer.

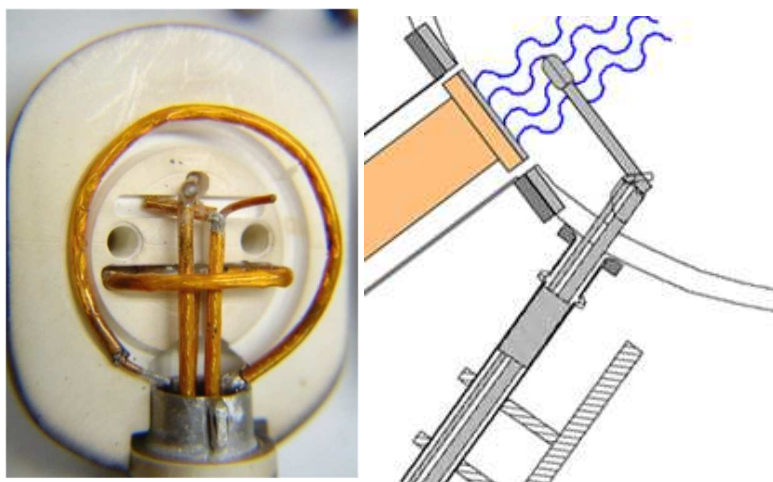


Figure 4.1. Insertable RF probe head showing two crossed dipole antennas and two crossed magnetic loops (left). Diagram of insertable probe positioned in front of 3.6GHz antenna (right).

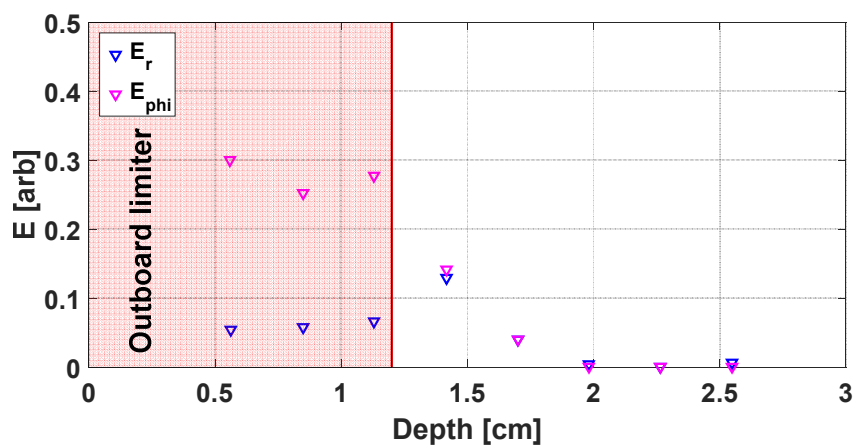


Figure 4.2. Insertable RF probe data for electric field perpendicular to propagation, E_{ϕ} , and parallel to propagation, E_r , shows a shift in wave polarization from perpendicular to parallel to the propagation direction as the X-mode wave crosses the UH layer, located ~ 1.5 cm from the wall. Measured field components go to zero past the UH layer as the EBW wavelength is too small to be detected by the probe.

4.1.1 Coupling efficiency to the EBW

Measurements of coupling efficiency over a range of plasma current indicated that the best coupling occurs for first harmonic resonance (**Figure 4.3**), with the fraction of launched power, Net/Forward, reaching as high at 90%. Coupling decreases to ~50% as I_p decreases down to the 5th harmonic absorption, and then slowly increases up to ~60% towards the 11th harmonic absorption. XB launch was found to have significantly better coupling than OXB launch. It is noted that the absorption location at a given harmonic does not affect coupling, as there is no repetitive structure over the I_p values leading to a given harmonic absorption, rather, there is a smooth variation in coupling across all harmonics, with no jump in coupling when crossing from one harmonic to the next.

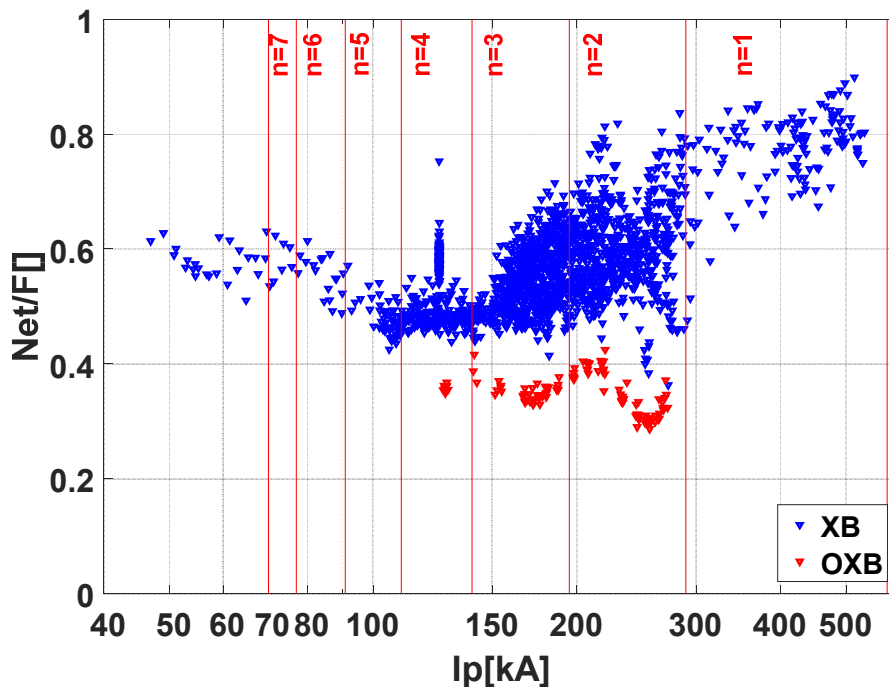


Figure 4.3. Net launched RF power vs forward power for plasma currents between 1st and 11th harmonic. Net launched power is highest for first harmonic absorption and decreases up to the 5th harmonic, then increases slightly up to the 11th harmonic. Significantly better coupling occurs for XB launch(blue) than for OXB launch(red). Harmonic jumps marked with red lines.

4.1.2 Heating non-linearity with RF power

Measurement of HXR flux from the LHCD antenna during third harmonic EBW heating were used to examine the dependency between net RF power launched into the plasma and heated electron intensity. Net power is defined as forward minus reflected in the waveguide feeding the antenna, and represents the total power exiting the antenna, not necessarily the amount mode converted to the EBW. The HXR emission from the LHCD antenna is taken to be proportional to the total power deposited in the plasma, though the spatial distribution may vary, e.g. only a fraction of the heated electrons may strike the limiter. An I_p scan over the peak LHCD emission location for third harmonic heating was conducted at several net power levels. Each measured intensity point is the area under the Gaussian fit of HXR flux from the LHCD antenna normalized to the net launched RF power. Intensity measurements show a non-linear relationship between HXR emission and launched power. A plot of the peak location at varying net RF showed both a non-linear increase in HXR emission, and a slight, but measurable shift in the peak location to higher plasma currents (**Figure 4.4**).

The amplitude of these curves is plotted vs net RF at constant I_p , better illustrating the non-linear nature of the power dependency (**Figure 4.5**). While non-linear at low power, the HXR flux eventually linearized at higher net RF power levels, particularly near the peak in emission. Away from the peak, emission requires higher net RF power before the relation

becomes linear. Use of a quadratic normalization of HXR flux to net RF power was found to significantly improve data correlation when compared to a linear normalization method (**Figure 4.6**). The assumption of non-linearity in heating depends on the measurement of HXR emission $>10\text{keV}$, it is possible that electron energy, and thus HXR emission, partially shifts below the detector noise floor at lower heating power giving the appearance of a non-linear dependence on power.

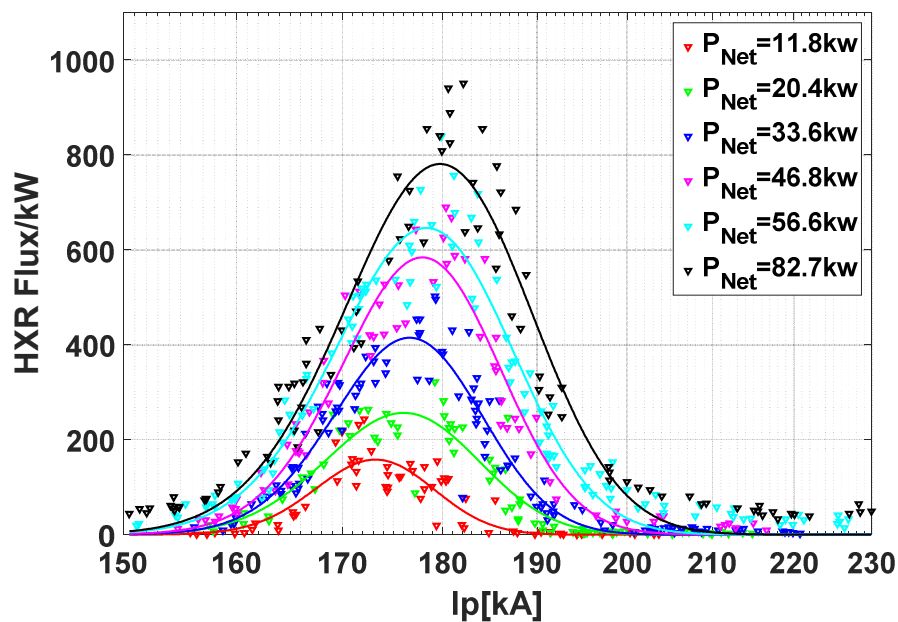


Figure 4.4. HXR flux from LHCD antenna per kW net launched power for third harmonic heating in standard plasmas at increasing power levels.

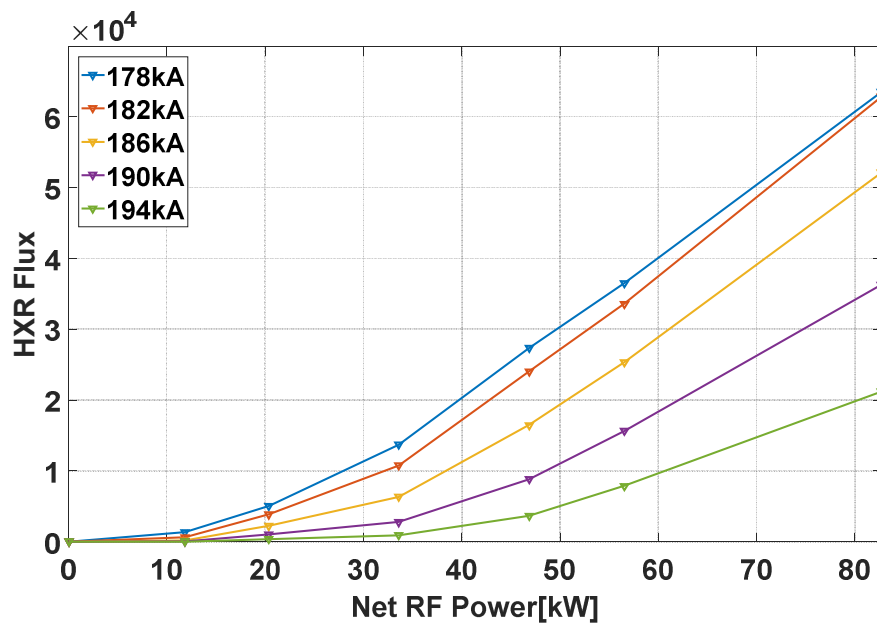


Figure 4.5. HXR flux from LHCD antenna for third harmonic heating in standard plasmas vs power level at various plasma currents.

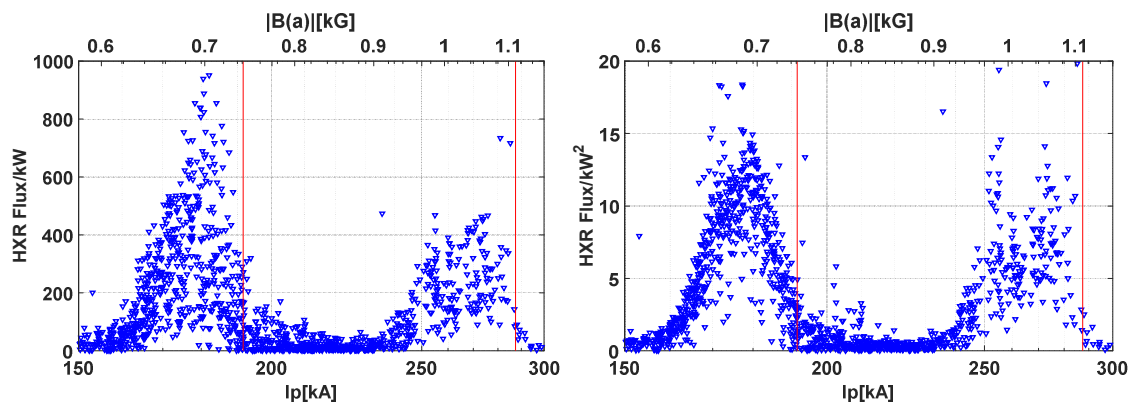


Figure 4.6. Grouping of emission data points normalized linearly by Flux/kW(left) and non-linearly by Flux/kW²(right). The non-linear normalization produces significantly closer grouping of data by modeling the non-linear dependence on HXR flux on net RF power.

4.2 EBW Heating and Accessibility in the RFP

Measurements of the radial distribution of heated electrons are used to examine the accessibility limits of EBW heating in the RFP, and I_p control of deposition location. Probe measurements at varying positions around the machine explore toroidal falloff of heated electrons due to radial diffusion as they drift around the machine. High harmonic EBW heating in the RFP is demonstrated and the coupling to net launched power over a plasma current scan is analyzed. Spectrum measurements in standard and PPCD plasma are presented, and the effects of PPCD operation are analyzed.

4.2.1 Radial deposition control of the EBW and accessibility limits.

A spatial distribution of solid targets with diametrically opposed x-ray detectors measures the dynamics of EBW-heated electrons. Target bremsstrahlung from the array of insertable molybdenum-tipped probes and fixed limiters is measured by energy resolved single photon counting HXR detectors [91] as shown in **Figure 4.7**. Target probes (example labeled P1) are positioned at several toroidally-displaced locations from the launch antenna. Trapped and passing electrons both play an important role in the heated distribution since a large EBW k_{\parallel} upshift [4] and absence of a high toroidal field side trap only a modest fraction. An inboard limiter displaced 12 degrees toroidally from launch (shown in blue) is used as a key diagnostic of electrons on passing orbits at the last closed flux surface (LCFS). An example trapped orbit (green) is plotted in **Figure 4.7**. As ∇B is in the minor radial direction (no high field side) trapped electrons experience a steady and rapid toroidal drift and zero banana width in the R-Z plane. Careful consideration of shadowing of the 1.27 cm outboard limiter (shown in black in

Figure 4.7) on downstream measurements is required to properly analyze EBW deposition measurements.

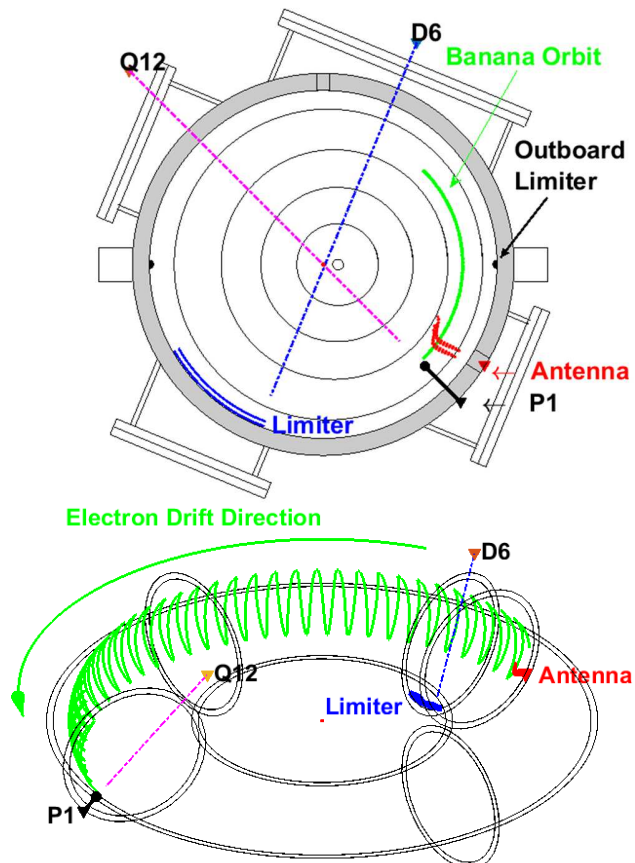


Figure 4.7. Poloidal cross section and 3D view of MST with magnetic field (black contours), possible EBW trajectory @138° Toroidal (red dots), banana orbit of heated electrons (green), and limiter @150° Toroidal (blue solid line) and target probe P1 @300° Toroidal (black line) observed by HXR detectors D6 and Q12, respectively.

By radially scanning the probe over an ensemble of reproducible shots at varying I_p , a map of radial deposition profile with respect to plasma current is obtained. Radial accessibility of

the EBW in an RFP with porthole field error effects is measured for the $n=2$ harmonic, as direct probing in of the fundamental ($n=1$) harmonic is not feasible due to high plasma currents and deeper required probe insertion depth. At a given nominal current, 5 shots were taken for each probe insertion depth between 0 and 10cm, in 1cm steps. Due to natural fluctuations in current a typical 5-8kA variation occurred. Averaging of the resulting dataset was accomplished by defining an approximate center point in current and a ~ 10 kA current window around the center. Points falling in the window were averaged together to provide a single HXR flux result at a given I_p and depth. Examples at two plasma currents are shown in **Figure 4.8**, where a modest change in deposition center is expected from the varied field strength. The flux is plotted versus probe position (\blacktriangledown , color keyed to plasma current). Note that in both plasma current cases, the emission is zero with the insertable probe tip in the shadow of the outboard limiter (depth < 1.25 cm).

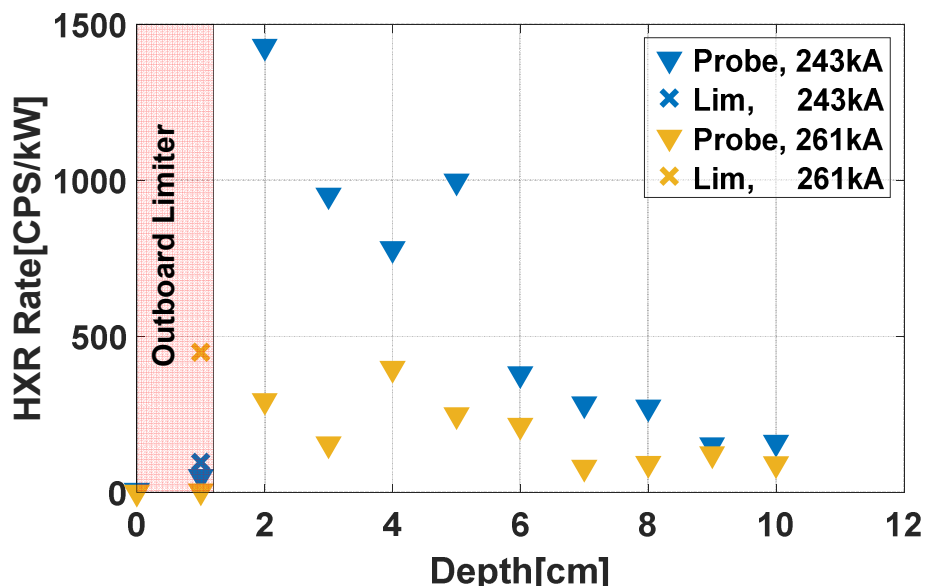


Figure 4.8. Radial profile of fast electron population from 0-10cm for select plasma currents measured with a target probe (\blacktriangledown) and limiter (X), toroidally displaced 162 degrees and 15

degrees, respectively, from EBW antenna. Midplane limiters (red box) fix the LCFS at 1.27 cm from the wall. Probe positions outside the LCFS measure negligible fast electron population.

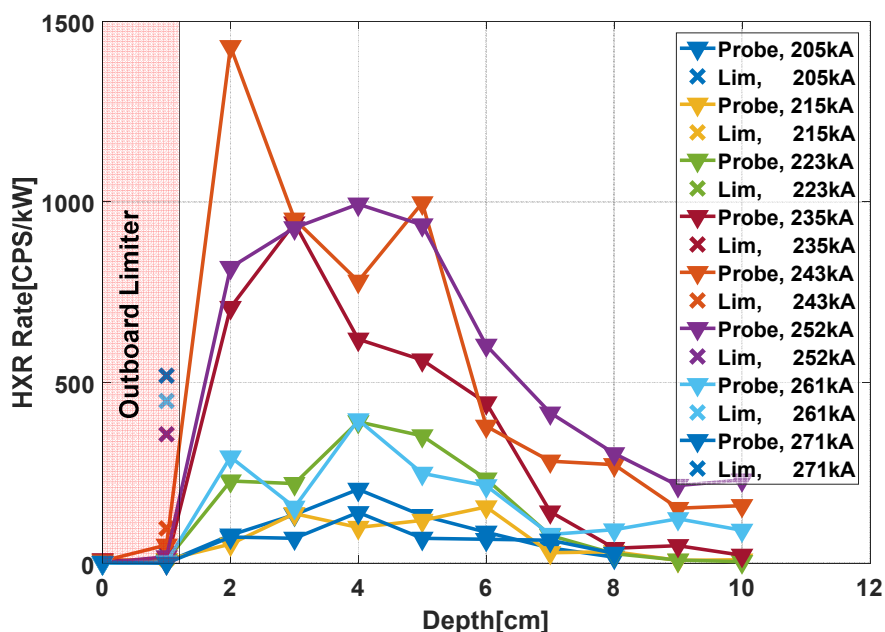


Figure 4.9. Radial profile of fast electron population from 0-10cm for all plasma currents measured with a target probe (\blacktriangledown) and limiter (X), toroidally displaced 162 degrees and 15 degrees, respectively, from EBW antenna. Midplane limiters (red box) fix the LCFS at 1.27 cm from the wall. Probe positions outside the LCFS measure negligible fast electron population.

Accurate estimation of deposition location requires compensation for shadowing effects of the outboard limiter on probe measurements in the edge (shown as an X plot symbol in **Figure 4.8**). A calculation of the first moment of emission profile given in(4.2), where r is the probe radius and ϵ is the HXR emission form the probe. As shown in **Figure 4.9**, probe measurements for the $r=1\text{cm}$ position are near zero, as heated electrons at these positions are lost to the

outboard midplane limiter, which extends 1.27cm from the wall. This distinct transition from heated electrons striking the insertable probe, to electrons hitting LHCD and outboard limiters provides inaccurate deposition estimates when calculating a first moment from probe data alone. To compensate for the shadowing effect, emission from the limiter is included in the first moment calculation, given in(4.2), where subscripts “lim” indicate data from limiter. Constants, $r_{lim}=1$ and $C_{lim}=40$, where C_{lim} is a scaling factor representing differences in emission from the probe and limiter, accurately match deposition location with analytical models of the Doppler shifted cyclotron resonance. Resulting first moment calculations with and without the correction for limiter emission are plotted in **Figure 4.10**. The large width of the deposition is likely caused by the substantial radial diffusion of electrons in the RFP edge [92]. Data points are approximately the same with exception of the three highest Ip values. These correspond to Ip values where a large fraction of heated electrons strike the limiters, making the shadowing effect a noticeable contribution to the probe data.

$$\langle r_{HXR} \rangle = \frac{\sum_0^{10} r \mathcal{E}}{\sum_0^{10} \mathcal{E}} \quad (4.1)$$

$$\langle r_{HXR} \rangle = \frac{C_{Lim} r_{Lim} \mathcal{E}_{Lim} + \sum_0^{10} r \mathcal{E}}{\mathcal{E}_{Lim} + \sum_0^{10} \mathcal{E}} \quad (4.2)$$

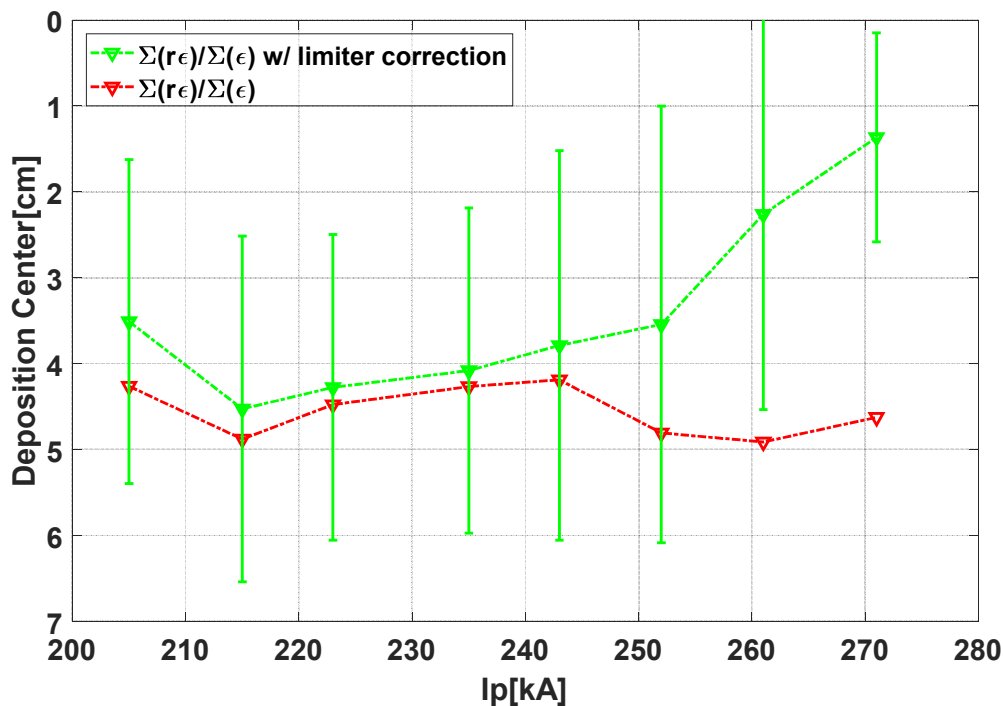


Figure 4.10. Reconstructed deposition location with correction for shadowing for the outboard limiter (green) and without correction (red), showing inaccurate location for the three highest I_p points. These I_p values correspond to high emission from the LHCD limiter.

Although the differences in the two deposition centers plotted in **Figure 4.8** are subtle, repeating the measurement on a series of plasma currents, shown in **Figure 4.9**, yields a very clear trend. In **Figure 4.11** (b) the measured absorption center is plotted in green symbols as a function of plasma current ($I_p=200-270\text{kA}$ where $n=2$ resonant absorption is expected). The trend of deeper wave penetration with decreasing plasma current is both measured and expected. The expected deposition curve for the $n=2$ harmonic (solid blue line) is computed from the equilibrium magnetic field strength which gives the electron cyclotron resonance location for a frequency of 5.5GHz, with corrections for porthole-induced field error and a substantial Doppler

shift (details on each below). The quantitative agreement is confirmation of wave propagation across the edge of the tearing-dominated RFP discharge.

The ability to resonantly deposit the EBW on several harmonics is clearly demonstrated by a measure of limiter emission over a large scan of plasma current. The equilibrium is similar for each discharge in the scan, making the plasma current axis equivalent to edge magnetic field strength. **Figure 4.11** (a) shows (in blue symbols) the power-normalized HXR emission from a limiter located 12 degrees toroidally from the launch antenna. Data points were filtered to remove points outside 3 standard deviations of a sliding window. Distinct peaks and troughs in intensity occur at particular values of plasma current. Limiter emission is measurable when the EBW is damped 1.5-3 cm from the wall and maximized for a depth of absorption of 2.5 cm. Only harmonics $n=1-4$ are plotted as a matter of clarity; measurements extending the plasma current from 50 to 550 kA show resonant absorption peaks for $n=1$ through 7. When the deposition is more than ~ 3 cm from the wall, no edge emission is observed on the lower hybrid antenna limiter. We attribute this to low single-pass absorption of the harmonic X mode and shadowing of the outboard limiter. In the single pass absorption case, the width of any possible x-mode resonance layer will be very narrow, and potential absorption would be on higher harmonics where damping is weak, thus any potential edge heating would be negligible compared to the transmitted power fraction. In addition, any heated electrons in the extreme edge would be outside the last closed flux surface, and would be lost to the midplane limiter.

The driving electromagnetic wave (incident from the $\text{depth}=0$ region) propagates inward for ~ 1 cm before encountering the right hand cutoff. Conversion to the Bernstein wave occurs at the upper hybrid layer, whose position is estimated by Langmuir probe measurements of the

edge density profile and plotted in **Figure 4.11(b)** in red, varying from about 1.7 to 1.0 cm from the edge as a function of plasma current. Bright limiter emission is evidence of strong edge damping of the Bernstein wave on each harmonic.

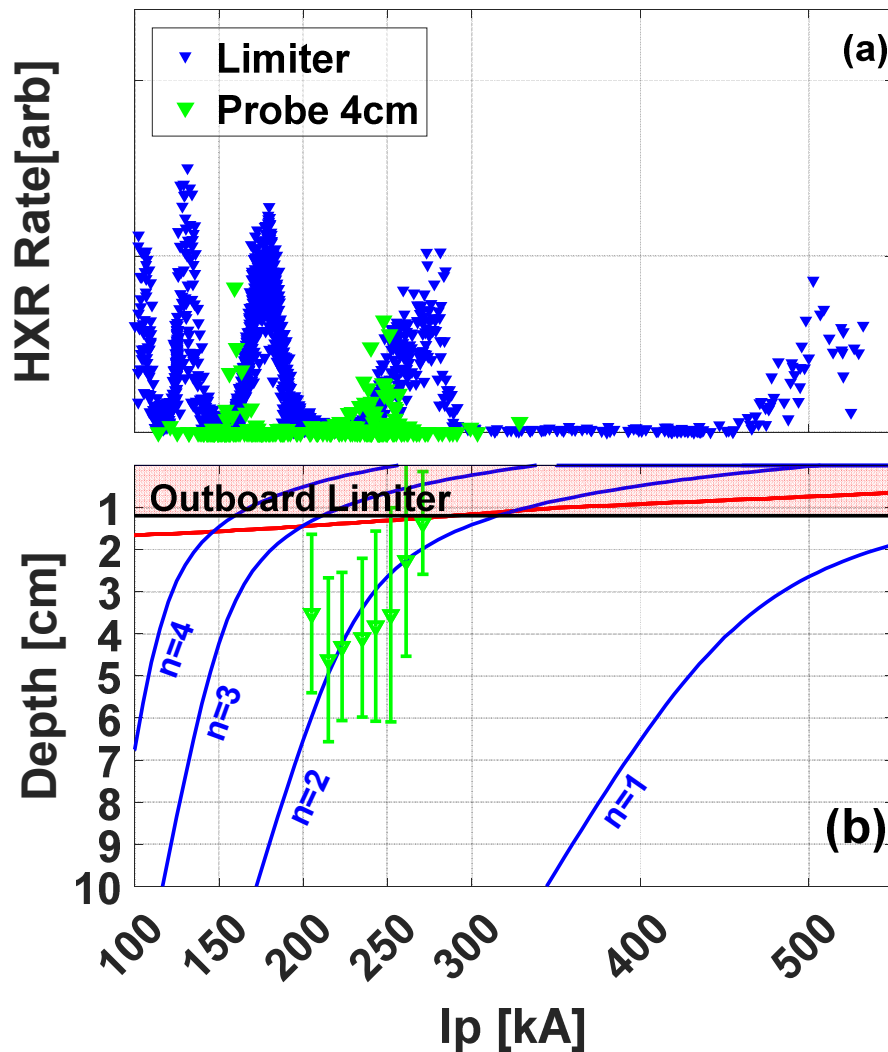


Figure 4.11. (a) HXR emission from limiter (blue) has distinct transitions between absorption outside (low) and inside (high) the LCFS. Peak emission from a target probe 4 cm from the wall occurs at lower I_p than peak from limiter due to increasing deposition depth. (b) Doppler shifted resonance location with porthole field error (blue) for harmonics ($n=1-4$) matches measured first

moment ($n=2$) of deposition (green) and transitions to absorption outside LCFS. UH layer plotted in red.

Nulls in limiter emission indicate windows of substantial radial accessibility for each harmonic. For example, the insertable probe measurements of deposition on the $n=2$ harmonic show maximum radial deposition in a plasma current region free of limiter emission. The lowest plotted plasma current point, at $I_p=205$ kA, halts the trend of deeper deposition with decreasing current due to introduction of the $n=3$ harmonic at the wall. This illustrates the main effect of the local decrease in field strength due to the porthole: in the absence of this field error, the radial accessibility of $n=2$ deposition is maximum of 10 cm at $I_p=165$ kA.

The computed Doppler-shifted and porthole field error corrected cyclotron resonance for $n=1-4$ harmonics plotted in **Figure 4.11(b)** predicts the deposition depth as a function of plasma current. GENRAY is used with the unperturbed magnetic equilibrium reconstruction to estimate the Doppler shift of a particular ray. For the cases plotted, the launched wave, centered on $n_{||}=0$, upshifts to an $n_{||}$ of -3 to -6 before absorption on electrons with $E_{||}=50$ eV to 175 eV. Coupled with the thermal distribution in the edge plasma, this gives a spatial Doppler shift (radially outward) of up to 10 cm for deep wave penetration, dropping steadily to zero at the plasma edge as temperature decreases. Porthole field error [51] decreases the $|B|$ profile in the vicinity of the porthole, from the edge to a 5 cm depth, equal to the diameter of the perturbing porthole. This correction is applied to the location of the electron cyclotron harmonic, and the spatial Doppler shift is added. The peak perturbation to the field strength occurs at the wall, and reduces the field by 50%. As the spatial extent of the field error is quite limited, its main effect is introduction of the next-higher harmonic at the wall for a given plasma current limiting the radial

accessibility. The deepest heating available in MST is 5 cm from the edge on $n=2$ (measured), and 10-12 cm from the edge on the fundamental resonance at $|B(a)| = 0.13$ T ($I_p \sim 330$ kA). The latter accessibility limit is a projection from GENRAY simulation rather than measurement as the conditions are not conducive to external probing due to thermal limits of the probe and higher HXR background.

4.2.2 Toroidal falloff of drifting electrons and effects of field pitch

Target probes at varying toroidal locations allows for measurement of the fast electron population falloff as electrons drift around the machine due to ∇B drift. Probe measurements are made at several toroidal locations, where a probe port is located on the outboard side of the machine with a beryllium x-ray window and detector diametrically opposed. Due to limited probe locations, the resolution of the toroidal scan can be increased by reversed I_p operation for each probe location. The resulting configuration reverses field line pitch, and grad B/curvature drift directions, allowing each probe location to provide two points on the toroidal scan. Due to the vertical symmetry of the banana orbits, the top/bottom mirroring of the probe location does not affect the measurement.

Effects of field line pitch were examined with HXR emission from the LHCD limiter measured over a current scan for normal and reversed helicity plasmas (where the pitch of the magnetic field lines is reversed) (**Figure 4.12**). The location of the HXR emission from the LHCD antenna was not affected by the pitch of the field line indicating that locations of high emission are controlled by deposition depth, and that the pitch of the field line that the EBW is absorbed on does not greatly influence toroidal transport.

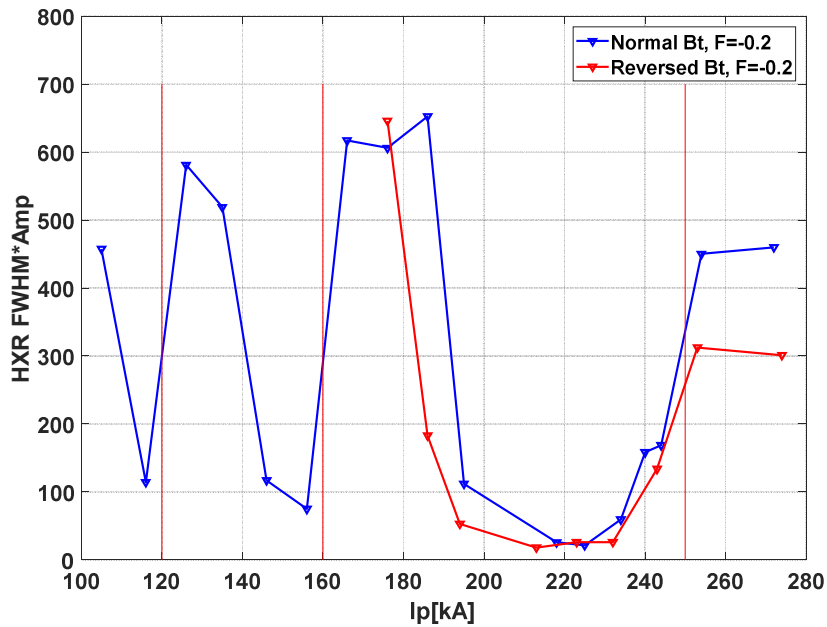


Figure 4.12. HXR flux measured on LHCD antenna for normal and reversed Bt direction. Reversing Bt flips field line pitch but does not effect currents corresponding to high limiter emission.

Toroidal falloff measurements for probe insertion depth of 2.5cm and 4cm (**Figure 4.13**) for plasma currents where EBW absorption is inside the LCFS for third harmonic absorption ($I_p=140,145,150\text{kA}$) indicate that the average $1/e$ folding angle is approximately 17 degrees. This illustrates the high loss rate of heated electron population in the RFP as electrons are transported toroidally.

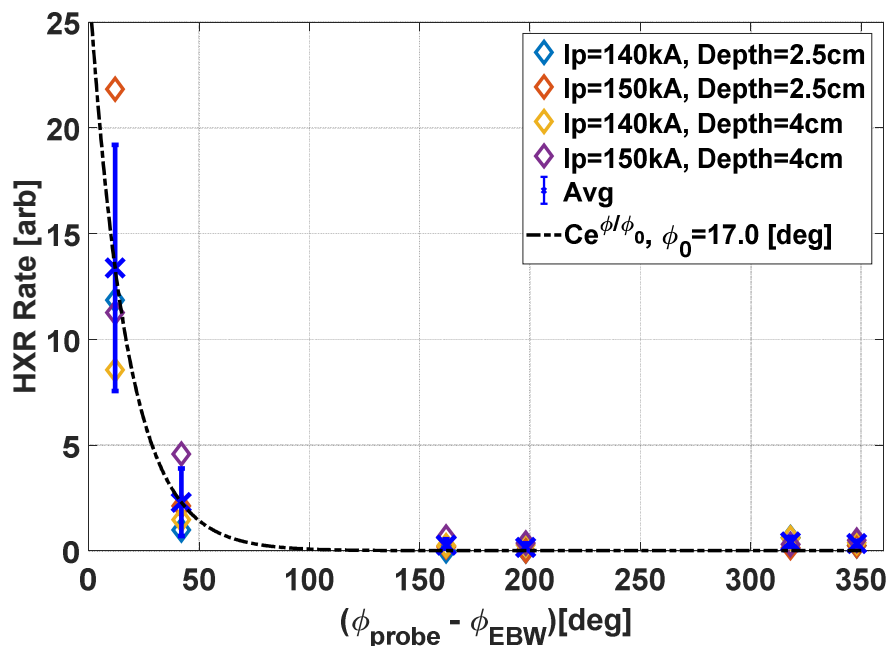


Figure 4.13. Toroidal decay of heated electron population at 2.5cm and 4cm from the wall represented by decreasing HXR production rate from an inserted target probe. An exponential fit of averaged data is plotted in black.

4.2.3 High harmonic EBW heating

Low I_p operation allows the possibility of high harmonic EBW heating by reducing magnetic field. Distinctive peaks in limiter emission from deposition just inside the LCFS are observable up to 7th harmonic as plotted in **Figure 4.14**, with corresponding windows of radial accessibility within the plasma marked in red. Absorption on the 8th through 11th harmonics lack distinct regions of low emission, indicating that overlap of EBW resonances restrict radial accessibility to the extreme edge. High harmonic heating is not effectively applicable to heating in the RFP where deeper radial accessibility is needed, however, it may be applied in component

test facilities, such as MPEX and proto-MPEX, conducting tokamak first wall material studies [93].

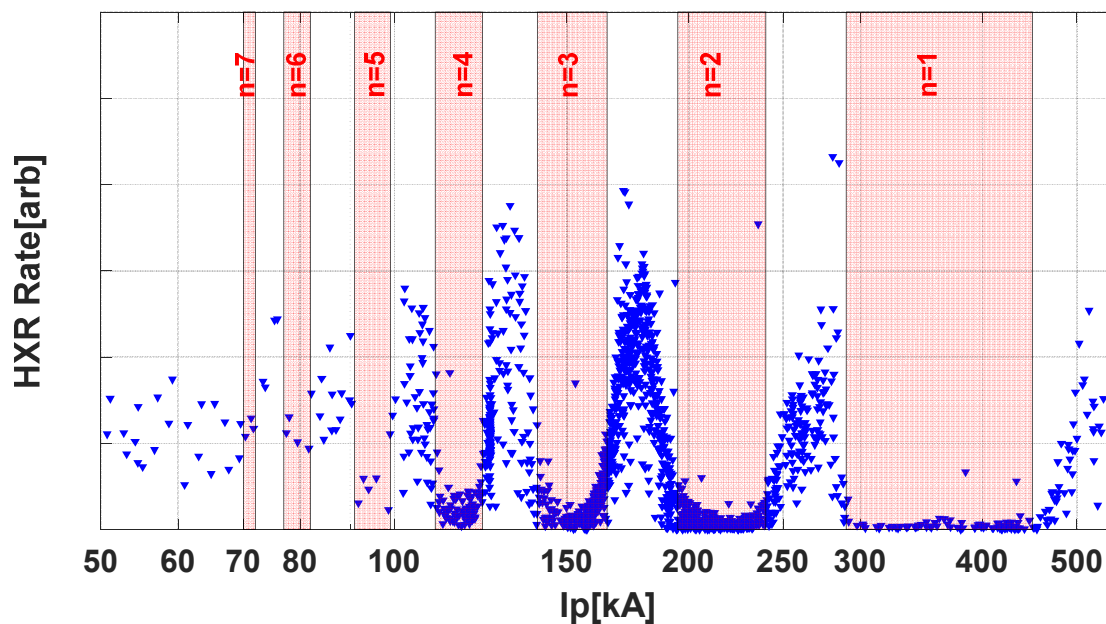


Figure 4.14. HXR emission from limiter (blue) has distinct transitions between absorption outside(low) and inside(high) the LCFS. Accessibility windows in I_p , where the EBW is damped within the LCFS, are marked in red for $n=1-7$ harmonics. Harmonics $n=8-11$ are damped outside the LCFS.

4.2.1 EBW heating in PPCD plasmas

Pulsed poloidal current drive (PPCD) plasmas are likely to be an improved target discharge due to improved electron confinement and increased coupling of launched power to the EBW. Magnetic stochasticity in the RFP can be reduced by providing auxiliary parallel inductive current drive in the edge. During a PPCD discharge, the inductive current drive causes an increase in reversal parameter, effectively sweeping the edge magnetic field upward in strength.

Unlike in a standard discharge, where EBW heating occurs during the current flat top and therefore a relatively constant magnetic field strength, a PPCD discharge is characterized by a steadily increasing edge magnetic field during the PPCD period (typically until ~ 20 ms). One effect of this increasing magnetic field, is that the EBW deposition position is radially swept during a PPCD shot, and may jump between harmonics for certain plasma currents. Careful selection of discharge current is required to select a given harmonic and average heating location in the plasma.

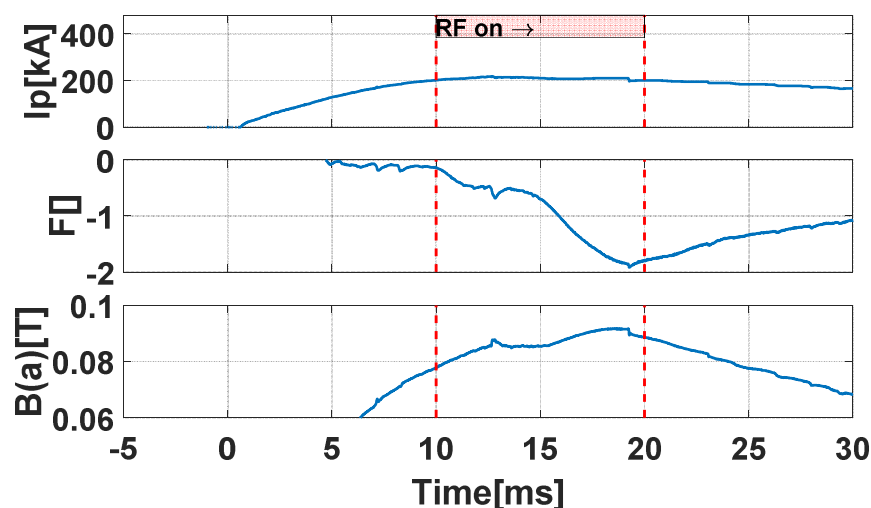


Figure 4.15. Time evolution of a typical PPCD discharge. Although plasma is nearly constant during the RF heating pulse, the inductive current drive continuously reduces the reversal parameter F , resulting in a steady increase in edge magnetic field.

EBW heating during the reduced stochasticity period of PPCD plasmas demonstrated RF heating in $\beta=15-20\%$ plasmas, the highest observed beta in a toroidal magnetic confinement device at this time. Ensemble averages of multiple shots with varying RF injection times allowed

the EBW enhancement to the PPCD background to be measured over an extended time window from 10-20ms. EBW enhancement to LHCD limiter emission in a 270kA plasma due to edge absorption terminated midway through the shot as shown in (**Figure 4.16** left) due the increasing magnetic field shifted the second harmonic edge absorption to first harmonic absorption at the maximum accessible depth. When the variation in field strength is taken into account, the HXR flux from the LHCD antenna plotted vs. $|B(a)|$ matches with peak locations seen during standard plasma shots (**Figure 4.16** right).

The increased background is also visible during PPCD plasmas as measured on both the Be1,2 detectors and the HXR array. This background is caused by Ohmic heating of the reduced stochasticity PPCD plasma and is distinct from the suprathermal electron tail caused by EBW heating. In these shots, HXR emission $>15\text{keV}$ is used as a gauge of EBW heating electrons.

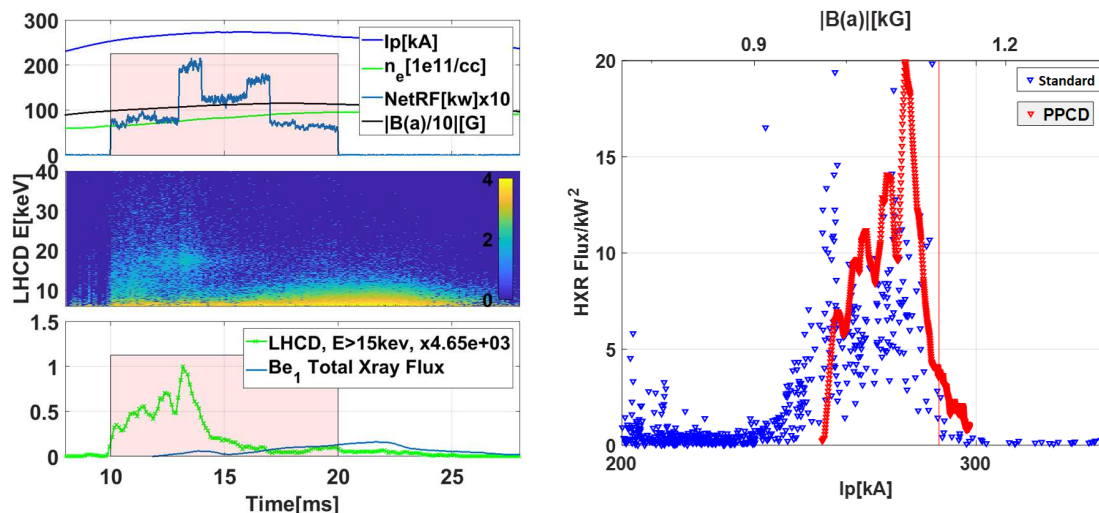


Figure 4.16. HXR spectrum during a PPCD plasma showing termination of 2nd harmonic EBW enhancement at $\sim 15\text{ms}$ (left) while $|B(a)|$ increases. Emission from the LHCD antenna plotted vs $|B(a)|$ shows absorption at magnetic fields consistent with standard plasmas on the right.

4.3 Heated electron confinement time

An RF pulse train allows the measurement electron confinement times by measuring the population decay rate after the end of the RF pulse. For this study, a modulated rf pulse (2 kHz at 50% duty cycle) at ~30 kW net power (launched minus reflected) is injected into many reproducible 175 kA RFP discharges. Experimentally this occurs during a 3ms window between 16-25 ms into the MST discharge during steady plasma current and line-averaged electron density. The line-averaged density is roughly $7 \times 10^{18} \text{ m}^{-3}$, core electron temperature ~150eV and parameters at the upper hybrid layer are $n_e \sim 2 \times 10^{17} \text{ m}^{-3}$ and $T_e \sim 10 \text{ eV}$. Efficient coupling of 60-70% (inferred from measured reflected power) occurs without any antenna-specific limiter as the typical edge density gradient scale length ($L_n \sim 0.5\text{-}2 \text{ cm}$) is in a range favorable to X-B mode conversion [8] in the antenna near field ($k_0 L_n \sim 1$ where k_0 is the vacuum wavenumber). Deposition is on the $n=3$ harmonic at an expected radial depth of 2.5 cm from the wall. A 5 pulse train of 250us pulses with 250us separation was injected over an ensemble of reproducible shots to produce good statistics. The HXR counts over the pulses were added together from all shots in the ensemble (**Figure 4.17**, left) and then aligned to overlap in time by applying a modulus function with the pulse period (**Figure 4.17**, right). HXR counts from both the LHCD antenna at 150T and the target probe were recorded with 200um Al filters on both the probe and HXR array.

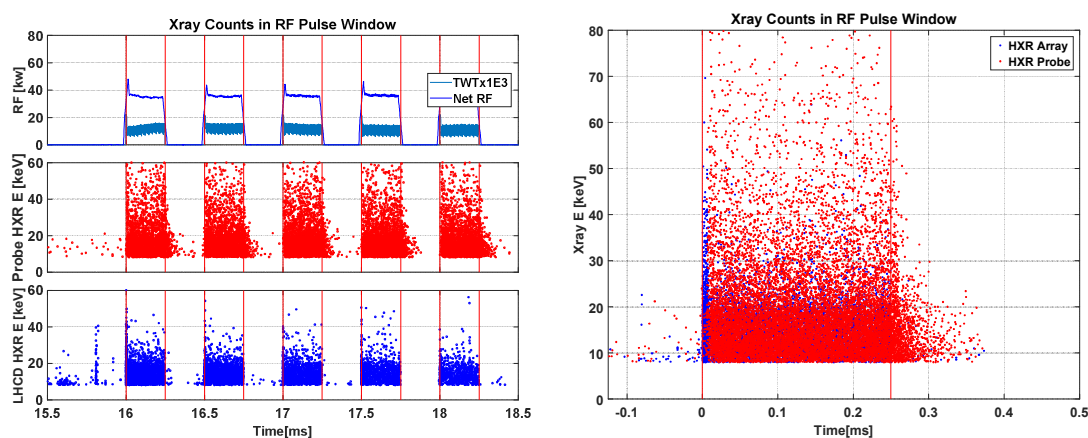


Figure 4.17. Ensemble of HXR counts recorded on inertable target probe and LHCD antenna over an RF pulse train(left), and sumation of counts aligned in time(right).

Histogram binning of the resulting counts shown in **Figure 4.18** (a)-(d) allowed fitting of an exponential decay function to the heated electron population falloff. Measured background flux from the non-rf heated discharge prior to rf turn on is negligible; for these plasma conditions the x-ray flux is generated entirely from the EBW-heated electrons. The typical x-ray spectrum is shown in **Figure 4.18** (e) with measurable flux between the 5 keV detector noise floor to 80 keV.

The difference in timescales between passing and trapped electrons implies heating in a stochastic magnetic field [94]. The radial diffusion rate is proportional to the parallel velocity in a stochastic field; in MST this is greater for the passing electrons than for trapped electrons. Average measures of energy-integrated x-ray flux (HXR) from the probe are plotted for the rising **Figure 4.18** (a) and falling **Figure 4.18** (b) edges of the rf pulse. Following rf turn-off a characteristic decay of flux is used to infer a fast electron confinement time. Although the probe is capable of measuring both trapped and passing electrons, the trapped timescale is much larger

than the passing timescale, thus the probe signal is dominated by the trapped fraction of electrons. Trapped fast electron confinement time in standard plasmas was 17.4 μs at 4cm depth, as shown in **Figure 4.18** (b). Radial diffusion in the RFP controls electron loss; collisional times with electrons and neutrals are on the order of one millisecond, as calculated in chapter 2. Measured HXR rate decay time constant of $\sim 20\text{-}100$ ns on the inboard limiter shown in **Figure 4.18**(d) implies rapid loss of passing fast electrons. Experiments in similar conditions with reduced stochasticity plasmas [95] achieved similar HXR emission from insertable probes with falloff times increasing 3-5 fold, as shown in **Figure 4.19**, due to reduced radial diffusion [96]. In these shots, equilibrium reconstruction indicated a beta of 15-20%.

The total RF energy added to the plasma in steady state conditions by EBW heating may be determined from the population falloff time constants. A heat balance equation, (4.3), where N is the number of heated electrons, S is a source term due to EBW heating, and τ is the confinement constant, is set equal to 0 for steady state conditions.

$$\frac{dN}{dt} = S - \frac{N}{\tau} = 0 \quad (4.3)$$

Since $N=S\tau$, the heat added to the plasma volume is proportional to the RF power and the confinement time constant. Solutions for rising and falling electron populations after RF turn on and turn off are given in (4.4) and (4.5), respectively, and indicate the expected exponential rising and falling behavior in x-ray observed during RF pulse experiments. For the rising population equation, electron population in the plasma builds up to a steady state value proportional to the source power multiplied by the time constant. The astute observer will note that there is a short delay between rf turn on and buildup of electron population in **Figure 4.18**(a) caused by the time required for trapped electrons to drift to the probe location. For a heating

scenario where 50kW is coupled into the plasma with a confinement time constant of $\sim 20\mu\text{s}$, the net energy added by EBW heating would equate to $\sim 1\text{J}$. Modification to the plasma temperature is therefore not expected or observed in this EBW heating scenario. Agreement between (4.5) and the exponential falloff in HXR emission observed in **Figure 4.18** (b) following rf turn off justifies the simple model.

$$N_{\uparrow}(t) = S\tau(1 - e^{-t/\tau}) \quad (4.4)$$

$$N_{\downarrow}(t) = S\tau e^{-t/\tau} \quad (4.5)$$

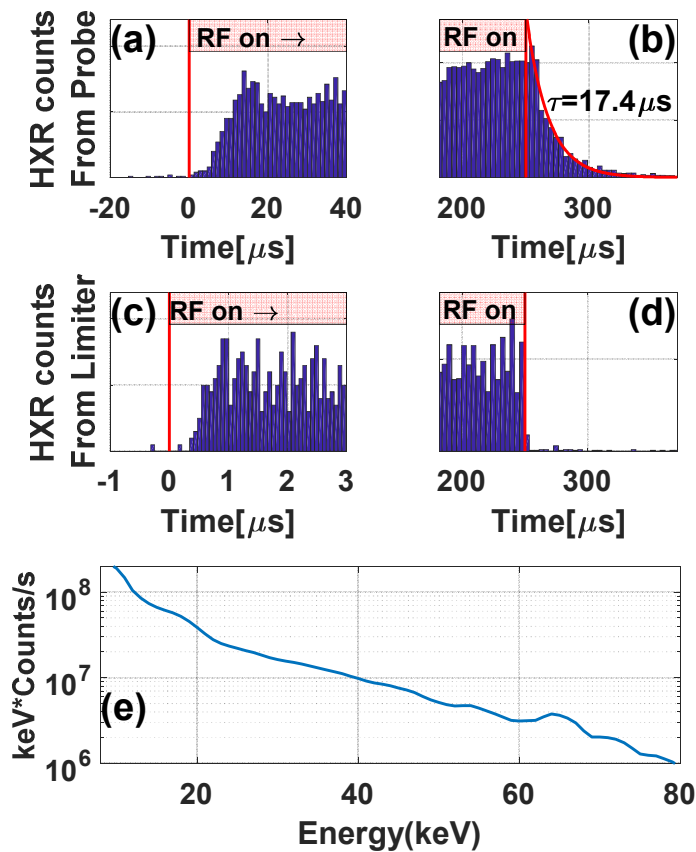


Figure 4.18. EBW induced x-ray measurements using a target probe inserted 3 cm from the wall 162° toroidally away from the EBW heating location in a 175 kA plasma. HXR rise time from

probe (a) and limiter (c) is shown following the start of the pulse (note different timescale). HXR fall time from probe (b) and limiter (d) following rf pulse end. Time axis is with respect to pulse start. (e) HXR spectrum from target probe is shown averaged over pulse period.

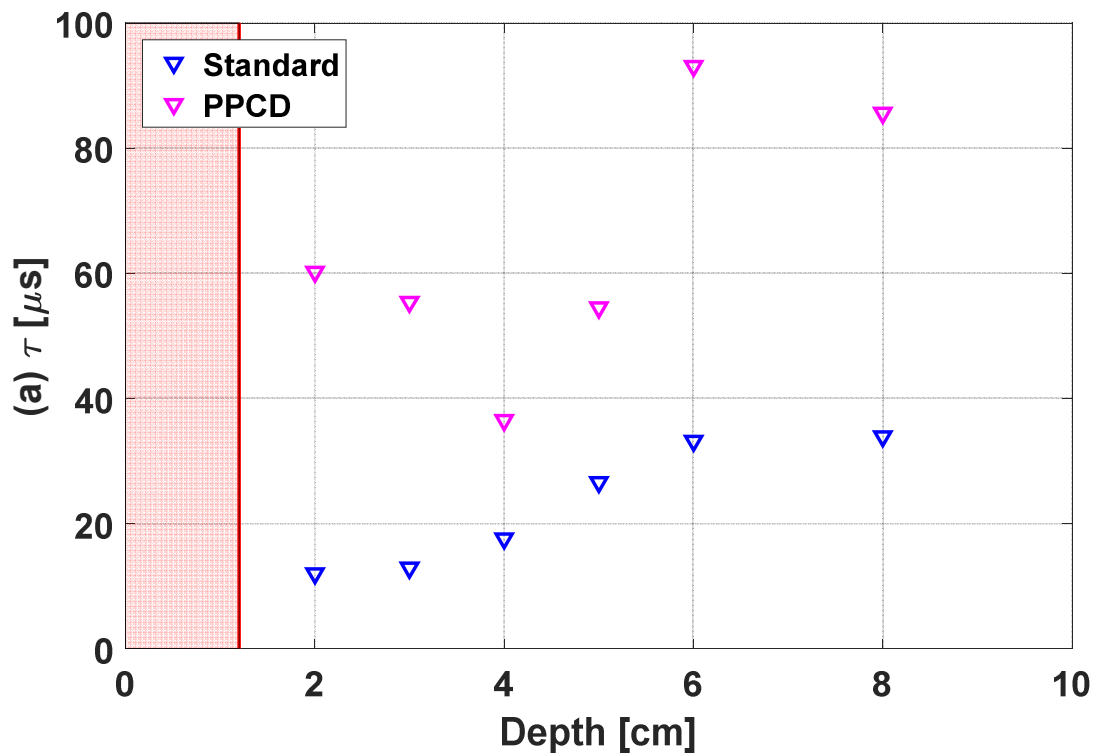


Figure 4.19. Time constant of electron population decay rate in a 240kA plasma for standard(blue) and PPCD(red) plasmas showing increased electron confinement during reduced stochasticity periods.

4.4 Reconstruction of electron energy distribution function

Measurement of the HXR spectrum measured on the LHCD limiter and probes detected several distinct characteristics. A vacuum bremsstrahlung spectrum generated by non-relativistic electrons of energy E is always monotonically decreasing with energy (as mentioned in Ch3) up to E . No inflection points are generated by a Kramer's law model, with the exception of a global maxima in the 10s of eV if thick target backscatter corrections are accounted for. This effect is not relevant for the EBW experiment since our detectors only measure HXR energies above 5keV. The integrated bremsstrahlung spectrum produced by a non-monoenergetic electron distribution will likewise be monotonically decreasing with energy. Peaks from K-shell emission will occur when a target material is struck with electrons with energy exceeding the K-edge energy of the target material.

4.4.1 Electron energy distribution function reconstruction

Observations of HXR spectrums in standard and PPCD plasmas showed some notable differences. Compared to a standard plasma, a PPCD plasma has a considerably higher free-free emission rate due to improved energy confinement during low magnetic fluctuation periods. This low energy (<15keV) background will saturate the HXR detectors and must be removed by the use of x-ray filters. The filter of choice was a 200um Al filter placed over the 150um beryllium vacuum window, which was found to successfully remove the majority of the unwanted x-ray background while allowing good sensitivity to higher energies. Corrections applied to the resulting spectrum by dividing by the transmission coefficient of the filter + window assembly will then recover the vacuum bremsstrahlung spectrum. Standard plasmas generated negligible

free-free emission, with a near zero background during RF off periods, with the exception of low energy HXR detection during saw tooth crashes. These were observed to be much less than the EBW generated HXR intensity, of low energy, and were found not to effect the measured spectrum.

Spectral measurements during PPCD operation displayed a distinct bump on the measured HXR spectrum in the 14-22keV range for HXR detectors looking at the LHCD antenna, but not for detectors looking at the outboard limiter (**Figure 4.20**). Recall the development in chapter 3 where non-monotonic spectra can not be generated from bremsstrahlung alone, even with a monoenergetic electron source, therefore the bump on the measured spectra must be due to non-bremsstrahlung effects. This bump on the spectrum corresponds to the K-alpha and K-beta emission lines from the molybdenum interdigital straps on the LHCD antenna. These lines are centered on 19.96keV, 19.61keV, 19.59keV, 17.48keV, and 17.374keV, with a line width of $\sim 5\text{eV}$, however the measured line widths are significantly broadened by the finite resolution of the CdZnTe HXR detectors which have a FWHM of $\sim 2\text{keV}$. The additive effects of the individual broadened gaussians produces the single bump on the HXR spectrum observed from the LHCD antenna during EBW heating, produced by the minority electron population that exceeds the $\sim 20\text{keV}$ K-edge energy of molybdenum. The HXR detectors observing the outboard limiter do not detect such a bump on the spectrum, due to the K shell line from the carbon limiter tiles being below the detectable energy at 277eV . During the RF pulse, spectrums are plotted at several time intervals, the distinct bump on the spectrum only occurs during EBW heating, implying that the heated electrons are on field lines that strike the molybdenum components of the antenna.

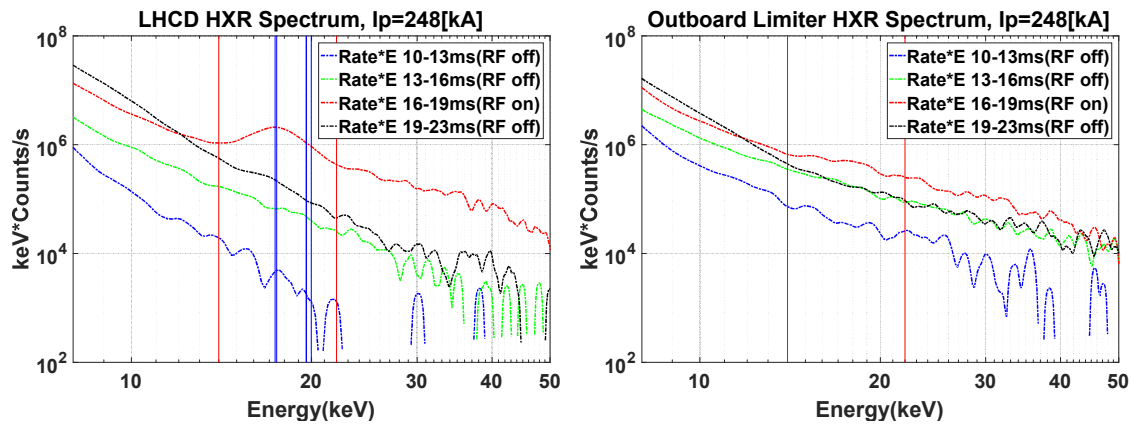


Figure 4.20. Comparison of HXR spectrum emitted from the LHCD antenna(left) and outboard limiter(right) during a 248kA PPCD plasma. 14keV and 22keV are marked by vertical red lines, K-shell lines are marked by blue lines.

In standard plasmas the HXR background decreased by a factor of $\sim 10^2$ compared to PPCD plasmas, allowing HXR detector operation without the use of aluminum filters. The resulting measurements of the bremsstrahlung spectrum from the insertable target probe may be used to reconstruct the electron energy distribution spectrum (**Figure 4.21**) by iterative methods based on a Kramer's law model. Resulting reconstructions indicate a dominant portion of sub-10keV EBW heated electrons present at 315T during second harmonic EBW heating.

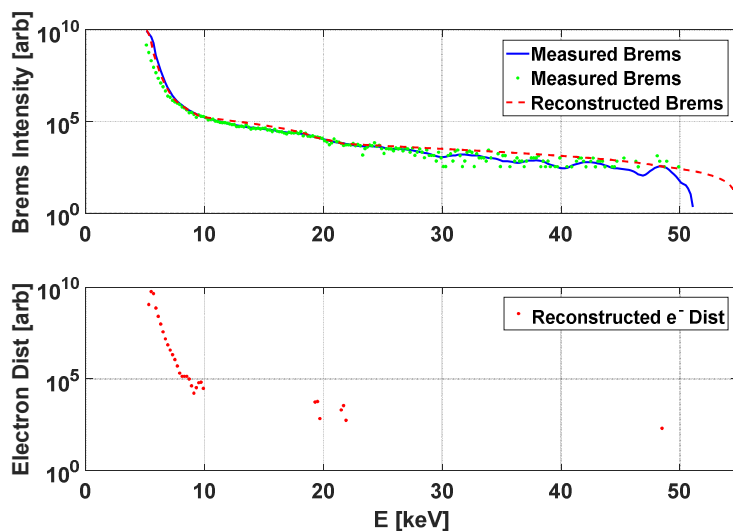


Figure 4.21. HXR energy spectrum(top) and electron energy reconstruction(bottom) from target probe in a 235kA plasma measuring EBW heated electrons inside the LCFS at 315T.

For these measurements, the bremsstrahlung spectrum consists of the summation of all HXR counts detected during a probe depth scan between 0-10cm insertions into a 235kA plasma. In such a plasma good HXR emission amplitude is seen for a peak located well within the LCFS. The spectrum does not have a bump indicating a minority of heated electrons above the K—edge energy of 20keV. Electron energy spectrum reconstructions confirm this assumption, indicating the electron population is still increasing in intensity below 5keV, with the population density at 5keV more than $1E7$ greater than the population density at 20keV. Although the reconstruction does not give an exact fit of the electron population at high energies, the bremsstrahlung spectrum generated by the reconstructed electron distribution is well matched to the initial measured spectrum from the probe. The lack of a high energy electron population is consistent

with the significantly higher radial diffusion these electrons experience during their travel from the EBW heating location to the probe at 315T.

4.5 Summary

This chapter presented observations and analyses of EBW heating effects in the RFP, including studies of deposition location control, radial accessibility and profile, toroidal falloff, heated electron transport and population falloff during RF pulses, bremsstrahlung spectrum and electron energy distribution recovery, non-linear dependence between heated electron population and RF power, coupling to launched power as a function of plasma current, and observation of EBW heating up to the 11th harmonic.

Radial probe scans determined the deposition profile of EBW heated electrons allowing an average position to be calculated from the first moment. The lack of a sharp peak is attributed to the large radial diffusion coefficient for heated electrons combined with the large toroidal displacement between the EBW antenna and the target probe. The toroidal falloff was observed due to losses attributed to radial diffusion. The difference in falloff in time in HXR rate from limiters and probes after RF pulse termination indicated heating in either a stochastic magnetic field or field with broken flux surfaces.

Measurements of bremsstrahlung spectra in PPCD and standard plasmas indicated a bump in the bremsstrahlung spectrum between 14-22keV which was determined to be the K-alpha and K-beta emission lines from the molybdenum straps on the LHCD antenna broadened by the finite resolution of the HXR detectors. Spectrum measurements from the graphite limiters did not observe such a peak. Reconstruction of the electron energy distribution function from the bremsstrahlung spectrum indicated the dominant majority of EBW heated electrons exist below 10keV, however a high energy tail up to >80keV exists at a significantly lower ($1E-7$) fraction of the value at 5keV.

Measurements of heated electron population as a function of net launched RF power indicate a non-linear relationship between observed bremsstrahlung intensity and RF injection. Normalization by (Net RF power)² was found to significantly increase point grouping, particularly for lower RF power where the non-linear effects are more pronounced.

Comparisons of XB and OXB launch scenarios indicate significantly better coupling for XB launch. Additionally best coupling occurs for first harmonic launch with a smooth decrease in coupling efficiency with increasing harmonic number. A slight increase in coupling over the minimum at 5th harmonic launch was seen for higher harmonics. No correlation between deposition position and coupling efficiency was observed.

EBW heating was verified up to 11th harmonic absorption, with clear transitions between heating inside and outside the LCFS observable up to 5th harmonic absorption; 6th through 11th harmonic absorption locations were always outside the LCFS producing a uniformly high HXR emission from the LHCD antenna over deposition locations corresponding to those harmonics.

In summary, the first observation of RF heating in the RFP using the EBW is reported for fundamental and higher harmonics (n=1-7) utilizing XB mode conversion in the near field of a waveguide antenna. Heating within the LCFS is limited to harmonics less than or equal to n=7 due to the narrowing window of accessibility; heating in currents corresponding to harmonics up to n=11 has been observed, however measurement of limiter emission indicates absorption outside the LCFS. Deposition location was controllable with |B|. In the thick-shelled MST RFP, the radial accessibility of EBW is limited to $r/a > 0.8$ (~10 cm) by magnetic field error induced by the porthole necessary for the antenna.

Chapter 5 Conclusions and Recommendations

This thesis documents the construction of an EBW heating system on MST and subsequent demonstration of EBW heating in a thick walled RFP. The first observation of RF heating in the RFP using the EBW was demonstrated by mode conversion from an edge launched X mode wave at 5.5GHz with ~30-100kW of launched power. Propagation of the EBW across, and heating in a magnetic field that is either stochastic or has broken flux surfaces was implied by the difference in timescales of passing and trapped heated electrons. High radial diffusion rates in the RFP limited the heated electron population; confinement times were measured in the 10s of μs . High Ohmic heating power in the RFP compared to RF heating power prevented observation of increases in plasma temperature. Development of novel techniques involving insertable target probes allowed measurement of radial profiles of heated electrons.

Deposition location control of the EBW was measured on the $n=2$ harmonic where plasma currents allow direct probing. Deposition location matched analytical models of the porthole field error corrected Doppler shifted resonance. Coupling of launched power was found to be in the 60-80% range, with a slight non-linearity in x-ray generation to power ratio at low launched powers. Population falloff of heated electrons was measured with a train of RF pulses and found to be dominated by RFP transport; collisional timescales are much longer than diffusive processes in a stochastic field. Falloff times increases at greater depths, consistent with

a cylindrical diffusion process. Heated electrons were used to probe edge diffusion rates in standard and PPCD plasmas, with a modest increase in confinement during low magnetic stochasticity periods. An overview of EBW heating results are presented in the summary of research section.

Limitations were identified in the EBW system involving maximum pulse length, maximum launched power, and deposition limits imposed by the porthole field error. Pulse length was limited to ~3ms by the voltage droop on the capacitor bank powering the klystron power supply. Maximum power was limited to ~150kW launched power by arcing in the antenna and pillbox window. The presence of a porthole field error introduces higher harmonics at the wall causing a jump to edge heating and reducing radial accessibility. Methods of correcting these limitations are addressed in the future work section.

5.1 Summary of Research

The Electron Bernstein wave (EBW) presents an alternative for heating and current drive in overdense plasmas where conventional extraordinary (X-mode) and ordinary (O-mode) electromagnetic waves do not propagate past the periphery. The confining magnetic field in the RFP is generated almost entirely from current within the plasma, resulting in a dynamic equilibrium with $|B|$ maximized on the magnetic axis (no high field side exists). The shape of $B(r)$ profiles is nearly fixed through the relaxation process that generates the equilibrium [97], with magnitude proportional to the plasma current. The resulting electromagnetic cutoffs, shown in **Figure 5.1** (left), restrict accessibility of electromagnetic waves to within a few cm of the edge, with cutoffs enclosing the plasma volume.

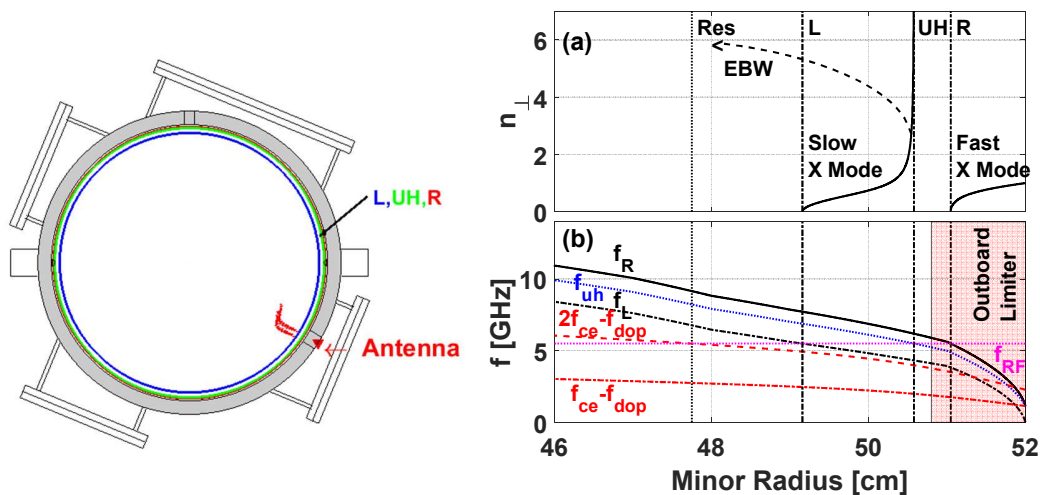


Figure 5.1. (Left) X mode electromagnetic waves do not propagate past the periphery in the RFP due to cutoffs within a few cm of the wall, shown in blue and red. Mode conversion to the EBW, shown in red, at the UH layer, shown in green, allows accessibility to RF heating within the electromagnetic cutoff layers.

(Right) Plotted in (a) are index of refraction calculated for the X-mode wave, an illustrative curve for EBW, left (L) and right (R) cutoffs, upper hybrid (UH) resonance and Doppler shifted resonance (Res) locations. Plotted in (b) are the plasma frequencies, first and second harmonic Doppler shifted frequencies for 5.5GHz (f_{RF}) X-mode edge launch in a 210kA plasma.

Close spacing of the L and UH layers, shown in **Figure 5.1** (right), allow efficient evanescent coupling of an edge launched X mode wave to the UH layer where mode conversion to the EBW occurs.

Coupling to the X mode wave, and mode conversion to the EBW occurs within the antenna near field. Coupling between 60-80% efficiency is typically observed for n=1-2 harmonics, indicating an efficient launch in the RFP due to the naturally steep edge density gradients. Absorption on the Doppler shifted resonance provides radially localized heating, however, due to high radial diffusion in the RFP, radial electron distribution profiles measured 162 degrees toroidally away are broad. Careful consideration of shadowing of the 1.27 cm outboard limiter on downstream measurements is required to properly analyze EBW deposition location. By integrating measurements from an inboard limiter and an insertable probe, the radial electron distribution may be reconstructed. The first moment of the electron distribution matches analytical models of the Doppler shifted cyclotron resonance, as shown in **Figure 5.3** left. Measurements of electron confinement time, shown in **Figure 5.3** right, indicate a difference in falloff times between an inboard limiter, on the order of ~100ns, and on an insertable probe, on the order of 17 μ s. The difference in timescales between passing and trapped

electrons implies heating in either a stochastic magnetic field [64] or on broken flux surfaces. The radial diffusion rate is proportional to the parallel velocity in a stochastic field; in MST v_{\parallel} is greater for the passing electrons than for trapped electrons. Emission from the inboard limiter, 12° toroidally from the antenna, is determined by passing electron; much more common than deeply trapped electrons. Conversely, passing particles require several confinement times to reach the probe, located $\sim 162^{\circ}$ toroidally away; probe emission is dominated by electrons on trapped orbits.

Short confinement times with respect to the RF pulse limit the total added energy to the plasma to $\sim 2\text{J}$ over a 1 m^3 volume. No increase in plasma temperature is expected or observed. Measured confinement times increase with increasing probe depth, consistent with a cylindrical diffusion of heated electrons following the end of the RF pulse. Experiments in similar conditions with reduced stochasticity plasmas achieved similar HXR emission from insertable probes with falloff times increasing 3-5 fold due to reduced radial diffusion [98]. In these shots, equilibrium reconstruction indicated a beta of 15-20%, as shown in **Figure 5.2**.

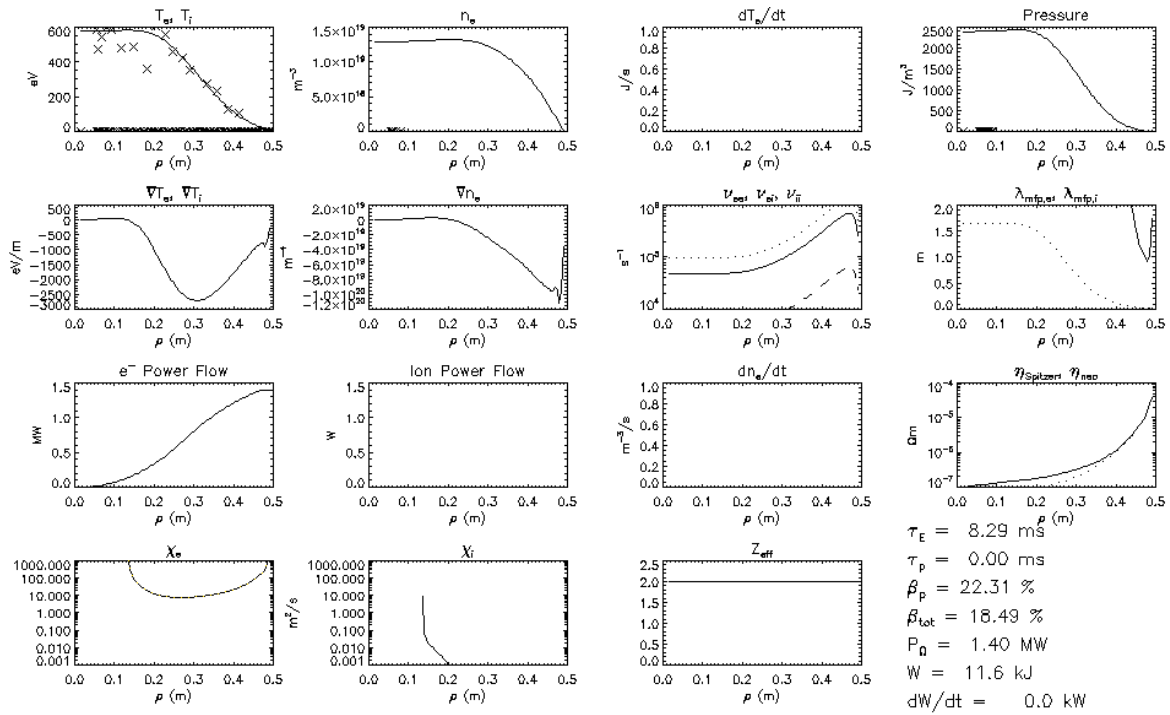


Figure 5.2. Equilibrium reconstruction of an $I_p=265\text{kA}$ shot achieving $\beta=18.5\%$ during PPCD operation.

Reconstruction of heated electron energy spectrum indicates formation of a suprathermal electron tail, with lower energies dominating. The spectrum is monotonically decreasing with energy.

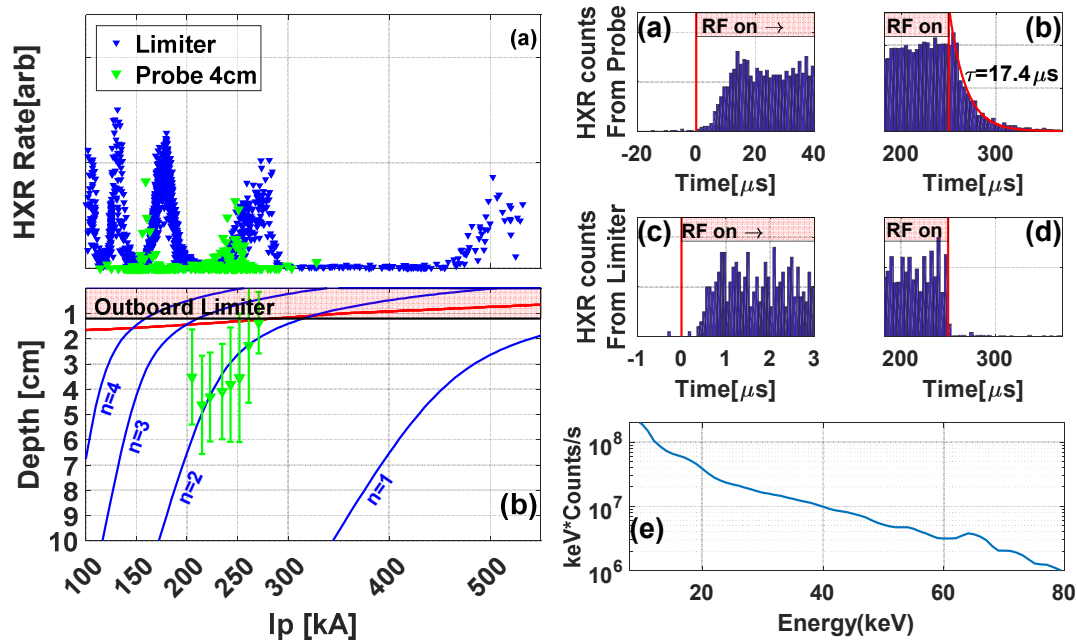


Figure 5.3. (Left) (a) HXR emission from limiter (blue) has distinct transitions between absorption outside (low) and inside (high) the LCFS. Peak emission from a target probe 4 cm from the wall occurs at lower I_p than peak from limiter due to increasing deposition depth. (b) Doppler shifted resonance location with porthole field error (blue) for harmonics ($n=1-4$) matches measured first moment of $n=2$ deposition (green) and transitions to absorption outside LCFS. UH layer plotted in red.

(Right) EBW induced x-ray measurements using a target probe inserted 4 cm from the wall 162° toroidally away from the EBW heating location in a 175 kA plasma. HXR rise time from probe (a) and limiter (c) is shown following the start of the pulse (note different timescale). HXR fall time from probe (b) and limiter (d) following rf pulse end. Time axis is with respect to pulse start. (e) HXR spectrum from target probe is shown averaged over pulse period.

Reduction in edge field due to porthole field error imposes a significant reduction in radial accessibility in the thick shelled RFP. Shown in **Figure 5.4**, are Doppler shifted resonances for the EBW without porthole field error, shown in green, and with porthole field error, shown in blue. The most noticeable effect is the reduction in edge field, within one porthole diameter (~5 cm) of the EBW antenna. The resonance locations with porthole field error included (blue) are seen to curve over as they approach the wall, whereas without field error, the curves are almost linear. Due to this inflection in the deposition curve, core absorption on the $n=1$ harmonic jumps to the wall at ~320kA achieving a maximum radial accessibility of ~12cm; without field error, this transition would occur at ~240kA achieving a maximum radial accessibility of ~18cm from the wall. The main effect of the field error is introduction of higher harmonics near the wall at a higher plasma current, corresponding to a deposition location closer to the wall than could be attained if the field reduction was not present. Correction of field error in a thick shelled RFP, such as MST, or use of EBW heating in a thin shelled RFP such as RFX-mod, is likely to result in radial accessibilities approaching $r/a > 0.5$, as shown in a GENRAY simulation plotted in **Figure 5.5**.

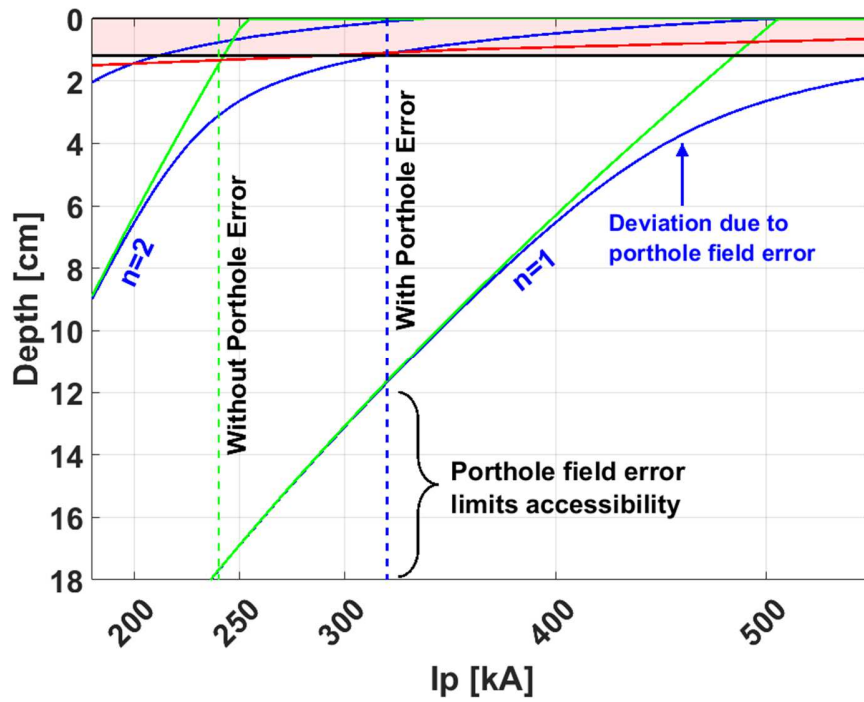


Figure 5.4. Porthole field error reduces local magnetic field near the wall resulting in introduction of higher harmonic resonances near the edge, shown in blue. Radial accessibility is reduced by the transition to edge absorption at a higher I_p than would occur in the absence of a porthole, shown in green.

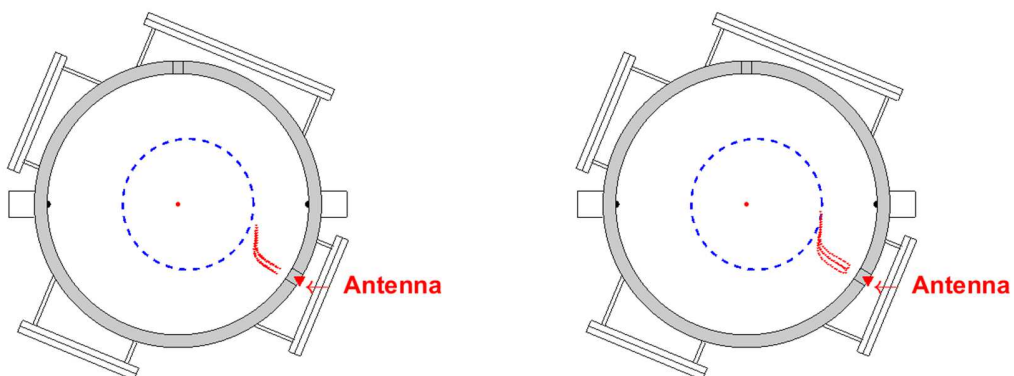


Figure 5.5. Genray plot of first harmonic EBW deposition in a 260kA standard plasma (left) and 225kA PPCD plasma (right). Approximate location of the $r/a=0.5$ flux surface is marked in blue.

5.2 Conclusions

In summary, the first observation of RF heating in the RFP using the EBW is reported for fundamental and higher harmonics ($n=1-7$) utilizing XB mode conversion in the near field of a waveguide antenna. Propagation across, and heating in, regions of magnetic field that is either stochastic or has broken flux surfaces are demonstrated. Deposition location was controllable with $|B|$. In the thick-shelled MST RFP, the radial accessibility of EBW is limited to $r/a > 0.8$ (~ 10 cm) by magnetic field error induced by the porthole necessary for the antenna; accessibility in a thin-shelled device with actively controlled saddle coils (without the burden of substantial porthole field error) is likely to be $r/a > 0.5$ in agreement with ray tracing studies. Addition of field error correction coils to thick shelled RFPs will result in improved accessibility. High radial transport rates in the RFP limit heated electron confinement times. Reduction of magnetic stochasticity with PPCD increases confinement, however farther increases in heated electron confinement time and launched power are required to achieve observable increases in plasma temperature. EBW heating is presently applicable for diagnostic use in the RFP by providing a population of toroidally drifting trapped suprathermal electrons at a controllable edge location.

5.3 Future Work

Several areas of the EBW heating process in the RFP require further research to improve accessibility, heating power, and applications of the EBW in the RFP. Porthole field error limits accessibility in thick shelled RFPs, such as MST, due to interruption of wall currents. Limitations in antenna power handling capability impose an upper bound on the maximum RF heating power available; particularly important in the RFP where the Ohmic heating power can be in the MWs. Applications of EBW heating in the RFP require further development to address uses such as probing of profile stiffness, exploration of ETG modes, and off axis current drive.

The presence of porthole field error limits $n=1$ radial accessibility of the EBW to $r/a=0.8$ in a thick walled RFP by reducing $|B|$ at the launch point, thus introducing the second harmonic at a higher magnetic field than would normally occur. In the absence of porthole field error, radial accessibility is predicted to be $r/a=0.5$. Field error may be corrected or reduced in a thin walled RFP using actively driven saddle coils for plasma control, such as RFX, or by using error field correction coils around the launch porthole.

Antenna power handling requires further optimization on the 5.5GHZ system. Power limitations could be improved by optimization of the pillbox window assemble and antenna structure to allow increased launch power without arcing. Addition of a local limiter around the antenna structure, and correction of porthole field error to reduce plasma bombardment of the antenna aperture may also increase heating capabilities and improve coupling. In potential future RFPs, higher field devices will allow use of higher frequency EBW heating, increasing power handling of a given antenna cross sectional area.

There are several factors that motivate continued study of the EBW in varied magnetic geometries. EBW finds use in component test facilities conducting first wall material studies for next-step fusion devices [93]. In advanced stellarators, EBW allows accessibility of the core to rf heating in high density. EBW propagation across a stochastic magnetic field implies feasibility in advanced tokamak heating scenarios, where resonant magnetic perturbations (RMP) generate edge stochastic fields for edge localized mode (ELM) control [99]. Localized electron heating with the EBW remains relevant for diagnostic applications in RFP plasmas with low electron confinement. EBWs may be used to probe profile stiffness during low magnetic fluctuation periods, as well as probe local beta limit and electron thermal gradient (ETG) stability in the RFP by localized heating in the well confined region of the strong temperature gradient at the edge.

Bibliography

- [1] I. B. Bernstein, Waves in a Plasma in a Magnetic Field. *Physical Review*. 109, 10 (1956)
- [2] J. Preinhaelter And V. Kopeck, Penetration of high-frequency waves into a weakly inhomogeneous magnetized plasma at oblique incidence and their transformation to Bernstein modes. *J. Plasma Physics*. 10, 1 (1973)
- [3] R.N. Dexter et.al. *Fus. Sci. and Tech*. 19,131 (1991)
- [4] C.B. Forest, P.K. Chattopadhyay, R.W. Harvey, and A.P. Smirnov, *Phys. Plasmas* 7, 1352 (2000)
- [5] T. Stix, *Waves in Plasmas*, American Institute of Physics; 1992 edition (1997)
- [6] D. G. Swanson, *Plasma Waves*, Academic Press (2012)
- [7] M. Cengher, Thesis, University of Wisconsin
- [8] M. Cengher, J.K. Anderson, V. Svidzinski, C.B. Forest. *Nuc. Fusion*. 46, 521, (2006)
- [9] J. Preinhaelter and V. Kopecký, *J. Plasma Phys*. 10, 1(1973).
- [10] A.K. Ram, A. Bers, C. N. Lashmore-Davies. Emission of electron Bernstein waves in plasmas. *Phys. Plasmas* 7, 4084–9 (2000)
- [11] H. Laqua. Electron Bernstein wave heating and diagnostic. *Plasma Phys. Control. Fusion* 49, R1–R42 (2007)
- [12] A. Surkov. Et.al. Parametric decay instability accompanying electron Bernstein wave

-
- heating in MAST. 32nd EPS Conference on Plasma Phys. ECA Vol.29C, P-5.103 (2005)
- [13] E. Albers, K. Krause, H. Schluter. Experimental study of parametric decay close to the upper hybrid frequency. *Plasma Physics*, 20,361 (1978)
- [14] Shevchenko, V., et al. "Development of electron Bernstein wave research in MAST." *Fusion science and technology* 52.2 (2007): 202-215.
- [15] C. B. Forest et. al. Radio frequency wave experiments on the MST reversed field Pinch. *AIP Conference Proceedings* 485, 193 (1999);
- [16] Harvey, R. W., and M. G. McCoy. "The cql3d fokker-planck code." *IAEA TCM, Montreal* (1992).
- [17] Petrov, Yu V., and R. W. Harvey. "Finite orbit width features in the CQL3D code." *24th IAEA Fusion Energy Conference, San Diego*. 2012.
- [18] J. Anderson. RF Heating and Current Drive Experiments on MST, 14th IEA RFP Workshop
- [19] MHD simulation of RF current drive in MST, E.R. Hendries, J.K. Anderson, S. Diem, C.B. Forest, R.W. Harvey, J.A. Reusch, A.H. Seltzman, C.R. Sovinec, *Radiofrequency Power in Plasmas: AIP Conference Proceedings* 1580, 510 (2014)
- [20] H. Sugai, Mode Conversion and local Heating below the Second Electron Cyclotron Harmonic. *Phys. Rev. Lett.* 47, 1899 (1981)
- [21] Y.Y. Podoba et al. Direct Observation of Electron-BernsteinWave Heating by O-X-B-Mode Conversion at Low Magnetic Field in the WEGA Stellarator. *Phys. Rev. Lett.* 98 255003 (2007)

-
- [22] P.K. Chattopadhyay, *et al.* Electron Bernstein wave emission from an overdense reversed field pinch plasma. *Phys. Plasmas* 9, 752 (2002)
- [23] H. P. Laqua et al. Electron Bernstein Wave Emission from an Overdense Plasma at the W7-AS Stellarator. *Phys. Rev. Lett.* 81, 2060 (1998)
- [24] B. Jones et al. Controlled Optimization of Mode Conversion from Electron Bernstein Waves to Extraordinary Mode in Magnetized Plasma. *Phys. Rev. Lett.* 90, 165001 (2003)
- [25] S. J. Diem et al. Collisional Damping of Electron Bernstein Waves and its Mitigation by Evaporated Lithium Conditioning in Spherical-Tokamak Plasmas. *Phys. Rev. Lett.* 103, 015002 (2009)
- [26] P.K. Chattopadhyay, *et al.* Electron Bernstein wave emission from an overdense reversed field pinch plasma. *Phys. Plasmas* 9, 752 (2002)
- [27] H. P. Laqua et al. Resonant and Nonresonant Electron Cyclotron Heating at Densities above the Plasma Cutoff by O-X-B Mode Conversion at the W7-As Stellarator. *Phys. Rev. Lett.* 78, 3467 (1997)
- [28] H. P. Laqua et al. Electron-Bernstein-Wave Current Drive in an Overdense Plasma at the Wendelstein 7-AS Stellarator. *Phys. Rev. Lett.* 90, 075003 (2003)
- [29] Y.Y. Podoba et al. Direct Observation of Electron-BernsteinWave Heating by O-X-B-Mode Conversion at Low Magnetic Field in the WEGA Stellarator. *Phys. Rev. Lett.* 98, 255003 (2007)
- [30] T. Maekawa et al. Doppler-Shifted Cyclotron Absorption of Electron Bernstein Waves via Nk-Upshift in a Tokamak Plasma. *Phys. Rev. Lett.* 86, 3783 (2001)

-
- [31] V. Shevchenko et al. Generation of Noninductive Current by Electron-Bernstein Waves on the COMPASS-D Tokamak. *Phys. Rev. Lett.* 89, 265005 (2002)
- [32] Forest, C. B., R. W. Harvey, and A. P. Smirnov. "Power deposition by mode converted electron Bernstein waves in the DIII-D 'heat pinch' experiments." *Nuclear fusion* 41.5 (2001): 619.
- [33] Luce, T. C., C. C. Petty, and J. C. M. De Haas. "Inward energy transport in tokamak plasmas." *Physical review letters* 68.1 (1992): 52.
- [34] S. Shiraiwa et al. Heating by an Electron Bernstein Wave in a Spherical Tokamak Plasma via Mode Conversion *Phys. Rev. Lett.* 96, 185003 (2006)
- [35] M. Uchida *et al.* Rapid Current Ramp-Up by Cyclotron-Driving Electrons beyond Runaway Velocity. *Phys. Rev. Lett.* 104, 065001 (2010)
- [36] Taylor, J. Brian. "Relaxation of toroidal plasma and generation of reverse magnetic fields." *Physical Review Letters* 33.19 (1974): 1139.
- [37] B. Chapman et.al. The physics of sawtooth stabilization. *Plasma Phys. Control. Fusion* 49,B386 (2007)
- [38] Sarff, J. S., et al. "Fluctuation and transport reduction in a reversed field pinch by inductive poloidal current drive." *Physical review letters* 72.23 (1994): 3670.
- [39] J. Reynolds, C. Sovinec, S. Prager Nonlinear magnetohydrodynamics of pulsed parallel current drive in reversed-field pinches. *Phys. Plasmas* 15, 062512 (2008)
- [40] M. Kaufman, Lower Hybrid Experiments Using an Interdigital Line Antenna on the Reversed Field Pinch, Thesis, University of Wisconsin-Madison (2009)

-
- [41] D. Burke, Kinetic modeling and lower hybrid current drive in the reversed field pinch, Thesis, University of Wisconsin-Madison (2010)
- [42] C.B. Forest, P.K. Chattopadhyay, R.W. Harvey, and A.P. Smirnov, *Phys. Plasmas* 7, 1352 (2000)
- [43] Fisch, N. J., and Allen H. Boozer. "Creating an asymmetric plasma resistivity with waves." *Physical Review Letters* 45.9 (1980): 720.
- [44] J. Decker. ECCD for Advanced Tokamak Operations Fisch-Boozer versus Ohkawa Methods, Proc. of 15th Top. Conf. Radio Freq. Power in Plasmas, (2003)
- [45] G. Taylor, et.al. Efficient generation of non-inductive, off-axis, Ohkawa current, driven by electron Bernstein waves in high β , spherical torus plasmas. PPPL report PPPL-3943 (2004)
- [46] P. J. Fimognari, et al. *Plasma. Phys. Cont. Fusion.* 52, 095002 (2010)
- [47] M. Cengher, J.K. Anderson, V. Svidzinski, C.B. Forest, Coupling to the electron Bernstein wave using a phased array of waveguides in MST reversed field pinch. *Nuc. Fusion.* 46, 521, (2006)
- [48] R. O'Connell et.al. *Phys. Rev. Lett.* 91, 045002 (2003)
- [49] R. B. Howell, H. F. Vogel, Magnetic field perturbations due to a hole in a conducting wall on the ZT-40M reversed field pinch, *J. Appl. Phys.* 56, 2017 (1984)
- [50] J. W. Rudmin, J. R. Drake. Magnetic field perturbations due to a hole in a conducting wall near a time changing magnetic field, *J. Appl. Phys.* 84, 1032 (1984)

-
- [51] P. J. Fimognari, *et al.* Port hole perturbations to the magnetic field in MST. *Plasma. Phys. Cont. Fusion.* 52, 095002 (2010)
- [52] V. Erckmann, U. Gasparino, Electron Cyclotron resonance heating and current drive in toroidal fusion devices. 36, 1869 *Plasma phys. Control. Fusion* (1994)
- [53] R.C. Myer, M. Porkolab, G.R. Smith, A.H. Kritz, Electron Cyclotron Wave Propagation and Absorption in the Compact Ignition Tokamak, PFC/JA-89-2 *Nuc. Fusion* (1989)
- [54] Yong-Soon Bae, Won Namkung. *Theory of Waves in Plasmas. Lecture notes*, <http://psl.postech.ac.kr/> (2016)
- [55] T. Biewer. *Electron Thermal Transport in the Madison Symmetric Torus. Thesis*, UW Madison, (2002)
- [56] M. Miller. *Non-axisymmetric Flows and Transport in the Edge of MST. Thesis*, UW Madison (2011)
- [57] W. Stacey. *Fusion Plasma Physics*. Wiley-VCH (2005)
- [58] J.D. Callen. *Coulomb Collisions. Notes Ch2* (2006)
- [59] Huba, J. D. (Joseph D.), 1950-. *NRL Plasma Formulary*. Washington, DC :Naval Research Laboratory, 1998. Print.
- [60] H. Tawara *et.al.* Cross Sections and Related Data for Electron Collisions with Hydrogen Molecules and Molecular Ions. 19, 617 *J. Phys. Chem. Ref. Data* (1990)
- [61] C.F. Barnett *et.al.* Atomic and molecular collision cross sections of interest in controlled thermonuclear research. ORNL-3113 (1964)

-
- [62] T. D. Rempel, et.al. Edge Electrostatic Fluctuations and Transport in a Reversed-Field Pinch. *Phys. Rev. Lett.* 67, 1438 (1991)
- [63] N. E. Lanier et.al. Control of Density Fluctuations and Electron Transport in the Reversed-Field Pinch. *Phys. Rev. Lett.* 85, 2120 (2000)
- [64] A. B. Rechester, M. N. Rosenbluth. *Phys. Rev. Lett.* 40, 38 (1978)
- [65] R. O'Connell et.al. Observation of Velocity-Independent Electron Transport in the Reversed Field Pinch. *Phys. Rev. Lett.* 91, 045002-1 (2003)
- [66] A. P. Smirnov and R. W. Harvey, *Bull. Am. Phys. Soc.* 40, 1837 (1995)
- [67] C.B. Forest, P.K. Chattopadhyay, R.W. Harvey, and A.P. Smirnov, *Phys. Plasmas* 7, 1352 (2000)
- [68] M. Kaufman, "Lower hybrid experiments using an interdigital line antenna on the reversed field pinch" Thesis, University of Wisconsin Madison (2009)
- [69] Choi, D. W. et al. "Digital complex demodulation applied to interferometry." *Review of Scientific Instruments* 57.8 (1986)
- [70] A. Seltzman. Design of a resonant soft switching power supply for stabilized dc impulse delivery. Thesis, University of Wisconsin – Madison (2012)
- [71] A. H. Seltzman. P. D. Nonn, and J. K. Anderson. Design and Modeling of Nanocrystalline Iron Core Resonant Transformers for Pulsed Power Applications. *IEEE Transactions on Dielectrics and Electrical Insulation*, 20,1153 (2013)
- [72] H.A. Kramers, On the theory of X-ray absorption and of the continuous X-ray spectrum, *Philos. Mag.* 46 (1923) 836–871.

-
- [73] M, Semaan and C. A. Quarles. A model for low-energy thick-target bremsstrahlung produced in a scanning electron microscope. *X-Ray Spectrom.* 30, 37 (2001)
- [74] J. Trincavelli, G. Castellano. The prediction of thick target electron bremsstrahlung spectra in the 0.25–50 keV energy range. *Spectrochimica Acta Part B* 63, 1–8, (2008)
- [75] G. Castellano, J. Osan, J. Trincavelli. Analytical model for the bremsstrahlung spectrum in the 0.25–20 keV photon energy range. *Spectrochimica Acta Part B* 59 313–319, (2004)
- [76] J. Small, S. Leigh, D. Newbury, R. Myklebust, Modeling of the bremsstrahlung radiation produced in pure-element targets by 10–40 keV electrons, *J. Appl. Phys.* 61, 459–469. (1987)
- [77] Tables of Physical & Chemical Constants (16th edition 1995). 4.2.1 X-ray absorption edges, characteristic X-ray lines and fluorescence yields, Kaye & Laby Online. Version 1.0 (2005) www.kayelaby.npl.co.uk
- [78] Dewey, Mapes and Reynolds (1969) *Progress in Nuclear Energy, Series IX, Analytical Chemistry*, Elion and Stewart (eds), Pergamon.
- [79] B. G. Gokhale *Ann. Phys.* 7, 852 (1952)
- [80] L. Obert and J. A. Bearden *Phys Rev* 54, 1000 (1938)
- [81] D. J. Clayton et.al. An upgraded x-ray spectroscopy diagnostic on MST. *Review Of Scientific Instruments* 81, 10E308 (2010)
- [82] J. Brown et.al. Evaluation Of Algorithms For Reconstructing Electron Spectra From Their Bremsstrahlung Hard X-Ray Spectra. *The Astrophysical Journal*, 643:523–531, (2006)

-
- [83] A. Arkhipov et.al. Reconstruction of Energy Distributions in Electron Beams on the Basis of Bremsstrahlung X-Ray Spectra. IEEE Trans. On Plasma Science, 41,10 (2013)
- [84] A. Seltzman et.al. X-ray analysis of electron Bernstein wave heating in MST. Rev Sci Instrum. 87(11):11E329 (2016)
- [85] D. Reilly, N. Ensslin, H. Smith Jr., S. Kreiner. Passive Nondestructive Assay of Nuclear Materials. US-NRC (1991)
- [86] J. H. Hubbell and S. M. Seltzer, Tables of X-Ray Mass Attenuation Coefficients and Mass Energy-Absorption Coefficients from 1 keV to 20 MeV for Elements Z = 1 to 92 and 48 Additional Substances of Dosimetric Interest. Radiation Physics Division, PML, NIST (1996)
- [87] B.L. Henke, E.M. Gullikson, and J.C. Davis. X-ray interactions: photoabsorption, scattering, transmission, and reflection at E=50-30000 eV, Z=1-92, Atomic Data and Nuclear Data Tables Vol. 54 (no.2), 181-342 (July 1993).
- [88] B.L. Henke, Filter Transmission, http://henke.lbl.gov/optical_constants/filter2.html
- [89] G. Weber, X-Ray attenuation & absorption calculator, http://web-docs.gsi.de/~stoe_exp/web_programs/x_ray_absorption/
- [90] CR-200 Gaussian shaping amplifier: application guide, FAST Comtec GMBH
- [91] A. H. Seltzman, J. K. Anderson, A. M. DuBois, A. Almagri, and C. B. Forest. Rev. Sci. Instrum. 87, 11E329 (2016)
- [92] T. D. Rempel, et.al. Phys. Rev. Lett. 67, 1438 (1991)
- [93] J. Rapp, et al. IEEE Trans. on Plas. Sci. 44.12,3456 (2016)

-
- [94] R. Jaspers, et.al. Phys. Rev. Lett. 72, 4093 (1994)
 - [95] B.E. Chapman, et.al. Phys. Plasmas 9,2061 (2002)
 - [96] R. O'Connell et.al. Phys. Rev. Lett. 91, 045002 (2003)
 - [97] J. B. Taylor. Phys. Rev. Lett. 33, 1139 (1974)
 - [98] R. O'Connell et al. Phys. Rev. Lett. 91, 045002 (2003)
 - [99] T.E. Evans, et al. J. Nuc. Materials. 337, 691-696 (2005)

Appendix A

A more detailed review of previous EBW experiments is presented in this appendix.

1.1.1 Direct Measurement of EBW Mode Conversion

EBW mode conversion was first observed in a laboratory scale device by H. Sugai in 1981 [100]. Direct observation of mode conversion from both fast X-mode waves launched from the outside of the plasma and slow X-mode waves launched from inside the plasma are presented. As the launched wave propagates into increasing density (**Figure A.1**), it evanescently couples through the R cutoff layer and mode converts into the EBW at the UH resonance.

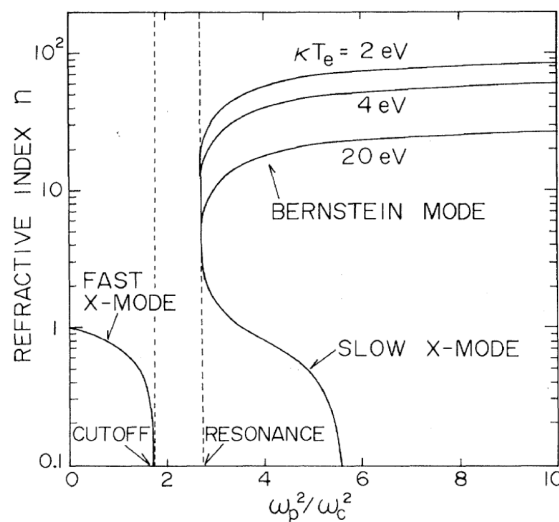


Figure A.1. Refractive index of plasma as a function of ω_p^2/ω_c^2 showing mode conversion from fast and slow X-mode to EBW at the UH resonance. Figure courtesy of [100].

This experiment was performed in a cylindrical pulse discharge device 70cm in diameter and 3m long filled with argon plasma at 0.3mTorr. The plasma characteristics were $\kappa T_e \approx 1.5eV$, $\kappa T_i \approx 0.2eV$, $n_0 = 10^9 - 10^{12} cm^{-3}$, and $B_0 < 500G$. An X-mode wave was launched radially from a waveguide antenna with a 2kW, 0.75-3.0GHz microwave source. A 3mm wire antenna was mounted on an insertable probe and connected to an interferometer. The resulting signal is

proportional to $p(r)\cos(k_{\perp}r)$. For a fast X-mode launch from the plasma edge, the antenna is scanned inward (**Figure A.2**), and a slow variation in phase is shown outside the R cutoff layer (a, left), while after the UH layer (a, right) a rapid variation in phase is seen due to the shorter wavelength of the EBW. Additional experiments were performed for a slow X-mode launch from a loop antenna between the L and UH layers. In this case the slow X-mode propagates outward until it is mode converted to the EBW at the UH layer. The presence of mode conversion to the EBW was verified by comparing the measured k_{\perp} from the interferometer to the theoretical value for the EBW (**Figure A.2**, right).

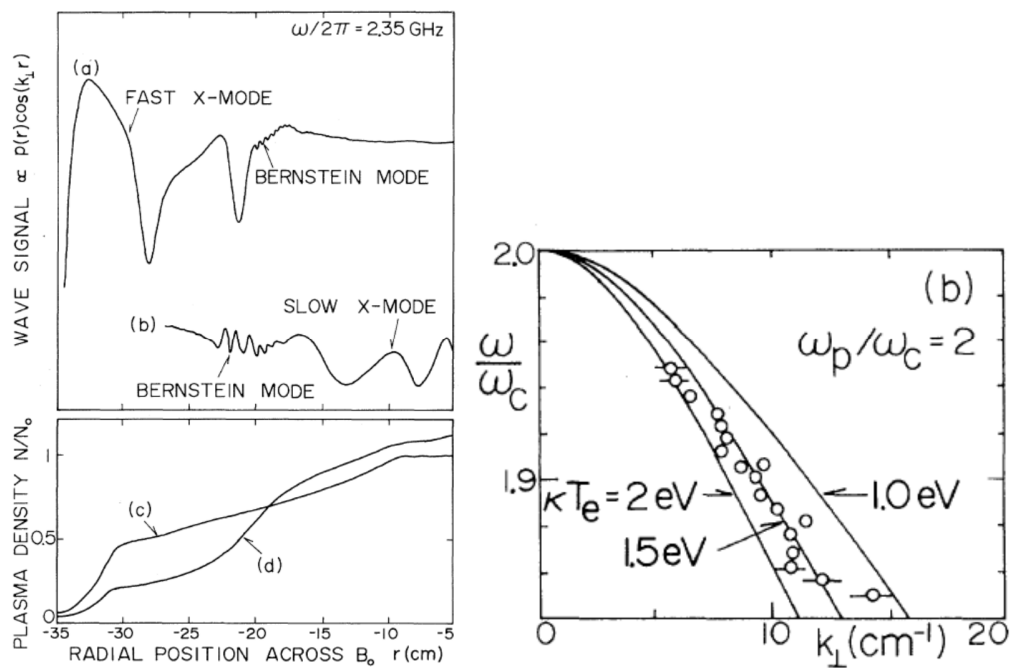


Figure A.2. Interferometer output of radially scanned antenna observing mode conversion between fast x-mode and EBW waves as density increases(a, left plot), and comparison of measured k_{\perp} to theoretical value for the EBW. Figure courtesy of [100].

1.1.2 Observation EBE and EBW Heating and Current Drive in a Stellarator

A series of experiments on the W7AS and WEGA stellarators demonstrated heating, current drive and EBE diagnostics in both X and O mode configurations to access plasma conditions above the density limit. The first EBW heating result was performed in the OXB configuration on the W7AS stellarator [101] using two 70GHz gyrotrons with 110kW power each. The target plasma has a central magnetic field of 1.25-2.0T, a temperature of 560eV, and a central plasma density of $1.6 \times 10^{20} m^{-3}$, chosen to be more than twice the O-mode cutoff density. An O-wave was launched at an oblique angle from the low field side and was converted to an X-wave at the O-wave cutoff layer. The X-wave then propagates back to the UHR layer and mode converts to the EBW. For an optimal launch angle the trajectory of the X and O mode waves will not enter the evanescent region, further improving coupling. The EB will either resonantly damp on a cyclotron harmonic, or non-resonantly deposit the power into the plasma due to collisional damping. Once launched into the plasma, the EBW experiences a cutoff at the UHR layer. For plasmas in this experiment with $\omega_{ce} / \omega < 1$, the UHR completely encloses the plasma, trapping the EBW. The EBW reflects off the UHR, or for oblique angles, converts to an X-wave which converts back to an EBW at the next contact with the UHR; the EBW can only escape the plasma by mode conversion to the X and O wave in a small angular window. EBWs trapped in a non-resonant plasma deposit their power via collisional damping within 6 passes, and non-resonant heating was observed at fields up to 2.0T (**Figure A.3**).

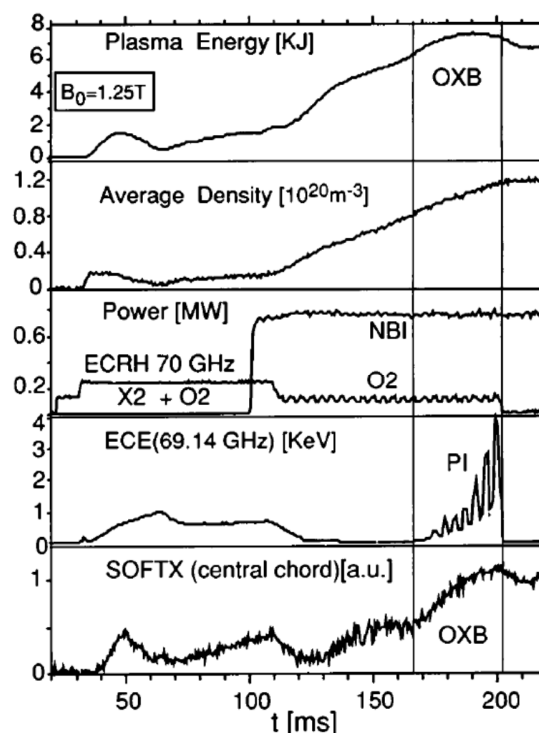


Figure A.3. ECE and SXR emission from plasma correlated with non-resonant OXB heating (between markers). Figure courtesy of [101].

Further experiments in W7AS demonstrated electron Bernstein emission (EBE) from overdense plasma as a diagnostic [102] to overcome the limited radial accessibility during overdense plasma conditions. Since no density limit exists for the EBW, the accessibility of the ECE diagnostic can be extended using an antenna with an oblique viewing angle detecting EBWs that mode convert to x-mode at the plasma edge. The cyclotron resonance is optically thick for the EBW, thus the plasma acts as a blackbody source allowing radiometry. Ray paths were modeled with a ray-tracing code by launching rays between 58 and 68GHz from the detector and following the trajectory until 99% of the power was absorbed; nominally the termination of the ray indicates the emission position of the EBW from the plasma (**Figure A.4**,

left). Each emitting volume in the plasma will have a characteristic frequency, determined by local magnetic field, and will radiate at the thermal level. The EBE diagnostic was calibrated by running W7AS at a plasma density below the O-mode cutoff and measuring thermal ECE at a 90 degree viewing angle. Measurements of EBE from the plasma center compared to measured T_e from SXR measurements during density ramp up in (Figure A.4, right). As the density increases past the O-mode cutoff, the BXO window opens allowing higher EBE frequencies to be detected.

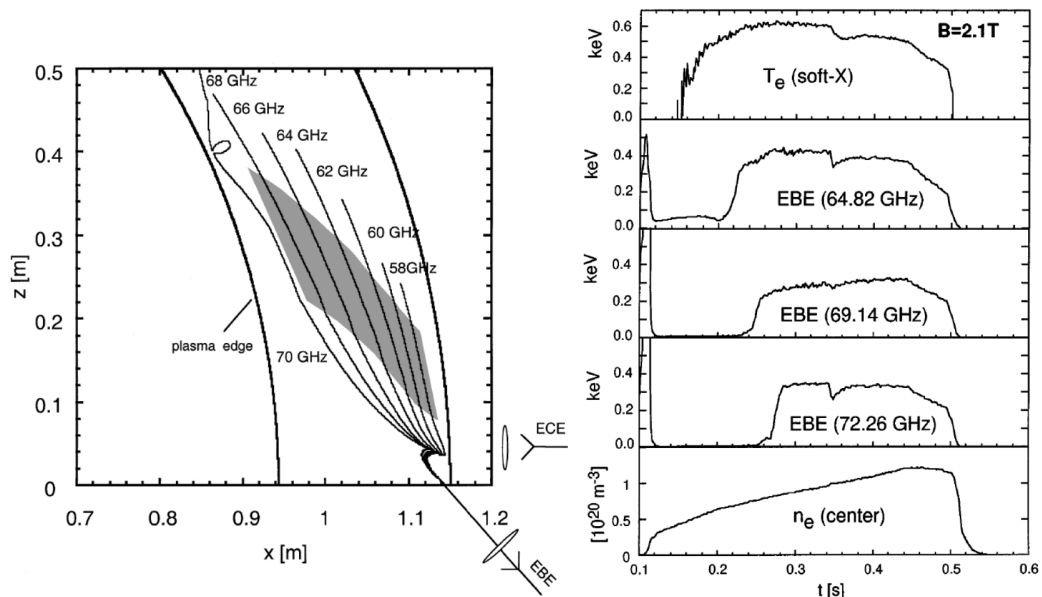


Figure A.4. EBW ray tracing for OXB launch between 58GHz and 68GHz from the edge of W7AS (left). Shaded volume indicates emitting portion of plasma that will be measured on the EBE diagnostic. Measurements of EBE emission channels shown compared to T_e from SXR during a ramp up of density (right). EBE chord signal turns on as O-mode cutoff is reached for the given frequency, opening the BXO window. Figure courtesy of [102].

Successful current drive using OXB has also been demonstrated in W7AS [103]. Stellarators present an ideal target plasma for low power EBW current drive experiments due to

their ability to sustain a current-free plasma, eliminating the problem of separating an inductively driven background current from RF driven currents as in a tokamak, ST or RFP.

In this experiment EBW driven currents were measured by two methods; using inductive current feedback to maintain current free plasma, and allowing driven current to freely evolve in the stellarator. A 70GHz gyrotrons capable of providing up to 450kW power was used to drive current in a neutral beam sustained plasma with a flat density profile of $n_e = 1.05 \times 10^{20} m^{-3}$ to $n_e = 1.2 \times 10^{20} m^{-3}$, $B_0 = 2.15T$, and an electron temperature of 500-800eV. Resonant absorption of the EBW at the Doppler shifted cyclotron resonance was utilized.

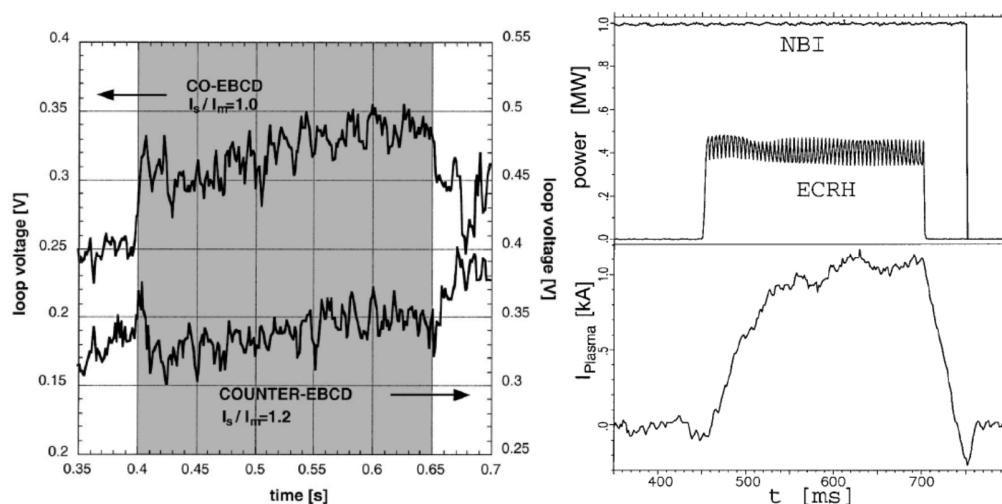


Figure A.5. Co and counter EBW current drive in a current free plasma, measured as a function of loop voltage (left). Freely evolving EBW driven current in a stellarator plasma (right). Figure courtesy of [103].

The measurement of the effects of co and counter current drive on a current free plasma is demonstrated (**Figure A.5**, left) as an enhancement in loop voltage for CO-EBCD and reduction in loop voltage for counter-EBCD. For a plasma where current is allowed to freely

evolve (**Figure A.5**, right), plasma current increases to 1.2kA with 400kW of injected power, yielding a current drive efficiency of 3A/kW.

Direct observation of the OXB mode conversion process and measurement of the resulting EBW heated electrons has also been measured in the WEGA stellarator [104]. In WEGA a 2.45GHz, 26kW microwave source is used to launch two lobes at +42 degrees toroidally, chosen to be near the optimum launch angle of 50 degrees as calculated with WKB and full wave codes. The target plasma has density $n_e = 10^{18} m^{-3}$ and electron temperature of 12eV. Electrostatic probe measurements in the plasma determined that the amplitude of the E_y electric field component increased as the wave approached the UHR, additionally the phase of the wave, measured with a heterodyne system, jumps at the UHR (**Figure A.6**, left). To confirm the presence of heated electrons, RF power is modulated at 12 kHz, faster than the typical 1ms confinement time and the amplitude and phase of the perturbed fast and thermal electron fraction, measured with Langmuir probes, is measured. (**Figure A.6**, right). It is observed that the fast electron perturbation amplitude increases sharply inside the LCFS along with an increase in plasma temperature verifying EBW deposition and heating inside the LCFS.

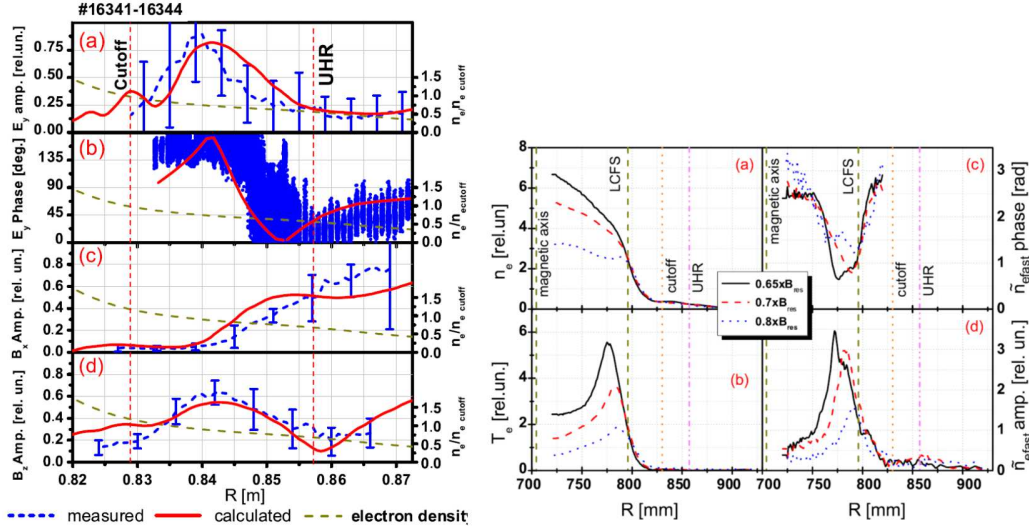


Figure A.6. Increase in electric field amplitude of E_y electric field and phase jump as EC wave crosses the UHR (left). Amplitude and phase of EBW heated thermal and fast electrons showing majority of power deposition occurs on the Doppler shifter fast electron tail inside the LCFS (right). Figure courtesy of [104].

1.1.3 Observation EBW Heating and Current Drive in a Tokamak

EBW heating was determined to be the root cause of off axis power deposition in the DIII-D tokamak [105] which was originally inferred to be due to a “heat pinch” effect during X-mode heating. In these experiments, an X-mode polarized wave was launched from the inboard side of the DIII-D tokamak using a 60GHz, 1MW gyrotrons into a $B_{t0} < 2.14T$ target plasma with $n_e = 1 \times 10^{13} \text{ cm}^{-3}$ to $n_e = 4 \times 10^{13} \text{ cm}^{-3}$. The launched wave encountered an X-mode resonance before reaching the core, partially depositing some of the wave power. Due to relatively high transmission rates, up to 50% of the X-mode wave passed through the first harmonic resonance

and propagated outward until it hit the UHR layer where it was mode converted into the EBW and was reflected back towards the core. The Doppler shifted resonance caused the EBW to be strongly damped at a location closer to the core than the X-mode resonance, providing a core-localized heat source. Initial theories in previous publications were that a “heat pinch” effect caused heated electrons to be transported up the electron temperature gradient, however subsequent modeling with Genray indicated that the core localized heating was due to the transmitted fraction of the X-mode wave being mode converted to the EBW and reflected back inward where it was absorbed at a more core localized location (**Figure A.7**). These effects were found to increase with increasing density, as the transmitted fraction of the X-mode wave increased.

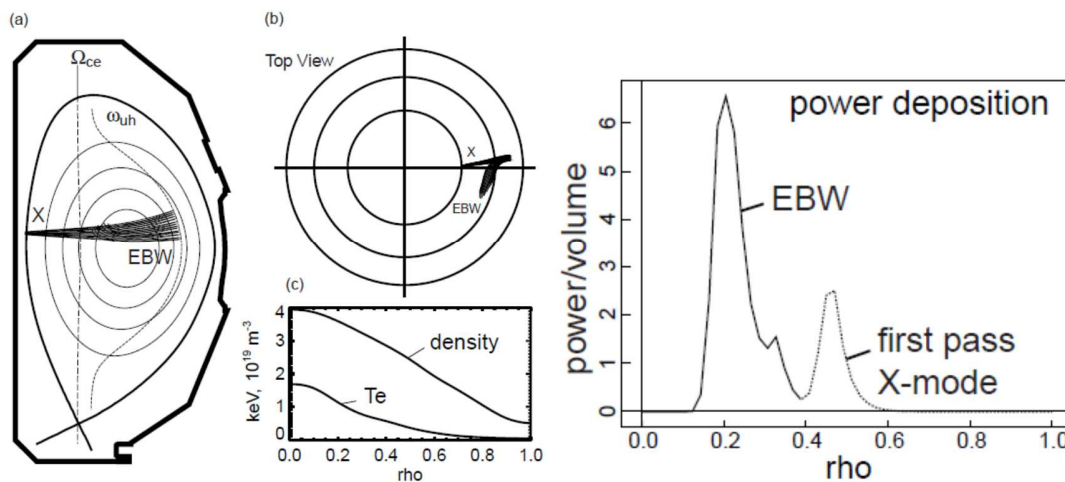


Figure A.7. Ray trajectory of launched X-mode wave passing through the first harmonic resonance, mode converting to the EBW at the UHR and being absorbed near the core (left). Power deposition profile of X-mode and EBW waves showing EBW absorption nearer to the core than the x-mode deposition (right). Figure courtesy of [105].

EBW heating was first observed in the WT-3 tokamak [106] using XB conversion after reflection from a mode converter plate. A 48GHz, 150kW gyrotrons launched into a $B_{t0} < 1.75T$ target plasma with density $n_e = 1.1 \times 10^{13} \text{ cm}^{-3}$ from a launcher located at the top of the machine. The launch was initially an O mode Gaussian beam but was reflected off a polarizer located on the inboard side of the vacuum vessel. The polarizer plate converts the O-mode wave into an X-mode wave that is reflected back into the plasma for XB conversion. During EBW heating loop voltage was observed to decrease along with an increase in H-alpha, SXR, HXR, and ECE emissions (**Figure A.8**, left). Both ECE and HXR emissions had a finite ramp-up time and persisted after turn-off of EBW heating indicating the production of a supra-thermal electron population. The constant value of loop voltage and SXR emission during the RF pulse implies that the bulk electron temperature keeps a constant profile and the population of fast electrons is not significant. The time constant for bulk electron temperature change is estimated to be $\sim 1\text{ms}$. Ray tracing predictions and SXR tomography during EBW heating indicates that the heated electrons form an annular ring near the center of the plasma (**Figure A.8**, right).

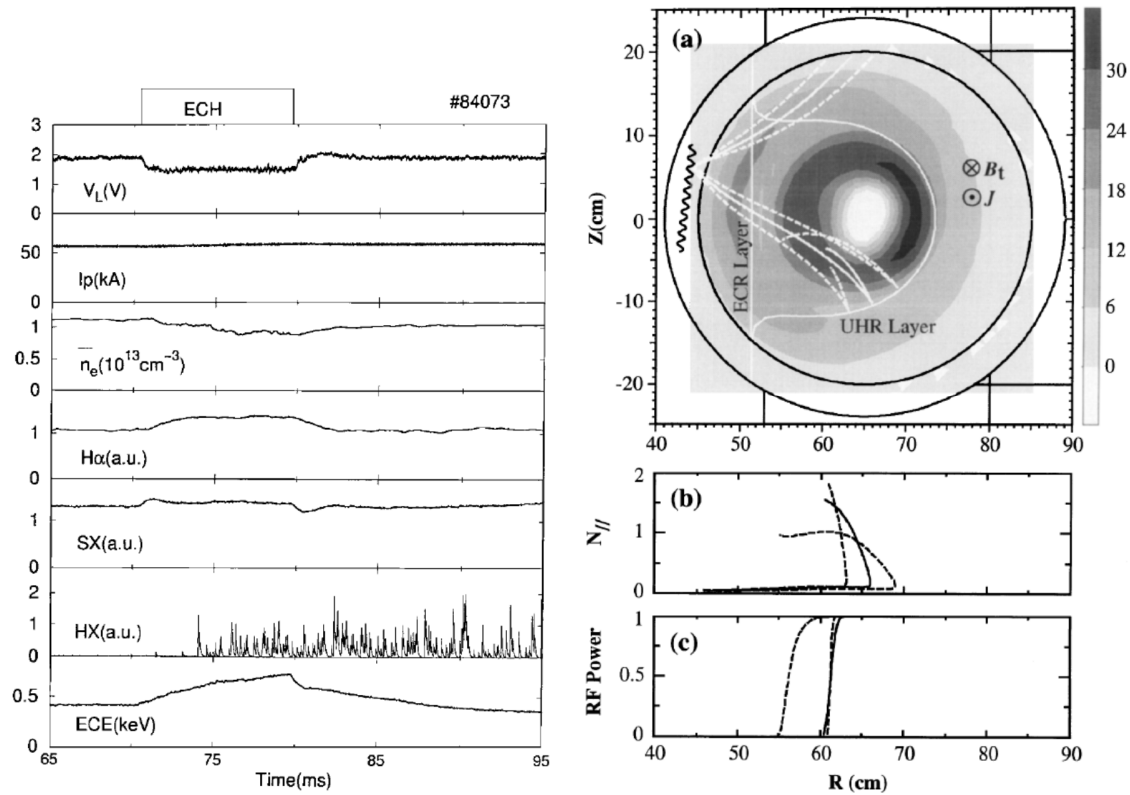


Figure A.8. EBW heating of the plasma is correlated with a decrease in loop voltages as well as increase in H-alpha, SXR, HXR and ECE emission (left). SXR tomography of plasma demonstrating EBW heating location is shown with an overlay of ray paths (right). Figure courtesy of [106].

Demonstration of EBW current drive as successfully achieved in the COMPASS-D tokamak [107] using XB mode conversion. An X-mode wave was launched from the high field side by a 60GHz gyrotron operating at 600kW for 100ms into a target plasma of $n_e = 1.8 \times 10^{19} \text{ m}^{-3}$, 150kA and $B < 2.05T$ within a ± 32.6 degree toroidal angle which was varied in 8.4 degree increments. The central electron temperature was typically 1.5keV. Ray tracing

codes were used to simulate X and B mode propagation; n_e and T_e were measured in 50ms increments using Thomson scattering (**Figure A.9**).

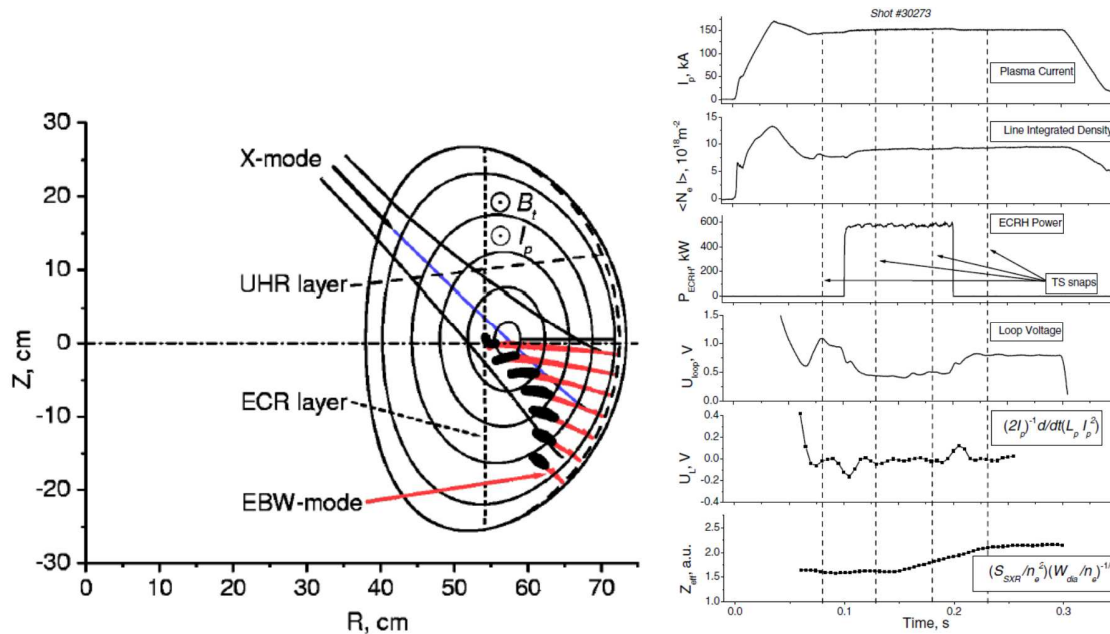


Figure A.9. EBW ray tracing simulation for heating scenario in Compass-D showing X-mode launch through ECR layer at perpendicular angle, mode conversion at UHR and subsequent EBW absorption (left). Plasma parameters during EBW experiment showing locations of Thomson scattering measurements (right). Figure courtesy of [107].

During the ECH period, the loop voltage decreased by 0.5V and there was a slight increase in SXR emission during the last half of the RF pulse. It was noted that at perpendicular angles the X-mode was weakly absorbed at the EC layer, allowing most wave power to reach the UHR for mode conversion. The EBW mode was found to be most strongly absorbed for perpendicular angles, indicating that the highest heating efficiency occurs with use of the EBW rather than X-mode alone.

The Thomson scattering system was used to measure central electron temperature profiles and determine central electron temperature as a function of toroidal launch angle, showing a peak at a perpendicular launch. Measurements of V_{loop} and T_e were used to estimate the driven current in the plasma. Non-inductive currents of 100kA were observed in counter current drive mode (**Figure A.10**). EBW current drive efficiency was found to be much greater than ECCD efficiency.

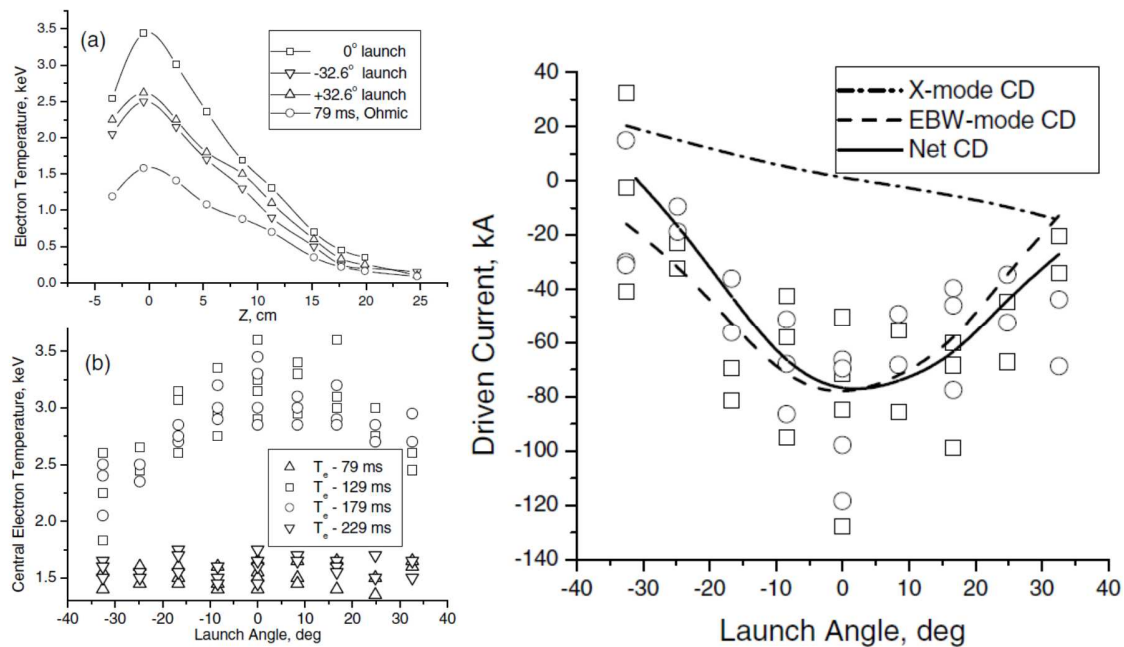


Figure A.10. Thomson scattering measurements of central electron temperature profiles and measurement of central electron temperature vs. toroidal launch angle showing peak heating efficiency occurs at 0 degrees (left). Current drive vs. toroidal launch angle estimated from V_{loop} and T_e measurements showing a peak at 0 degrees (right). Figure courtesy of [107].

1.1.4 Observation EBW Heating and Current Drive in a Spherical Tokamak

Due to the low aspect ratio of a spherical tokamak (ST), reduction in volume of the central solenoid is of considerable benefit. The use of EBW current drive in the ST has been of considerable interest for startup and non-inductive current drive. A number of EBW experiments have been performed on a variety of devices examining EBE, EBW properties in collisional plasmas, EBW heating, and EBCD based ramp up.

The first observations of EBE were performed in the CDXU spherical tokamak [108], using an X-mode polarized antenna a radiometry diagnostic. The use of EBE allows a higher data rate to be achieved with simpler instrumentation than a Thomson scattering system. Comparisons with Thomson scattering indicate ~100% conversion to X-mode of thermally emitted EBW. A movable local limiter was used to optimize the edge density scale length for optimum coupling from the EBW. The confirmation of EBE in the ST implies that the inverse process may be used for EBW heating, allowing current drive in the overdense core of the plasma. CDXU was operated with plasma parameters of $n_e = 4 \times 10^{13} \text{ cm}^{-3}$, and $B < 0.21 \text{ T}$, yielding a highly overdense plasma with $f_{pe} / f_{ce} = 3-10$. Mode conversion efficiency was found to be highly dependent on L_n . Previous experiments with the antenna located outside a vacuum window achieved a mode conversion efficiency of $C \sim 10\%$. Subsequent relocation of the antenna inside the vacuum vessel and installation of a movable limiter to optimize L_n resulted in achieving mode conversion efficiencies of up to $C \sim 100\%$ by shortening L_n in the scrape off layer reducing the evanescent region between f_R and f_{UH} from a few cm to a few mm. Measured emission intensity with the installation of the local limiter was observed to increase by an order of magnitude (**Figure A.11**).

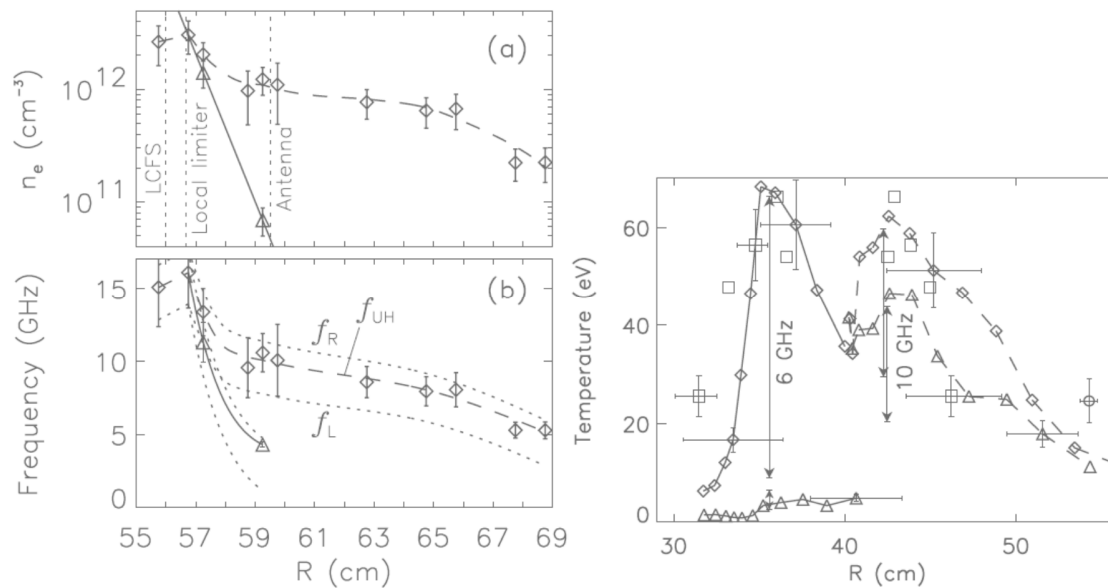


Figure A.11. Density profiles with (triangles) and without (diamonds) installation of the local limiter showing steepening of the edge density gradient (left). Measured emission with (diamonds) and without (triangles) installation of a local limiter for Ln optimization showing an order of magnitude increase in measured signal (right). Figure courtesy of [108].

Observation of such a significant increase in mode conversion efficiency with edge Ln control demonstrates the sensitivity of Bernstein wave conversion to edge density scale length. With the implementation of an adjustable limiter, $C \sim 100\%$ conversion efficiency has been attained allowing successful Te radiometry in an overdense plasma.

EBW heating in a spherical tokamak was first observed in TST-2 utilizing XB mode conversion [109], achieving 50% heating efficiency. Due to the location of the L cutoff, a high field side launch is not possible in the ST, further the lack of physical accessibility due to the dimensions of the central solenoid further constrain high field side launch locations (**Figure A.12**, left). In TST-2, a low field side launch with XB conversion was chosen to simplify the

launcher design. The low field side launch required a local limiter to steepen the edge density gradient to enhance mode conversion efficiency. The local limiter design on TST-2 was modeled after the one used on the CDX-U experiment; the limiter consists of a movable structure surrounding the launcher antenna which shortened the density scale length from 30mm to ~6mm. Microwave power at 8.2GHz and up to 200kW was injected through a launcher structure consisting of 8 horns positioned on the low field side of the torus at a target plasma of $n_e = 1 \times 10^{19} m^{-3}$, $B < 0.3T$, and $\omega_{pe}^2 / \omega_{ce}^2 \sim 10$ with 300kW of ohmic heating power. When the density scale length was optimized, over 80% mode conversion efficiency was realized with 140kW net RF power injection. During EBW heating a significant increase in stored plasma energy was observed indicating the EBW heated the plasma with 50% efficiency. During RF injection, observation of high energy electron generation was observed, as well as an increase in H-alpha, $P_{rad}(X_{uv})$, and SXR(1-10keV). The SXR detector consisted of a 20ch PIN diode array capable of spatial measurements of the plasma cross section. Observations of SXR emission indicated that the RF heating location is localized to the core region, where ray tracing analysis predicts the EBW will be absorbed (**Figure A.12**, left). It was further observed that heating efficiency decreases as edge density decreases causing the mode conversion region to move outside the local limiter, increasing density scale length. It was calculated that collisional damping in the edge is not a dominant contributor to edge heating for a single pass.

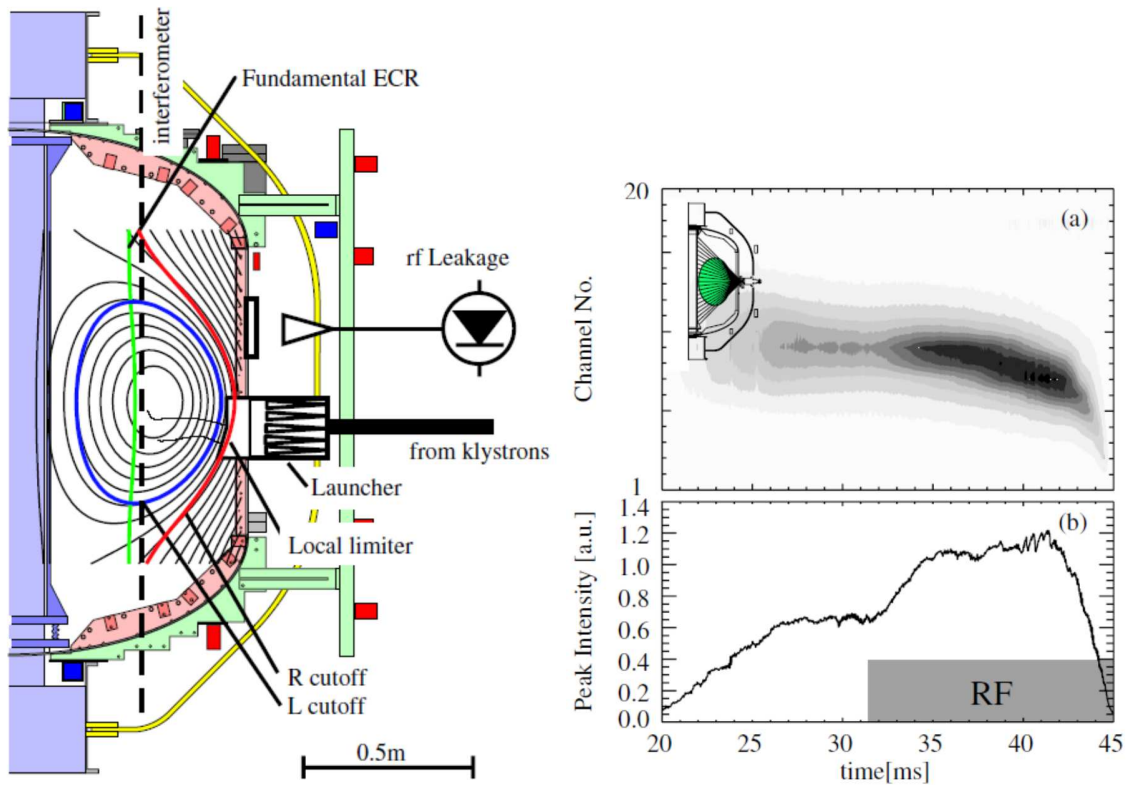


Figure A.12. Cross section of TST-2 showing locations of R and L cutoffs, and launcher (left). Measured SXR emission during RF shot (right). Figure courtesy of [109].

Experiments with EBE diagnostics on NSTX [110] were used to examine the effect of collisional damping in the plasma edge and enhancement of mode conversion efficiency when lithium wall conditioning was used for reduction of edge collision frequency. BXO emission was observed from a plasma with $I_p = 1\text{MA}$, $n_e = 3\text{--}6 \times 10^{19}\text{m}^{-3}$, $T_e(0) < 0.9\text{keV}$, and $B_t(0) < 0.4T$. Simulations showed that strong collisional damping in the edge would absorb a significant fraction of the EBW wave if $\nu_{ei} / \omega > 10^{-4}$ with ν_{ei} being the electron-ion collision rate near the mode conversion layer. This effect was mitigated in this experiment by introducing lithium wall

conditioning to deplete the electron density in the edge plasma, thus moving the mode conversion layer into a region where $v_{ei}/\omega < 10^{-4}$ and electron temperatures increased from 5-9eV to 20eV, improving EBE wave transmission. EBE emission was observed with a quad ridged horn antenna measuring frequencies between 18-36GHz. Observation of EBW transmission efficiency showed an increase from 10% to 60% when lithium wall conditioning was introduced to reduce edge electron density (**Figure A.13**). EBW mode conversion in a ST is predicted to suffer from significant collisional damping in the edge when $v_{ei}/\omega > 10^{-4}$ leading to reduction in current drive efficiency.

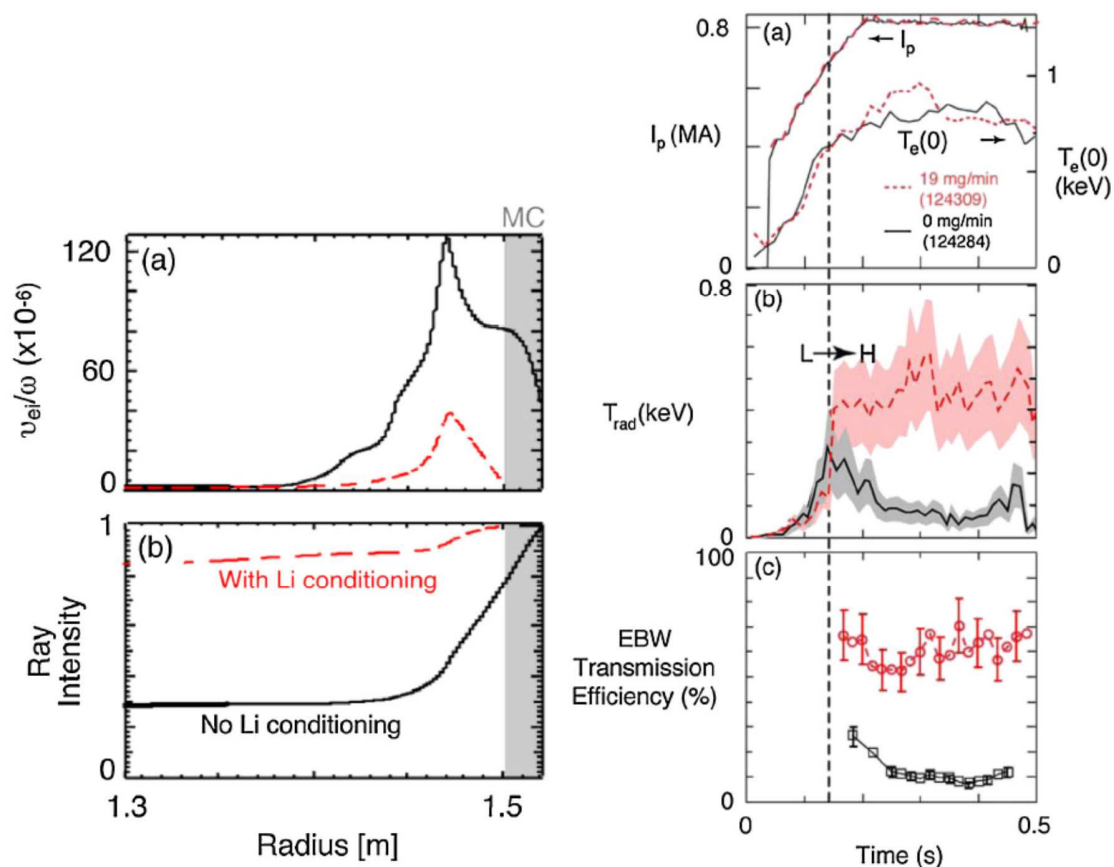


Figure A.13. Simulation of reduction in V_{ei}/ω strongly effecting intensity of EBW ray (left). Comparison of measured EBW transmission efficiency and T_e at the UHR layer with (red) and without (black) Li wall conditioning (right). Figure courtesy of [110].

Observation of EBW current drive in a ST was first demonstrated during current ramp up experiments in the LATE ST [111]. Traditionally, the ST plasma is initiated with inductive current drive methods from the CS, however the structure of the ST design can be greatly simplified if the CS is removed, leading to a decrease in aspect ratio. In this experiment EBW current drive was used to ramp up plasma current at $\sim 260\text{kA/s}$; comparable to observed LHCD ramp up rates. The current carrying fraction was observed to be fast electrons traveling above the runaway velocity. Microwaves at 5GHz and $P_{rf}\sim 190\text{kW}$ were launched obliquely to the magnetic field of $B_T=0.096T$ from a cylindrical waveguide located on the midplane. Observation of RF driven current indicated that a 190kW RF pulse was able to drive up to 20kA in LATE (**Figure A.14**).

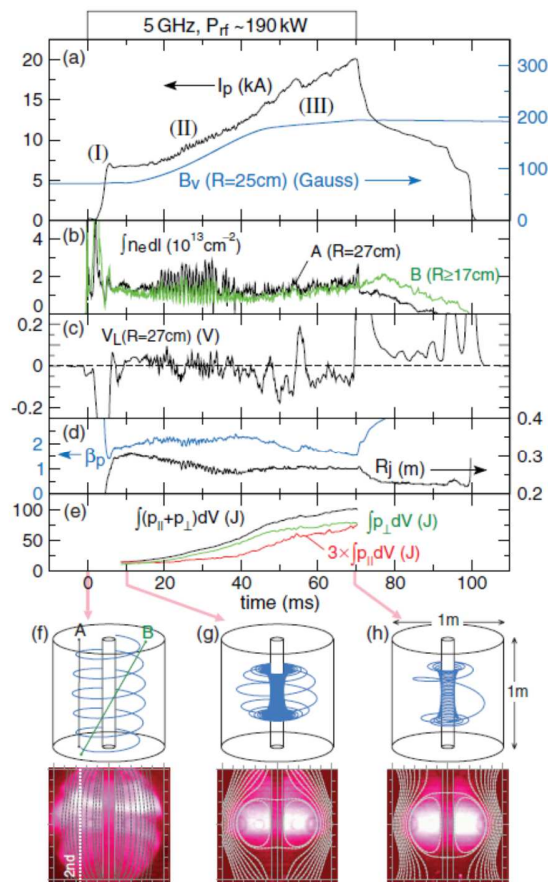


Figure A.14. Measurement of EBW driven current ramp up to 20kA in LATE. Figure courtesy of [111].

1.1.5 EBW Simulations and Observation of Emission and Coupling in the RFP

Previous experiments including EBE, EBW coupling and simulations of EBW heating and current drive have been conducted on MST. To date, MST has been the only RFP on which EBW has been implemented. Several aspects of MST, and the RFP in general, make EBW launch challenging. MST has a close fitting conducting shell, carrying significant wall currents used to initiate and sustain the plasma. Plasma extends up to 1.2cm from the wall prohibiting the

use of an oblique launching structure, or RF mirror assembly for oblique launches. All suitable portholes for RF antennas are aimed perpendicular to the local magnetic field, thus any oblique launch scenario must use electronic beam steering through a phased array setup. Such a setup requires a multiple waveguide array to be installed in a porthole, thus increasing the porthole size requirements.

Porthole access for launcher antennas creates a field error, reducing the field strength in the proximity of the porthole and shifting the EBW resonance outward. In addition the field lines bend outward into the porthole, pulling plasma into the antenna aperture, in many cases causing arcing unless a boron nitride cover is used. Additionally the magnetic geometry of the RFP is such that cutoffs occur within a few cm from the edge in the antennas near field, complicating the launch scenario. Reduction of porthole size decreases the effect of the field error but restricts operation to higher frequencies and may limit launcher design to single waveguides.

EBW coupling was observed in MST [112] using a phased array waveguide at 3.6GHz. Coupling efficiency with respect to launch angle and edge density gradient was measured for both X and O mode launches. Theoretical predictions indicate that an oblique launch increases coupling efficiency for XB mode conversion. Variation of phasing in a multi-arm phased array waveguide antenna allows electronic steering of launch angle to achieve optimal coupling efficiency. The target plasma for this experiment was $I_p = 180-260kA$, $n_e = 0.4-1.2 \times 10^{19} m^{-3}$, $T_e \approx 200eV$, and $|B|(a) = 0.07-0.1T$ with ohmic power of approximately $P_\Omega \approx 2MW$. The plasma core is overdense with $f_{pe} / f_{ce} > 5$. Coupling into a pulsed poloidal current drive (PPCD) plasma yields lower fluctuation plasma and a steepening in edge density gradient leading to better EBW coupling. Edge density profiles were measured with an array of 5 Langmuir probes drawing ion

saturation current mounted on the tip of the antenna for both standard and PPCD plasmas. Measurement of edge density and magnetic field allow the calculation of the R, UH, and L cutoff frequencies (**Figure A.15**, left). Transmission through the evanescent layer was found to be strongly related to the edge density gradient. Spacing of the cutoff layers can be arranged such that the R, UH, and L layers form a cutoff-resonance-cutoff resonator, further improving EBW mode conversion. Measurement of the edge density gradient scale length was found to be about 2.5cm in standard plasmas and reduced to 1.2cm during the good confinement period of PPCD plasmas (**Figure A.15**, right).

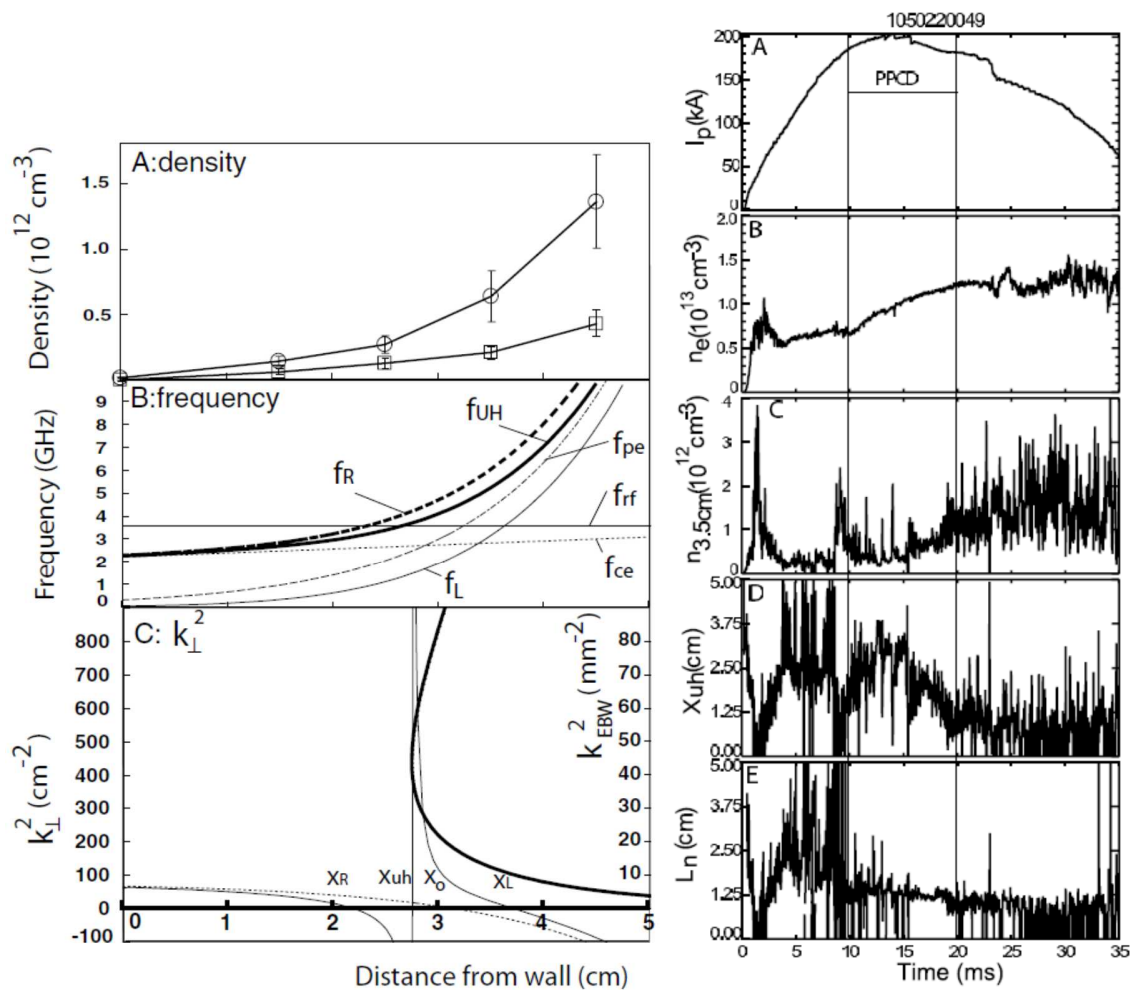


Figure A.15. Edge density in standard (O) and PPCD (square) plasmas, characteristic frequencies, and dispersion relation (left). Evolution of I_p , n_e , n_e at 3.5cm, position of UHR (X_{uh}), and density scale length during a PPCD shot for 3.6GHz. Figure courtesy of [112].

Peak coupling of $C \sim 100\%$ was predicted to occur at $L \sim 1\text{cm}$ and $B = 0.07\text{T}$. In general it was observed that a steeper edge density gradient allows a higher fraction of incident X/O mode power to be converted into EBW by placing the resonance and cutoff layers closer together. Similar results have been observed in tokamak, stellarator, and ST experiments where the

presence of a local limiter to steepen edge density gradient around the antenna significantly improved coupling efficiency to the EBW. Measured values of reflection coefficient vs. density scale length are compared to theoretical predictions in (**Figure A.16**) and the optimal value was determined to be 0.8-1.5cm.

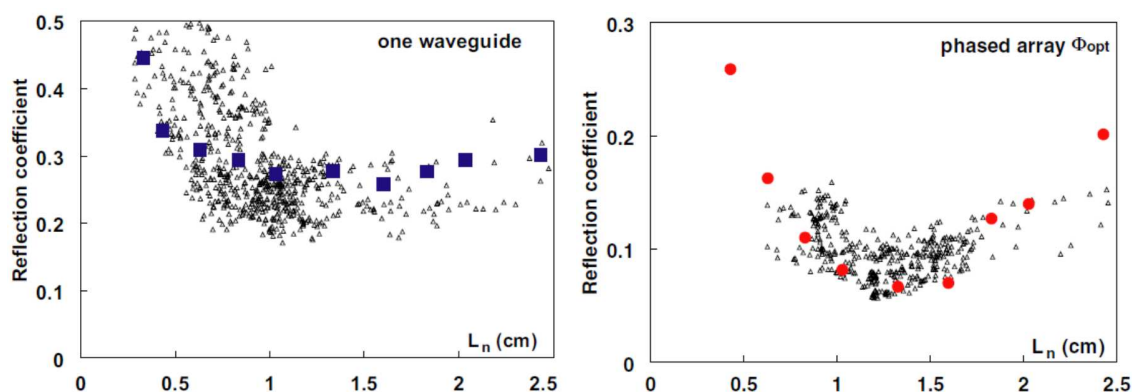


Figure A.16. Reflection coefficient vs. density scale length from a single waveguide (triangles) compared to theoretical values (blue squares) (left). Reflection coefficient vs. density scale length from a phased array at optimum launch angle (triangles) compared to theoretical values (red circles) (right). Figure courtesy of [112].

Coupling to the EBW vs. launch angle was measured using a double waveguide phased array to sweep the launch angle for both X and O mode launches. In this experiment, 10W of power at 3.6GHz was used in each antenna arm with forward and reflected power measured in each arm with a directional coupler. The frequency of one antenna arm was set at 1 kHz above the other and the phase difference was measured using digital complex demodulation. Tests were conducted with no antenna cover as well as with both flat BN covers and ones with grooves milled perpendicular to the wave electric field to resist deterioration of transmitted power when a slightly conductive coating is sputtered onto the cover from the plasma. Use of the BN cover in

PPCD plasmas was found to significantly improve coupling (**Figure A.17**) and optimal launch angle of the X-mode wave was found to occur at -90 degrees phase between the antenna arms.

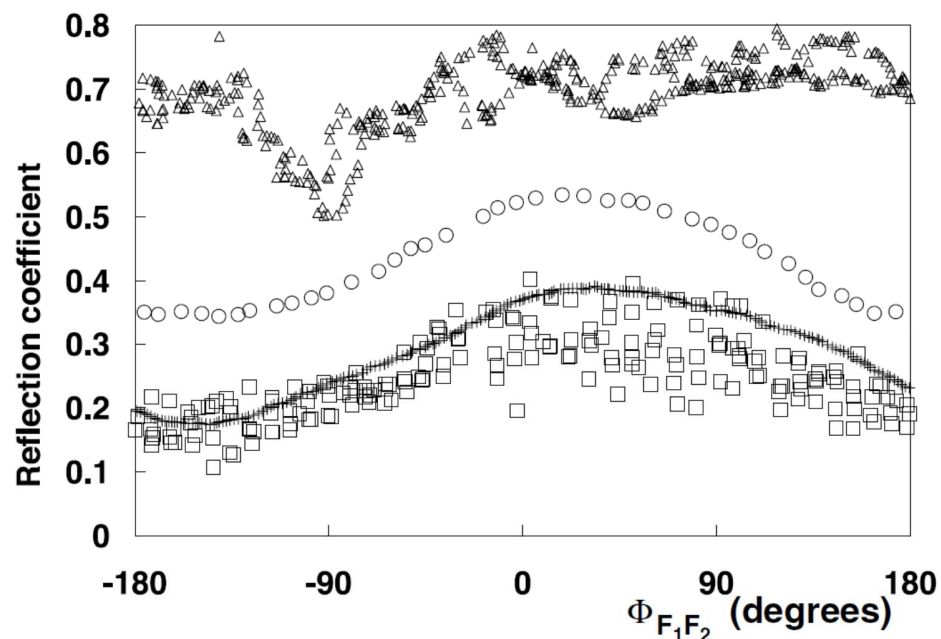


Figure A.17. Measurement of reflection coefficient vs phase for 3.6GHz X-mode launch into a 190kA PPCD plasma. Launch with a BN cover at 1W (square), 50kW (+) and without a BN cover 1W (triangle), and standard plasma at 1W (o). Figure courtesy of [112].

EBE has been observed in MST and utilized for radiometry applications. Comparison of EBE measured radiation temperature to Thomson data indicates that mode conversion efficiency up to 75% has been measured. Observed emission was determined to be preferentially oriented in the X-mode polarization and strongly dependent on edge density gradient and magnetic field profiles [113]. EBW emission in the core of the plasma propagates outward to the UHR layer where it is mode converted into X-mode waves capable of propagating to the edge. Detection of the X-mode spectrum with a low noise absolutely calibrated radiometer allows

measurement of the radiation temperature from the core. The radiometer consisted of a quad ridged horn antenna with a 3.8-8.2GHz bandwidth. Received power was amplified by 80dB with a pair of low noise amplifiers and split into 16 bandpass limited diode detectors. Each diode detector was equipped with a 125MHz bandwidth cavity filter. Absolute calibration of the radiometer was achieved by measuring blackbody emission from a microwave absorbing material measured at room temperature and in a liquid nitrogen bath. The plasma is considered to be optically thick for EBW emission and thus can be considered as a blackbody source with well localized emission. Modeling of received waves with Genray allows mapping of measured radiation temperature onto the emitting flux surface which can be converted to minor radius and compared to Thomson data (**Figure A.18**).

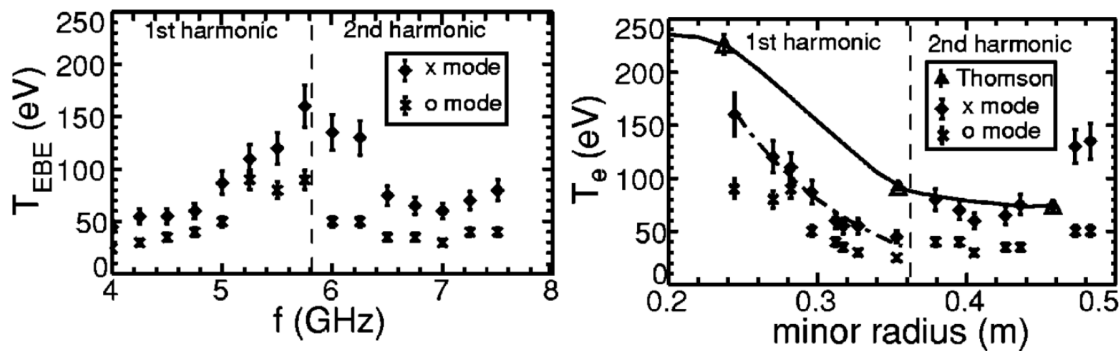


Figure A.18. Measurement of X and O mode EBE over 4-8GHz(left). Temperature measurement mapped to minor radius and compared to Thomson data(right). Figure courtesy of [113].

Comparison of the absolute magnitude of EBE and Thomson profiles of measured data can be used to compute the mode conversion efficiency. In MST conditions of $n_e = 0.4 \times 10^{19} \text{ m}^{-3}$, $L_n \sim 1.4 \text{ cm}$, $\alpha = 2$ for 5.75GHz emission lead to $\eta = 0.46$ and a theoretical maximum mode

conversion efficiency of $C_{\max} \sim 70\%$. Experimental mode conversion efficiencies of 75% were found to be in good agreement with this prediction.

By reciprocity, an emitted wave from the plasma will follow the same path as an EBW wave launched for heating or current drive applications. The measurement of core emission through mode conversion in the 4-8GHz range demonstrates the X-mode accessibility to EBW heating in these frequency bands.

Simulations of EBW current drive in MST [114] have predicted that efficient localized current drive is possible in an RFP plasma. Current drive in the RFP is challenging due to the high dielectric strength ($\omega_{pe} / \omega_{ce} > 5$) which imposes accessibility limitations and leads to ion damping of high harmonic fast waves in the plasma edge that reduces current drive efficiency. Unlike LHCD, EBW offers ray trajectories that may be effectively used for current profile control. The sign of n_{\parallel} at the absorption location determines the direction of driven current (**Figure A.19**). Generally, in MST, launch above the mid-plane results in co-current drive, while launch below the midplane results in counter-current drive. In each case the EBW ray bends toward the midplane before being absorbed. Absorption locations are shifted radially outward from the cold plasma cyclotron location; for EBW the rays are absorbed at the Doppler shifted cyclotron resonance. The shift in n_{\parallel} is strongly affected by the large poloidal field in the RFP; the rate at which n_{\parallel} increases becomes larger as the wave approaches resonance leading to highly localized current deposition on the tail of the electron distribution. Radial accessibility

becomes limited when the magnetic field is reduced to a point where the second harmonic passes the inner wall, leading to strong EBW absorption in the edge.

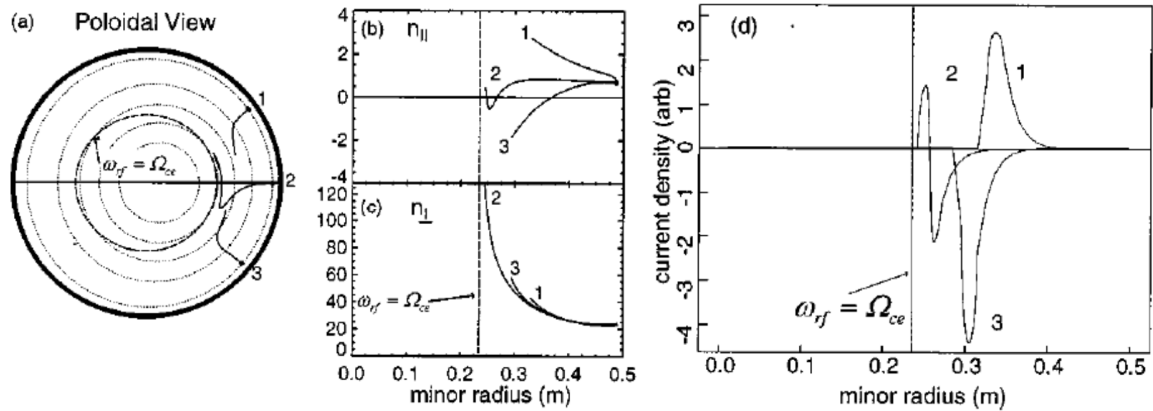


Figure A.19. Genray trajectories of EBW at 3 poloidal launch angles(left). Value of N_{\perp} and N_{\parallel} as the ray approaches the absorption location(center). Magnitude of driven current density(right). Figure courtesy of [114].

Appendix References

- [100] H. Sugai, Mode Conversion and local Heating below the Second Electron Cyclotron Harmonic. *Phys. Rev. Lett.* 47, 1899 (1981)
- [101] H. P. Laqua et al. Resonant and Nonresonant Electron Cyclotron Heating at Densities above the Plasma Cutoff by O-X-B Mode Conversion at the W7-As Stellarator. *Phys. Rev. Lett.* 78, 3467 (1997)
- [102] H. P. Laqua et al. Electron Bernstein Wave Emission from an Overdense Plasma at the W7-AS Stellarator. *Phys. Rev. Lett.* 81, 2060 (1998)
- [103] H. P. Laqua et al. Electron-Bernstein-Wave Current Drive in an Overdense Plasma at the Wendelstein 7-AS Stellarator. *Phys. Rev. Lett.* 90, 075003 (2003)
- [104] Y.Y. Podoba et al. Direct Observation of Electron-BernsteinWave Heating by O-X-B-Mode Conversion at Low Magnetic Field in the WEGA Stellarator. *Phys. Rev. Lett.* 98, 255003 (2007)
- [105] C.B. Forest, R.W. Harvey, A.P. Smirnov. Power deposition by mode converted electron Bernstein waves in the DIII-D 'heat pinch' experiments. *Nuclear Fusion.* 41, 619 (2001)
- [106] T. Maekawa et al. Doppler-Shifted Cyclotron Absorption of Electron Bernstein Waves via Nk-Upshift in a Tokamak Plasma. *Phys. Rev. Lett.* 86, 3783 (2001)
- [107] V. Shevchenko et al. Generation of Noninductive Current by Electron-Bernstein Waves on the COMPASS-D Tokamak. *Phys. Rev. Lett.* 89, 265005 (2002)

-
- [108] B. Jones et al. Controlled Optimization of Mode Conversion from Electron Bernstein Waves to Extraordinary Mode in Magnetized Plasma. *Phys. Rev. Lett.* 90, 165001 (2003)
- [109] S. Shiraiwa et al. Heating by an Electron Bernstein Wave in a Spherical Tokamak Plasma via Mode Conversion *Phys. Rev. Lett.* 96, 185003 (2006)
- [110] S. J. Diem et al. Collisional Damping of Electron Bernstein Waves and its Mitigation by Evaporated Lithium Conditioning in Spherical-Tokamak Plasmas. *Phys. Rev. Lett.* 103, 015002 (2009)
- [111] M. Uchida *et al.* Rapid Current Ramp-Up by Cyclotron-Driving Electrons beyond Runaway Velocity. *Phys. Rev. Lett.* 104, 065001 (2010)
- [112] M. Cengher, J.K. Anderson, V. Svidzinski, C.B. Forest, Coupling to the electron Bernstein wave using a phased array of waveguides in MST reversed field pinch. *Nuc. Fusion.* 46, 521, (2006)
- [113] P.K. Chattopadhyay, *et al.* Electron Bernstein wave emission from an overdense reversed field pinch plasma. *Phys. Plasmas* 9, 752 (2002)
- [114] C.B. Forest, P.K. Chattopadhyay, R.W. Harvey, and A.P. Smirnov, C.B. Forest, *Phys. Plasmas* 7, 1352 (2000)